

# **Origin, symmetry and elastic tuneability of charge density waves in the superconductor $\text{BaNi}_2(\text{As}_{1-x}\text{P}_x)_2$**

Zur Erlangung des akademischen Grades eines  
DOKTORS DER NATURWISSENSCHAFTEN (Dr. rer. nat.)

von der KIT-Fakultät für Physik des  
Karlsruher Instituts für Technologie (KIT)  
genehmigte

Dissertation

von

M.Sc., Lacmann, Tom Laurin

Tag der mündlichen Prüfung: 22.11.2024

1. Referent: Prof. Dr. Matthieu Le Tacon
2. Korreferent: Prof. Dr. Jörg Schmalian









# Abstract

The interplay between charge orders, such as nematicity, charge density waves (CDWs) and superconductivity and their origin are a conspicuous research interest in the field of quantum materials. Especially the tuning of quantum materials via chemical substitution or chemical “pressure”, hydrostatic and uniaxial pressure has proven insightful.  $\text{BaNi}_2\text{As}_2$  is a promising system for the study of the origin and interplay of (dynamic) nematicity, CDWs and superconductivity. The origin, ordering mechanism, orbital structure, symmetry and tuneability, especially of the two CDWs, are unknown and largely unexplored. This thesis will answer the aforementioned open questions using (non-resonant) inelastic X-ray scattering (IXS) combined with thermal diffuse scattering (TDS) and density functional perturbation theory (DFPT), resonant elastic X-ray scattering (REXS) and X-ray diffraction (XRD). All of these methods were performed on non- and phosphorus-substituted samples to study the effect of chemical “pressure”. The XRD investigations are further combined with externally applied hydrostatic and uniaxial pressure.

This thesis shows that the incommensurate CDW (I-CDW) in  $\text{BaNi}_2\text{As}_2$  is soft-phonon driven and only weakly influenced by phosphorus substitution. The first-principles calculations show that the I-CDW does not originate from Fermi surface nesting or  $\vec{q}$ -dependent electron-phonon coupling (EPC), indicating its unconventional nature. In contrast, no soft-phonon driving the commensurate CDW (C-CDW) could be found experimentally. The energy and azimuthal dependent REXS measurements clearly show that both CDWs are linked to a highly comparable orbital ordering, likely of the nickel  $d_{xz,yz}$  orbitals. From the investigation of the tensor atomic form factor, the local nickel symmetry of the I-CDW is monoclinic or lower and a full description requires dipole-quadrupole interactions. The hydrostatic pressure investigation reveals new CDW instabilities related to two new monoclinic structures. Remarkably, the ambient pressure I-CDW is very resistant against the application of hydrostatic pressure. Furthermore, above roughly 11 GPa, all CDW instabilities disappear and a “collapsed” monoclinic structure is observed. This structure shows some resemblance to the collapsed tetragonal (cT) structure seen in other pnictides under pressure. Within this structure, the nickel-arsenic bonds are significantly altered, highlighting the importance of orbital hybridization to the CDW formation. The combination of hydrostatic pressure with phosphorus substitution suppresses partially or fully the low temperature structures and the associated CDW instabilities. Finally, under applied uniaxial pressure, an enhancement of the I-CDW along the pressure direction and a suppression of the I-CDW perpendicular to it is only observed in the ordered and not fluctuating regime. Altogether, this thesis highlights the importance of the orbital hybridization and their ordering in  $\text{BaNi}_2\text{As}_2$  especially regarding the CDW formation.



# Zusammenfassung

Der Ursprung und die Wechselwirkung verschiedener elektronischer Ordnungsphänomene wie Ladungsdichtewellen und Supraleitung sind ein hochinteressantes Forschungsfeld in vielen Quantenmaterialien. Insbesondere die Beeinflussung durch chemische Substituierung oder chemischen „Druck“, sowie hydrostatischen und uniaxialem Druck haben sich als besonders erkenntnisreich erwiesen.  $\text{BaNi}_2\text{As}_2$  ist ein aussichtsreiches Material zur Untersuchung des Ursprunges und der Wechselwirkung zwischen (dynamischer) Nematizität, Ladungsdichtewellen und Supraleitung. Der Ursprung, Ordnungsmechanismus, Symmetrie und Beeinflussbarkeit durch Druck, vor allem für die Ladungsdichtewellen, sind größtenteils unbekannt und unerforscht. In dieser Doktorarbeit werden die zuvor genannten offenen Fragen genauer untersucht. Dafür werden inelastische Röntgenstreuung, thermische diffuse Röntgenstreuung, Dichtefunktionaltheorie, resonante elastische Röntgenstreuung und Röntgendiffraktion an reinem und phosphorsubstituiertem  $\text{BaNi}_2\text{As}_2$  angewendet. Die Röntgendiffraktion wird zusätzlich unter hydrostatischem und uniaxialem Druck durchgeführt.

In dieser Doktorarbeit wird gezeigt, dass die inkommensurable Ladungsdichtewelle in  $\text{BaNi}_2\text{As}_2$  durch ein niederenergetisches Phonon getrieben wird und nur wenig durch Phosphorsubstituierung beeinflusst wird. Die Ab-Initio-Rechnungen finden keine Anzeichen für Fermi-Flächen-Nesting oder  $\vec{q}$ -abhängige Elektron-Phonon-Kopplung, was auf eine unkonventionelle Natur der Ladungsdichtewelle hindeutet. Im Gegensatz dazu lässt sich für die kommensurable Ladungsdichtewelle in den Experimenten kein vergleichbares niederenergetisches Phonon ausmachen, das für die Instabilität verantwortlich ist. Die energie- und azimutwinkelabhängigen resonant elastischen Röntgenstreuungsexperimente offenbaren eine größtenteils vergleichbare orbitale Ordnung für beide Ladungsdichtewellen, die wahrscheinlich mit den  $d_{xz,yz}$  Orbitalen zusammenhängt. Dabei zeigt die Untersuchung des tensoriellen atomaren Strukturfaktors, dass die lokale Symmetrie an der Nickelposition monoklin oder niedriger ist. Zudem wird für eine vollständige Beschreibung des Experiments neben Dipole-Dipole Übergängen auch Dipole-Quadrupole Übergänge benötigt. In den Diffraktionsexperimenten unter hydrostatischem Druck werden zwei neue monokline Strukturen, die eng mit neuen Ladungsdichtewellen zusammenhängen, gefunden. Die ursprüngliche inkommensurable Ladungsdichtewelle, zeigt sich dabei als ungewöhnlich widerstandsfähig gegenüber hydrostatischem Druck. Erst in einer monoklinen Struktur über 11 GPa sind alle Ladungsdichtewellen verschwunden. Die monokline Struktur weist dabei einige Übereinstimmungen mit der kollabierten tetragonalen Struktur, die in anderen Pniktiden gefunden wurde, auf. Innerhalb dieser Struktur sind die Nickel-Arsen Bindungen deutlich verändert. Dies hebt die Bedeutung der Hybridisierung der Nickel- und Arsenorbitale für die Formierung der Ladungsdichtewellen hervor. Die Kombination von Phosphorsubstitution und hydrostatischem Druck zeigt weitgehend das gleiche Phasendiagramm. Allerdings werden alle Tieftemperaturstrukturen und die damit verbundenen Ladungsdichtewellen teilweise oder vollständig unterdrückt. Die Messungen unter uniaxialem Druck zeigen eine Verstärkung der inkommensurablen Ladungsdichtewelle entlang der Druckrichtung und eine Unterdrückung der inkommensurablen Ladungsdichtewellen orthogonal dazu. Dies ist jedoch nur in der geordneten Phase und nicht in der fluktuierenden Phase zu beobachten. Zusammengefasst zeigt diese Doktorarbeit die Wichtigkeit der orbitalen Ordnung und Hybridisierung in  $\text{BaNi}_2\text{As}_2$ , insbesondere für die Formierung der Ladungsdichtewellen, auf.



# Contents

<b>Abstract</b> . . . . .	<b>iii</b>
<b>Zusammenfassung</b> . . . . .	<b>v</b>
<b>1. Introduction</b> . . . . .	<b>1</b>
<b>2. Introduction to <math>\text{BaNi}_2\text{As}_2</math></b> . . . . .	<b>5</b>
<b>3. Physical basics</b> . . . . .	<b>11</b>
3.1. Charge density waves . . . . .	11
3.2. Introduction to X-ray scattering . . . . .	15
3.2.1. Classification and generation of X-rays . . . . .	15
3.2.2. Interaction of X-rays with the crystal . . . . .	17
3.3. Pressure generation . . . . .	26
3.3.1. Overview . . . . .	26
3.3.2. Diamond anvil cell . . . . .	27
3.3.3. Piezoelectric uniaxial pressure cells . . . . .	29
<b>4. Origin of the charge density waves</b> . . . . .	<b>31</b>
4.1. Introduction . . . . .	31
4.2. Experimental and computational details . . . . .	32
4.2.1. Experimental details . . . . .	32
4.2.2. Computational details . . . . .	33
4.3. Incommensurate charge density wave . . . . .	34
4.3.1. Thermal diffuse scattering and incommensurate charge density wave transition temperature . . . . .	34
4.3.2. Thermal diffuse scattering simulations . . . . .	41
4.3.3. Soft phonon origin of the incommensurate charge density wave for $x=0;0.1$ . . . . .	43
4.3.4. IXS along the longitudinal and diagonal directions . . . . .	46
4.3.5. First-principles calculations on the soft phonon origin of the incommensurate charge density wave . . . . .	48
4.4. Commensurate charge density wave . . . . .	49
4.4.1. Diffuse scattering of the commensurate charge density wave . . . . .	49
4.4.2. Phonons at the commensurate charge density wave phase transition . . . . .	50
4.5. Summary and discussion . . . . .	52
<b>5. Symmetry of the charge density waves</b> . . . . .	<b>57</b>
5.1. Introduction . . . . .	57
5.2. Experimental details . . . . .	58
5.3. Energy and temperature dependence of the charge density waves . . . . .	59
5.4. Azimuthal dependence of the charge density waves . . . . .	61
5.4.1. Azimuthal dependence measurements . . . . .	61

5.4.2.	Tensor atomic form factor of the incommensurate charge density wave . . . . .	62
5.4.3.	Tensor atomic form factor of the commensurate charge density wave . . . . .	67
5.5.	Discussion . . . . .	69
<b>6.</b>	<b>Pressure tuning of the charge density waves . . . . .</b>	<b>73</b>
6.1.	Introduction . . . . .	73
6.2.	Experimental details . . . . .	75
6.2.1.	General . . . . .	75
6.2.2.	Hydrostatic pressure experiments on pristine $\text{BaNi}_2\text{As}_2$ . . . . .	75
6.2.3.	Hydrostatic pressure experiments on phosphorus substituted $\text{BaNi}_2\text{As}_2$ . . . . .	76
6.2.4.	Uniaxial compression experiments . . . . .	77
6.3.	Hydrostatic pressure tuning of pristine $\text{BaNi}_2\text{As}_2$ . . . . .	78
6.3.1.	Isotherm at 140 K . . . . .	78
6.3.2.	Isotherm at 94 K . . . . .	81
6.3.3.	Isobars and temperature dependence of the phases . . . . .	82
6.3.4.	Connection of high pressure structures and atomic position changes . . . . .	86
6.3.5.	First principles calculations . . . . .	88
6.3.6.	Phase diagram and summary . . . . .	91
6.4.	Substitution effect on the high-pressure phases diagram . . . . .	92
6.4.1.	Isotherm at 80 K . . . . .	92
6.4.2.	Isotherm at 25 K . . . . .	94
6.4.3.	Phase diagrams and summary . . . . .	97
6.5.	Uniaxial pressure tuning on pure and phosphorus substituted $\text{BaNi}_2\text{As}_2$ . . . . .	98
6.6.	Comparison of chemical, hydrostatic and uniaxial pressure and discussion . . . . .	102
<b>7.</b>	<b>Conclusion and outlook . . . . .</b>	<b>107</b>
	<b>Acknowledgements . . . . .</b>	<b>109</b>
	<b>Bibliography . . . . .</b>	<b>111</b>
	<b>List of figures . . . . .</b>	<b>121</b>
	<b>List of tables . . . . .</b>	<b>125</b>
	<b>Symbols . . . . .</b>	<b>127</b>
	<b>Acronyms . . . . .</b>	<b>131</b>
<b>A.</b>	<b>Appendix to Chapter 4 . . . . .</b>	<b>133</b>
<b>B.</b>	<b>Appendix to Chapter 5 . . . . .</b>	<b>137</b>
<b>C.</b>	<b>Appendix to Chapter 6 . . . . .</b>	<b>141</b>
C.1.	Samples and pressure paths . . . . .	141
C.2.	Structural details . . . . .	142
C.3.	I-CDW1 intensity and linecuts . . . . .	146
C.4.	Uniaxial compression of a $x=0$ sample at 140 K . . . . .	147
<b>D.</b>	<b>Inelastic X-ray scattering at the I-CDW2 position in an P-substituted <math>x=0.1</math> sample at ambient pressure . . . . .</b>	<b>149</b>



# 1. Introduction

Electronic orders are common but intriguing phenomena in many quantum materials. During a period extending over slightly more than the past century, a series of electronic order phenomena have been discovered. The most important of these were, in 1911, the discovery of superconductivity by Heike Kamerlingh Onnes [1] and, in the 1950s, the description of charge density waves (CDWs) by Fröhlich [2] and Peierls [3]. Moreover, further phenomena, such as nematicity and new types of magnetism, for example the spin density wave (SDW) [4] or altermagnetism [5], were discovered.

Often several of the aforementioned phenomena coexist in close vicinity in the phase diagram, as is found in the cuprates [6], iron-based superconductors [7] or transition metal dichalcogenides [8]. Some orders seem to compete, such as superconductivity and CDWs in the cuprates [8], while, for others, a mutual enhancement is proposed. For example, enhancement of superconductivity by nematicity has been suggested [9]. Understanding the interplay and origin of these different orders is one of the main research areas in modern condensed matter research. One promising path is to investigate the tuneability of the phases and compare the response in different materials. Common tuning parameters are chemical substitution or chemical “pressure” and externally applied hydrostatic pressure. Especially since the development of piezoelectric uniaxial pressure cells, uniaxial pressure has become a common and insightful tuning parameter [10–13].

The introduction of the use of synchrotron radiation in the second half of the 20<sup>th</sup> century enabled the investigation of electronic orders via an entirely new set of X-ray diffraction and scattering techniques which would otherwise have been impossible or very difficult [14–17]. The higher photon flux and brilliance made it possible to investigate, for example, phonons using (non-resonant) inelastic X-ray scattering (IXS) in much smaller samples than with inelastic neutron scattering (INS) [15]. This is especially important because many quantum materials cannot yet be grown as large crystals. The tuneability of the incoming X-ray energy also allows for measurements in resonance between atomic levels. This allows for element and orbital specific measurements, which provide insight into both the orbital states of charge orders and magnetic states [16]. Furthermore, the higher flux and superior beam characteristics made it feasible to combine different X-ray techniques and externally applied pressure to study the tuneability of various electronic orders using X-rays [12, 17].

Over time, there have been studies of electronic orders and their tuneability in a wide variety of materials.  $\text{BaFe}_2\text{As}_2$  has proven to be a promising system in which the interplay between spin degrees of freedom, for example a SDW, nematicity and superconductivity has been examined [7, 18, 19]. It is generally believed that spin degrees of freedom are important for the physics of  $\text{BaFe}_2\text{As}_2$ . New insight can come from the investigation of charge or orbital instead of spin degrees of freedom. For this,  $\text{BaNi}_2\text{As}_2$  is an ideal platform, as it is isostructural to  $\text{BaFe}_2\text{As}_2$ , but no long range magnetic order has been found [20, 21]. In addition, two CDWs (instead of the SDW seen in  $\text{BaFe}_2\text{As}_2$ ), dynamic nematicity and superconductivity at ambient pressure have been observed [22–24]. Further studies showed tuneability by chemical “pressure” and found the first indications of orbital ordering [25–27]. The ordering mechanisms and symmetries of the CDWs, the influence of the orbitals on them and the response to hydrostatic and uniaxial pressure remain unknown.

In this thesis, these remaining open questions of the physics of  $\text{BaNi}_2\text{As}_2$  will be explored. The focus is on the ordering mechanism, symmetry, orbital order and tuneability of the incommensurate CDW (I-CDW) and commensurate CDW (C-CDW) in  $\text{BaNi}_2\text{As}_2$ . For this purpose, various X-ray diffraction and scattering techniques, performed at large-scale synchrotron radiation facilities, are used, together with chemical “pressure” via phosphorus substitution, hydrostatic pressure and uniaxial pressure at low temperatures. More precisely, combined thermal diffuse scattering (TDS) and IXS measurements are used to examine the phonons in  $\text{BaNi}_2(\text{As}_{1-x}\text{P}_x)_2$ , in order to answer the question of the ordering mechanism of the CDWs. Resonant elastic X-ray scattering (REXS) is used to investigate the symmetry of the CDWs, the orbitals, their order and their influence on the CDW formation. Finally, X-ray diffraction (XRD) is used in combination with external pressure to study the external tuneability of the crystal structure and the CDWs. The thesis is divided into two introductory chapters, three experimental main chapters and a final chapter summarizing the results of the thesis.

Before discussing the details of the CDWs, first, in Chapter 2, the current status of research on  $\text{BaNi}_2\text{As}_2$  is reviewed. In the following chapter the possible ordering mechanisms and phenomenology of CDWs is introduced. In addition, the generation of X-rays and their interaction with matter are presented. In the last section of this chapter, the generation of hydrostatic and uniaxial pressure, with a focus on diamond anvil cells (DACs) and piezoelectric uniaxial pressure cells, is explored.

In Chapter 4, the TDS and IXS experiments, along with density functional perturbation theory (DFPT) and TDS intensity calculations on phosphorus substituted  $\text{BaNi}_2\text{As}_2$  are presented. The experiments reveal that a soft phonon drives the I-CDW transition in non-substituted and phosphorus substituted  $\text{BaNi}_2\text{As}_2$ . The DFPT calculations are in good agreement with the experimental data. However, the calculations show no indication of Fermi surface nesting or locally enhanced electron-phonon coupling (EPC), meaning that no conventional ordering mechanism can explain the formation of the CDW. For different phosphorus substitution levels, the underlying ordering mechanisms of the I-CDW are comparable, although the transition temperature is lowered and the transition is broader. For the C-CDW, no comparable soft phonon driving the transition could be found experimentally.

The symmetry of the CDW and orbital order are discussed in Chapter 5. The dependence on the incoming photon energy of the resonant elastic (REXS) and inelastic X-ray scattering (RIXS) experiments reveals a resonance of the CDW at the rising flank of the X-ray absorption. This energy range was earlier attributed to the  $d_{xz,yz}$  orbitals. The azimuthal dependence discloses that the local I-CDW symmetry at the nickel site has a lower symmetry than orthorhombic. The highest possible symmetry is monoclinic, with the twofold axis being along the I-CDW direction ( $y$ -direction in the experiment). The differences in the energy dependence and azimuthal dependence between the I-CDW and C-CDW are small, suggesting that they have a similar orbital order.

In the last experimental chapter — Chapter 6 — the different phases are tuned by hydrostatic pressure and uniaxial pressure and investigated by XRD. First, the response to hydrostatic pressure of non-substituted  $\text{BaNi}_2\text{As}_2$  is discussed. The measurements reveal two new monoclinic phases, new CDW instabilities and an unusually high resilience of the I-CDW against pressure. Above approximately 11 GPa, all CDW instabilities are suppressed. At the same pressure, a “collapsed” monoclinic phase appears, which exhibits some resemblance to the collapsed tetragonal (cT) structure observed in other pnictides. This occurs in conjunction with changes to the nickel and arsenic bonds, emphasizing the importance of the hybridization of the nickel and arsenic orbitals to the formation of the CDWs. Afterward, the hydrostatic pressure  $p$ – $T$  phase diagrams for samples below and above the critical phosphorus substitution level are discussed. In general, the same phases are observed, but all low-temperature phases are suppressed, similarly to the behavior at ambient pressure. In the last section, XRD experiments with uniaxial pressure applied along the  $a$  direction are presented. The I-CDW is enhanced along the pressure direction with increasing pressure while the superstructure peaks in the

orthogonal direction are suppressed. This change is, however, not compatible with an orthorhombic detwinning. Furthermore, a clear response is only observed in the ordered state of the I-CDW.

In the final chapter, the results of this thesis are summarized, discussed and an outlook for future research is given.



## 2. Introduction to BaNi<sub>2</sub>As<sub>2</sub>

BaNi<sub>2</sub>As<sub>2</sub> was initially synthesized by Pfisterer and Nagorsen [28] in 1980 and subsequently investigated as a member of the so-called 122 compounds, which possess the general formula AT<sub>2</sub>Pn<sub>2</sub> (A = alkaline-earth or rare-earth atom, T = transition metal atom and Pn = pnictogen atom [As, P or Sb]) [28–30]. Similar to many members of this series, BaNi<sub>2</sub>As<sub>2</sub> crystallizes at ambient conditions in the ThCr<sub>2</sub>Si<sub>2</sub> structure with tetragonal *I4/mmm* symmetry with lattice parameters  $a = b = (4.1413 \pm 0.0006) \text{ \AA}$  and  $c = (11.6424 \pm 0.0024) \text{ \AA}$  [27]. The crystal structure is depicted in Figure 2.1a. BaNi<sub>2</sub>As<sub>2</sub> can be grown using lead or self-flux and plate-like, metallic, shiny crystals with sizes up to 3 mm × 2 mm × 0.5 mm can be removed from the flux [20, 23, 24, 27].

With the discovery of superconductivity in iron-based materials, the research interest in BaNi<sub>2</sub>As<sub>2</sub> was rekindled. BaNi<sub>2</sub>As<sub>2</sub> was considered to be the isostructural, but non-magnetic, counterpart to the

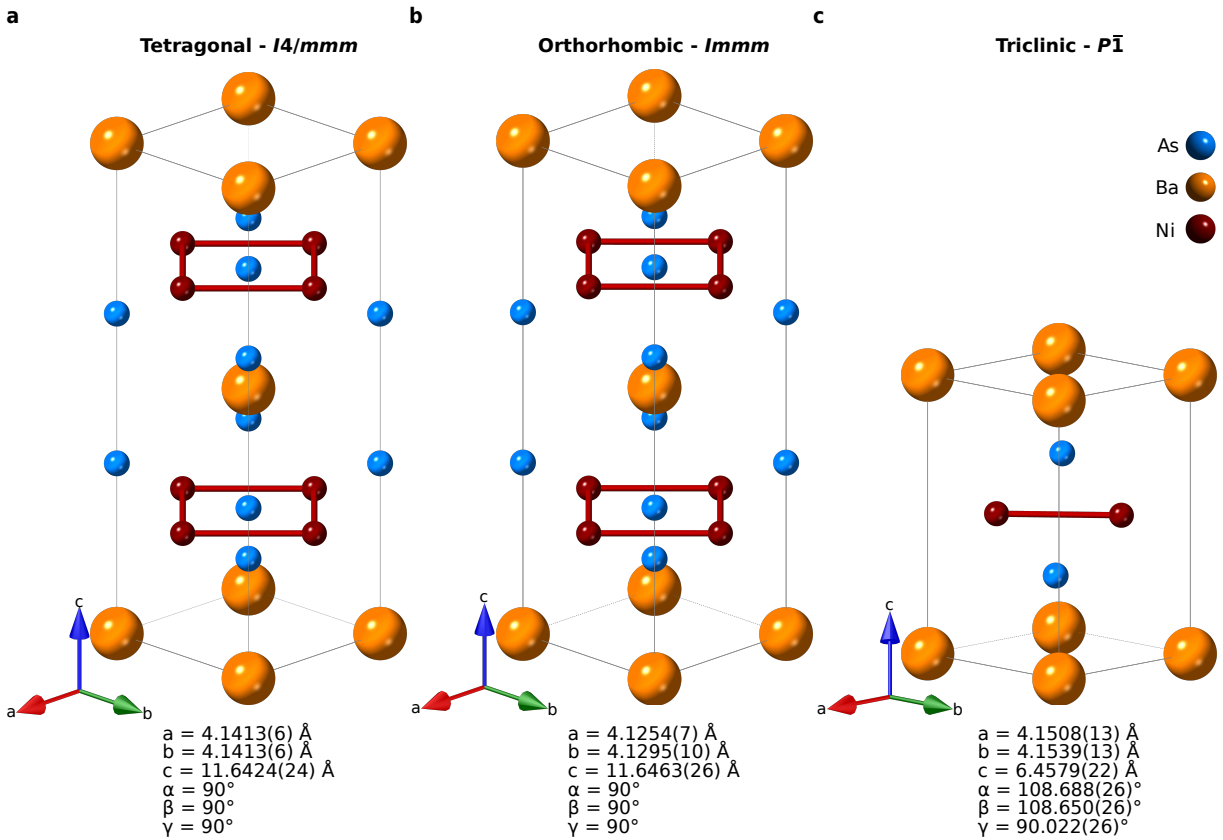


**Figure 2.1.:** Sketch of the different crystal structures of BaNi<sub>2</sub>As<sub>2</sub>. **a** Tetragonal structure with Ni-Ni bonds of BaNi<sub>2</sub>As<sub>2</sub> at 295 K and ambient pressure. **b** Orthorhombic structure with Ni-Ni bonds of BaNi<sub>2</sub>As<sub>2</sub> at 140 K and ambient pressure. **c** Triclinic structure with Ni-Ni bonds of BaNi<sub>2</sub>As<sub>2</sub> at 90 K and ambient pressure. The lattice parameters shown and used for the plot of the crystal structure were taken from Merz et al. [27]. The arsenic atoms are shown in light blue, the barium atoms in light orange and the nickel atoms in dark red.

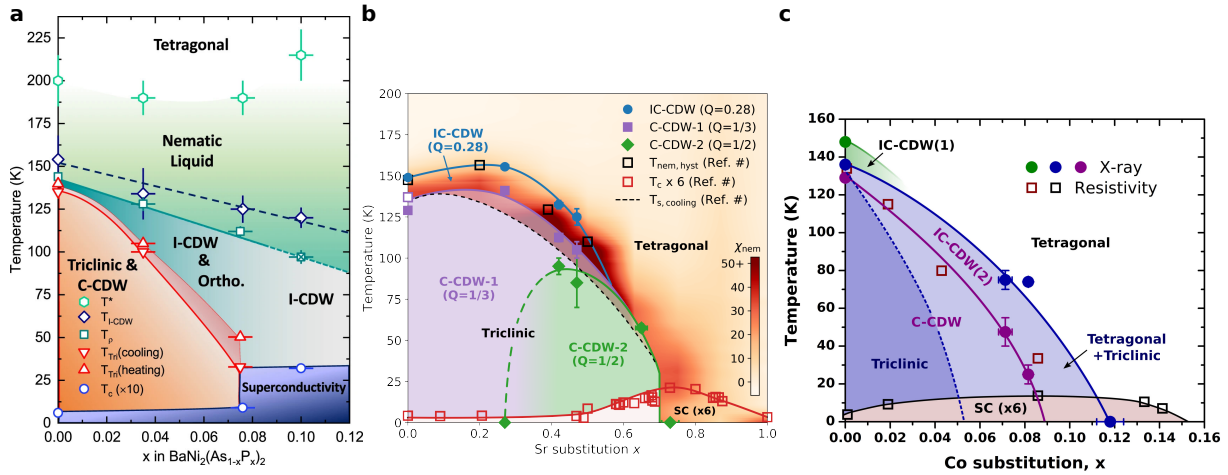


**Figure 2.2.: Phosphorus, strontium and cobalt substitution phase diagrams of  $\text{BaNi}_2\text{As}_2$ .** **a** Phosphorus substitution phase diagram of  $\text{BaNi}_2(\text{As}_{1-x}\text{P}_x)_2$ . The nematic liquid, I-CDW, orthorhombic, triclinic and superconducting phases are indicated. The figure is reproduced from Yao et al. [23] under the CC-BY 4.0. **b** Strontium substitution phase diagram of  $\text{BaNi}_2\text{As}_2$ . The I-CDW and triclinic phases with C-CDW 1 and C-CDW 2 and the superconducting phase are indicated. Reprinted figure with permission from S. Lee, J. Collini, S. X.-L. Sun, M. Mitrano, X. Guo, C. Eckberg, J. Paglione, E. Fradkin, and P. Abbamonte, Physical review letters **127**, 027602 (2021) [26]. Copyright 2021 by the American Physical Society. **c** Cobalt substitution phase diagram of  $\text{BaNi}_2\text{As}_2$ . The I-CDW and triclinic phases with C-CDW and the superconducting phase are indicated. Reprinted figure with permission from S. Lee, G. d. La Peña, S. X.-L. Sun, M. Mitrano, Y. Fang, H. Jang, J.-S. Lee, C. Eckberg, D. Campbell, J. Collini, J. Paglione, F. M. F. d. Groot, and P. Abbamonte, Physical review letters **122**, 147601 (2019) [22]. Copyright 2019 by the American Physical Society.

parent compound of the iron-based superconductors  $\text{BaFe}_2\text{As}_2$ . Subsequently, superconductivity below 0.7 K [24] was found in  $\text{BaNi}_2\text{As}_2$ , but no signs of long-range magnetic ordering [21].

Similar to  $\text{BaFe}_2\text{As}_2$ , a structural phase transition at 137 K (on heating) was found [24, 27]. However, the transition is a strong first-order transition to a triclinic symmetry with space group  $P\bar{1}$  [20] instead to orthorhombic  $Fmmm$ . The crystal structure is presented in Figure 2.1c. In both phases  $\text{BaNi}_2\text{As}_2$  is a good metal with mainly nickel bands crossing the Fermi level [31–34]. The resistivity and the resistivity jump at the triclinic transition is very anisotropic between in-plane and out-of-plane [20].

More recent studies revealed that the structural transition is preceded by a unidirectional I-CDW with wavevector  $q_{\text{I-CDW}} = (0.28 \ 0 \ 0), (0 \ 0.28 \ 0)$  at around 150 K [22, 27]. Furthermore, in the triclinic phase the I-CDW is replaced by a C-CDW with wavevector  $q_{\text{C-CDW}} = (\pm 1/3 \ 0 \mp 1/3), (0 \ \pm 1/3 \ \mp 1/3)$  (in tetragonal notation). Several angle-resolved photoemission spectroscopy (ARPES) investigations did not find signatures for Fermi surface nesting compatible with the CDWs [33–37], but Guo et al. [36] identifies band folding compatible with the C-CDW. In the same study ARPES measurements with uniaxial stress suggest independent, but strongly coupled order parameters for the triclinic phase and C-CDW. In addition to XRD, the C-CDW was also observed by scanning tunneling microscope (STM), which confirmed the unidirectional character of the C-CDW [38].

Around the same temperature of 142 K as the I-CDW formation, high-resolution thermal expansion measurements revealed a second-order phase transition that distorts the in-plane square. The XRD measurements show that the nickel atom moves in the structure to the new position  $(1/2 \ 0 \ 1/4 + \delta)$ , leading to the distortion of the nickel-arsenic tetrahedral by elongating and shortening two bonds. This breaks the fourfold rotational symmetry and the most-likely structure is an orthorhombic structure with space group  $Immm$  [27]. The same study shows the resulting distortion of the nickel square to a rectangle with additional modulation along the  $c$  direction, forming nickel zigzag chains in the orthorhombic phase. In the triclinic phase, the chains are further distorted to nickel dimers. The

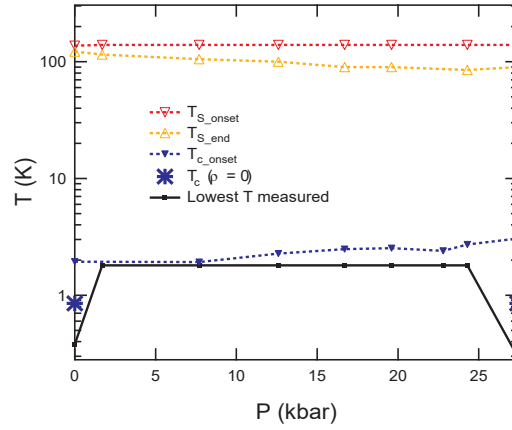


**Figure 2.3.: Hydrostatic pressure phase diagram of BaNi<sub>2</sub>As<sub>2</sub> up to 2.74 GPa.**  $p$ - $T$  phase diagram of BaNi<sub>2</sub>As<sub>2</sub> up to 2.74 GPa showing the triclinic and superconducting transitions including their width. The transitions are extracted from resistivity data and the black squares indicate the lowest measured temperature at this pressure. This figure is reproduced from T. Park, H. Lee, E. D. Bauer, J. D. Thompson, and F. Ronning, Journal of Physics: Conference Series **200**, 012155 (2010) [45]. © IOP Publishing. Reproduced with permission. All rights reserved.

additional near edge X-ray absorption fine structure (NEXAFS) measurements support the importance of orbital ordering and reveal the change of relative weight from  $d_{xy}$  to  $d_{xz,yz}$  orbitals [27]. Furthermore, theoretical calculations indicate that the arsenic-arsenic bond patterns are important for the electronic structure in BaNi<sub>2</sub>As<sub>2</sub> [39].

The structural and CDW transitions can be effectively tuned by chemical substitution or chemical “pressure”. For all substituents — phosphorus [23, 25, 40], strontium [26, 41], cobalt [22, 42] and copper [43] — a suppression of the triclinic phase is reported. A selection of phase diagrams is presented in Figure 2.2. At the substitution level at which the triclinic phase is suppressed, the superconducting transition temperature jumps up to 3.5 K [41]. Studies reporting the CDWs also reveal a suppression of the I-CDW and C-CDW with increasing substitution [22, 23, 25, 26]. However, in the details, the substituents exhibit differences. For phosphorus substitution, the triclinic and C-CDW phase is already suppressed for a phosphorus level of  $\approx 7\%$  [23, 40]. At the same substitution level the superconducting  $T_c$  jumps to 3.3 K and the orthorhombic phase is exchanged with a new phase X with currently unknown symmetry. The I-CDW, however, is also observed at higher substitution levels [23, 25]. In addition, thermodynamic measurements indicate a strong softening of the phonons, probably related to an unstable phonon branch related to the I-CDW [25, 40]. The same study does not find an indication for a nematic critical behavior at the critical phosphorus substitution, but a diverging uniaxial phonon Grüneisen parameter, which could be related to a phonon quantum critical behavior [25]. For strontium substitution, the triclinic phase is only suppressed with a substitution of around 70%, but the superconducting  $T_c$  jumps to a similar value of 3.5 K. In contrast to the phosphorus case, the I-CDW is completely suppressed at a lower substitution level. A newer study, however, indicates that the I-CDW is suppressed at a higher substitution level than the triclinic transition [44]. Furthermore, the C-CDW is already suppressed at a substitution of around 50% and replaced by a C-CDW 2 with wavevector  $q_{\text{C-CDW2}} = (\pm 1/2, 0, \mp 1/2), (0, \pm 1/2, \mp 1/2)$ . For the strontium system, at the strontium level where the triclinic phase is suppressed, a recent ARPES study suggests changes in the Fermi surface with a Lifshitz transition and good nesting between electron and hole pockets related to the nickel  $d_{xz,yz}$  orbitals [37]. Moreover, the change of the lattice parameters varies between different substituents.

Besides chemical substitution, the application of hydrostatic pressure has proven to be an efficient tuning parameter in the iron counterpart BaFe<sub>2</sub>As<sub>2</sub> [46]. For BaNi<sub>2</sub>As<sub>2</sub>, however, so-far only one resistivity study up to 2.74 GPa was conducted [45]. Park et al. [45] find only a small dependence of the

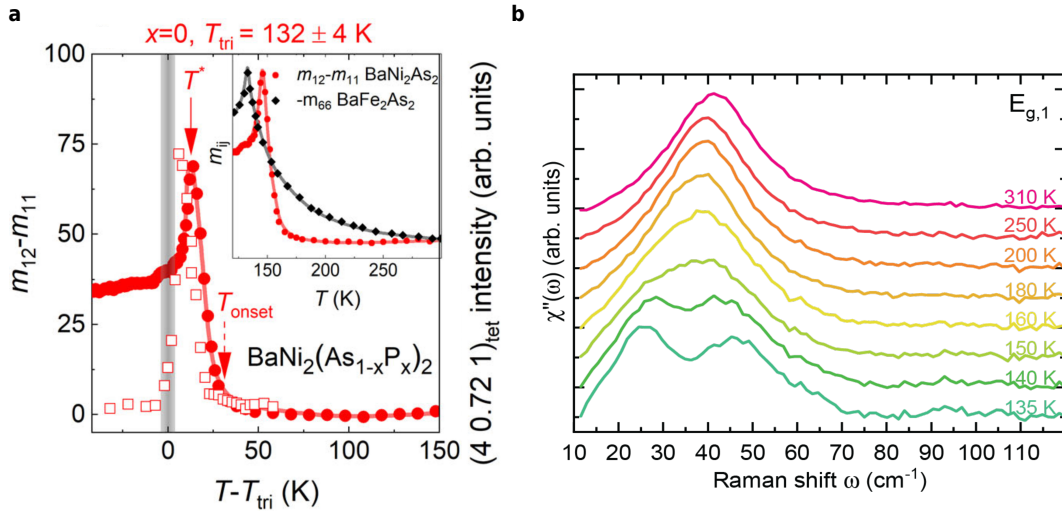


**Figure 2.4.: Elastoresistance and  $E_g$  phonon mode splitting in  $\text{BaNi}_2\text{As}_2$ .** **a** Integrated intensity of the I-CDW superstructure reflection and  $B_{1g}$  symmetry resolved elastoresistance coefficient  $m_{12} - m_{11}$  for non-substituted  $\text{BaNi}_2\text{As}_2$ . In the inset a comparison with the elastoresistance coefficient of  $\text{BaFe}_2\text{As}_2$  in  $B_{2g}$  symmetry is presented. The figure is reproduced from Frachet et al. [47] under the CC-BY 4.0 and adapted to present only the original subfigure a. **b** The temperature dependence of the  $E_{g,1}$  phonon mode measured by Raman spectroscopy indicating the increasing splitting of the mode in  $\text{BaNi}_2\text{As}_2$ . The figure is reproduced from Yao et al. [23] under the CC-BY 4.0 and adapted to show only the original subfigure c.

triclinic and superconducting transition temperature upon increasing pressure, except for a broadening of the transition as indicated in Figure 2.3.

In analogy to the nematicity in  $\text{BaFe}_2\text{As}_2$ , signatures of nematicity were also investigated in  $\text{BaNi}_2\text{As}_2$ . In the strontium substituted system, nematicity was claimed by the observation of elastoresistance in the  $B_{1g}$  direction (instead of  $B_{2g}$  in the iron case) [41]. However, later studies in the phosphorus-substituted system showed that the elastoresistance cannot be described by a Curie-Weiss dependence and shows a peak at the orthorhombic transition, contrary to what would be observed in the case of nematicity [47]. The corresponding elastoresistance coefficient for non-substituted  $\text{BaNi}_2\text{As}_2$  is presented in Figure 2.4a. A recent study for a 77% strontium substituted sample, does not find indications for lattice driven nematic fluctuations [48]. In contrast to the case of static nematicity in the elastoresistance measurements, Raman studies revealed the presence of dynamic nematicity in the phosphorus-substituted system. The nematicity was evidenced by the unusually large splitting of the  $E_g$  phonon modes, well above the orthorhombic transition, as shown in the Raman spectra in Figure 2.4b. This splitting could be described by a coupling of the phonon mode to  $B_{1g}$  nematic fluctuations that shows some analogy to the spin liquid. Consequently, the phase of dynamic nematicity can be described as a nematic liquid. Electronic Raman scattering in the  $B_{1g}$  symmetry further support the existence of fluctuations [23]. In addition, thermal expansion measurements indicate fluctuations in a similar temperature range [25]. However, as mentioned above, no nematic quantum critical behavior could be observed at the suppression of the triclinic and orthorhombic phases. While in  $\text{BaFe}_2\text{As}_2$  spin degrees of freedom are a crucial ingredient for nematicity, in  $\text{BaNi}_2\text{As}_2$  charge and orbital degrees of freedom are likely responsible for the dynamic nematicity since there is no magnetic order [23].

With the claims of nematicity, the pairing mechanism for superconductivity was also debated. First studies on the non-substituted  $\text{BaNi}_2\text{As}_2$  suggested a fully gapped superconducting state that can be described with BCS theory [50–52]. Later, the increase in the superconducting transition temperature at the suppression of the triclinic phase, was suggested to be due to nematic fluctuation enhanced Cooper pairing [37, 41, 53]. In contrast, a recent study shows that superconductivity can be described



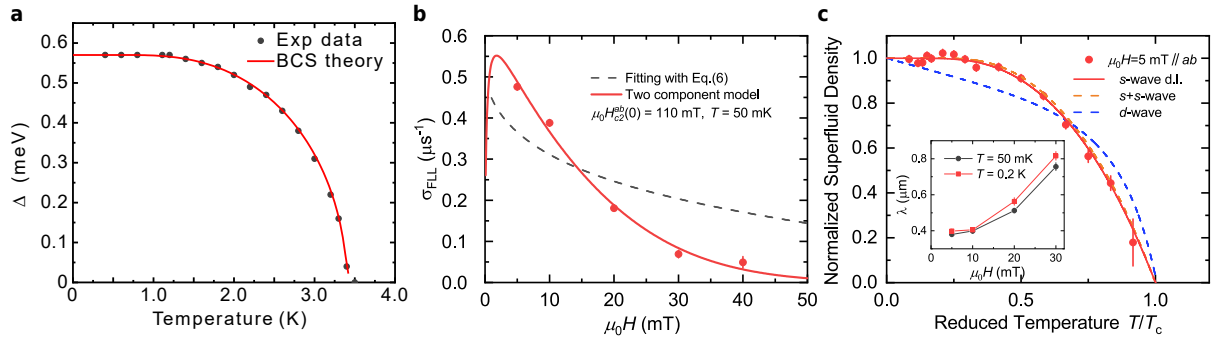


**Figure 2.5.: Superconducting gap, muon spin relaxation rate and superfluid density in strontium and non-substituted BaNi<sub>2</sub>As<sub>2</sub>.** **a** Measured temperature dependence of the superconducting gap and Bardeen-Cooper-Schrieffer (BCS) theory fit for Ba<sub>0.29</sub>Sr<sub>0.71</sub>Ni<sub>2</sub>As<sub>2</sub>. The figure is reproduced from Yu et al. [49] and adapted to show only the original sub-figure d. **b** Shown is the magnetic-field dependence of muon spin relaxation rate with a fit with a numerical Ginzburg-Landau model and a two component Ginzburg-Landau model. The figure is reproduced from Chen et al. [48] under the CC-BY 4.0. **c** Temperature dependence of the normalized superfluid density and fits for different superconducting gap symmetries. In the inset the magnetic field dependence of the penetration depth is shown. The figure is reproduced from Chen et al. [48] under the CC-BY 4.0.

by BCS theory even at the critical strontium substitution level [49]. This is shown by the temperature dependence of the superconducting gap and the BCS theory fit in Figure 2.5a. This is further supported by INS experiments revealing a strong change in the EPC at the critical strontium level. In this line, the change of superconductivity, should be considered more as a suppression of superconductivity for lower substitution levels [54]. Recent muon spin relaxation measurements further support the case of a fully gapped multiband superconductor in the non-substituted compound [55]. This is evidenced by the magnetic field dependence of the muon spin relaxation rate and the temperature dependence of the superfluid density in Figures 2.5b-c.



### 3. Physical basics

#### 3.1. Charge density waves

One-dimensional metals are intrinsically unstable at low temperatures against a periodic lattice deformation. This instability was first described by Fröhlich [2] and Peierls [3] nearly 70 years ago. Nowadays, this instability is often denoted as Peierls instability.

In such one-dimensional metals EPC enables the formation of electron-hole pairs with total wavevector  $|\vec{q}| = 2k_F$ . In contrast to the Cooper pairing in BCS theory of superconductivity, an electron-hole pair is formed instead of an electron-electron pair. Furthermore, the total momenta of the pairs are different [56]. The formation of the electron-hole pairs leads to the opening of a gap in the single electron spectrum [57]. The gap opening results in a lowering of the energy of the electrons involved close to the Fermi energy  $E_F$ . To achieve this gap opening, the lattice must be distorted in the form of a periodic lattice distortion (PLD) of the ions in the one-dimensional chain. The PLD increases the elastic energy of the lattice due to Coulomb repulsion. While the increase in the elastic energy is quadratic in the distortion  $u$ , the energy gained by the electrons is  $u^2 \ln(u)$  for small lattice distortions [58]. Consequently, for some finite distortions, the total energy is lowered. At finite temperatures, electron-hole pairs can be broken and single electrons can be excited across the gap. These single electrons can screen the EPC and result in a reduction of the gap and magnitude of the PLD. By

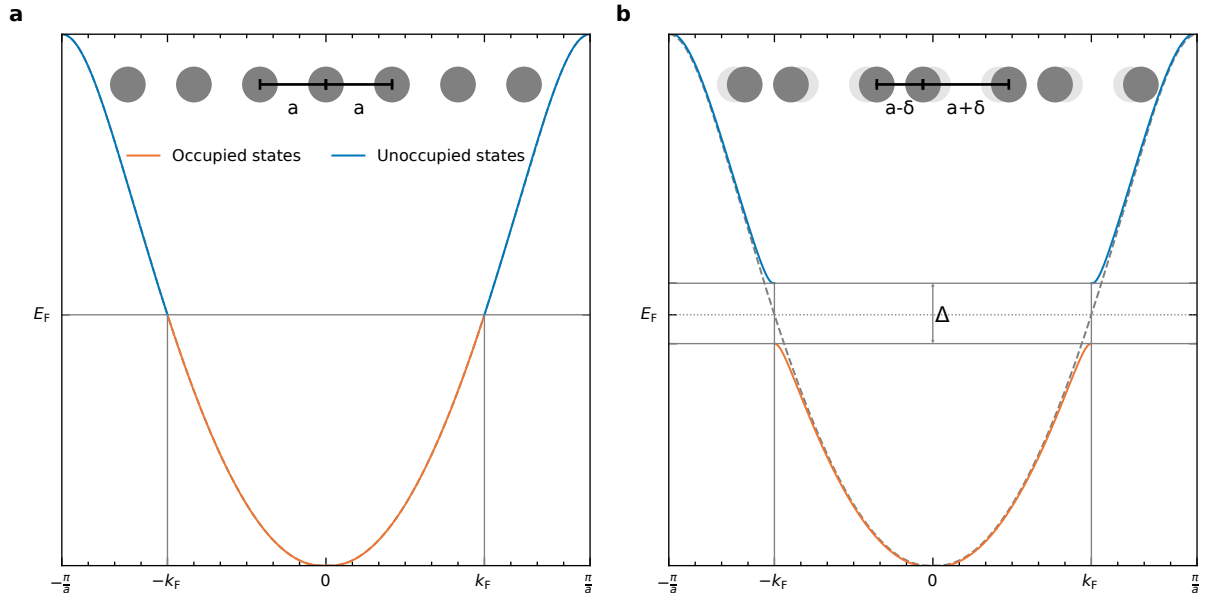


**Figure 3.1.:** Sketch of the atom arrangement and band structure of a one-dimensional metallic chain in the normal and charge density wave state. **a** Arrangement of the ions in a one-dimensional metallic chain and band structure above the CDW transition temperature  $T_{CDW}$ . **b** Illustration of the periodic lattice distortion (PLD) formed in the one-dimensional chain below  $T_{CDW}$ . Moreover, the gap opening at the Fermi energy is shown in the band structure.

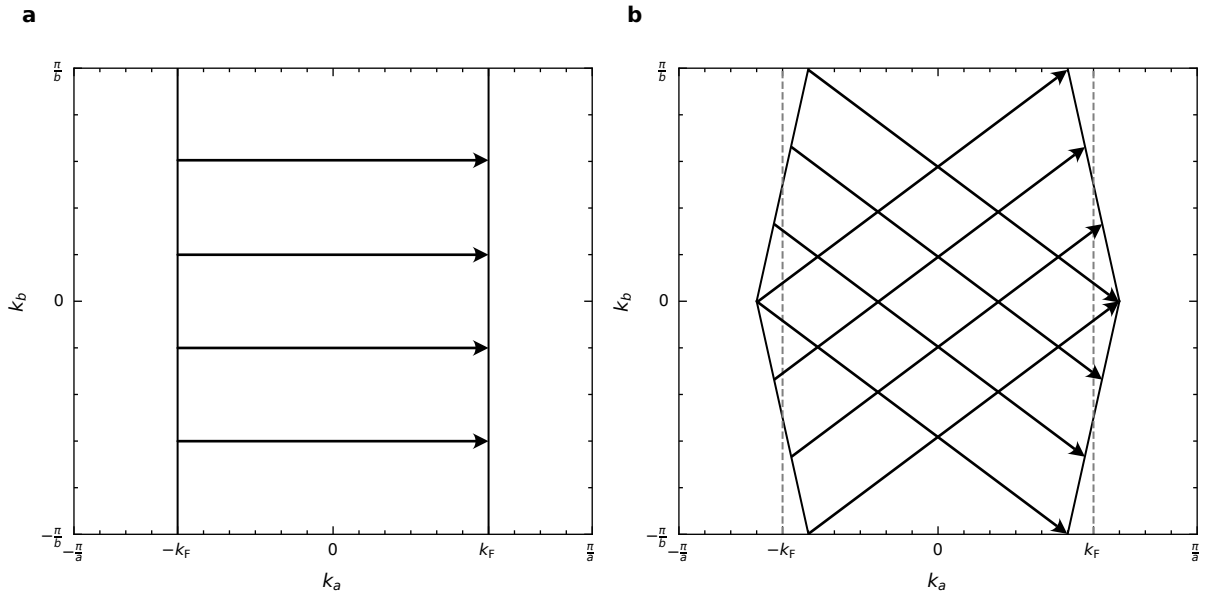


**Figure 3.2.: Sketch of the Fermi surface nesting in the one- and nearly one-dimensional system.** **a** Sketch of the Fermi surface of a one dimensional chain in the  $x$ -direction. Moreover, the nesting vector  $(2k_F, 0)$  is depicted. **b** Sketch of the Fermi surface of a nearly one dimensional system in the  $x$ -direction. Moreover, the nesting vectors in this case are sketched.

increasing the temperature up to the transition temperature  $T_{\text{CDW}}$  the system undergoes a second-order transition to the normal state [57]. The gap opening and PLD are depicted in Figure 3.1.

In the Peierls instability state, the electron-hole pair condensate modulates the charge density  $\rho(\vec{r})$  to

$$\rho(\vec{r}) = \rho_0 + \rho_1 \cos(2\vec{k}_F \vec{r} + \psi) \quad (3.1)$$

with the unperturbed charge density  $\rho_0$  and phase  $\psi$ . As the charge density forms a wave form, the condensate is called a charge density wave (CDW). The wavevector of the CDW is the same as the wavevector of the electron-hole pair and thus  $|\vec{q}_{\text{CDW}}| = 2k_F$ . A comparable state with a modulation of the spin density, instead of the charge density, is called a SDW.

While several aspects of the description of CDWs in mean field theory and superconductivity in BCS theory are similar, one important difference exists: for CDWs phase excitations of the collective mode of the electron-hole pairs are gapless. Accordingly, the collective mode can be easily pinned by electrostatic potentials, as the potential breaks the translational symmetry. This results in a nonconducting state of the collective mode [57]. Only in the absence of pinning and damping can the collective modes carry a current that leads to superconductivity.

As stated before, the total wavevector of the electron-hole pair is  $|\vec{q}| = 2k_F$ . In a one-dimensional system as discussed here, the Fermi surface consists of two planes at  $\pm k_F$ . Consequently, the wavevector of the electron-hole pair connects each point of one Fermi surface with the corresponding point on the second Fermi surface. This connection is called (perfect) Fermi surface nesting and is sketched in Figure 3.2. This perfect Fermi surface nesting allows for an alternative way in describing the development of a CDW. Therefore, we must also consider the Lindhard response function which is defined as

$$\chi(\vec{q}) = \int \frac{f(\vec{k}) - f(\vec{k} + \vec{q})}{E(\vec{k}) - E(\vec{k} + \vec{q})} \frac{d\vec{k}}{(2\pi)^d} \quad (3.2)$$

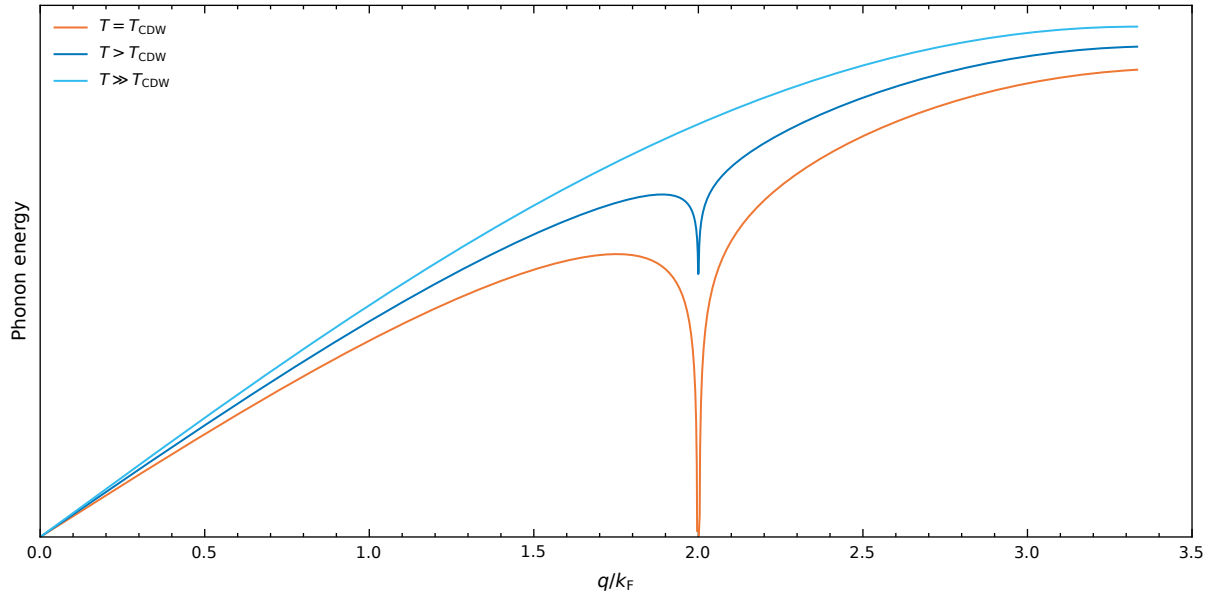


**Figure 3.3.: Sketch of the Kohn anomaly at different temperatures.** Sketch of the Kohn anomaly at the CDW transition (orange), above the CDW transition (dark blue) and the non-renormalized phonon dispersion far above the CDW transition (light blue).

with the dimension  $d$  and the Fermi function  $f(k)$  [56]. From the definition, it can be seen that, with perfect Fermi surface nesting, the Lindhard response function  $\chi(\vec{q})$  diverges at  $|\vec{q}| = 2k_F$ . At this vector, there are many states with nearly identical energies at which the state at  $\vec{k}$  is occupied and the state at  $\vec{k} + \vec{q}$  is empty. The Lindhard response function couples the induced charge density

$$\rho^{\text{ind}}(\vec{q}) = \chi(\vec{q})\Phi(\vec{q}) \quad (3.3)$$

with any potential  $\Phi(\vec{q})$ .

Kohn [59] found that EPC leads to a connection between the phonon frequency and the induced charge density. Induced charge density, and therefore, the Lindhard response function. This divergence of the Lindhard response function leads to a strong renormalization of the phonon frequency. This renormalization appears as a dip in the phonon dispersion, as sketched in Figure 3.3. At temperatures far above the CDW transition, the dispersion shows the normal behavior. On cooling, a dip develops that reaches zero energy at the CDW wavevector at  $T_{\text{CDW}}$ . At this temperature, the vibrations of the ions freeze in and the static PLD is formed. The formation of the PLD then results in the gapping in the electronic band structure and the formation of the CDW. This anomaly in the phonon dispersion is also called Kohn anomaly. The strong temperature dependence of the Kohn anomaly results from the temperature dependence of the Lindhard response function [56]. For a one-dimensional electron gas, in mean field theory the renormalization of the phonon frequency at the CDW wavevector near the transition temperature can be calculated and is given by

$$\tilde{\omega}_{\text{ren}}(q_{\text{CDW}} = 2k_F) = \tilde{\omega}(q_{\text{CDW}} = 2k_F) \left( \frac{T - T_{\text{CDW}}}{T_{\text{CDW}}} \right)^{\frac{1}{2}}. \quad (3.4)$$

Where  $T$ ,  $\tilde{\omega}$  and  $\tilde{\omega}_{\text{ren}}$  represent the temperature, the original and renormalized phonon energy respectively.

In the picture of a CDW formed by electron-hole pairs the Kohn anomaly results from effective screening of the vibrations of the ions at the CDW wavevector by zero energy electronic excitations with the same wavevector [56, 60].

Real, perfect one-dimensional systems do not exist, as all physical systems are three-dimensional. Hence, the one-dimensional perfect Fermi surface nesting does not exist either. However, if only metallic chains in one direction exist, which are only weakly coupled in the perpendicular directions, e.g. through insulating atoms in between, a nearly one-dimensional Fermi surface can be preserved. For such systems, the Fermi surface is slightly warped. In this case, as sketched in Figure 3.2b, wavevectors still exist that can connect parts of one Fermi surface with the other. However, only fractions of the Fermi surface can be nested by a single vector and the wavevectors gain additional components perpendicular to the metallic chains. This also leads to the fact that a gap opens only in parts of the Fermi surface, with metallic behavior being preserved in the other parts. In nearly one-dimensional systems, e.g. in blue bronze [61] or the charge transfer salts [62, 63], CDWs were observed supporting the upper picture.

So far, the discussion has only considered one-dimensional or nearly one-dimensional systems. However, in reality CDWs have also been observed in two- and three-dimensional systems. In such systems, the CDW can originate from similar mechanisms to those discussed previously. These conventional mechanisms are (partial) Fermi surface nesting or locally enhanced EPC. While in the discussion of the one-dimensional case, where the instability intrinsically exists, both were discussed as equivalent, here it makes sense to differentiate the two. Both involve excitations of electrons from filled to empty states, but Fermi surface nesting only involves elastic scattering processes and locally enhanced EPC inelastic scattering processes [60]. Besides this for many CDW systems the origin is unclear or under debate. One additional explanation for the formation of CDWs in strongly correlated electron systems is that electron-electron interaction can be the driving force [64]. But also other origins are discussed for several systems [65–67].

Experimentally, CDWs can be observed with various techniques. In resistivity measurements, CDW transitions often show up as an anomaly. In a (perfect) one-dimensional system, the CDW would show up as a metal-insulator transition. Another possibility is to use ARPES measurements to investigate nesting features in the Fermi surface. A rather direct, but only surface sensitive, method is to use a STM to directly measure the modulation of the charge density.

Two further techniques are XRD and IXS. With the first, the superstructure peaks resulting from the PLD can be measured. Furthermore, the wavevector and correlation length of the CDW can be derived from the XRD data. With IXS (or INS equivalently) the phonon dispersion can be measured. In the case of a CDW, the Kohn anomaly and temperature dependent phonon renormalization can be observed.

Especially for the diffraction and scattering techniques, it is sensible to further classify the CDWs depending on their wavevector. If the CDW wavevector is related to a commensurate value of the unit cell, the CDW is denoted as a commensurate CDW (C-CDW). For example, in the one-dimensional case with half filling, the CDW state corresponds to a doubling of the unit cell with a wavevector  $q_{\text{CDW}} = 1/2$ . If the wavevector of the CDW is not a commensurate value of the unit cell, then the CDW is classified as an incommensurate CDW (I-CDW). I-CDWs can show additional physical properties that differ from ordinary crystals [58].

## 3.2. Introduction to X-ray scattering

### 3.2.1. Classification and generation of X-rays

X-rays are a form of electromagnetic radiation with higher photon energy than (extreme) ultraviolet light. Commonly, X-rays are further divided into soft and hard X-rays, which can be distinguished by their ability to scatter from crystals and the resulting technical differences needed. Hard X-rays have a high enough energy that the scattering of crystals can be used for optical components, such as monochromators and mirrors, and large parts of the reciprocal space can be covered in experiments. Further, the use of ultra-high vacuum (UHV) is not needed, as hard X-rays can penetrate air. Soft X-rays have a lower energy and for many materials not even the complete first Brillouin zone can be reached. Accordingly, the scattering and reflection from multilayers must be used for the monochromator and other optical components. This can affect the properties of these optical components, such as the energy resolution of the monochromator, because multilayers are typically of lower quality than crystals. In addition, due to the very short penetration depth of soft X-rays in air, the entire experiment must be performed under UHV conditions. It turns out that many relevant atomic resonances are in the soft X-ray regime [14, 68, 69], which makes this type of X-ray technically challenging but physically interesting.

Based on this a definition of the two types of X-rays based on their energy can be made. For this tender X-rays are often included as a third type which lay between soft and hard X-rays. The definition of the X-ray energies varies for different sources. In this thesis, the following definition will be used. The energy of soft X-rays is  $250 \text{ eV} \leq E \leq 2000 \text{ eV}$ . Between  $2 \text{ keV} \leq E \leq 7 \text{ keV}$  are tender X-rays and above  $7 \text{ keV} \leq E$  are hard X-rays [70]. While originally  $\gamma$ -rays only described high energy electromagnetic waves from a radioactive decay process, nowadays, it is often also used in a broader context of electromagnetic waves with higher energy than (hard) X-rays ( $40 \text{ keV}$  to  $100 \text{ keV} \leq E$ ).

For the generation of X-rays, two different mechanisms can be used [68]. First, from Maxwell's equations, it can be derived that accelerated charges, such as electrons, generate electromagnetic waves. The wavelength of the electromagnetic radiation depends on the acceleration. Consequently, if the acceleration is of the right order of magnitude, X-rays are generated. Examples of X-rays generated with this mechanism are Bremsstrahlung and synchrotron radiation. A second mechanism is the use of the atom-specific emission lines. If an electron is removed from an atomic shell, for example by other high-energy electrons, this leads to the decay of an electron from a higher shell. During this decay, a photon with a specific energy is emitted. Depending on the specific shell and atom, the energy of the emitted photon changes. The  $K_\alpha$  line for many metals lies in the range of a few keV and can therefore be used for the generation of X-rays [14].

Based on these physical properties, nowadays mainly two ways for the generation of X-rays are used. For lab-based systems, mostly X-ray tubes are used. In X-ray tubes, electrons are accelerated with a high voltage of a few kV. The accelerated electrons are shot at a metal target, most commonly copper or molybdenum. In some cases, the target can also be made of silver, tungsten, chromium or a liquid metal such as gallium or indium. The X-ray tube generates a spectrum with the specific emission lines of the target material superimposed on a broad Bremsstrahlung background produced by the decelerating electrons in the target material. Typically, for the experiment the X-rays of the  $K_\alpha$  lines ( $8 \text{ keV}$  for copper and  $17.48 \text{ keV}$  for molybdenum) are selected with a monochromator [14, 68].

Large-scale facilities such as synchrotron radiation facilities or free electron lasers (FELs) can generate X-rays with superior X-ray beam properties and with energies that are not available from X-ray tubes. For example, the flux, brilliance and (spacial and temporal) coherence are significantly higher and the

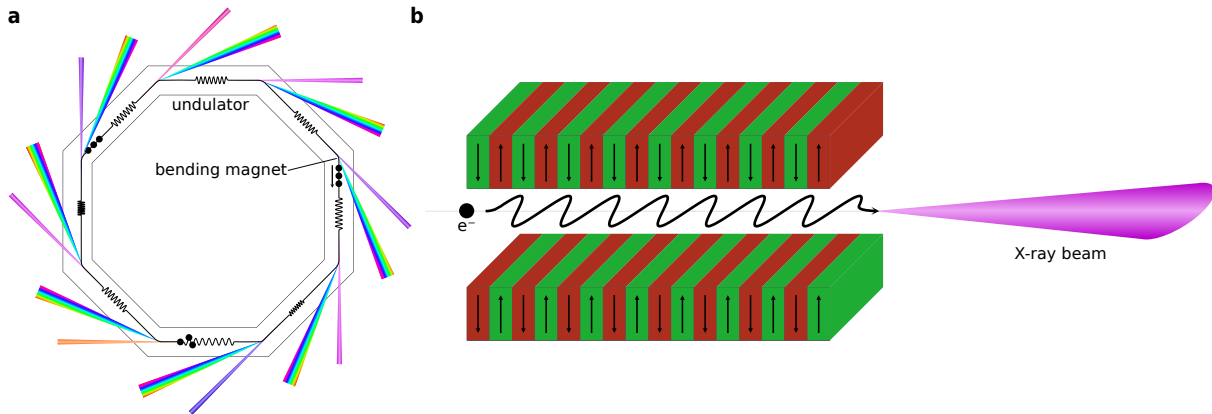


**Figure 3.4.: Sketch of a synchrotron radiation facility and an undulator insertion device.** **a** Simplified sketch of a modern synchrotron radiation facility with bending magnets with a broad X-ray spectrum and tunable undulators with a much sharper X-ray spectrum. Further, the path of the electrons through the synchrotron is sketched. **b** Simplified sketch of an undulator insertion device with the permanent magnets, electron beam path and generated X-rays.

divergence is lower. Experiments in resonance that rely on a tunable X-ray energy and time-resolved experiments can only be practically performed with X-rays generated from synchrotrons or FELs. In this thesis, only X-rays generated from synchrotron radiation sources are used and will be discussed further in the following.

The X-rays generated in synchrotron radiation sources only use accelerated charges to generate the X-rays. Therefore, electrons (or rarely also positrons) are accelerated close to the speed of light and forced on a circular path in a synchrotron. This is done in a circular evacuated tube, the “ring”. The acceleration itself is done, e.g., with microwaves in cavities that generate oscillating high voltages that are synchronized with the electrons in the ring and therefore accelerate the electrons [71]. As the electrons on this circular path are permanently accelerated to stay on the circular path they generate electromagnetic waves, the so-called synchrotron radiation [68]. In a synchrotron the X-ray energy is given by the energy or speed of the electron and the magnetic field strength used to keep the electrons on the circle [68].

Practically, a synchrotron is not built as a true circle, as this would have many drawbacks. Instead, the synchrotron radiation facilities are built as polygons with straight sections, as shown in Figure 3.4a. With strong magnets, the bending magnets, the electrons are “bent” to the next straight section. Only at these bending magnets, a centripetal acceleration acts on the electrons and therefore they generate X-rays. The spectrum produced at a bending magnet is relatively broad and not further tuneable as indicated by the broad spectrum in Figure 3.4a.

Over time, two other so-called insertion devices, which can be mounted in the straight sections, were developed for the generation of X-rays. Both are made from a series of magnets which force the electrons on a sinusoidal path. While the so-called wigglers only use a few strong magnets and can be seen as a series of bending magnets, a so-called undulator uses much more and weaker magnets along the path [68]. A sketch of the electron path and an undulator is shown in Figure 3.4. Wigglers are no longer installed in modern synchrotrons. The reasons for this are that wigglers distort the electron beam too much and the X-ray beam characteristics of undulators are far superior for most applications. In an undulator, the magnets and path of the electrons are designed in such a way that the X-rays from the different oscillations are in phase and the amplitudes add up [68]. Accordingly, the X-ray characteristics, such as the energy, linewidth, intensity, divergence, and coherence, depend on the field strength of the permanent magnets, the periodicity of the magnets, the electron energy and the number



**Table 3.1.:** List of different X-ray techniques and their common type of interaction with a crystal.

	Interaction	Interaction with	Energy change	Resonant
Thompson scattering/ X-ray diffraction	scattering	predominantly charge	elastic	no
Inelastic X-ray scattering	scattering	predominantly charge	inelastic	no
Resonant Inelastic X-ray scattering	scattering	charge and magnetic	inelastic	yes
X-ray absorption spec- troscopy	absorption	charge and magnetic	-	yes
X-ray magnetic circular dichroism	absorption	magnetic	-	yes
X-ray fluorescence	fluorescence	-	-	-

of periods [72]. Generally, more periods lead to better beam characteristics, that is used in FELs that basically consists of two long undulators in which also a lasing process sets in after a certain length of the FEL.

Undulators have the large benefit that the wavelength is tunable and the linewidth significantly smaller than for bending magnets. Further, the divergence is smaller and the flux is higher compared to bending magnets. With modern, more advanced undulators additionally the polarization can be freely chosen. Depending on the undulator, different linear, circular and elliptical polarizations are possible. An example of such undulators is the APPLE X undulator [73]. The tuneability of the polarization is reached by having multiple banks of permanent magnets that can be shifted relative to each other. This can be used to get the oscillation of the electrons into any phase within the undulator and also shift it to be in-plane, out-of-plane or anything in between. The path of the oscillation determines the polarization of the generated X-rays. With the ability to move the magnets closer, the magnetic field strength at the electron beam can be adjusted. Together with the possibility of choosing different harmonics of the undulator, the X-ray energy can be set over a large energy range.

More recent advances are the usage of undulators that are inside the UHV of the ring, allowing shorter periods of the magnets, a higher quality of the field and bringing the magnets closer to the beam [74]. Cryogenically cooled undulators allow further increases in field strength and reductions in periodicity [75]. Although most undulators are still based on permanent magnets, the use of superconducting magnets is an active and promising field for further optimization of undulator properties. [76].

### 3.2.2. Interaction of X-rays with the crystal

#### 3.2.2.1. Introduction

The interaction of X-rays with matter can be described using the classical picture of an electromagnetic wave or using quantum mechanics in the particle picture. For the interactions discussed in the following sections, the latter description is advantageous.

Before doing so, first we discuss the different possible interactions. Generally, there are many possible ways of interaction. A subset of the possible interactions is shown in Figure 3.5 and listed in Table 3.1. First, the photons of the X-ray beam can be either scattered, absorbed, emitted, reflected or transmitted. In the simplest case of (elastic) scattering of the charge, the first is described by Thomson scattering and the second by the photoelectric effect. Nevertheless, there are further possible interactions and a

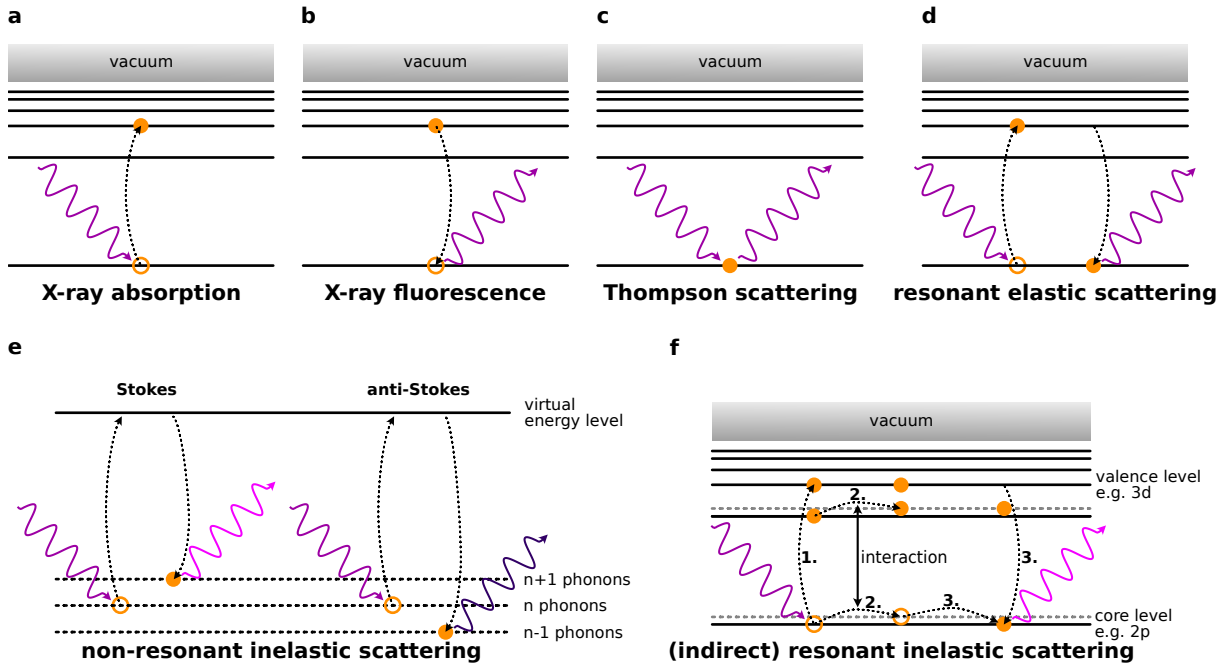


**Figure 3.5.: Sketch of a subset of the possible interactions of X-rays with a crystal.** Sketch of a subset of the possible interactions of X-rays with a crystal. The sketches apply an atomic energy model, instead of the bands in a crystal, with the energy levels of the system indicated by lines. The dashed lines indicate the energy levels with a different number of phonons. The orange circles indicate the relevant electrons or holes. For the resonant inelastic process only the indirect process is shown. For the non-resonant inelastic scattering instead the atomic energy levels, the energy levels with different phonon number and the virtual energy level are shown. For all cases, the distance of the energy levels is not to scale.

selection of techniques and their interaction are listed in Table 3.1. First, the X-ray can interact with the charge of the electron cloud or with the magnetic moments of the crystal. Second, the scattering process can be elastic (as in the classical picture) or inelastic by gaining/losing some energy to excitations in the crystal such as phonons or magnon. Finally, the process can be out-of-resonance or in-resonance. All these possibilities can in principle also be combined. These many possible interactions can be exploited by a wide variety of experimental techniques for the investigation of different physical properties. Each technique thereby often focuses on one or a subset of possible interactions.

The first case shown in Figure 3.5a is the case of X-ray absorption, as used in X-ray absorption spectroscopy (XAS) measurements. In the X-ray absorption process, a photon is absorbed and lifts a core level electron to a valence state. In resonance between the two states, the absorption is drastically enhanced. The opposite effect, as shown in in panel b, can be used for X-ray fluorescence (XRF) measurements. Both involve either the creation or annihilation of a photon. A scattering process, however, involves an incoming and outgoing photon. In the non-resonant Thomson case, the photon is elastically scattered from an electron. In resonant scattering, a photon is absorbed and a core level electron is lifted into a valence state. The electron relaxes back after a specific lifetime and emits a photon with the same energy.

In the case of inelastic scattering, additional excitations, such as phonons and magnons, can be created or annihilated. In the case of non-resonant scattering, an electron is lifted to a high energy virtual level. Then it relaxes back and creates an excitation (Stokes scattering) or annihilates an excitation (anti-Stokes scattering). This changes the energy of the emitted photon. The virtual energy state is not a real state, but often used to split of the energy exchange of the radiation field and the crystal into two single photon transitions [77]. This is different from the resonant case. First, a core-level

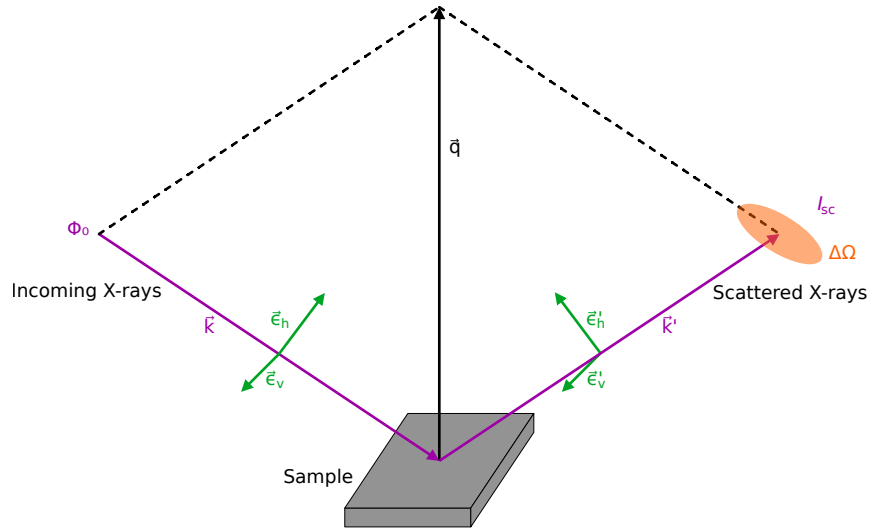


**Figure 3.6.: Sketch of the scattering geometry.** Sketch of the incoming and outgoing X-ray beam with wavevectors  $\vec{k}$  and  $\vec{k}'$ . Further the directions of vertical and horizontal incoming  $\vec{\epsilon}$  and outgoing polarization  $\vec{\epsilon}'$ , incoming flux  $\Phi_0$ , scattered intensity  $I_{sc}$  and the solid angle into which the X-rays are scattered  $\Delta\Omega$  are indicated.

electron is lifted to a valence state under the absorption of the incoming photon. Then there are two possibilities. In the direct RIXS process, an electron from an occupied state relaxes back and generates a valence excitation. In the indirect RIXS process the excitation is created in an intermediate state through Coulomb interaction of an electron in an occupied level and the generated core hole. In the final step the excited electron relaxes back [69]. The indirect process is sketched in Figure 3.5f.

In this thesis only scattering techniques are used. Accordingly, in the following sections different scattering processes are discussed in more detail.

### 3.2.2.2. Quantum mechanical description

First, we will discuss the quantum mechanical description of X-ray scattering. Important for the experimental observed intensities is the differential scattering cross-section

$$\left(\frac{d\sigma}{d\Omega}\right) = \frac{I_{sc}}{\Phi_0 \Delta\Omega} \quad (3.5)$$

with the incoming X-ray flux  $\Phi_0$ , the scattered intensity in the detector  $I_{sc}$  and the covered solid angle  $\Delta\Omega$  [68]. The scattering geometry with the important quantities is sketched in Figure 3.6. The differential scattering cross-section  $\left(\frac{d\sigma}{d\Omega}\right)$  describes how many photons are scattered into a given solid angle per second. An alternative way to describe the scattering intensity is to use the scattering amplitudes  $f(\vec{k}, \vec{k}', \vec{\epsilon}, \vec{\epsilon}')$ . Following Dmitrienko et al. [78], the scattering process from different atoms can be treated as being independent. In this so-called isolated-atom approximation, the scattering amplitude can be expressed with the tensor atomic form factor

$$f(\vec{k}, \vec{\epsilon}, \vec{k}', \vec{\epsilon}') = -\frac{e^2}{mc^2} f_{jk}(\vec{k}', \vec{k}) \vec{\epsilon}'_j \vec{\epsilon}_k \quad (3.6)$$

with the incoming wavevector  $\vec{k}$  and polarization  $\vec{\epsilon}$  and scattered wavevector  $\vec{k}'$  and polarization  $\vec{\epsilon}'$ . Further, the elementary charge  $e$ , mass  $m$  and speed of light  $c$  are included. To calculate the tensor

atomic form factor  $f_{jk}(\vec{k}', \vec{k})$  we need to know the transition rate between two states. To describe all effects properly, we need to employ second-order perturbation theory (as will become clear after the discussion of the Hamiltonian). In second-order perturbation theory, the transition rate  $W_{|i\rangle \rightarrow |f\rangle}$  from the initial state  $|i\rangle$  to the final state  $|f\rangle$  is given by

$$W_{|i\rangle \rightarrow |f\rangle} = \frac{2\pi}{\hbar} \left| \langle f | \mathcal{H} | i \rangle + \sum_n \frac{\langle f | \mathcal{H} | n \rangle \langle n | \mathcal{H} | i \rangle}{E_i - E_n} \right|^2 D(E_f) \quad (3.7)$$

with the Hamiltonian  $\mathcal{H}$ , the density of states  $D(E)$ , the reduced Planck constant  $\hbar$  and the energy of the states  $E_i$ . The states  $|i\rangle$  and  $|f\rangle$  describe the complete system of the crystal and the X-rays. Accordingly, the states include the photon, electrons of the crystal and excitations like phonons.

Before using Equation (3.7), we need the interaction Hamiltonian of the photons and electrons of our crystal. Using the vector potential  $\vec{A}(\vec{r}_i)$  at position  $\vec{r}_i$ , spin angular momentum  $\vec{s}_i$  and the momentum  $\vec{p}_i$  of the  $i^{\text{th}}$  electron, the interaction Hamiltonian between photons and electrons is

$$\begin{aligned} \mathcal{H} = & \frac{e^2}{2mc^2} \sum_i \vec{A}^2(\vec{r}_i) - \frac{e}{mc} \sum_i \vec{p}_i \cdot \vec{A}(\vec{r}_i) \\ & - \frac{e\hbar}{mc} \sum_i \vec{s}_i \cdot \nabla \times \vec{A}(\vec{r}_i) \\ & - \frac{e^2\hbar}{2(mc^2)^2} \sum_i \vec{s}_i \cdot \left( \dot{\vec{A}}(\vec{r}_i) \times \vec{A}(\vec{r}_i) \right) \end{aligned} \quad (3.8)$$

as derived from Blume [79, 80]. Scattering processes involve both the annihilation and the creation of a photon. As the vector potential  $\vec{A}(\vec{r}_i)$  is linear in photon creation and annihilation, only terms quadratic in  $\vec{A}(\vec{r}_i)$  lead to scattering terms in first-order perturbation theory. Nonetheless, using second-order perturbation theory, also the terms linear in  $\vec{A}(\vec{r}_i)$  lead to scattering processes. Terms not leading to a scattering process will be neglected in this discussion, e.g. terms describing X-ray absorption. Doing the second-order perturbation with the Hamiltonian described in Equation (3.8) leads to the transition rate for the scattering processes. For further discussions the atomic scattering factor is more relevant, that involves the transition rate. Putting all together the atomic scattering factor becomes

$$\begin{aligned} f_{jk}(\vec{k}', \vec{k}) = & \sum_{|g\rangle} P_g \left\{ \left\langle g \left| \sum_i \exp(i\vec{q} \cdot \vec{r}_i) \right| g \right\rangle \delta_{jk} \right. \\ & - i \frac{\hbar\omega}{mc^2} \left\langle g \left| \sum_i \exp(i\vec{q} \cdot \vec{r}_i) \left( -\frac{[\vec{q} \times \vec{p}_i]_l}{\hbar q^2} A_{jkl} + s_l^i B_{jkl} \right) \right| g \right\rangle \\ & - \frac{1}{m} \sum_{|n\rangle} \frac{E_g - E_n}{\hbar\omega} \frac{\langle g | O_j^\dagger(\vec{k}') | n \rangle \langle n | O_j(\vec{k}) | g \rangle}{E_g - E_n + \hbar\omega - i\frac{\Gamma}{2}} \\ & \left. - \frac{1}{m} \sum_{|n\rangle} \frac{E_g - E_n}{\hbar\omega} \frac{\langle g | O_j^\dagger(\vec{k}') | n \rangle \langle n | O_j(\vec{k}) | g \rangle}{E_g - E_n - \hbar\omega} \right\} \end{aligned} \quad (3.9)$$

with scattering vector  $\vec{q} = \vec{k} - \vec{k}'$ , photon energy  $\hbar\omega$  and the occupation probability  $P_g$  of state  $|g\rangle$  [78, 81]. The operator  $\vec{O}(\vec{k})$  can be expressed as,

$$\vec{O}(\vec{k}) = \sum_i \exp(i\vec{k} \cdot \vec{r}_i) \left( \vec{p}_i - i\hbar [\vec{k} \times \vec{s}_i] \right). \quad (3.10)$$

In this case, only scattering from  $|g\rangle$  back to the same state  $|g\rangle$  is included. This description where the initial and final states are identical only describes the coherent and elastic scattering processes. The inelastic processes will be discussed later. To avoid confusion between the running index  $i$  and the initial state  $|i\rangle$ , the latter is replaced by  $|g\rangle$  in the description of the elastic scattering process. The first term in Equation (3.9) describes the non-resonant Thomson scattering process, while the second line describes non-resonant magnetic scattering. The non-resonant magnetic scattering amplitude is, for a single electron, a factor  $\hbar\omega/(mc^2)$  smaller than the charge scattering, and hence it often can be neglected [68]. The magnetic scattering itself involves the two 3<sup>rd</sup> rank tensors  $A_{jkl}$  and  $B_{jkl}$  associated with the orbital and spin magnetic momenta. As in this thesis only non-magnetic systems are discussed, the magnetic part will not be discussed further. The last line itself is also usually neglected, but can be an important correction to the non-resonant scattering at photon energies far from resonance. The third term diverges close to a resonance and describes the magnetic and non-magnetic resonant scattering. For the scattering also, the linewidth  $\Gamma$  of the intermediate state  $|n\rangle$  is relevant. Accordingly, the imaginary part  $i\frac{\Gamma}{2}$  must be added to the denominator of the resonant part [82].

For easier discussion, the atomic form factor can be split, following the discussion above, into Thomson, magnetic and resonant scattering. In this form, the atomic form factor can be expressed as

$$f_{jk}(\vec{k}', \vec{k}, \omega) = \underbrace{f_0(|\vec{q}|)\delta_{jk}}_{\text{Thomson scattering}} + \underbrace{f_{jk}^{\text{mag}}}_{\text{non-resonant magnetic scattering}} + \underbrace{f'_{jk}(\vec{k}', \vec{k}, \omega) + if''_{jk}(\vec{k}', \vec{k}, \omega)}_{\text{resonant scattering}}. \quad (3.11)$$

The resonant part is typically split into the real part  $f'_{jk}(\vec{k}', \vec{k}, \omega)$  and the imaginary part  $f''_{jk}(\vec{k}', \vec{k}, \omega)$ . Alternatively, the tensor atomic form factor can be divided into the isotropic and anisotropic parts. Doing so results in

$$f_{jk}(\vec{k}', \vec{k}, \omega) = \underbrace{[f_0(|\vec{q}|) + f'_0(\omega) + if''_0(\omega)]\delta_{jk}}_{\text{isotropic}} + \underbrace{f'_{jk}(\vec{k}', \vec{k}, \omega) + if''_{jk}(\vec{k}', \vec{k}, \omega) + f_{jk}^{\text{mag}}}_{\text{anisotropic}} \quad (3.12)$$

with the Thomson atomic form factor  $f_0(|\vec{q}|)$ , the magnetic contribution  $f_{jk}^{\text{mag}}$  and the resonant corrections [78]. The anisotropic resonant parts are sensitive to the local symmetry of the resonant atom and also its magnetism [78]. Accordingly, in the case of pure charge scattering away from resonance, only isotropic parts exist and therefore the atomic form factor is often simplified to a scalar.

### 3.2.2.3. Polarization dependence of the resonant part

As seen above, only magnetic and resonant contributions lead to anisotropic atomic form factors. Therefore, these interactions clearly result in the more complex parts of the tensor atomic form factor. As no magnetic scattering is discussed in this thesis, we can neglect this contribution and focus on the resonant (charge) scattering. A common example of resonant charge scattering is the investigation of the orbital contribution to the scattering. In this case, one has to investigate the complete scattering tensor. One way of doing so is an azimuthal and polarization dependence in resonance. In an azimuthal dependence, the sample is rotated around the scattering vector of the investigated peaks. This leads effectively to a change of the polarizations with respect to the sample, which needs to be analyzed. This could be theoretically done with Equation (3.9). However, it is easier and more insightful to simplify the equation. Using the expansion

$$\exp(i\vec{k}\vec{r}_i) \approx 1 + i\vec{k}\vec{r}_i + \frac{1}{2}(i\vec{k}\vec{r}_i)^2 + \dots \quad (3.13)$$

the equation can be simplified. Following the works by Joly et al. [83] and Dmitrienko et al. [78], the matrix elements can be expanded into dipole and quadrupole components. In this case, we will use the expansion into Cartesian tensors, as this is more insightful. For theoretical investigations, it can be easier to expand the matrix elements into spherical tensors. The Cartesian expansion leads to

$$\langle n | O(\vec{k}) | g \rangle = D_i^n + i \frac{k}{2} Q_i^n + \dots \quad (3.14)$$

and for the signal amplitude

$$\langle g | O^*(\vec{k}') n \rangle \langle n | O(\vec{k}) | g \rangle \cong \underbrace{D_s^{n*} D_i^n}_{\text{dipole-dipole}} + i \frac{k}{2} \underbrace{(D_s^{n*} Q_i^n - Q_s^{n*} D_i^n)}_{\text{dipole-quadrupole}} + \underbrace{\frac{k^2}{4} Q_s^{n*} Q_i^n}_{\text{quadrupole-quadrupole}} \quad (3.15)$$

with the dipole component  $D_i^n$  and quadrupole component  $Q_i^n$  of the incoming  $i$  and scattered beam  $s$ . The components of the interaction can be described with the dipole-dipole rank-2 tensor  $D_{jk}$ , the dipole-quadrupole rank-3 tensors  $I_{jkl}$  and the quadrupole-quadrupole rank-4 tensor  $Q_{jklm}$ . Where  $j, k, l$  and  $m$  describe the Cartesian coordinates.

Using the expansion the resonant part of the atomic form factor becomes

$$f_{jk}^{\text{res}} = D_{jk} + \frac{i}{2} I_{jkl} k_l - \frac{i}{2} I_{kjl} k'_l + \frac{1}{4} Q_{jklm} k_m k'_l \quad (3.16)$$

and by reintroducing the polarization vectors the intensity can be described as

$$I(\vec{k}, \vec{k}', \vec{\epsilon}, \vec{\epsilon}') \propto \left| \sum_{j,k} \epsilon_j'^* \epsilon_k D_{jk} + \frac{i}{2} \sum_{j,k,l} \epsilon_j'^* \epsilon_k (k_l I_{jkl} - k'_l I_{kjl}) + \frac{1}{4} \sum_{j,k,l,m} \epsilon_j'^* \epsilon_k k'_l k_m Q_{jklm} \right|^2. \quad (3.17)$$

In systems with an inversion center at the atom position the dipole-quadrupole interaction is strictly zero [83, 84]. Furthermore, in most cases the quadrupole-quadrupole interaction is so weak that only the dipole-dipole interaction is important. However, there are exceptions to this [85]. All the tensors fulfill further symmetries, which can differ between charge and magnetic scattering. Nonetheless, according to Neumann's principle, all tensors have to fulfill at least the symmetry of the crystal, in this case, the local symmetry of the atom in resonance. For charge scattering, for example, the  $D_{jk}$  and  $I_{jkl}$  tensors are symmetric [84] and  $D_{jk}$  has only imaginary off-diagonal elements for magnetic scattering [83].

In the soft X-ray regime, the determination of the outgoing polarization is experimentally challenging. Such experiments require an additional scattering process on a multilayer, reducing the intensity significantly and adding experimental challenges [86, 87]. Accordingly, it is for many experiments only feasible to look at the combination of both possible polarizations, e.g. horizontal and vertically linear polarized. The intensities of both are summed up in the experiment. Considering only the dipole-dipole terms, and using the matrix formulation with the dipole-dipole matrix  $\mathbf{D}$ , this leads to

$$I_v = \left| \vec{\epsilon}_{s,v}^* \mathbf{D} \vec{\epsilon}_{i,v} + \vec{\epsilon}_{s,h}^* \mathbf{D} \vec{\epsilon}_{i,v} \right|^2 \quad (3.18)$$

$$I_h = \left| \vec{\epsilon}_{s,v}^* \mathbf{D} \vec{\epsilon}_{i,h} + \vec{\epsilon}_{s,h}^* \mathbf{D} \vec{\epsilon}_{i,h} \right|^2 \quad (3.19)$$

for incoming vertical and horizontal polarization. Experimentally, also getting trustworthy absolute intensities while rotating the sample is difficult. This can be due to small movements on the sample

or that the sample is not perfectly flat. Therefore, the ratio of the two intensities is the more reliable quantity and given by

$$\frac{I_v}{I_h} = \frac{|\vec{\epsilon}_{s,v}^* \mathbf{D} \vec{\epsilon}_{i,v} + \vec{\epsilon}_{s,h}^* \mathbf{D} \vec{\epsilon}_{i,v}|^2}{|\vec{\epsilon}_{s,v}^* \mathbf{D} \vec{\epsilon}_{i,h} + \vec{\epsilon}_{s,h}^* \mathbf{D} \vec{\epsilon}_{i,h}|^2}. \quad (3.20)$$

Instead of using the dipole-dipole tensor, an effective tensor atomic scattering tensor calculated from Equation (3.16) can be used to include higher order multipoles for the intensity ratio.

#### 3.2.2.4. Inelastic scattering

**General formula for inelastic X-ray scattering** After discussing the elastic scattering processes, now we will add the inelastic parts. As with inelastic scattering the additional freedom of a change of energy is introduced, it is more insightful to define the double differential cross-section  $\left(\frac{d^2\sigma}{d\Omega dE}\right)$  instead of the differential cross-section  $\left(\frac{d\sigma}{d\Omega}\right)$ . The double differential cross-section describes the scattered intensity in a certain solid angle and energy range. Using the transition rate  $W_{|i\rangle \rightarrow |f\rangle}$  (as defined in Equation (3.7)) the double differential cross-section can be expressed as

$$\left(\frac{d^2\sigma}{d\Omega' dE'}\right) = \frac{W_{|i\rangle \rightarrow |f\rangle} V^2 \omega'^2}{8\pi^3 \hbar c^4} \quad (3.21)$$

by including the density of states and the reachable volume  $V$  of the photons in the solid angle and energy range [82]. After dividing by the flux and  $d\Omega' dE'$  and some reformulation, the upper expression is reached. Similarly to above, the Hamiltonian from Equation (3.8) can be inserted, leading to

$$\begin{aligned} \left(\frac{d^2\sigma}{d\Omega' dE'}\right)_{|i\rangle \rightarrow |f\rangle} &= \left(\frac{e^2}{mc^2}\right)^2 \frac{\omega'}{\omega} \left\langle f \left| \sum_j \exp(i\vec{q}\vec{r}_j) \right| i \right\rangle \vec{\epsilon} \cdot \vec{\epsilon}'^* \\ &\quad - i \left[ \frac{\hbar(\omega + \omega')}{2mc^2} \right] \left\langle f \left| \sum_j \exp(i\vec{q}\vec{r}_j) \frac{\vec{s}_j}{\hbar} \right| i \right\rangle (\vec{\epsilon}'^* \times \vec{\epsilon}) \\ &\quad + \frac{1}{m} \sum_{|n\rangle} \sum_{j,j'} \left( \frac{\langle f | \vec{\epsilon}'^* \cdot \vec{p}_j - i(\vec{k}' \times \vec{\epsilon}') \vec{s}_j \exp(-i\vec{k}'\vec{r}_j) | n \rangle \langle n | \vec{\epsilon} \cdot \vec{p}_{j'} + i(\vec{k} \times \vec{\epsilon}) \vec{s}_{j'} \exp(i\vec{k}\vec{r}_{j'}) | i \rangle}{E_i - E_n + \hbar\omega - i\frac{\Gamma_n}{2}} \right. \\ &\quad \left. + \frac{\langle f | \vec{\epsilon} \cdot \vec{p}_j + i(\vec{k} \times \vec{\epsilon}) \vec{s}_j \exp(i\vec{k}\vec{r}_j) | n \rangle \langle n | \vec{\epsilon}'^* \cdot \vec{p}_{j'} - i(\vec{k}' \times \vec{\epsilon}') \vec{s}_{j'} \exp(-i\vec{k}'\vec{r}_{j'}) | i \rangle}{E_i - E_n - \hbar\omega'} \right)^2 \\ &\quad \cdot \delta(E_i - E_f + \hbar(\omega - \omega')). \end{aligned} \quad (3.22)$$

The main difference to Equation (3.9) is that a different initial state  $|i\rangle$  and final state  $|f\rangle$  with energies  $E_i$  and  $E_f$  and photon energies  $\hbar\omega$  and  $\hbar\omega'$  respectively are now possible [82]. To avoid confusion with the initial state  $|i\rangle$ , now  $j$  and  $j'$  are used as running index of the electrons. Similarly to the elastic expression, the first term describes the non-resonant charge scattering term and the second the non-resonant magnetic scattering term. The third term is the resonant contribution and the last term a correction far from the resonance. The delta function takes care of energy conservation. For further discussion it is more convenient to express the energy difference of the incoming and outgoing beam or, equivalently, the energy of the excitation as  $\tilde{\omega} = \omega - \omega'$ .

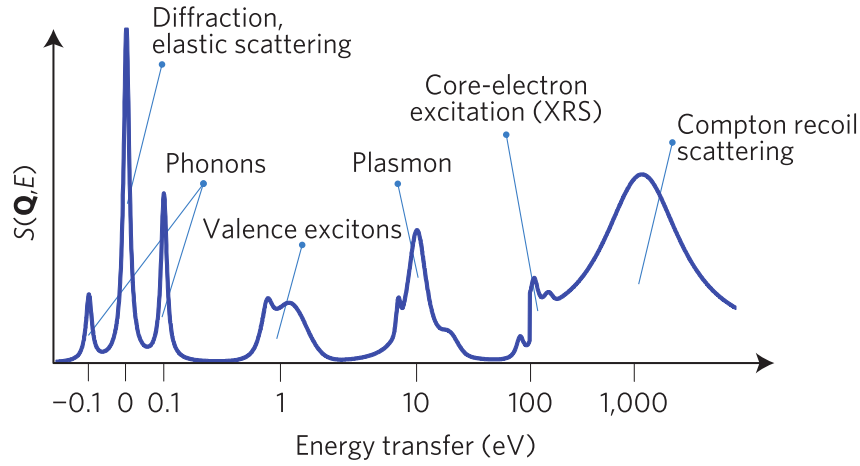


**Figure 3.7.: Sketch of the possible excitations measured with inelastic X-ray scattering.** Sketch of the lineshape and energy range of different excitations which can be measured with IXS. Material from S. Huotari, T. Pylkkänen, R. Verbeni, G. Monaco, and K. Hämäläinen, *Nature Materials* **10**, 489 (2011) [88] reproduced with permission of SNCSC.

**Non-resonant inelastic X-ray scattering** One important application of inelastic scattering are IXS experiments, and so these will be discussed first. These experiments are commonly performed far from any resonance and therefore the resonant terms can be neglected. Further, as in this thesis only non-magnetic  $\text{BaNi}_2\text{As}_2$  is investigated, the magnetic term and fourth term of the double differential cross-section are also neglected. In this case, the double differential cross-section simplifies to

$$\left( \frac{d^2\sigma}{d\Omega' dE'} \right)_{|i\rangle \rightarrow |f\rangle} = r_0^2 \frac{\omega'}{\omega} |\vec{\epsilon} \cdot \vec{\epsilon}'^*|^2 \sum_{|i\rangle, |f\rangle} \sum_{j, j'} P_i \langle i | \exp(-i\vec{q}\vec{r}_j) | f \rangle \langle f | \exp(i\vec{q}\vec{r}_{j'}) | i \rangle \delta(E_i - E_f + \hbar\omega). \quad (3.23)$$

The double differential cross-section in this case consists of the Thomson scattering differential cross-section

$$\left( \frac{d\sigma}{d\Omega'} \right)_{|i\rangle \rightarrow |f\rangle} = r_0^2 \frac{\omega'}{\omega} |\vec{\epsilon} \cdot \vec{\epsilon}'^*|^2 \quad (3.24)$$

and the dynamic structure factor

$$S(\vec{q}, \tilde{\omega}) = \sum_{|i\rangle, |f\rangle} \sum_{j, j'} P_i \langle i | \exp(-i\vec{q}\vec{r}_j) | f \rangle \langle f | \exp(i\vec{q}\vec{r}_{j'}) | i \rangle \delta(E_i - E_f + \hbar\tilde{\omega}) \quad (3.25)$$

where the energy of the excitation is  $\tilde{\omega}$  [82]. The Thomson scattering cross-section describes the photon-electron interaction and the dynamical structure factor  $S(\vec{q}, \tilde{\omega})$  the strength of the excitation during the scattering process.

In real IXS experiments, there are many possible excitations that can be studied. Most of them have different excitation energies and therefore require different instruments to measure them. A sketch of the possible excitations and their line shape are presented in Figure 3.7. However, in this thesis IXS is used to investigate the phonons. Accordingly, the dynamical structure factor for phonons is important. A full derivation is too lengthy for this thesis and not very useful in aiding understanding the experimental sections of the thesis. Further discussions of the dynamical structure factors from phonons are given by Burkel [89] and Baron [90] and for electronic excitations by Schülke [82]. Following their discussions, it is insightful to express the dynamical structure factor with time-dependent operators [82, 89, 90]. In particular, this factor can be expressed using the charge density operator. For phonons, the dynamical structure factor can be expressed as

$$S(\vec{q}, \tilde{\omega}) = S_0(\vec{q}, \tilde{\omega}) + S_1(\vec{q}, \tilde{\omega}) + S_2(\vec{q}, \tilde{\omega}) + \dots \quad (3.26)$$



by modeling them in the simplest possible case of harmonic motions and including some simplifications justified by experimental implementations. In the dynamical structure factor,  $S_i(\vec{q}, \tilde{\omega})$  describes the contribution from  $i$  phonons [90]. The first term

$$S_0(\vec{q}, \tilde{\omega}) = N_l^2 |f_0(\vec{\tau})|^2 \delta(\vec{q} - \tau) \delta(\hbar\tilde{\omega}) \quad (3.27)$$

describes the usual Bragg scattering term with  $l$  being the index of the primitive cell with total count of  $N_l$  and  $f_0(\vec{\tau})$  the Thomson structure factor for the Bragg reflection with  $\vec{\tau}$  being the reciprocal lattice vector of the Bragg reflection. For a single phonon, the dynamical structure factor, including corrections for effects beyond the harmonic model of phonons, is given by

$$S_1(\vec{q}, \tilde{\omega}) = N_l \sum_{\vec{Q}} \sum_j |f_{1p}(\vec{\tau}, \vec{Q}, j)|^2 \delta(\vec{q} - \vec{Q} - \vec{\tau}) L_{\vec{q}j}(\tilde{\omega}, T) \quad (3.28)$$

with the one-phonon structure factor

$$|f_{1p}(\vec{\tau}, \vec{Q}, j)|^2 = \frac{1}{\omega_{\vec{q}j}} \left| \sum_d \frac{f_{0,d}(\vec{\tau} + \vec{Q})}{\sqrt{2M_d}} e^{-W_d(\vec{\tau} + \vec{Q})} \cdot \vec{\epsilon}_{\vec{Q}jd} e^{i(\vec{\tau} + \vec{Q}) \cdot \vec{\tau}_d} \right|^2 \quad (3.29)$$

and the phonon line shape and phonon occupation factor

$$L_{\vec{q}j}(\tilde{\omega}, T) = \frac{1}{\pi} \frac{1}{1 - e^{\frac{-\hbar\tilde{\omega}}{k_B T}}} \frac{4\tilde{\omega}\omega_{\vec{Q}j}\gamma_{\vec{q}j}(\tilde{\omega})}{(\tilde{\omega}^2 - \Omega_{\vec{q}j}(\tilde{\omega})^2)^2 + 4\tilde{\omega}^2\gamma_{\vec{q}j}(\tilde{\omega})^2} \quad (3.30)$$

with the  $d$  giving the atom index in the cell and the energy of the phonon  $\omega_{\vec{q}j}$  at the corresponding vector/index and the Debye-Waller factor  $W_d$  [90]. In addition, the temperature  $T$ , Boltzmann constant  $k_B$ , the half width at half maximum (HWHM) of the phonon  $\gamma_{\vec{q}j}$ , renormalized phonon frequency

$$\Omega_{\vec{q}j}(\tilde{\omega})^2 = \omega_{\vec{Q}j}^2 + 2\omega_{\vec{Q}j}\Delta_{\vec{q}j} \quad (3.31)$$

and the shift of the phonon mode frequency  $\Delta_{\vec{q}j}$  are included. The reciprocal space vector  $\vec{Q}$  is a vector in the first Brillouin zone describing the phonon wavevector, and the delta function ensures

$$\vec{q} = \vec{Q} + \vec{\tau}. \quad (3.32)$$

Similar terms can also be derived for multi-phonon excitations [90]. Experimentally, the important observation is, that the one-phonon line shape, which typically dominates the spectrum, can be described by a damped harmonic oscillator (DHO) function with renormalized phonon energy  $\Omega_{\vec{q}j}(\tilde{\omega})$  by incorporating some further simplifications described by Fåk and Dorner [91]. Furthermore, phonon modes with lower energy have higher intensity. The last point is especially important for TDS measurements.

**Resonant inelastic X-ray scattering** Similar to the earlier sections, there is also a resonant contribution to inelastic X-ray scattering. Close to the resonance, all non-resonant contributions can be neglected, as the resonant part dominates the scattering. This part is mainly probed in RIXS experiments. Similar to the case for the non-resonant scattering, the cross-section can be further analyzed and simplified for different excitations. A sketch of the measurable excitations with RIXS are shown in Figure 3.8. As a further evaluation is not beneficial for the understanding of the thesis and is therefore omitted. More details can be found, for example in the book by Schülke [82] or the review by Ament et al. [69].

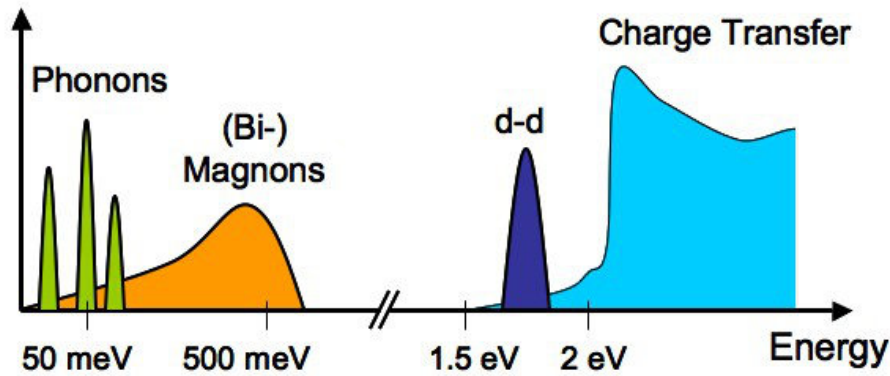


**Figure 3.8.:** Sketch of the possible excitations measured with resonant inelastic X-ray scattering. Sketch of the lineshape and energy range of different excitations which can be measured with RIXS. The figure is reproduced from Brink [92] under CC-BY 4.0.

### 3.3. Pressure generation

#### 3.3.1. Overview

The application of pressure or stress is a helpful tool in modern condensed matter physics to tune e.g. competing orders in a series of materials such as the cuprates [93–96], iron-based superconductors [46, 97–99], the transition-metal dichalcogenides [100, 101] or kagome metals [102, 103]. In the case of hydrostatic pressure, the pressure is applied uniformly from all directions in the compressive direction. However, in the case of uniaxial or biaxial stress, the stress is applied only along one or two axes, respectively, and can be applied in both compressive and tensile directions. Based on this, one difference is that hydrostatic pressure is inherently symmetry preserving (ignoring possible structural transitions under pressure). Uniaxial pressure, however, can be used to break symmetries deliberately. One common example is to break the fourfold rotation symmetry in tetragonal systems by changing the  $a$  or  $b$  axis. The actual direction can be chosen to be along a specific direction e.g. to probe for a certain symmetry. In this thesis, only hydrostatic pressure and uniaxial (compressive) stress will be used and further discussed.

Over time, different experimental setups were developed for the application of pressure and strain. Setups for hydrostatic pressure typically require a pressure transmitting medium that transmits the force that is typically applied in one direction into a uniform — hydrostatic — pressure. No pressure transmitting medium can ensure perfect hydrostatic conditions, but to stay as close as possible to hydrostatic conditions the pressure transmitting medium should be gaseous or liquid at the pressure and temperature used. If this is not possible, especially at high pressures and low temperatures, the pressure transmitting medium is ideally only a soft solid [104]. Accordingly, the best medium is helium as it has a very low melting point, but also other noble gases can be used [104, 105]. Depending on the pressures and temperatures also liquids as different oils (e.g. silicone or daphne oil) [105], mixtures of liquids (e.g. 16:3:1 mixture of methanol:ethanol:water) [105] or soft salts (e.g. NaCl, KBr, ...) [106] are used.

Depending on the pressure range and experiment different types of pressure cells were developed, each with advantages and disadvantages and more suited for certain types of experiments. For relatively low pressures ranging up to a few hundred bar [107], gas pressure cells with compressed gases can be used. For medium pressure up to  $\approx 50$  kbar or  $\approx 5$  GPa, piston cylinder cells can be used [108] with a

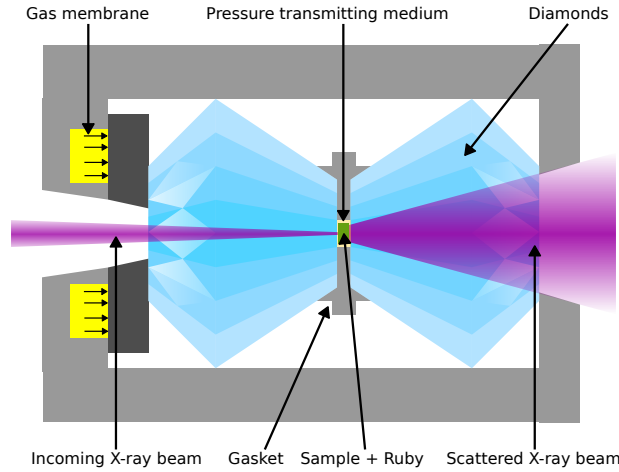


**Figure 3.9.: Sketch of a membrane type diamond anvil cell.** Sketch of a membrane type DAC. The diamond anvils, gas membrane for the external pressure application, gasket, sample and the X-rays are sketched.

relative large sample volume. Pressures up to 109 GPa were reached using large-volume presses [109]. Even higher pressures beyond 400 GPa are reported with DACs [110, 111]. However, DACs can also be used for lower pressures. Compared to the other cell types, they have the advantage of having easy access for optical light and X-rays, making them widely used for XRD, other X-ray techniques and also in this thesis. More details about the DAC are shown in Section 3.3.2.

A further important point is the pressure calibration. For pressure calibration, resistivity [112], lattice parameters [113], fluorescence lines [113, 114] and Raman shift [115] of calibrated standard materials are widely used. For medium-high pressures and diamond anvil cells, typically the R fluorescence lines of ruby (Cr-doped corundum) crystals are used for the pressure calibration [114], as this can easily be measured in-situ through the diamonds.

Similarly to hydrostatic pressure, different methods have been developed for the application of uniaxial pressure. A common technique is to clamp a sample between two pistons and compress them [116]. A further technique uses the bending of substrates to such transmit the pressure onto a sample [117, 118]. A similar approach directly bends microstructures prepared with a focused ion beam (FIB) [119]. Furthermore, the differential thermal expansion of a sample and substrate can be used to apply uniaxial [120] and biaxial pressure [99]. More easily tuneable is the use of piezoelectric materials as the substrate, in which the pressure can be tuned by the applied voltage [121].

These methods have different limitations and disadvantages, such as the controllability, tuneability and the compatibility with (transmission) X-ray experiments. With the development of a piezoelectric uniaxial compression device, a new method with higher controllability was available [116]. With modifications, this type of cell can also be used in (transmission) XRD and IXS experiments [93]. This type of cell will be used in the thesis and explained further in Section 3.3.3.

### 3.3.2. Diamond anvil cell

For generation of hydrostatic pressure, DACs were used in the work described in this thesis. A sketch of a membrane driven DAC is shown in Figure 3.9. In a diamond anvil cell, an external force is transmitted to the diamond anvils. The diamond anvils are cut in such a way that they have a large upper culet and a small culet towards the sample. This increases significantly the pressure applied at the sample side of the diamonds. Common designs of DAC apply the external force by screws or via the gas pressure

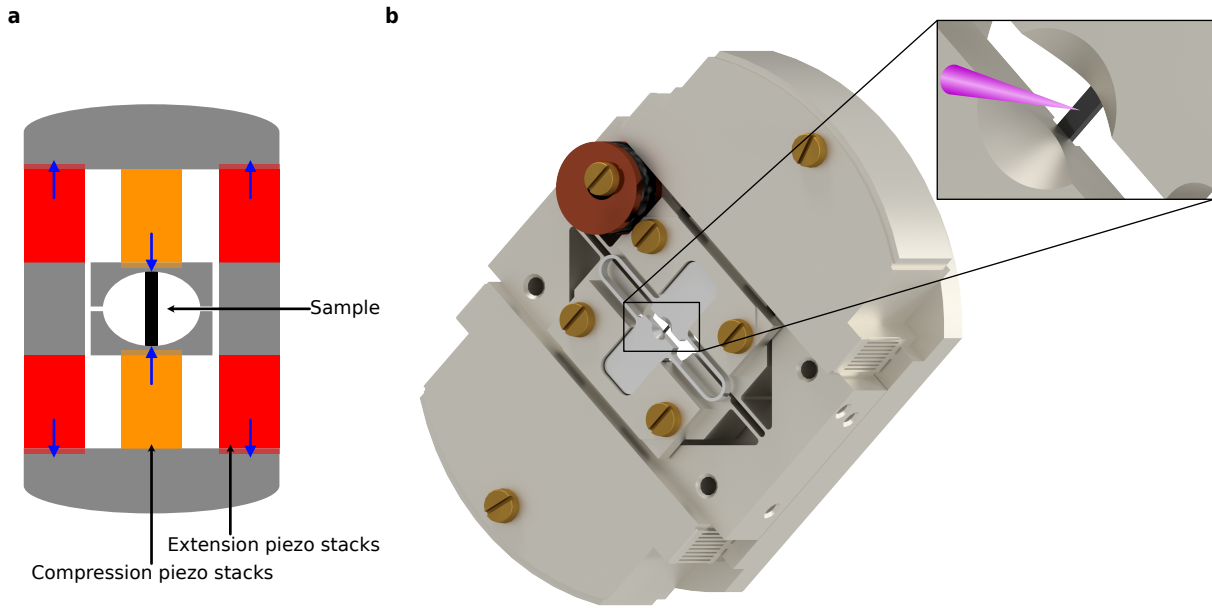


**Figure 3.10.: Sketch of a piezoelectric uniaxial pressure cell and rendering of the setup used.** **a** Sketch of a symmetric, transmission type, piezoelectric uniaxial pressure cell. The extension and compression piezo stacks are highlighted in red and orange, respectively. Furthermore, the length change of the piezostacks for positive voltages is sketched, with the direction indicated by blue arrows. The sample is shown in black. **b** Rendering of the used Razorbill Instruments CS200T uniaxial pressure cell. The used sample holder, thermometer and the sample are shown. In the inset a magnified view of the sample and the incoming X-ray beam is presented.

in a membrane. Such a membrane type DAC was used in this thesis and has the advantage that the pressure can be changed inside the cryostat and therefore at low temperatures.

The two diamond anvils compress a thin metallic gasket. Inside the gasket, a hole was drilled before closing the cell for the sample space. Inside this gasket hole, the sample, pressure transmitting medium and the pressure indicator are loaded. In the case of a gas loading, as performed for the experiments in this thesis, a highly compressed gas is inserted in a pressure vessel. The DAC is closed inside the pressure vessel with the applied gas. This captures the gas inside the gasket hole and allows for a comparable low starting pressure. The gasket itself, constrains the sample space and prevents the loss of the pressure medium during the experiment. The pressure applied from the diamond anvils is then converted by the pressure transmitting medium to a (nearly) hydrostatic pressure.

The size of the diamonds, thickness of the gasket, gasket hole, gasket material and pressure transmitting medium are determined by the intended pressure range of the experiment. Generally, the larger the intended final pressure of the experiment, the smaller the diamond culet and sample hole must be. This restricts the available sample volume for experiments.

Low-temperature XRD experiments, as used in this thesis, introduce further restrictions. Firstly, the experiment requires access for the incoming and scattered X-rays with a maximum opening cone. The opening cone restricts the accessible reciprocal space for the experiment. Ideally, the diamonds are as thin as possible to minimize the parasitic diamond scattering and the cell should be made from a low temperature compatible material, such as BeCu.

### 3.3.3. Piezoelectric uniaxial pressure cells

For the generation of uniaxial pressure, piezoelectric transmission uniaxial pressure cells were employed. A sketch of the cell and a rendering, including the used sample holder, thermometer and sample, are presented in Figure 3.10. The design of the uniaxial pressure cell consists of two groups of identical piezo stacks. When positive voltage is applied, the outer piezos lead to tension of the sample and the inner piezos lead to compression of the sample. The needle shaped sample is typically mounted freestanding inside a sample carrier which is mounted on the movable parts of the cell. The connection to the sample must be made with a very stiff, low thermal expansion glue. A common choice is LOCTITE STYCAST 2850 FT. For checking the nominal strain, a capacitive sensor, which measures the gap between the moveable parts of the cell, is used.

This approach has the advantage, compared to directly mounting the sample on a piezo stack, that (ideally) the use of the two opposite piezo stacks cancels the large thermal expansion of piezoelectric materials. At the same time, the controllability and tuneability is maintained. However, the compensation of the piezos is not perfect, the capacitance sensor has a temperature dependence and only measures the nominal strain. Furthermore, the differential thermal expansion between the titanium of the cell body and the sample remains. This can be partly compensated by measuring the capacitance change with a titanium dummy sample. Using the obtained corrections, the gap distance can be actively controlled during the cooldown. If the differential thermal expansion of the sample and titanium is known, this effect can be compensated, though this is not important for most experiments.



## 4. Origin of the charge density waves

Parts of this chapter were already published in:

- S. M. Souliou, T. Lacmann, R. Heid, C. Meingast, M. Frachet, L. Paolasini, A.-A. Haghighirad, M. Merz, A. Bosak, and M. Le Tacon, *Physical Review Letters* **129**, 247602 (2022)

### 4.1. Introduction

As discussed in Chapter 2,  $\text{BaNi}_2\text{As}_2$  exhibits two CDWs that can be suppressed with chemical substitution. Depending on the substituent, the suppression of the CDWs is different. This naturally raises the question of the origin and the mechanisms responsible for the formation of the CDWs. Furthermore, the difference between the phase diagrams raises the question of the connection between the two CDWs and whether the underlying ordering mechanisms change upon substitution. So far, the origin of the two CDWs in  $\text{BaNi}_2\text{As}_2$  is unknown, even though an unconventional mechanism was suggested at the time of its discovery [22]. However, a study directly investigating the potential (conventional) ordering mechanism has not yet been conducted. Hence, this chapter will examine the origin, ordering mechanism, connection and tuneability of both the I-CDW and C-CDW. For the tuneability, a study of phosphorus substituted  $\text{BaNi}_2\text{As}_2$  seems promising, as for this substituent the I-CDW is still observed even though the C-CDW is completely suppressed.

As discussed in Section 3.1, in Peierls-like CDW instabilities a complete softening of an unstable phonon branch at the CDW wavevector [56] is observed to drive the CDW instability. In many Peierls-like systems, but also in systems which cannot be described by this model, a phonon softening was found [123–130]. Nonetheless, there are exceptions, such as the kagome superconductors where, so far, no Kohn anomaly has been observed at the CDW transition [131, 132]. The phonon anomaly itself can originate from a Peierls-like mechanism — Fermi surface nesting or locally enhanced EPC [56, 59, 60, 133] — or unconventional mechanisms [64, 66, 67].

Therefore, to investigate the questions raised, a detailed investigation of the phonons in  $\text{BaNi}_2\text{As}_2$  is crucial. The combination of first principles calculations, TDS and IXS is a powerful tool to investigate the origin of the CDW. The DFPT calculations can be used to guide the experiment to promising Brillouin zones to observe the phonon anomaly. Furthermore, with these calculations, Fermi surface nesting and the locally enhanced EPC can be investigated. TDS is comparably fast ( $\leq 1$  h per scan), allowing multiple samples to be screened and large areas of reciprocal space to be measured. This opens up the possibility to measure the substitution and temperature dependence of the CDW intensity and correlation length. Moreover, the TDS maps can be used as a guide for Brillouin zones with intense diffuse scattering for the IXS measurements. Finally, the IXS measurements are energy resolved and provide access to the phonon softening, dispersion and linewidth.

As  $\text{BaNi}_2(\text{As}_{1-x}\text{P}_x)_2$  exhibits two CDWs, this chapter is divided into the investigation of the origin and tuneability of the I-CDW in Section 4.3 and the investigation of the transition from the I-CDW to the C-CDW in Section 4.4.

In the first section, the TDS investigation (Section 4.3.1) reveals intense diffuse scattering present already at room temperature which is enhanced and more narrow on approach to the I-CDW transition temperature. Throughout the complete substitution series of  $\text{BaNi}_2(\text{As}_{1-x}\text{P}_x)_2$  ( $0 \leq x \leq 0.12$ ), the formation is very similar. The transition is only suppressed in temperature and broadened. The additional features in the TDS maps and also the shape of the diffuse cloud of the I-CDW are well captured by TDS calculations, as presented in Section 4.3.2.

The IXS measurements in Section 4.3.3 show the complete softening of a transverse optical phonon branch on approaching the I-CDW transition. The softening is comparable for a non-substituted and  $x \approx 0.1$  sample. The phonon branch itself is, at the I-CDW position, intrinsically broad and close to being overdamped. Along the longitudinal direction, no softening, but instead the formation of an elastic peak, compatible with the TDS results, is found. Together with the TDS measurements these sections show a soft phonon origin of the I-CDW and only small variation of the I-CDW ordering under phosphorus substitution.

While the DFPT calculations (Section 4.3.5) capture the phonon instability and wavevector well, no signs of a conventional ordering mechanism are found. Both the joint density of states (JDOS) and phonon linewidth do not show an anomaly at the I-CDW position which could hint to Fermi surface nesting or locally enhanced electron phonon coupling. Accordingly, a pronounced Kohn anomaly drives the I-CDW, but the underlying ordering mechanism is still unconventional.

At the transition to the C-CDW (Section 4.4), the situation is different. Neither in the TDS nor in the IXS measurements, can precursors of the transition be seen in the phonons. The transition itself is rather sharp and shows a jump from an extended softened region emerging from the I-CDW to a static, resolution-limited peak at the C-CDW transition. Accordingly, for the C-CDW, no soft phonon origin is found, making the two I-CDWs from the phonon perspective distinct.

Finally, in Section 4.5, the results are summarized and discussed. However, in Section 4.2, first follows a rather technical description of the experimental and computational details. Readers not interested in those details can skip this section.

## 4.2. Experimental and computational details

### 4.2.1. Experimental details

The TDS and IXS experiments were performed at the side station and main station of the beamline ID28 of the European Synchrotron Radiation Facility-Extremely Brilliant Source (ESRF-EBS) [134, 135], respectively. For the TDS measurements, six samples with substitutions between  $0.0 \leq x \leq 0.12$  were used. From the  $x \approx 0.1$  substitution level two different samples were investigated in different temperature ranges. The IXS measurements on the I-CDW were performed on one  $x = 0$  sample and two  $x \approx 0.1$  samples, denoted as samples 1 and 2. No relevant difference was observed between the two samples. The measurements on the C-CDW were performed on a  $x \approx 0.037(5)$  sample. The samples were grown by the author of this thesis and Dr. Amir-Abbas Haghighirad. The growth is described in reference [136] and, for lower substitution levels, in the authors' master thesis [137].

For the IXS experiments, the incident X-ray beam energy was set to 17.794 keV using the (9 9 9) silicon reflection, with a consequent energy resolution of 3 meV. The beam was focused to a spot of  $25 \times 50 \mu\text{m}^2$  and the momentum resolution was set to  $\approx 0.25$  1/nm in the horizontal scattering plane and  $\approx 0.75$  1/nm perpendicular to it. The  $x = 0; 0.037$  samples were mounted on a glass needle using a two component epoxy (Huntsman Araldite rapid). The needles were mounted on a diffraction



goniometer head. An additional  $\chi$  motor was mounted for this experiment. The samples were cooled down with a Cryostream 700 Plus cooling system. The measurements on the  $x \approx 0.1$  samples were performed with a closed-cycle cryostat with a Joule-Thompson stage with kapton windows and an inner aluminized Mylar heat shield (base temperature  $\approx 2.2$  K). Differently from the experiments with the Cryostream 700 Plus, the cooldown in an evacuated cryostat requires a good thermal contact with the sample. Consequently, the samples were mounted on a copper rod. Sample 1 was mounted with a two component epoxy (Huntsman Araldite rapid) which was painted over with silver paint to improve thermal contact. Sample 3 was mounted with a two component silver epoxy (EPO-TEK H20E) and cured at  $\approx 90^\circ\text{C}$  in vacuum. The copper rod was screwed into the cryostat and, for better thermal contact, the pin and cryostat were connected by silver paint. For the measurements with the Joule-Thompson cryostat an additional  $\theta$  motor was used.

For the TDS measurements, the X-ray beam energy was set to 17.794 keV and the beam was focused to a spot of  $20 \times 40 \mu\text{m}^2$ . The data were recorded with a Pilatus3 X 1M detector in shutterless mode while continuously rotating the sample and recording images. Each image was integrated over an angular range of  $0.1^\circ$  or  $0.25^\circ$  and for 1 s. The CrysAlis Pro [138] software package was used to determine the unit cell and sample orientation. The two- and three-dimensional reciprocal space reconstructions were created with a software developed at the beamline ID28. Low-temperature conditions were achieved using an Oxford Cryostream 700 Plus cooling system. For the second  $x \approx 0.12$  sample, a closed cycle cryostat (base temperature of  $\approx 10$  K) with Kapton windows and internal shielding and beamstop to reduce the Kapton scattering was used.

Similarly to the IXS samples, the TDS samples used with the Cryostream were mounted on glass pins with a two component epoxy (Huntsman Araldite rapid) as good thermal contact is not needed and can be counterproductive. The glass pins were mounted on a goniometer head. The sample used with the closed cycle cryostat was mounted with a two component silver epoxy (EPO-TEK H20E) on a copper pin to achieve the best possible thermal contact. The epoxy was cured at  $\approx 90^\circ\text{C}$  in a vacuum. The thermal contact between the copper rod and cryostat was improved with silver paint.

The phosphorus substitution was determined by energy dispersive X-ray spectroscopy (EDX) using an COXEM EM-30AXN SEM-EDX with an Oxford Instruments Aztec EDX detector and AztecLiveLite Software. This revealed a substitution of  $x \approx 0; 0.036(5); 0.063(5); 0.066(5); 0.09(1); 0.12(1)$  for the TDS samples.

The TDS and IXS experiments were performed by the author of this thesis, Dr. Sofia-Michaela Souliou, Fabian Henßler, Dr. Mehdi Frachet, Dr. Philippa McGuinness, Dr. Luigi Paolasini, Dr. Alexei Bosak and Dr. Daniel Chaney.

#### 4.2.2. Computational details

For the density-functional calculations of the electronic structure and lattice dynamics, the mixed-basis pseudopotential method [139, 140] was used. This approach employs an efficient description of more localized components of the valence states by using a basis set combining plane waves and local functions at atomic sites. The electron-ion interaction is described by norm-conserving pseudopotentials, which were constructed following the descriptions of Hamann, Schlüter, Chiang [141, 142] for Ba and Vanderbilt [143] for Ni and As, respectively. Semi-core states Ba-5*p*, Ni-3*s*, Ni-3*p* were included in the valence space. The exchange-correlation functional was represented by the general-gradient approximation in the PBE form [144]. The mixed-basis set consisted of plane waves with a cutoff for the kinetic energy of 22 Ry and local functions of *p,d* type for Ba and *s,p,d* type for Ni, respectively. Lattice

dynamics properties were calculated within the linear response or density functional perturbation theory (DFPT) as implemented in the mixed-basis method [145].

Brillouin-zone integration was performed by sampling a  $16 \times 16 \times 8$   $k$ -point mesh in conjunction with a Gaussian broadening of 50 meV. The calculations were also performed with a Gaussian broadening of 500 meV to completely suppress the phonon anomaly. The Gaussian smearing simulates, in a strongly simplified manner, the temperature of the system. An increased Gaussian smearing therefore simulates higher temperatures, that lead to a suppression of the phonon instability. It is common that the energy of the Gaussian broadening corresponds to an unrealistic large temperature. To locate the positions of phonon anomalies in the momentum space, scans of the phonon dispersions on two-dimensional high-symmetry planes were performed as follows. Dynamical matrices were calculated within DFPT on an  $8 \times 8$  mesh, and interpolated on a much denser  $120 \times 120$  mesh using a standard Fourier interpolation technique. Diagonalizing the dynamical matrices provided the phonon frequencies. The DFPT calculations were performed by Dr. Rolf Heid.

For the calculation of TDS intensities, the unstable phonon branch must be stabilized. To achieve this the atomic positions were not relaxed and a larger Gaussian smearing of 0.1 eV was used. The actual TDS intensities, reciprocal space maps and IXS intensities were calculated using an adapted version of the software *ab2tds* [146] based on the eigenvalues and vectors from the DFPT calculations. To prevent too low or negative energies at the  $\Gamma$ -point leading to undefined TDS intensities all phonon energies were capped at  $1 \times 10^{-7}$  eV. As it is generally challenging to include substitutions in DFPT, all calculations are performed for non-substituted  $\text{BaNi}_2\text{As}_2$ . The calculation of TDS intensities were performed with the help of Dr. Rolf Heid. Changes to the *ab2tds* code were aided by Dr. Björn Wehinger.

### 4.3. Incommensurate charge density wave

#### 4.3.1. Thermal diffuse scattering and incommensurate charge density wave transition temperature

We begin by discussing the diffuse scattering above the triclinic transition in pristine and phosphorus substituted  $\text{BaNi}_2(\text{As}_{1-x}\text{P}_x)_2$ . Before focusing on a smaller part of the reciprocal space for a detailed temperature dependence, the different features observed in broad-range reciprocal space TDS maps must be identified. Based on these, a selection of a promising section of the reciprocal space can be made. Accordingly, in Figures 4.1a-b, large parts of the reciprocal space in the  $(h\ k\ 1)$ - and  $(4\ k\ l)$ -planes are presented.

Already at room temperature, intense diffuse scattering can be observed in the  $(h\ k\ 1)$ -plane. The dominant diffuse scattering features are lines along the  $h$  and  $k$ -direction with intense, triangular-shaped spots at the I-CDW wavevector of  $q_{\text{I-CDW}} \approx (0.28\ 0\ 0); (0\ 0.28\ 0)$ . On cooling to 102 K, the spots increase in intensity and get more narrow. Along the  $l$ -direction, the spots exhibit a similar change, but are much more elongated. At lower temperatures, also much weaker second order reflections of the I-CDW can be observed.

The peaks and the diffuse scattering at the I-CDW positions show a distinct structure factor with no significant intensity around certain Bragg reflections, e.g.  $h = 0; 1$ . On the other hand, the diffuse scattering is particularly intense around the  $\{4\ 1\ 1\}$  Bragg reflections. Higher values of  $l$  also show strong diffuse scattering, but for higher  $l$ -values the transverse and longitudinal modes mix. This makes a differentiation of the transverse and longitudinal modes challenging. Around the same  $\{4\ 1\ 1\}$  Bragg-peaks also further diffuse spots and lines are visible (highlighted in Figure 4.2). Especially at

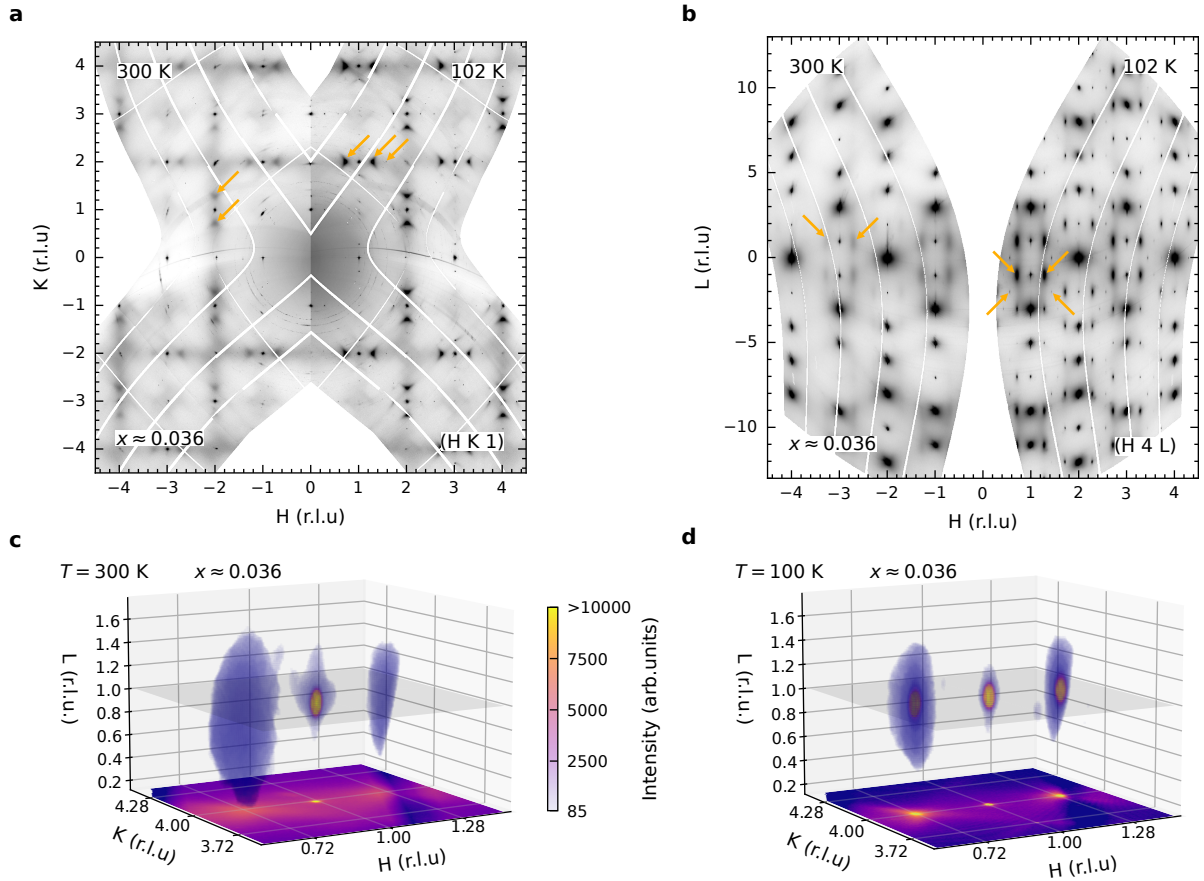


**Figure 4.1.: Two- and three-dimensional reciprocal space reconstructions for different temperatures.** **a** ( $h k l$ ) and **b** ( $h 4 l$ ) reciprocal space maps from TDS for a  $x \approx 0.036$  sample at 300 K and 102 K. The 300 K data set has been mirrored at  $h = 0$  for display purposes. **c-d** Three-dimensional reciprocal space reconstruction of the TDS intensity around the (1 4 1) Bragg reflection and the diffuse cloud at the I-CDW position for a  $x \approx 0.036$  sample at **c** 300 K and **d** 100 K. In addition, the two-dimensional projection of the intensities integrated along the  $l$ -direction are shown. The color scale indicates the color and opacity of each voxel in the three-dimensional reconstruction. To aid visibility, the opacity of the color scale is quadrupled.

lower temperatures, weak but sharp peaks in the longitudinal direction and rhombus shaped diffuse lines are visible.

As all of the diffuse features around the  $\{4 1 1\}$  Bragg reflections are particularly strong, they are good candidates for a more detailed investigation of the temperature dependence. This is in line with DFPT calculations and earlier works [27], which indicated a high phonon structure factor and I-CDW intensities around these reflections.

Based on this we now focus on the diffuse scattering around the (1 4 1) Bragg reflection. First, to examine the shape of the diffuse cloud at the I-CDW position, three-dimensional reciprocal space reconstructions around the (1 4 1) Bragg peak are shown in Figures 4.1c-d. The three-dimensional reconstructions have been scaled to provide an authentic aspect ratio in  $1/\text{\AA}$ . Similarly to those seen in the larger reciprocal space maps at room temperature, pronounced diffuse clouds are visible at the I-CDW position. Note that the cloud at (1.28 4 1) is cut due to a rod of missing intensities stemming from gaps between the detector elements of the used Pilatus detector.

The diffuse scattering does not exhibit the form of a simple rotational ellipsoid, but resembles a “kidney” with a triangular cross-section in the  $l$ -direction. It could also be described as a smoothed out spherical

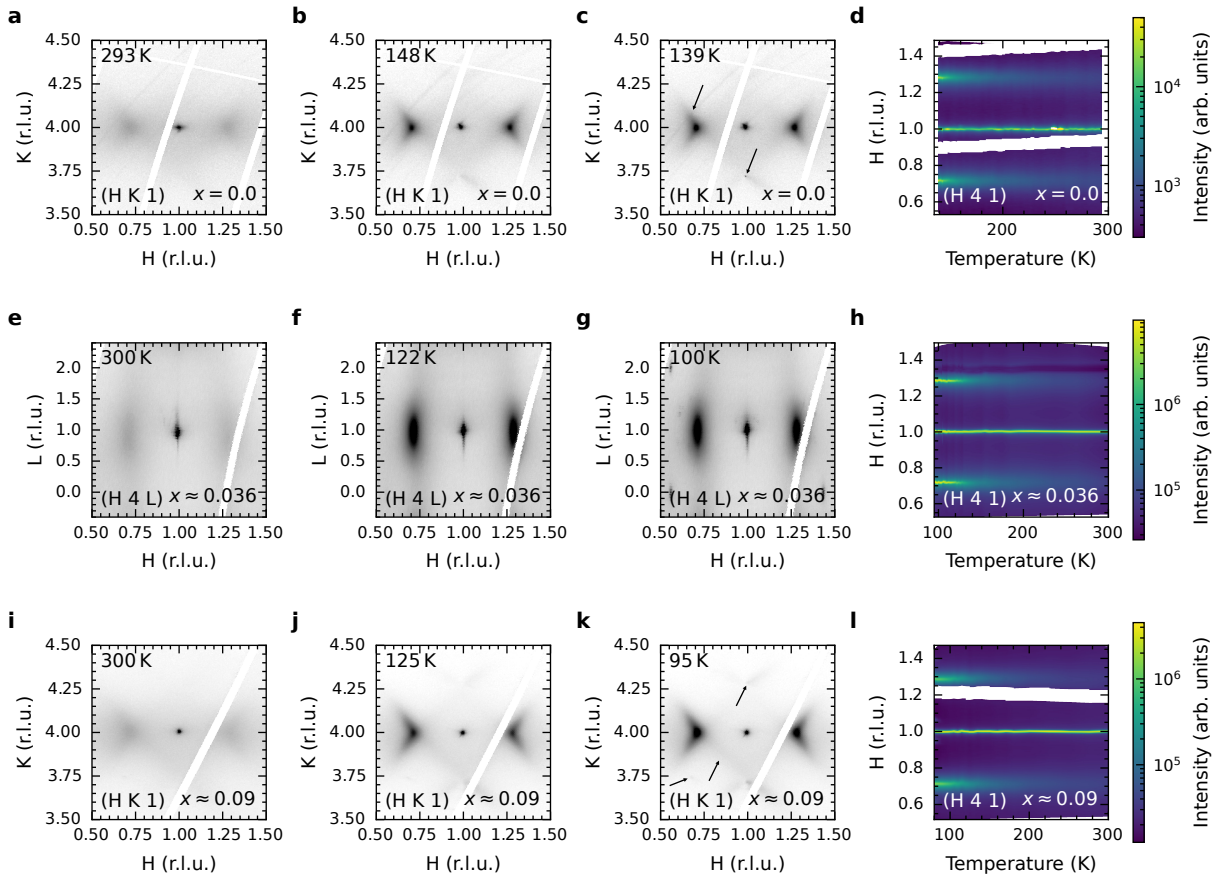


**Figure 4.2.: Reciprocal space maps and linecuts of the I-CDW at different temperatures and substitution levels.** **a-c** ( $h k 1$ ) reciprocal space maps around the  $(1\ 4\ 1)$  reflection for a non-substituted sample at **a** 293 K, **b** 148 K and **c** 139 K. The “tails” around the I-CDW diffuse scattering and the peak in the longitudinal direction are highlighted by arrows. **d** Colormap of the linecuts through the I-CDW and Bragg peak versus temperature for the non-substituted sample. **e-g** ( $h k 1$ ) reciprocal space maps around the  $(1\ 4\ 1)$  reflection for a  $x \approx 0.036$  sample at **e** 300 K, **f** 122 K and **g** 100 K. **h** Colormap of the linecuts through the I-CDW and Bragg peak versus temperature for the  $x \approx 0.036$  sample. **i-k** ( $h k 1$ ) reciprocal space maps around the  $(1\ 4\ 1)$  reflection for a  $x \approx 0.09$  sample at **i** 300 K, **j** 125 K and **k** 95 K. The diffuse rhombus and the longitudinal and diagonal peaks are highlighted by arrows. **l** Colormap of the linecuts through the I-CDW and Bragg peak versus temperature for the  $x \approx 0.09$  sample.

wedge. The shape of the cross-section is best seen in the two-dimensional projection. In the  $l$ -direction, the diffuse scattering is broader, indicating a smaller out-of-plane than in-plane correlation length. At 100 K, the cloud of diffuse scattering exhibits a similar shape but more intense and sharper. In the center of the diffuse cloud at the I-CDW position, a sharp, Bragg-like and intense peak is formed, signaling the transition to the ordered I-CDW. In addition, sharp, but weak peaks appear at  $(1\ 4 \pm 0.28\ 1)$ .

Further details of the in-plane diffuse scattering are presented in the  $(h k 1)$  and  $(h 4 l)$  reciprocal space maps for  $x \approx 0; 0.036; 0.09$  in Figure 4.2. A complete substitution series with  $(h k 1)$  and  $(h 4 l)$  maps can be found in Figure A.1 and Figure A.2 in the appendix. Similarly to the three-dimensional reconstructions, the intense, triangular-shaped diffuse scattering around the I-CDW positions is sharper and more intense at lower temperatures. The comparison between different substitution levels shows a similar behavior for all measured substitution levels, up to the maximum of  $x \approx 0.12$ . The only difference is that the temperature at which the sharp central peak is formed is lowered and the transition is smeared out. Below the temperature at which the intense central peak is formed, second order peaks

of the I-CDW also appear. At this temperature for all substitution levels, weak, but sharp peaks along the longitudinal direction, e.g.,  $(1\ 4.28\ 1)$  instead of  $(1.28\ 4\ 1)$  emerge. At slightly higher temperatures, a weak diffuse background develops close to this position. For phosphorus substituted crystals, a faint and more diffuse signal can also be seen in the diagonal direction, e.g.,  $(0.72\ 3.72\ 1)$ . Even though the diffuse scattering around the I-CDW position is not present in the  $(h\ k\ 0)$ -plane, the longitudinal, transverse and diagonal peaks also appear (see Figure 4.7c). Furthermore, higher order reflections for the longitudinal and transverse directions are visible. The diagonal peaks are more easily visible as there is generally less diffuse scattering in that region.

In addition to the diffuse scattering at positions similar to the wavevector of the I-CDW, also diffuse lines forming a rhombus around the Bragg peak are visible. Here, the edges are close to the I-CDW wavevector along the transverse and longitudinal direction, but at slightly lower  $q$ . The lines forming the rhombus extend to the tails of the triangular shaped diffuse scattering around the I-CDW position. The rhombus, tail and further features are indicated by black arrows in Figure 4.2.

No further pronounced features are visible in the presented diffuse scattering maps. However, diffuse lines similar to the rhombus are visible around the position of the forbidden Bragg reflections, especially in the  $(h\ k\ 0)$ -plane. Interestingly, they are close to the position at which a second I-CDW emerges under applied hydrostatic pressure, which will be discussed in Chapter 6. In this chapter, the second instability will be denoted as I-CDW2. Further diffuse lines between and around the Bragg reflections are observed in  $(h\ k\ 0)$ -plane. More details are presented in Section 4.3.2 and Appendix D.

The intensity and linewidth of the observed features in the TDS can be quantified by performing linecuts through the features. Starting with the diffuse scattering at the I-CDW position, the corresponding cuts in the  $h$ -direction are shown in a color map in Figure 4.2. The cuts show the two satellite peaks from the I-CDW around the Bragg peak. While the Bragg peak does not change, both satellites significantly gain in intensity and sharpen, as discussed above for the maps before.

In Figures 4.3a-c, similar cuts but in the  $l$ -direction are shown. They confirm the behavior observed in the plane and the lower correlation length along the  $c$ -direction.

More importantly, in Figures 4.3d-f and g-i similar cuts through the longitudinal and diagonal peaks, which are much harder to observe in the color plots are shown. For visualization, a linear background is subtracted. While this is a good approximation for the longitudinal peaks, this is not the case for the diagonal peaks. Due to the lower intensity and proximity of the TDS signal along the rhombus, as discussed previously, the background is much stronger and challenging to subtract. The proper way would be to fit the diffuse scattering from the rhombus and subtract the tails extending to the position of the diagonal peaks. However, due to the very high difference in intensity, this is not reliable and can easily change the intensity of the peak. Furthermore, other background fits, such as polynomials, also severely alter the results. In the end, the most reliable method is to subtract a linear background, even though the background is clearly not linear.

Returning to the linecuts along the longitudinal direction, a clear formation of a sharp peak is visible at low temperatures. However, first a diffuse and broad peak at slightly higher wavevector  $q \approx 0.3$  forms, which could be related to the rhombus and “tails” seen in the maps. Then, around the ordering temperature, a sharp peak emerges out of the diffuse background at the same wavevector as the I-CDW, but in the longitudinal, not transverse, direction. At a similar temperature, an even weaker peak at the diagonal direction  $(0.28\ 0.28\ 0)$  emerges in the other linecuts. On the one hand, the temperature dependence of the transverse (I-CDW), longitudinal and diagonal peaks is very similar, but, on the other hand, their absolute intensities are very different and the diagonal peak can only be observed in the phosphorous substituted samples. Nonetheless, except for these differences, all of the substitution

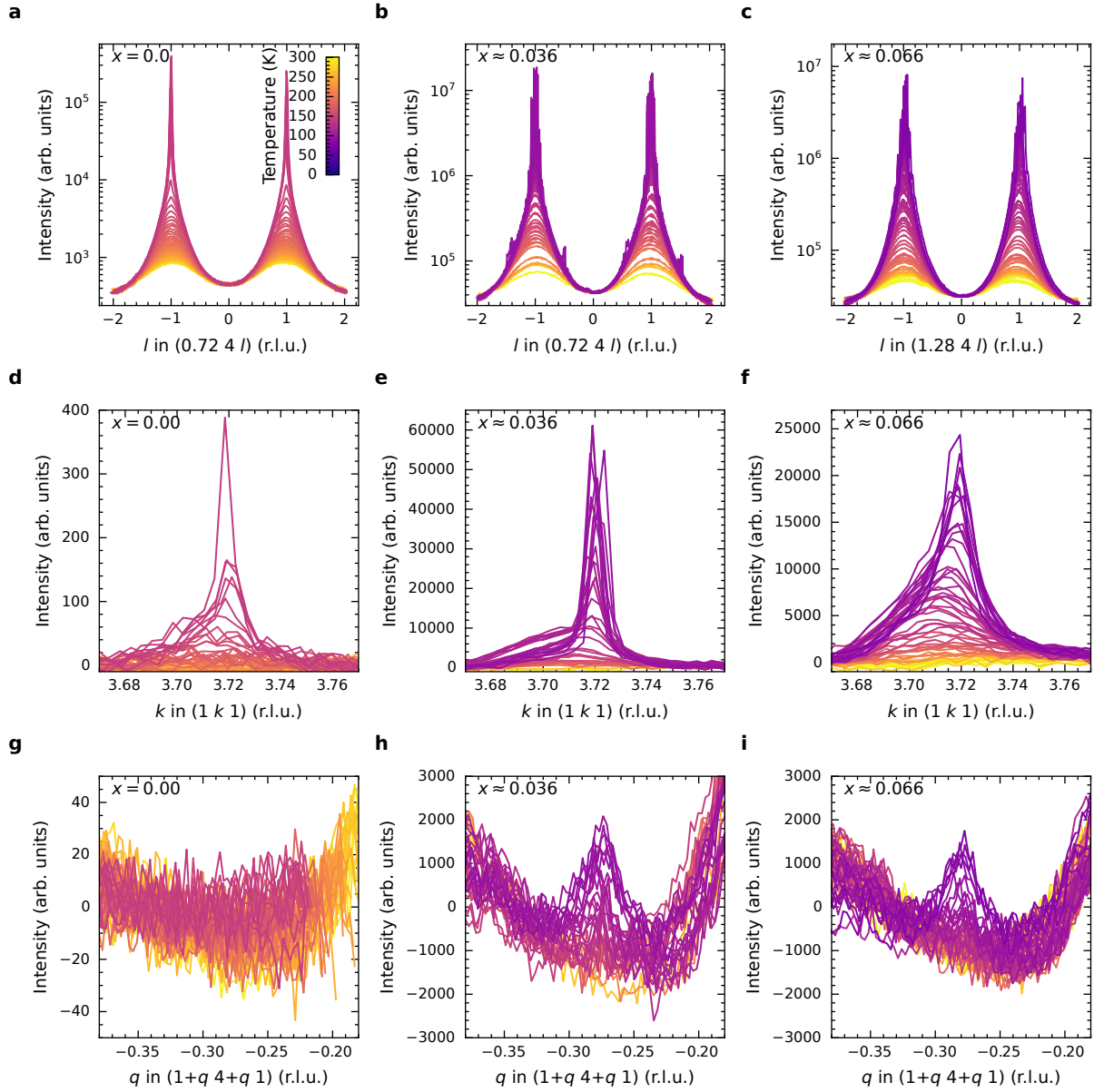


**Figure 4.3.:** Linecuts through the different peaks observed in the reciprocal space maps. **a-c** Linecuts in the  $l$  direction through the I-CDW peak at  $(0.72\ 4\ 1)$  or  $(1.28\ 4\ 1)$  for different temperatures in the **a**  $x = 0$ , **b**  $x \approx 0.036$  and **c**  $x \approx 0.066$  samples. **d-f** Linecuts in the  $k$  direction through the longitudinal peak at  $(1\ 3.72\ 1)$  for different temperatures in the **d**  $x = 0$ , **e**  $x \approx 0.036$  and **f**  $x \approx 0.066$  samples. **g-i** Linecuts in the  $[1\ 1\ 0]$  direction through the longitudinal peak at  $(0.72\ 3.72\ 1)$  for different temperatures in the **g**  $x = 0$ , **h**  $x \approx 0.036$  and **i**  $x \approx 0.066$  samples.

levels exhibit a very similar behavior. Similarly to the I-CDW peak, only the temperatures and absolute intensities change.

The I-CDW peaks can also be fitted to extract the intensity and the correlation length. The extracted inverse correlation lengths in the  $a$  and  $c$  directions are shown for all substitutions in Figures 4.4a,e. The correlation length at room temperature is only weakly dependent on the substitution, and is rather short with  $\xi_a \approx 60\ \text{\AA}$  and  $\xi_c \approx 22\ \text{\AA}$ . For all substitutions, the correlation length increases significantly upon reaching the transition temperature. However, with increased phosphorus content the transition temperature is continuously lowered and the increase in correlation length is less steep. This is



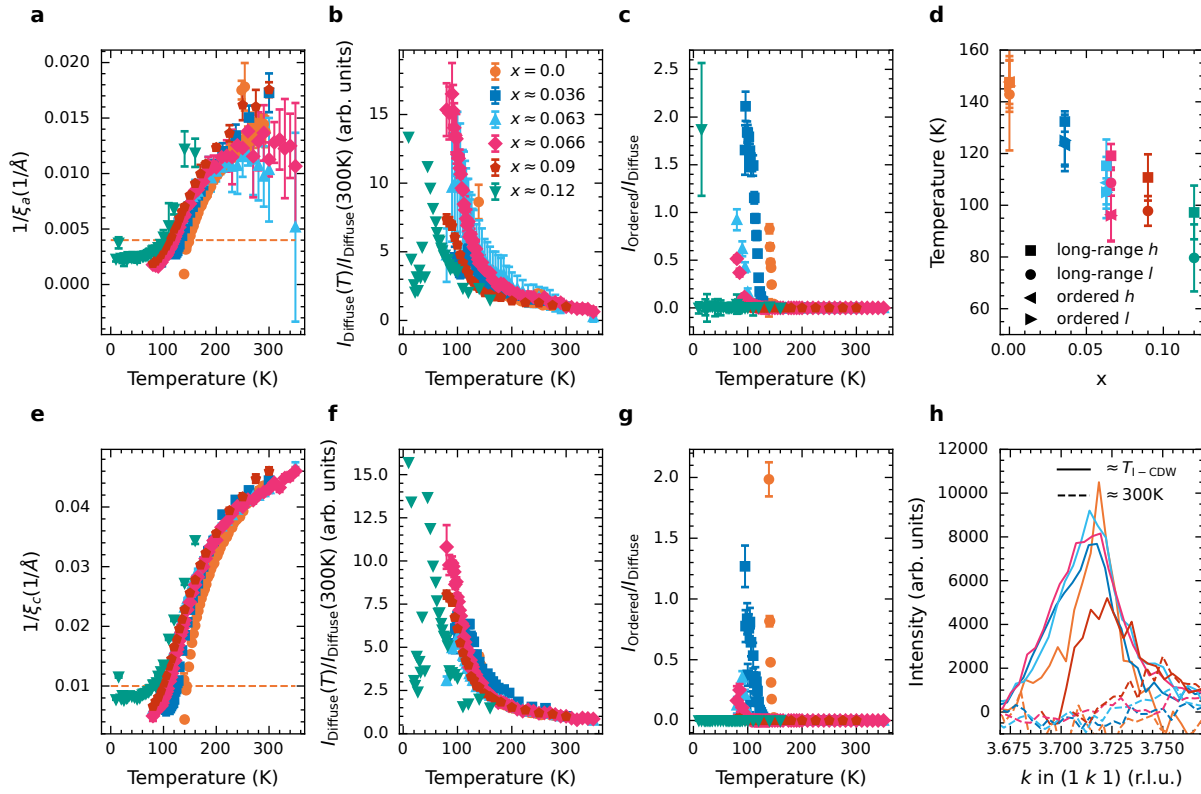


**Figure 4.4.: Fit parameters of the I-CDW peaks and intensity of the longitudinal and diagonal peaks.** **a, e** Temperature dependence of the extracted inverse correlation lengths in the  $h$  and  $l$ -direction for different substitution levels, respectively. The dashed orange line indicates the critical correlation length extracted from the non-substituted sample. **b, f** Temperature dependence of the intensity of the diffuse I-CDW peak in the  $h$  and  $l$ -direction. **c, g** Intensity ratio of the ordered and diffuse I-CDW peaks for different substitution levels extracted from linescans in the  $h$  and  $l$ -direction, respectively. **d** Extracted I-CDW transition temperature  $T_{I-CDW}$  from the critical correlation length and the intensity ratio in the  $h$  and  $l$ -direction. **g** Linecuts through the longitudinal direction close to the I-CDW transition temperature  $T_{I-CDW}$  and at 300 K

true both for the in-plane and the out-of-plane correlation lengths. As the out-of-plane correlation length is significantly smaller at room temperature, the correlation length in the  $c$ -direction exhibits a more pronounced and sharper increase. Through the smearing out of the transition with increasing phosphorus content, only the correlation length of low substituted samples can be described with a mean-field-like critical behavior.

This might also be partly caused by the fact, that at low temperatures, a single Lorentzian line is not sufficient to fit the superstructure peak. Instead, a Lorentzian for the diffuse scattering must be combined with a Bragg-like pseudo-Voigt line with a shared center. The pseudo-Voigt shape and width is constrained to the values of the nearby Bragg peak. The Bragg-like peak accounts for the sharp and intense peak in the center of the diffuse scattering in the reciprocal space maps and therefore must be included as soon as the peak appears.

Now looking at the intensities in Figures 4.4a-b and d-g, on cooling the intensity of the diffuse scattering  $I_{Diffuse}$  (the Lorentzian) increases significantly, even by more than fifteenfold for certain samples. First, there is a more gradual increase in intensity before a rapid increase at the point where the correlation length also increases. Similarly to the correlation length, with increasing phosphorous substitution the change in intensity is shifted to lower temperatures and broadened.

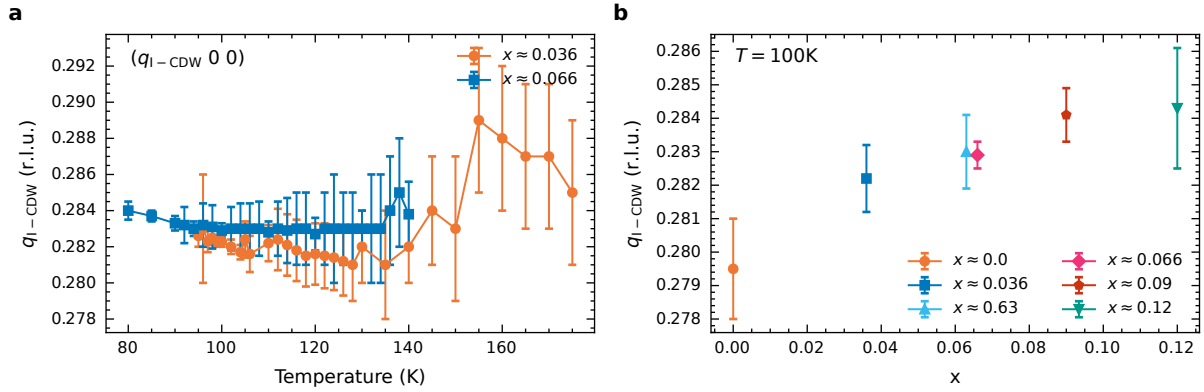


**Figure 4.5.: Temperature and substitution dependence of the I-CDW wavevector.** **a** Temperature dependence of the I-CDW wavevector in the  $h$  direction for  $x \approx 0.036$ ;  $0.066$ . **b** Phosphorus subsection dependence of the I-CDW wavevector at 100 K. The non-substituted sample wavevector is taken at 139 K.

The intensity of the Bragg like peak  $I_{\text{Ordered}}$  behaves differently. For most temperatures the intensity is zero, before at the transition it suddenly and very sharply gains intensity, eventually even more than than the diffuse part. The behavior is very similar for the in- and out-of plane directions and all substitution levels. A linear fit of the ratio of ordered and diffuse intensities  $I_{\text{Ordered}}/I_{\text{Diffuse}}$  can be used to define the onset of ordered intensity, and thus, the actual thermodynamic transition to static I-CDW order. The transition temperatures are shown in Figure 4.4d.

For at least the two lowest substitutions with the sharpest transition, the onset of the ordered intensity appear at a similar value of the correlation length. This can be used to define an alternative criterion for transitioning to a static I-CDW or at least long-range I-CDW fluctuation phase based on a "critical" correlation length. This "critical" correlation length amounts to  $\xi_{a,\text{crit}} \approx 250$  Å in the  $a$ -direction and to  $\xi_{c,\text{crit}} \approx 100$  Å in the  $c$ -direction. Importantly, the  $\xi_{c,\text{crit}}$  is always reached at a temperature slightly lower than that at which  $\xi_{a,\text{crit}}$  is reached, but which agrees very well with that at which the thermodynamic investigation revealed the small structural distortion. Notably however, for the two highest substitution levels ( $x \approx 0.09, 0.12$ ) investigated, the Bragg-like signature of the long-range ordering of the I-CDW remains elusive even though both "critical" lengths are reached (measurements down to base temperature for the  $x \approx 0.12$  sample shows a saturation of the in- and out-of-plane correlation lengths well above the width of the Bragg peaks or experimental resolution). In these samples the C-CDW is completely suppressed and no orthorhombic distortion could be resolved in the  $ab$  plane [25].

Using a linear fit of the correlation length close to the transition reveals the transition temperatures based on the "critical" correlation length presented in Figure 4.4d. This was performed for both the  $a$  and  $c$  correlation lengths.

As discussed previously, the longitudinal peaks also increase in intensity around the transition. Therefore, to cross-check the obtained transition temperatures, the linecuts at the first temperature below the extracted transition temperature are shown in Figure 4.4h. Moreover, the cuts from 300 K are presented as a background. For all substitutions, clear peaks are already formed. Together with the rather conservative choice of the critical correlation length, these temperatures should be seen more as a lower bound of the transition temperature.

As well as the correlation length and intensity, the wavevector can be extracted by investigating the peak position of several I-CDW peaks in a large volume of reciprocal space. An example temperature dependence for two substitution levels is shown in Figure 4.5a. While the temperature dependence



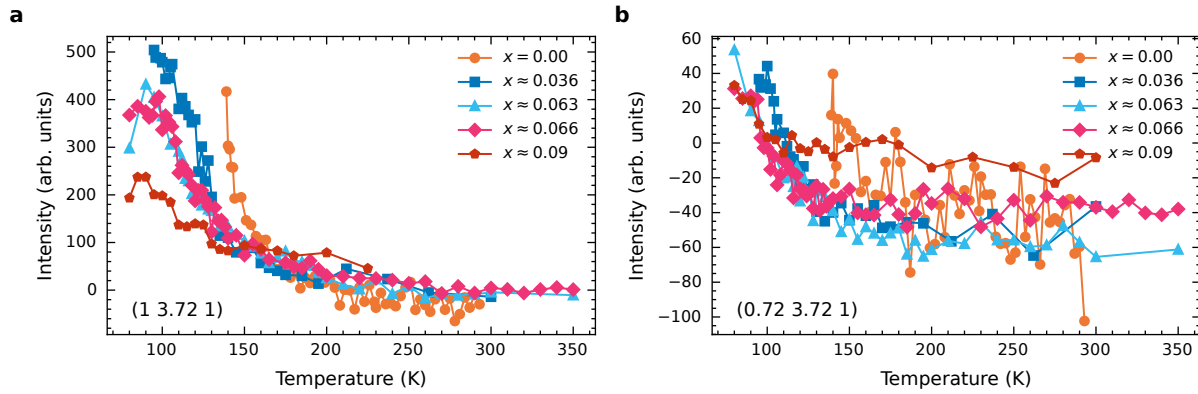


**Figure 4.6.: Integrated intensity of the longitudinal and diagonal peaks in TDS.** **a** Integrated intensity of the linecuts in the longitudinal direction versus temperature for the different substituted samples. **b** Integrated intensity of the linecuts in the diagonal direction versus temperature for the different substituted samples.

remains tiny and is comparable for different substitution levels, the wavevector increases with higher phosphorous content, as indicated in Figure 4.5b.

As the intensity for the peaks in the longitudinal and especially the diagonal directions is significantly weaker, a fit of the data would not be very reliable. In the raw data, the peaks also seem as sharp as a Bragg peak, and therefore the fitted width would not be insightful. However, the data can still be integrated to determine the integrated intensity of the peaks. The results from this are shown for the longitudinal and diagonal directions in Figure 4.6. Both peaks follow a similar trend of showing no or only a slight increase in intensity down to ordering temperature. Below this, a clear increase in intensity is observed. For higher substitution levels the increase is more shallow.

Altogether we observe intense diffuse scattering at the I-CDW wavevector, several diffuse lines (e.g. the rhombus around the Bragg-reflection) in reciprocal space and sharp peaks forming at lower temperatures. All observed peaks show a significant change around the ordering temperature of the I-CDW.

#### 4.3.2. Thermal diffuse scattering simulations

A first insight into the origin of the presented diffuse scattering features can be gained from first principle calculations. Based on the DFPT phonon calculations, the diffuse scattering from the phonons can be calculated. As mentioned in the methods section, all instabilities with imaginary eigenvalues must be first stabilized to calculate sensible intensities. Nonetheless, the instabilities must remain observable as a soft phonon. After doing so, features showing up in both the experiment and the calculations can be assigned to diffuse scattering from (soft) phonons, and the responsible phonon branch can be further investigated via DFPT calculations or (energy-resolved) IXS measurements. From this, for example, the type of the phonon branch can be evaluated.

For a comparison of the calculated and experimentally-measured TDS intensities, larger parts of reciprocal space in the  $(h \ k \ 1)$ ,  $(h \ k \ 0)$  and  $(h \ 4 \ l)$ -planes are shown in Figure 4.7. In addition, a three-dimensional TDS intensity calculation around the  $(1 \ 4 \ 1)$ -Bragg peak, similar to the experimental one displayed in Figure 4.1, is shown. Moreover, in Figure 4.7c a direct comparison of the most prominent features in the larger TDS maps is presented. Note that, while the TDS calculations do not include the actual Bragg reflections and show peaks at the Bragg positions due to the acoustic phonon modes going to zero energy, the experimental reconstructions show TDS and (oversaturated) Bragg peaks.

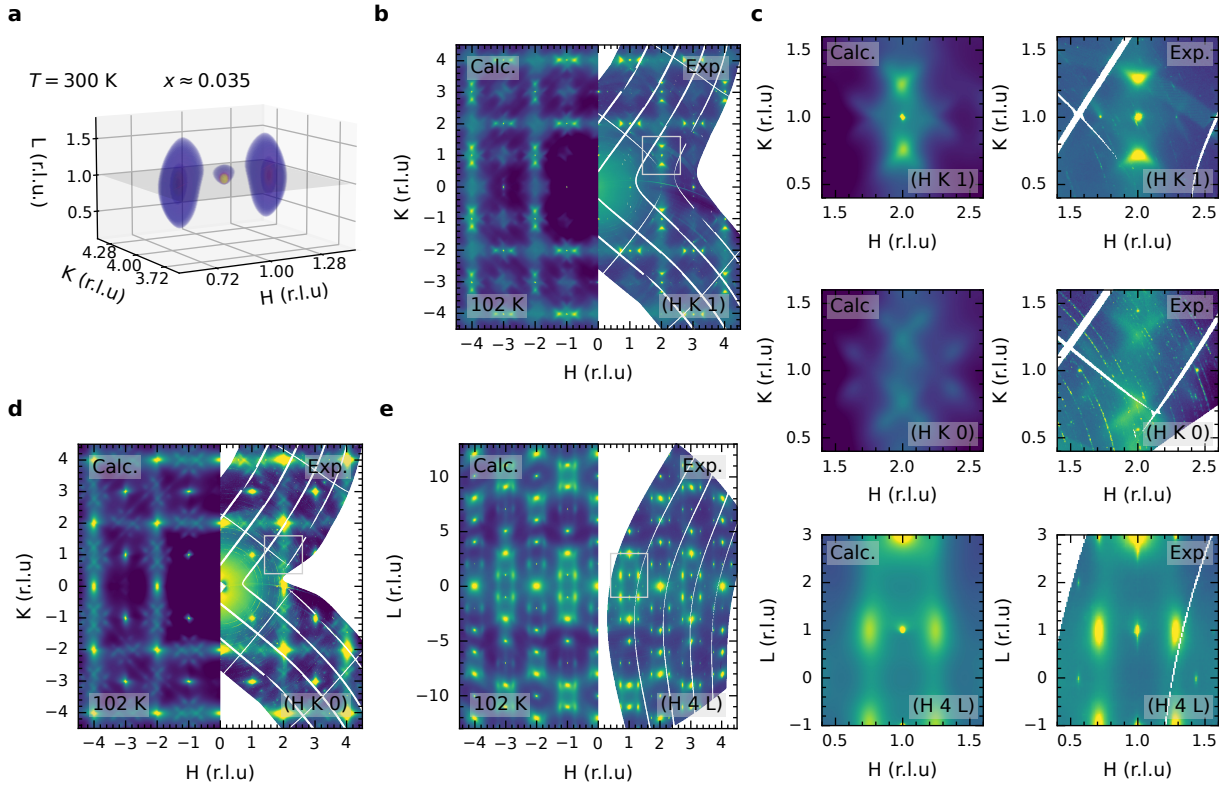


**Figure 4.7.: Thermal diffuse scattering calculations and comparison to experiment.** **a** Three-dimensional TDS calculations around the  $(1\ 4\ 1)$ -Bragg peak with temperature factors for  $102\text{ K}$ . **b,d-e** TDS calculations and experimental diffuse scattering maps in the **b**  $(h\ k\ 1)$ , **d**  $(h\ k\ 0)$  and **e**  $(h\ 4\ l)$ -planes at  $102\text{ K}$ . The grey rectangles indicate the part of reciprocal space shown in **c**. The experimental data are for the  $x \approx 0.036$  sample. **c** Direct comparison of the calculated and measured intensities in smaller parts of reciprocal space.

The calculated diffuse cloud around the I-CDW position manifests a similar “kidney”/wedge shape, prolonged in  $l$ -direction, as the experimentally observed one. Only the Bragg like central peak attributable to the static I-CDW order is missing. This is also confirmed in the  $(h\ k\ 1)$ -map, in which both the calculations and experiment show the rectangular shape diffuse scattering around the I-CDW and the rhombus around the Bragg peak. Furthermore, the diffuse lines between Bragg peaks along the  $h$  and  $k$ -direction and  $q$  dependence of the intensity of these features is well captured. However, while the diffuse scattering around forbidden Bragg peaks also shows up in the experiment, it is less pronounced than in the calculations. Only the transverse, longitudinal and diagonal peaks (including higher orders) which appear at low temperatures are not captured by the calculations.

The excellent agreement between the calculations and experiment is also true for the  $(h\ k\ 0)$ -map. Here, the shape of the diffuse scattering directly at the Bragg peaks and the lines between the Bragg peaks are well captured. Similarly to the  $(h\ k\ 1)$ -maps, the rhombuses and lines around forbidden Bragg reflections are less pronounced in the experiment. The lines correspond to the I-CDW2 developed under hydrostatic pressure which will be discussed in Chapter 6. The diffuse scattering emerges from already-soft phonon branches that are not yet unstable. However, the TDS shows, that the softening is, in reality, not yet developed at ambient pressure. This is also confirmed by IXS measurements presented in the appendix in Appendix D.

There is also good agreement in the  $(h\ 4\ l)$  plane. In particular, the elongation of the diffuse scattering along the  $l$  direction and the  $q$  dependence are well captured in the calculations.

Unlike the experiment, the calculations allow for the disentangling of the contribution of the vibration of different atoms in the unit cell to the TDS intensity. This indicates that the rhombus and diffuse scattering around the I-CDW position emerges exclusively from vibrations of the nickel and arsenic atoms. This is different for the scattering around the forbidden Bragg reflections. For this, all three kinds of atoms are involved. However, the  $q$ -dependence of the intensity is different for barium, nickel and arsenic such that only the combination of the TDS from all three leads to a comparable shape and intensity throughout larger parts of reciprocal space. Maps of the contribution of the different atoms to the TDS are shown in the appendix in Figure A.3. This difference might be relevant for observations under hydrostatic pressure discussed in Chapter 6. More details on this are discussed alongside the IXS measurements around this position in Appendix D.

As for all maps, the first- and second-order peaks of the I-CDW and the longitudinal and diagonal peaks are not in the calculations. This suggests that they are a static (elastic) signal emerging from the static I-CDW order, in line with the experimentally observed temperature dependence and the sharpness of the peaks. All other features discussed above are captured by the DFPT and TDS calculations, strongly suggesting a phononic origin.

#### 4.3.3. Soft phonon origin of the incommensurate charge density wave for $x=0;0.1$

The last open questions regarding the I-CDW phase are the exact softening of the unstable phonon branch, the driving force behind the softening and how this is influenced by phosphorous substitution. Moreover, the phonon origin of the diffuse scattering is not yet experimentally confirmed. These remaining questions can be answered employing temperature and  $q$ -dependent (energy resolved) IXS measurements of the phonons around the I-CDW and diffuse scattering positions.

First, in this section, the phonon dispersion around the I-CDW position will be discussed. The other features will be investigated in the following sections. As the DFPT calculations and the TDS measurements suggest a strong phonon signal around the  $\{4\ 1\ 1\}$  Bragg reflection, all of the IXS measurements were performed in this Brillouin zone. For the origin of the I-CDW, the phonon dispersion along the transverse direction through the I-CDW position is of relevance. The spectra measured along this line, for a pristine and  $x \approx 0.1$  sample, are presented in Figures 4.8a,d. Both the Stokes and anti-Stokes sites are presented. In the spectra, a central line, consisting of the resolution-limited elastic line and a low-energy soft phonon, and a second phonon at higher energies are visible. The central peak of the elastic line and the soft phonon in the spectra significantly narrow on approaching the I-CDW position. This indicates softening of the low-lying phonon. The behavior is very similar for both samples. For the substituted sample, the dispersion is shown for a lower temperature of 110 K and therefore the softening is more pronounced. Actually, at 110 K, the spectrum measured at the I-CDW position consisted only of a resolution-limited line.

The spectra are fitted with a resolution-limited elastic line and two DHO functions convoluted with the resolution functions. An example fit with the individual components is shown in Figure 4.8a. The resulting phonon dispersions at several temperatures and for the two substitutions are presented in Figures 4.8b,e. In the background, the calculated IXS intensities based on the same DFPT calculations used previously for the TDS calculations are shown. The intensities are broadened with a Gaussian with a FWHM of 0.7 meV for visualization and are presented on a logarithmic scale due to the large intensity change of the soft phonon. Calculations on a linear scale and broadened with the experimental resolution function are shown in the following sections.

While the higher energy phonon shows a normal dispersion and does not change significantly with temperature, a clear Kohn-anomaly and temperature dependence is visible for the low-energy phonon.

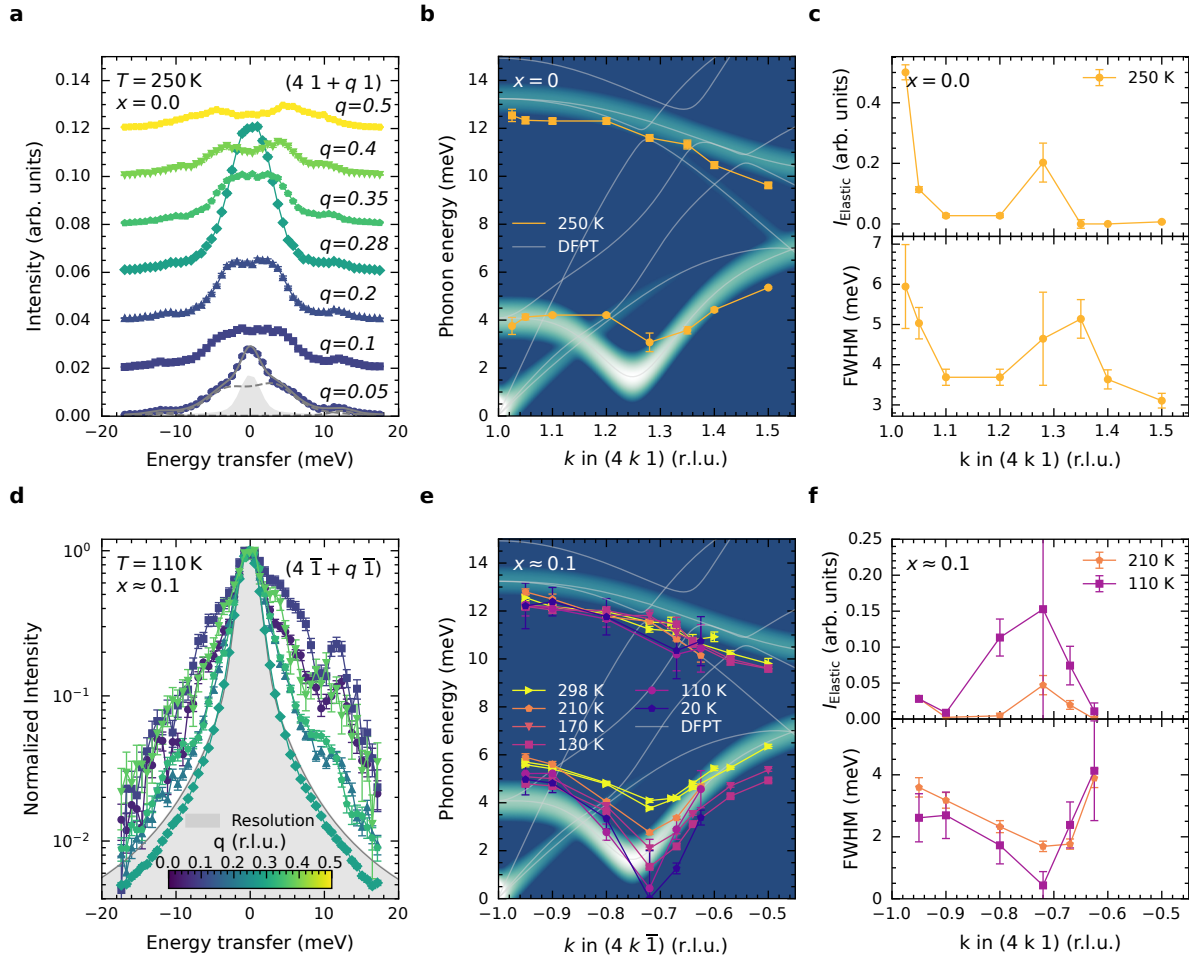


**Figure 4.8.: Measured and calculated phonon dispersion along the transverse direction.** **a** IXS spectra along the (transverse)  $[0\ 1\ 0]$ -direction with the  $(4\ 1\ 1)$  as the  $\Gamma$ -point. The measurements were taken at 250 K for the non-substituted sample. As an example, the fit and the individual components are shown for the measurement at  $q = 0.05$ . **b,e** Fitted phonon dispersion **b** the non-substituted sample at 250 K and **e** the two  $x \approx 0.1$  samples at different temperatures. In the background the calculated IXS intensity Debye-Waller factor for **b** 250 K and **e** 110 K. The intensities are broadened for visualization with a Gaussian with a full width at half maximum (FWHM) of 0.7 meV. The IXS intensity calculation is based on the same DFPT calculation that was used for the calculation of the TDS intensities. The dispersions of all phonons are indicated by gray lines. **c,f** Fitted elastic intensity and FWHM of the low lying phonon for **c** the non-substituted sample at 250 K and **g** the  $x \approx 0.1$  sample at different temperatures. **d** Normalized IXS spectra along the (transverse)  $[0\ 1\ 0]$ -direction with the  $(4\ \bar{1}\ \bar{1})$  as the  $\Gamma$ -point and experimental resolution function. The measurements are taken at 110 K for the  $x \approx 0.1$  sample.

Already at room temperature, the Kohn-anomaly is visible and is enhanced until reaching a (within resolution) zero energy static phonon at the I-CDW wavevector at low temperatures. The phonon dispersion, soft phonon mode and IXS intensities are well captured by the DFPT calculations. The position of the Kohn-anomaly is predicted at a slightly lower wavevector.

At the I-CDW position, an increased elastic line is observed at low temperatures, even before the phonon softens to zero energy and only elastic scattering is observed. Throughout the full dispersion, the low-energy phonon is intrinsically very broad and close to being overdamped, as shown by the phonon linewidth in Figures 4.8c,f. These results are comparable for both substitution levels. The dispersion also confirms the predictions from DFPT calculations that the unstable phonon branch is a transverse optical phonon branch.

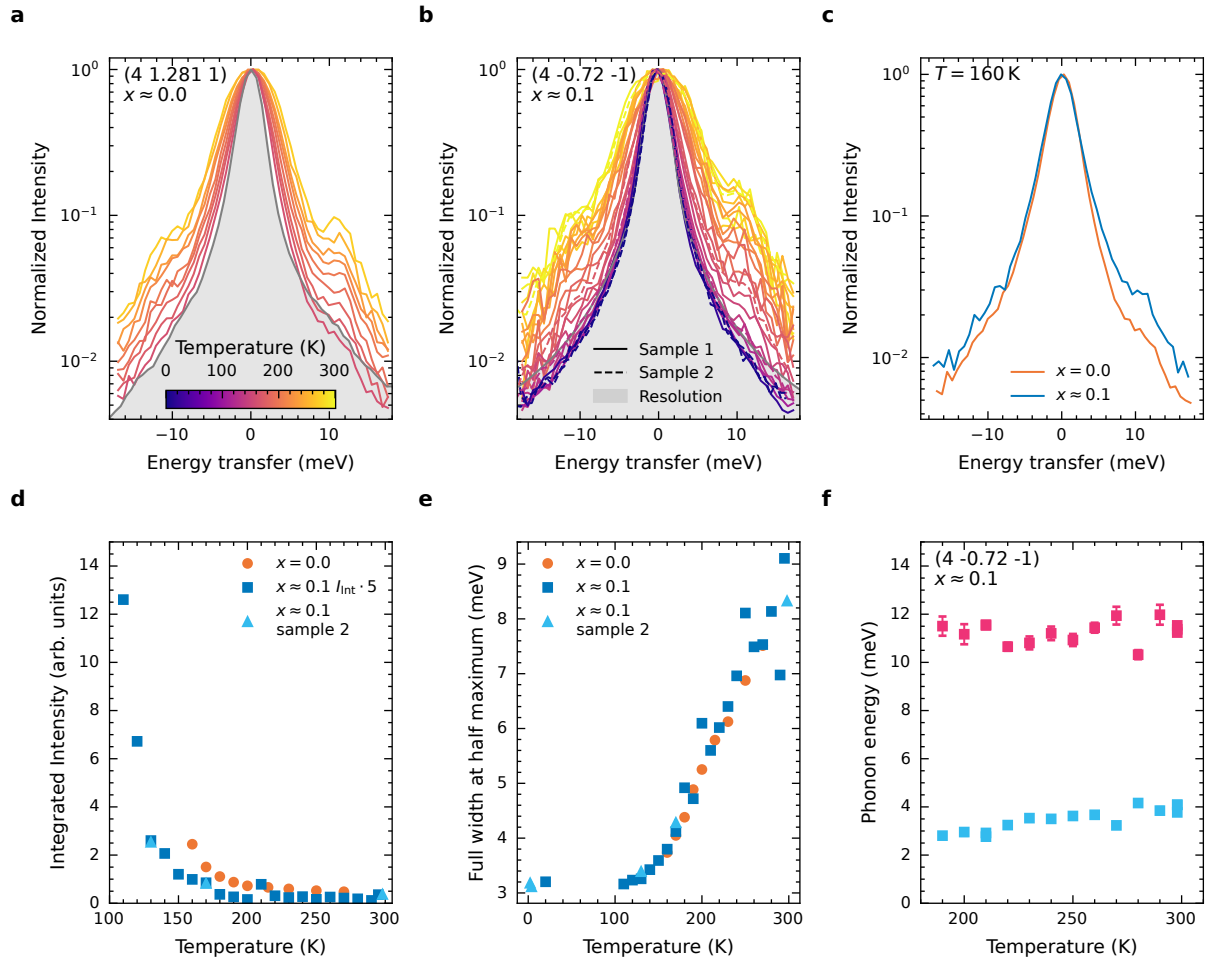


**Figure 4.9.: Temperature dependence of the phonon spectra at the I-CDW position.** **a-b** Temperature dependence of the normalized IXS spectra at the I-CDW position and experimental resolution for **a** the non-substituted sample and **b** the two  $x \approx 0.1$  samples. **c** One-to-one comparison of the IXS spectra at the I-CDW position at 160 K for the non- and phosphorous substituted samples. **d** Integrated intensity of the IXS spectra and **e** FWHM of the soft phonon at the I-CDW position versus temperature for the different samples. **f** Temperature dependence of the fitted phonon energy for the two phonons at the I-CDW position for the  $x \approx 0.1$  samples.

In Figures 4.9a-b the temperature dependence of the IXS spectra at the I-CDW wavevector for both the pristine and substituted samples are compared in more detail. A one-to-one comparison at the lowest temperature possible is shown in Figure 4.9c. In the appendix Figure A.4 similar spectra are shown for all temperatures.

For both substitution levels, the central peak narrows on cooling until a resolution-limited line is reached at lower temperatures, showing the softening and freezing of the phonon as discussed above. However, a detailed comparison shows that the IXS spectrum of the  $x \approx 0.1$  sample is broader at the same temperature. Hence, in line with the TDS results, the transition is lowered and the softening broader in temperature. This is confirmed by the integrated intensities and FWHM shown in Figures 4.9d-e.

The fitting of the spectra of the  $x \approx 0.1$  sample down to 190 K shows that only the low-energy phonon softens, as the energy of the high-energy phonon doesn't change (see Figure 4.9f). At lower temperatures, the fits are not shown as these are not reliable due to the lower energy and broad nature of the low-energy phonon. The same is true for the non-substituted sample. For the same reasons and, additionally,

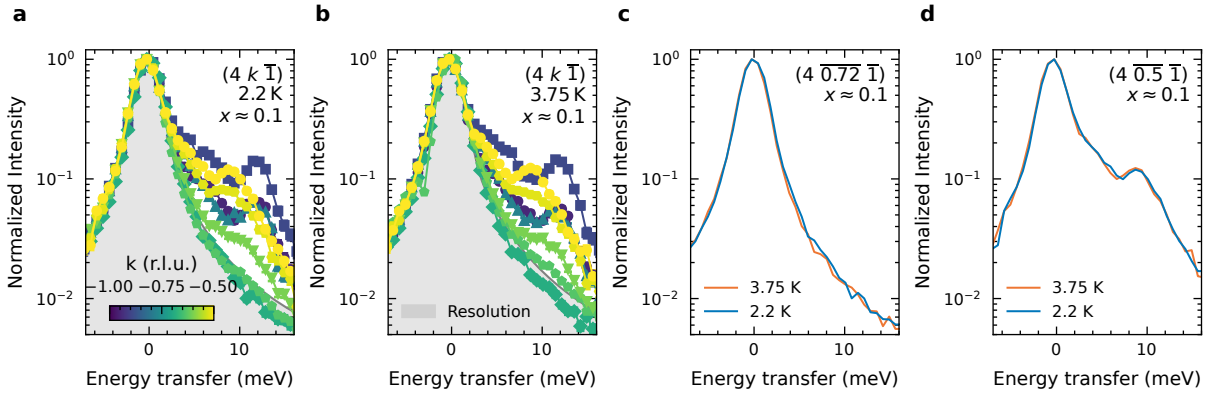


**Figure 4.10.: Phonon dispersion at 3.75 K and 2.2 K.** **a-b** Normalized IXS spectra along the  $[1\ 0\ 0]$ -direction with  $(4\ \bar{1}\ \bar{1})$  as the gamma point for the second  $x \approx 0.1$  sample at **a** 2.2 K and **b** 3.75 K. **c-d** One-to-one comparison of the normalized IXS spectra at 2.2 K and 3.75 K at **c**  $(4\ 0.72\ \bar{1})$  and **d**  $(4\ 0.5\ \bar{1})$

the 3 meV primarily Lorentzian resolution function, a clear statement regarding the proposed slowing down of I-CDW fluctuations in the pristine compound [147] can not be reliably made. Within these limitations, for the substituted sample at lower temperatures, the fit favors the overdamped zero energy phonon. On the other hand, for the non-substituted sample this does not give a better fitting result.

The cryostat used for the measurements of the  $x \approx 0.1$  sample has a base temperature of 2.2 K. As the superconducting  $T_c$  is 3.2 K for this substitution level, this allows, nominally, for measurements in the superconducting phase in order to investigate the interplay between superconductivity and the I-CDW. Nonetheless, the results have to be taken with a grain of salt, as the temperatures are nominal temperatures. A simultaneous resistivity measurement or a thermometer on the sample/very close to the sample was not possible due to experimental limitations. Furthermore, ideally, the measurements would have been performed at temperatures  $T < 1/3T_c$ .

The spectra along the  $[1\ 0\ 0]$ -direction at  $2.2\text{ K} < T_c$  and  $3.75\text{ K} > T_c$  are presented in Figures 4.10a-b. The spectra for both temperatures look nearly identical. This also confirmed by the one-to-one comparison at the I-CDW position and the last point measured in Figures 4.10c-d. Therefore, within the limits described above, no competition between I-CDW and superconductivity can be identified.

#### 4.3.4. IXS along the longitudinal and diagonal directions

As discussed before, the TDS investigation also showed features along the longitudinal and diagonal directions, despite that the soft phonon is a transverse optical phonon. With IXS measurements in, for example, the  $[1\ 0\ 0]$  and  $[\bar{1}\ 1\ 0]$ -directions with the  $(4\ 1\ 1)$  as the  $\Gamma$ -point, the origin of these features can be investigated.

First, in Figure 4.11 the IXS spectra and dispersion along the longitudinal direction are shown for the non- and phosphorous-substituted samples. Both are very similar, and show a normal dispersion with an increased elastic line at  $q = 0.28$ . This can best be seen in the temperature dependence, where the elastic line is enhanced but the phonons do not change significantly, except due to the thermal activation. This is different from the situation along the transverse direction, where the peak narrows and the phonons soften until a static order is formed. Accordingly, the fitted dispersion does not show an anomaly and exhibits a good agreement with the calculations. This result is also in agreement with the TDS measurements, which already hinted towards a static (elastic) ordered peak.



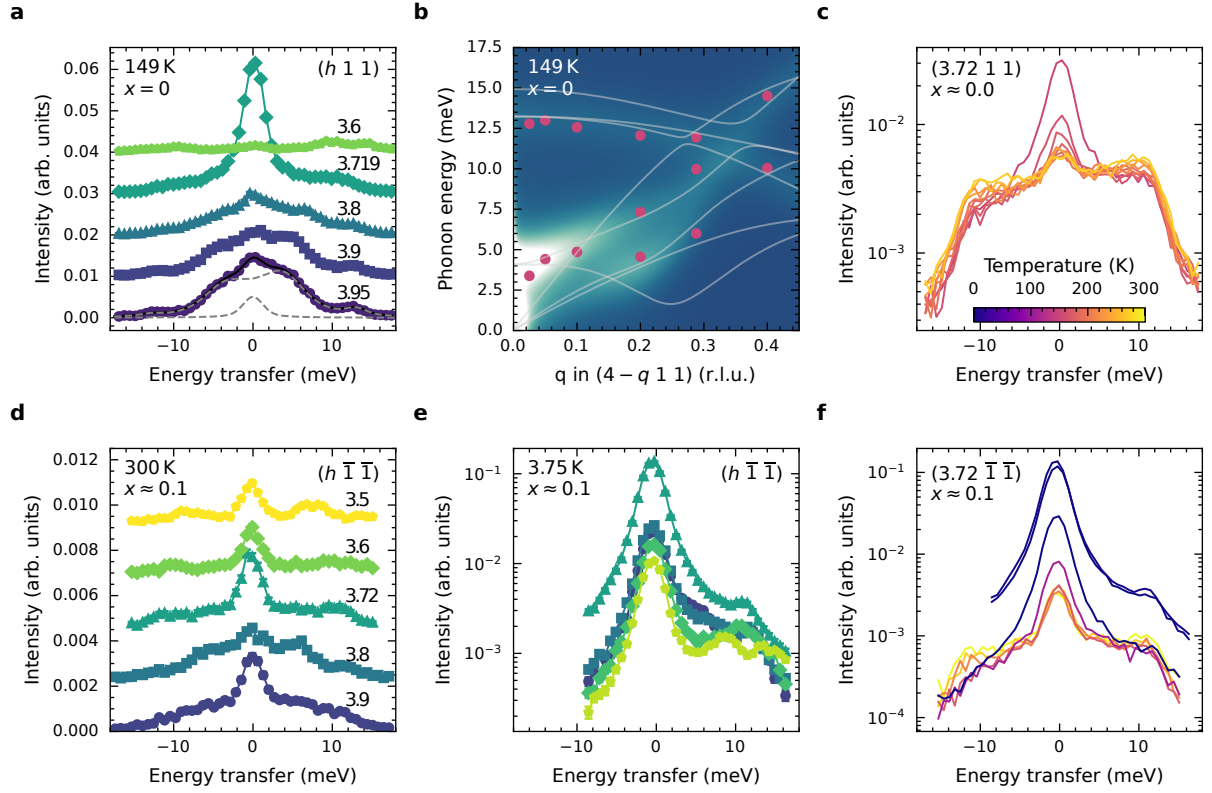


**Figure 4.11.: Measured and calculated phonon dispersion along the longitudinal direction.** **a,d-e** IXS spectra along the longitudinal direction for **a** the pristine sample at 149 K and the  $x \approx 0.1$  samples at **d** 300 K and **e** 3.75 K. **b** Fitted phonon dispersion along the longitudinal direction for the pristine sample at 149 K. In the background the calculated IXS intensities and phonon dispersion with the temperature factors of 149 K are shown. The IXS intensities are broadened by the experimental resolution function. **c,f** Temperature dependence of the IXS spectra at the longitudinal peak position for **c** the pristine sample and **f**  $x \approx 0.1$  samples.

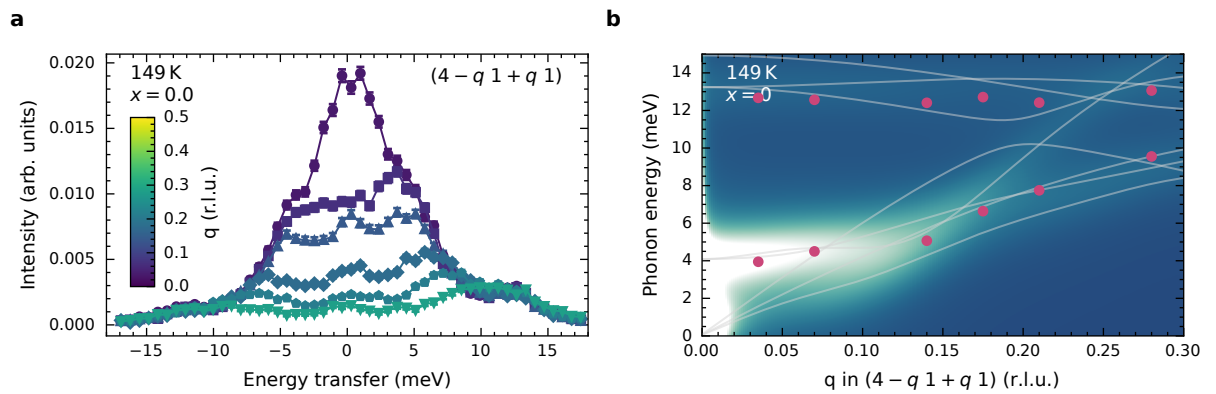


**Figure 4.12.: Measured and calculated phonon dispersion along the diagonal direction.** **a** IXS spectra along the  $[1\ 1\ 0]$ -direction with the  $(4\ 1\ 1)$  as the  $\Gamma$ -point for the non-substituted sample at 149 K. **b** Fitted phonon dispersion along the  $[1\ 1\ 0]$ -direction for the non-substituted sample at 149 K. In the background the calculated phonon dispersion and calculated IXS intensities are shown. The calculated intensities are broadened by the experimental resolution function and calculated with the temperature factors for 149 K.

The corresponding spectra along the diagonal direction for the pristine sample are shown in Figure 4.12. Both the raw data and the fitted dispersion do not show any anomalies. The flat phonon band for lower  $q$  agrees with the rhombus shaped diffuse scattering, confirming the phononic origin suggested by the TDS calculations. At the point (3.72 1.28 1), no anomaly in the phonons or an increased elastic line can be observed. This confirms that, in the pristine sample, the peak in the diagonal direction is absent. Similarly to the dispersion in the transverse and longitudinal directions, the measurements and the DFPT calculations show a good agreement.

#### 4.3.5. First-principles calculations on the soft phonon origin of the incommensurate charge density wave

As established in the other sections, the DFPT calculations show an excellent agreement with the experimental data and especially well capture the behavior of the soft phonon. This strongly suggests that the reason for the formation of the I-CDW is included within the DFPT calculations. As discussed in the introduction to this chapter and, in more detail, in Section 3.1, there are two mechanisms which could lead to the formation of a CDW. The first, a nesting in the Fermi surface, would show up as a peak at the CDW wavevector in the JDOS. A map of the calculated JDOS in the plane and a linecut along the I-CDW direction is presented in Figures 4.13a,d. Generally, the JDOS only shows broad features and, in particular, no peak can be observed close to the I-CDW wavevector. This rules out an origin of the I-CDW from Fermi surface nesting.

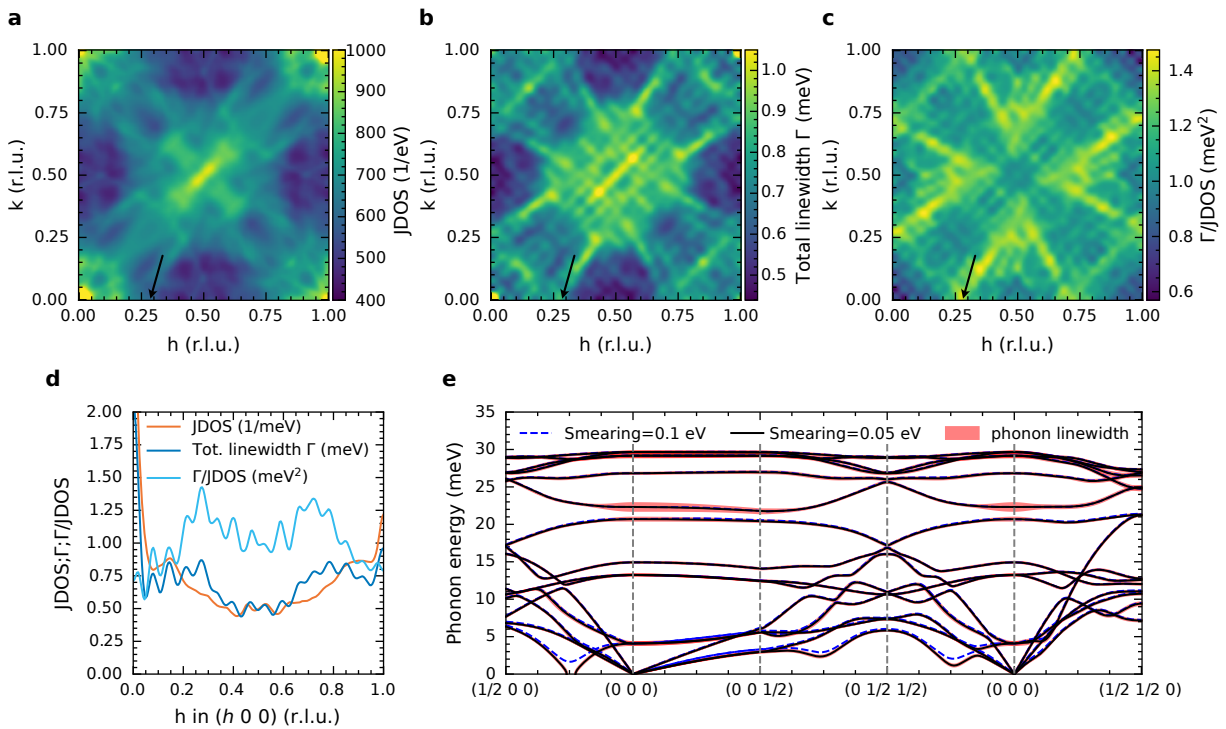


**Figure 4.13.: Calculated phonon linewidth, joint-density of states and phonon dispersion.** **a-c** Calculated in-plane maps of the **a** JDOS, **b** total linewidth of all phonon branches and **c** ratio of the linewidth and JDOS. The I-CDW position is indicated by black arrows. **d** Linecuts of the JDOS, total linewidth and ratio along the  $[1\ 0\ 0]$  direction. **e** Calculated phonon dispersion and phonon linewidth due to EPC along different directions in reciprocal space. For comparison the dispersion with the unstable phonon used for the JDOS and linewidth calculations and the dispersion with the soft, but stable phonon used for intensity calculation are shown.



The second mechanism, locally enhanced EPC, would show up in the coupling matrix element  $g_{kn, \vec{k}+\vec{q}m}^{\vec{q}\lambda}$ . A good indicator for this is the phonon linewidth due to EPC  $\gamma_{\text{EPC}}$ . A peak in the linewidth, especially if the JDOS is flat, then relates to a peak in  $g_{kn, \vec{k}+\vec{q}m}^{\vec{q}\lambda}$ . Therefore, the ratio of the linewidth and JDOS is a good quantity to check. The total phonon linewidth and the ratio to the JDOS are shown as maps and linecuts in Figures 4.13b-d. Similarly to the JDOS, both exhibit only broad features and any feature which is visible does not occur at the I-CDW wavevector. Looking at the EPC in the dispersion in Figure 4.13e, the soft phonon branch only has a minor contribution to the total EPC, also ruling out a formation of the I-CDW due to locally enhanced EPC. This makes the I-CDW unconventional as it shows up a typical Kohn-like anomaly, but none of the conventional ordering mechanisms – Fermi surface nesting and locally enhanced EPC – could be identified by the calculations.

## 4.4. Commensurate charge density wave

### 4.4.1. Diffuse scattering of the commensurate charge density wave

After investigating the I-CDW in detail, we now turn to the transition between the I-CDW and C-CDW in the orthorhombic and triclinic phases, respectively.

To get an overview and to guide the IXS measurements, we start again with TDS maps, as shown in Figure 4.14. Both  $(h\ k\ 1)$  and  $(h\ 4\ l)$  maps close to the triclinic transition for the  $x \approx 0.036$  sample are presented. Note that in this section, as throughout the complete thesis, the tetragonal notation is used for reciprocal space vectors.

At the highest temperature of 100 K, the situation is very similar to the one discussed in Section 4.3, with intense and sharp I-CDW peaks and surrounding diffuse scattering. Focusing on the  $(h\ 4\ l)$  maps, no signs of additional peaks at the C-CDW wavevector are visible. However, at a slightly lower

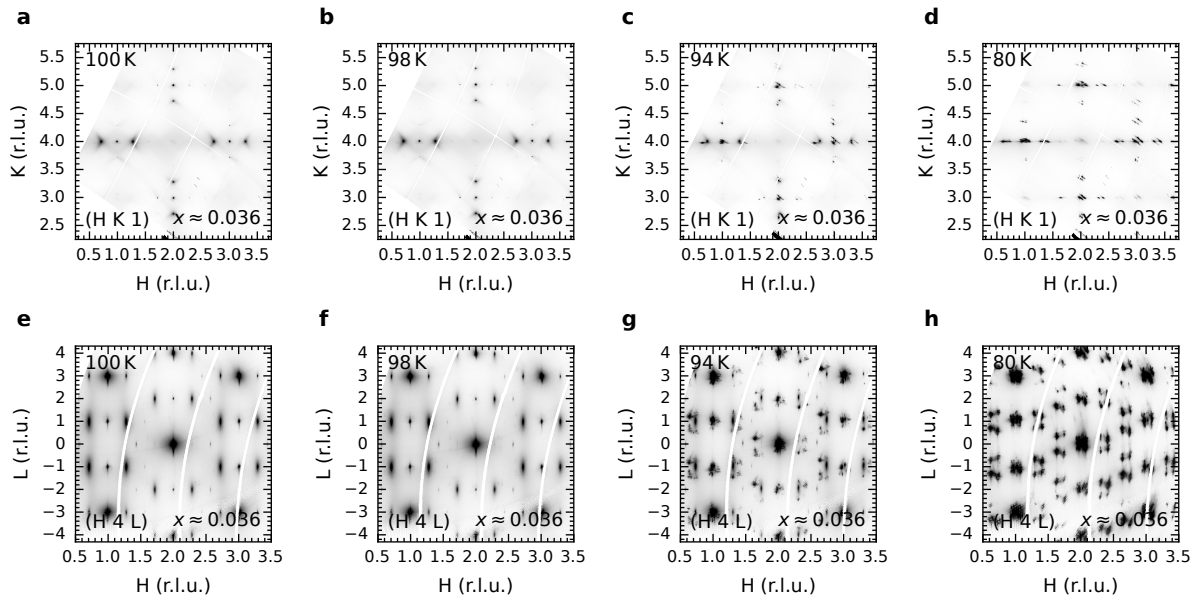


**Figure 4.14.: Reciprocal space maps around the triclinic transition temperature.** a-d  $(h\ k\ 1)$  reciprocal space maps for a 100 K, b 98 K, c 94 K and d 80 K for the  $x \approx 0.036$  sample. e-h  $(h\ 4\ l)$  reciprocal space maps for e 100 K, f 98 K, g 94 K and h 80 K for the  $x \approx 0.036$  sample. The reciprocal space vectors are given in the tetragonal notation.

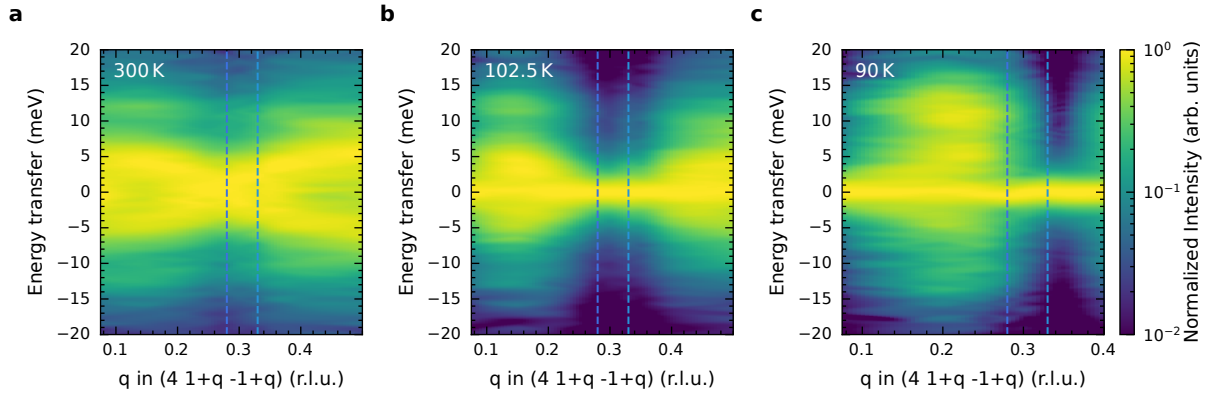


**Figure 4.15.: Phonon dispersion in the direction of the C-CDW.** **a-c** Colormaps of the normalized IXS spectra along the  $[0\ q\ q]$ -direction with the  $(4\ 1\ \bar{1})$  as the  $\Gamma$ -point. The data were measured at **a** 300 K, **b** 102.5 K and **c** 90 K on the  $x \approx 0.037$  sample. The dashed lines indicate the position closest to the I-CDW and the position of the C-CDW.

temperature of 98 K, faint but sharp peaks may be visible. Together with the similarly intense peaks forming around the Bragg peaks, this suggests that a small part of the sample has transitioned to the triclinic/C-CDW phase. At even lower temperatures, the different twins in the triclinic phase become more pronounced and the I-CDW loses intensity. At the same time, the C-CDW becomes more intense and exhibits the same additional peaks due to the twinning structure as the Bragg peaks. Finally, at the lowest temperature measured, any sign of the I-CDW or the high-temperature structure are lost and the C-CDW is fully developed. Looking at the  $(h\ k\ 1)$  map, the diffuse scattering observed at higher temperatures is also lost. The superstructure peaks still visible in the plane are not remnants of the I-CDW but instead the C-CDW. The peaks of the C-CDW appear from lower and higher  $l$  values as the different twins extend the region in reciprocal space in which scattering can be observed.

Altogether, just above the transition there are no signs of diffuse scattering which could hint to a (soft) phonon-driven transition to the C-CDW or triclinic phase. The only signs at 98 K are most likely due to the width of the transition and parts of the sample which have already transitioned.

#### 4.4.2. Phonons at the commensurate charge density wave phase transition

To confirm the results from the TDS with energy resolution and much better sensitivity, in the following section IXS measurements on a similar  $x \approx 0.037$  sample are discussed. In particular, to investigate whether the C-CDW is formed by a comparable soft phonon as the I-CDW, IXS spectra along the  $[0\ q\ q]$ -direction with the  $(4\ 1\ \bar{1})$  Bragg peak as the  $\Gamma$ -point are shown in Figure 4.15. The measurements were performed on a  $x \approx 0.037$  sample to enlarge the temperature range in which the I-CDW is present and to have the transition to the C-CDW in an experimentally easily accessible temperature range. At room temperature, the spectra show a comparable situation to that observed in the pristine and  $x \approx 0.1$  samples in Section 4.3. The low-lying transverse optic phonon softens on approaching the I-CDW positions, leading to sharper peaks in Figure 4.15. As the anomaly is broad in the  $l$ -direction, the softening is also visible in the  $[0\ q\ q]$ -direction on approaching  $(0\ 0.28\ 0.28)$ .

Moreover, the scans at 102.5 K, just above the transition, show a pronounced sharpening towards  $q = 0.28$ . This is further confirmed by the scan along the  $[0\ 0\ l]$ -direction around the C-CDW position in Figure 4.16b, which indicates a stronger softening at  $l = -1$ , as expected for the I-CDW, which does not exhibit a  $l$ -component in the wavevector. Furthermore, at room temperature and 102.5 K, no signature of a softening at the C-CDW position is visible.

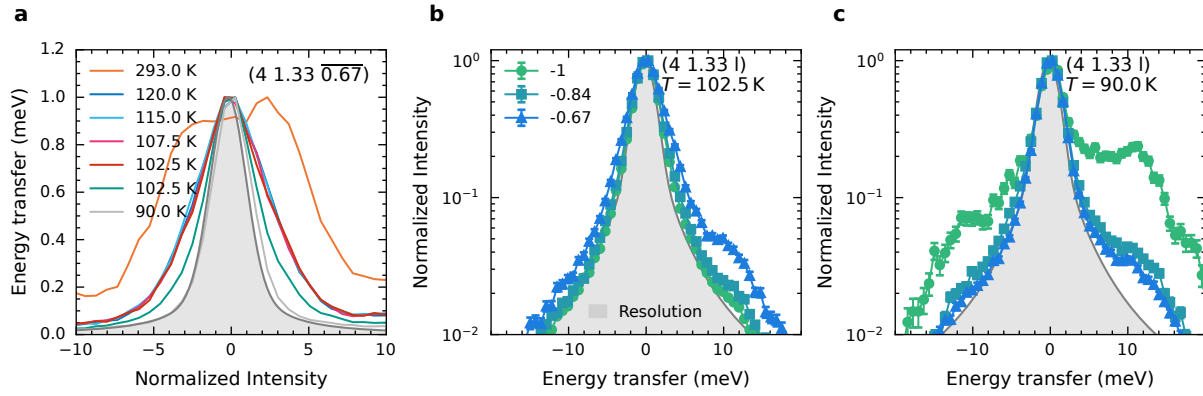


**Figure 4.16.: Temperature dependence of the phonon spectra at the C-CDW position and  $l$ -dependence.** **a** Normalized IXS spectra at  $(4\ 1.33\ 0.67)$  at different temperatures. **b-c** Normalized IXS spectra along the  $[0\ 0\ l]$ -direction through the C-CDW position at **b** 102.5 K and **c** 90 K. All data in this figure are measured on the on the  $x \approx 0.037$  sample.

At 90 K, just below the transition, the peak sharpens on approaching  $q = 1/3$ , indicating the static (elastic) C-CDW intensity. The spectrum at  $q = 0.28$ , however, broadens and shows again a normal mode.

This behavior is also confirmed by the temperature dependence at the C-CDW position in Figure 4.16a. The phonon is softening, but stays at finite energy above the transition. The scans along the  $[0\ q\ q]$ - and  $[0\ 0\ l]$ -directions also both confirm that this is the softening in an extended region which originates from the phonon anomaly of the I-CDW. No further softening was observed. At the transition, however, there is a jump to a resolution-limited/elastic peak indicating the formation of the static order without any observable precursor in the phonons at the C-CDW position. The absence of a signature of phonon softening just above the transition temperature indicates that the C-CDW transition is not (soft) phonon driven, unlike the I-CDW. This is also confirmed by scans along  $[0\ 0\ l]$  showing the centering of the anomaly at  $l = -2/3$ , the C-CDW position.

This behavior can be summarized in the measured and fitted phonon dispersions in Figure 4.17. At all temperatures, the upper phonon branch only marginally changes. The low-lying phonon, however, shows a softening around  $q = 0.28$ , indicating the softening due to the I-CDW as discussed above.

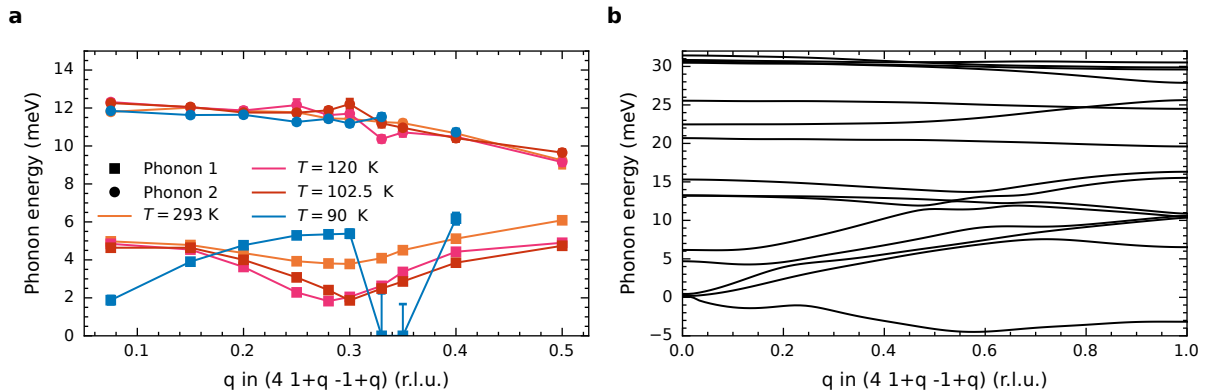


**Figure 4.17.: Measured and calculated phonon dispersion in the C-CDW-direction around the triclinic transition.** **a** Fitted phonon dispersion along the  $[0\ q\ q]$ -direction with the  $(4\ 1\ \bar{1})$  as the  $\Gamma$ -point for different temperatures above and below the triclinic transition. The dispersions were measured on the  $x \approx 0.037$  sample. **b** DFPT calculated phonon dispersion for the triclinic structure. The unstable phonon branch is present at negative energies.

At  $q = \frac{1}{3}$  no softening is visible. Below the transition, the peak at  $q = \frac{1}{3}$  is, within the experimental resolution, purely elastic. At a first glance, the phonon branch changes from an optical to an acoustic phonon branch. However, a more detailed look at the DFPT calculations suggests that the unstable phonon branch is likely the same branch as at higher temperatures and that there is a cross-over with the acoustic phonon branch, which gains intensity at lower  $q$ .

## 4.5. Summary and discussion

The combination of TDS, IXS and first-principles phonon and TDS intensity calculations show a clear phonon anomaly and softening at the I-CDW position. This clearly proves a soft phonon origin of the I-CDW. The unstable phonon mode is a transverse optical phonon. As the corresponding longitudinal phonon does not exhibit the same softening, this explains the pattern of the I-CDW observed previously in XRD experiments. The DFPT calculations do not find any conventional ordering mechanism for the I-CDW. This agrees with earlier first-principles calculations, which also do not show Fermi-surface nesting [52]. Furthermore, multiple ARPES studies on pristine and phosphorous substituted samples do not find Fermi-surface nesting at the I-CDW wavevector [33–37]. In line with recent time-resolved spectroscopy studies [148–150], which find an unusual resilience of the I-CDW against perturbation, the results from the IXS experiment and DFPT calculations highlight the unconventional nature of the I-CDW. To discard fully the possibility of a conventional order mechanism, the real part electronic susceptibility should be calculated as discussed by Johannes and Mazin [133]. However, for the calculation of the real part electronic susceptibility, the energy cutoff used in the calculations can have a significant influence on the obtained results. This leads to the fact that no good convergence criteria exist, which makes calculations challenging in their own.

Most likely, orbital degrees of freedom are responsible for the I-CDW formation. One possibility would be an orbital-dependent EPC, similar to that observed in  $\text{NbSe}_2$  [151]. Furthermore, orbitally driven Peierls states could be responsible for the CDW formation. In this case, an orbital ordering results in an effective reduction of dimensionality (e.g. by a dimerization), allowing for mechanisms similar to the conventional Peierls instability described in Section 3.1 [66, 67, 152]. Indications for this are given by a combined NEXAFS and XRD study from Merz et al. [27]. This study reveals the formation of Ni zigzag chains (in the orthorhombic phase) and Ni dimers (in the triclinic phase). This is accompanied by a transfer of weight from Ni  $d_{xy}$  to  $d_{xz,yz}$  orbitals, hinting towards an orbital order of the I-CDW and C-CDW. Above the orthorhombic transition there are indications for charge or orbital fluctuations [27]. In agreement with this, an ARPES study found an orbital dependent band renormalization due to an anisotropic Ni–Ni bond ordering [35]. Moreover, pre-empting the results in Chapters 5 and 6, this thesis also shows a strong orbital influence of the I-CDW and the importance of the Ni- and As-orbital hybridization in the formation of the I-CDW. Furthermore, another recent study reveals the coupling of  $B_{1g}$  nematic fluctuations to the  $E_g$  phonon modes at the  $\Gamma$ -point. This is evidenced by an unusual large splitting of the phonon mode and electronic Raman scattering [23]. Due to the lack of observation of magnetic order in  $\text{BaNi}_2(\text{As}_{1-x}\text{P}_x)_2$ , the fluctuations are likely of orbital nature. Interestingly, the  $E_g$  phonon modes are from the same phonon branch which exhibits the Kohn-anomaly at the I-CDW position.

The IXS and TDS data also show a striking similarity of the I-CDW formation throughout the complete phosphorus substitution series. In particular, the phonon-softening in the  $x \approx 0.1$  samples is still comparable even though the triclinic and C-CDW phase is completely suppressed. However, the TDS measurements did not reveal a clear signature of the sharp, ordered peaks which unambiguously indicate the transition to the static I-CDW phase. This is despite the fact that the "critical" correlation length is

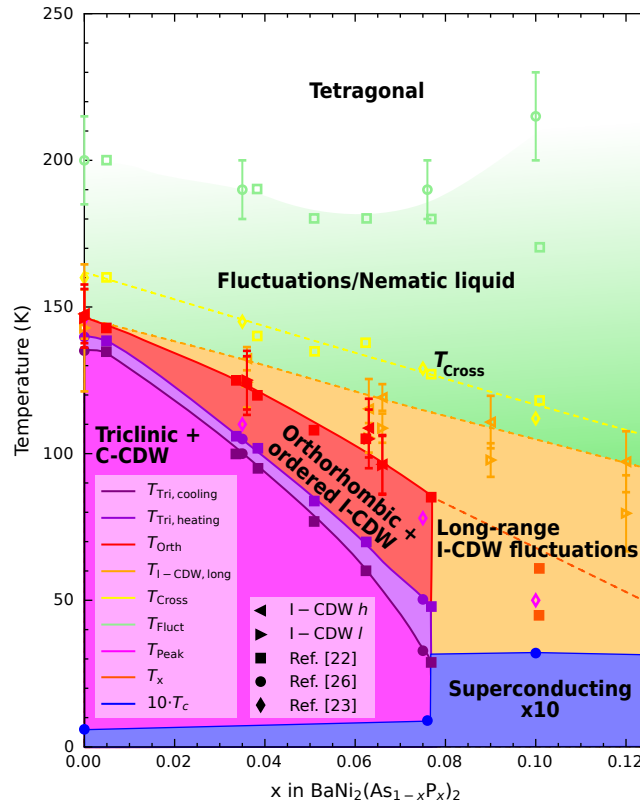


**Figure 4.18.: Phase diagram of  $\text{BaNi}_2(\text{As}_{1-x}\text{P}_x)_2$ .** Phosphorus substitution temperature phase diagram of  $\text{BaNi}_2(\text{As}_{1-x}\text{P}_x)_2$ . Shown are the triclinic transition including the hysteresis (purple), orthorhombic phase (red), long-range I-CDW phase (orange), maximum in elastoresistance (magenta), temperature of the cross of the in- and out-of-plane thermal expansion and onset of the elastoresistance (yellow) and the nematic liquid/fluctuating regime (green). Furthermore, the superconducting phase (temperature tenfolded, blue) and the currently unknown structure X are indicated (dark orange). All transitions, except for the I-CDW transition, are taken from Meingast et al. [25] (squares), Yao et al. [23] (circle) and Frachet et al. [47] (diamonds). Closed symbols indicate real thermodynamic phase transitions.

met and the phonon is completely soft according to the IXS measurements. Therefore, the transition to the fully static I-CDW phase remains elusive for the highest substitution contents. Similarly, a comparable soft phonon has recently been observed in the strontium-substituted system, even above the substitution level at which the C-CDW is suppressed. However, at the substitution level studied, the I-CDW is strongly suppressed, such that no static order is formed down to very low temperatures [48]. Furthermore, thermal expansion measurements reveal that, in this substitution range, there is no in-plane anisotropy as the orthorhombic phase is exchanged with a still unknown phase which preserves the square plane [25]. From this, we can conclude that the orthorhombic distortion seems not to be a necessary condition for the formation of the long-range I-CDW. As the structural distortions and the I-CDW appear in close vicinity in temperature, it is likely, therefore, that the I-CDW distorts the system and the lattice follows. More details on the new structure under phosphorous substitution are discussed in Chapter 6. A comparison of the orthorhombic transition temperatures,  $T_{\text{Orth}}$ , from thermal expansion and heat capacity measurements with the extracted I-CDW transition temperature,  $T_{\text{I-CDW}}$ , from the correlation length confirms the I-CDW precedes the structural transition. This is summarized in the phase diagram in Figure 4.18, which combines  $T_{\text{I-CDW}}$  with the transition temperatures from Frachet et al. [47], Meingast et al. [25] and Yao et al. [23].

This behavior might also be related to the suggested critical slowing down of the I-CDW fluctuations observed in another IXS study conducted at a similar time as this work [147]. This means the phonons

soften to zero energy but are overdamped, leading to a zero energy peak with larger width than the resolution. Only at lower temperatures does the I-CDW gain a truly static order. On one hand, in this work, fits with an overdamped phonon for the pristine samples lead to no better result. On the other hand, for the phosphorous substituted sample, where everything is broadened in temperature, the fit prefers overdamped phonons. Nonetheless, the mostly Lorentzian experimental energy resolution of 3 meV in this work and 1.4 meV in the work of Song et al. [147] make it difficult to conclusively differentiate between the phonon softening and the slowing down of I-CDW fluctuations. To safely differentiate between the scenarios, INS, especially with cold neutrons, would be advantageous. Firstly, the more Gaussian energy resolution makes it easier to differentiate between the elastic line and an underdamped and overdamped DHO and, secondly, the energy resolution is superior. However, for INS measurements, a larger single crystal than what is commonly possible to grow for  $\text{BaNi}_2\text{As}_2$  is required. Therefore, to perform such an experiment, multiple coaligned samples or the growth of a larger crystal is required. Accordingly, IXS measurements, which allow for smaller sample sizes, were used in this thesis.

Our first principle phonon and TDS calculations show that most features in the diffuse scattering maps can be described by TDS emerging from phonons. The exceptions to this are the sharp peaks emerging with the I-CDW order. Those peaks seem to be effectively resolution-limited, fully elastic and show a different structure factor than the intensity emerging from the soft-phonon. The peaks, including peaks in the transverse, longitudinal and diagonal directions in the plane, for example, are also observed in the  $(h\ k\ 0)$ -plane, where the soft phonon is basically absent. This suggests that the static order of the I-CDW has a more complicated structure and calls for an exact structural solution, including the superstructure, with XRD. However, the low intensity of the peaks in the longitudinal and diagonal direction make it challenging to include them in the structural refinement. Nonetheless, a refinement of the structure with the transverse peaks and simulations of the diffraction pattern afterward could be insightful.

Preempting the results from Chapter 6 and the results in the appendix in Appendix D, the experiment and calculations already show a precursor of a second instability (denoted I-CDW2 later in the thesis) forming under hydrostatic pressure. These precursors also suggest a soft phonon behavior, even though it has not yet developed at ambient pressure. The calculations show that for the diffuse scattering around the I-CDW2 position also the barium atoms are oscillating, suggesting a different structure of the I-CDW1 and I-CDW2. Further IXS studies under hydrostatic pressure could be insightful to investigate the differences between these orders.

Now we turn to the phonon spectra measured around the superconducting transition. Due to the limitations of the experimental setup, it is not possible to completely rule out competition between the I-CDW and superconductivity. However, the results do not provide evidence for such a competition. This contrasts with the situation in the superconducting cuprates [153–155] and other CDW materials [156–160]. This might be related to the findings in the strontium substituted system, where a similar superconducting transition temperature is observed in the absence of the C-CDW and at least significantly suppressed I-CDW [41, 48]. Recent studies in the strontium system indicate that the superconductivity is of BCS type [49] and the lower superconducting  $T_c$  is due to changed EPC [54]. Therefore, the change in superconducting  $T_c$  is likely not due to the changes seen in the CDWs in  $\text{BaNi}_2\text{As}_2$ . This could suggest, when considered with the results in this thesis, a different ordering mechanism, which could explain the absence of competition between the two ordered states.

The situation of the C-CDW is vastly different from that of the I-CDW. Both the transition and the C-CDW itself do not show signatures of a soft phonon origin, in stark contrast to the I-CDW. From the phononic perspective, the two CDWs seem not to be connected. This result contrasts with time resolved spectroscopy measurements, which find a smooth transition between the CDW modes, suggesting a

connection between the two CDWs [148–150]. One possible explanation is that, at the transition to the triclinic phase, the I-CDW locks in to a commensurate value and forms the C-CDW. Nonetheless, the differences between the methods and the possible lock-in generally raise the question of the connection between the different CDW instabilities and crystal structures. Some more insight is given by measurements under applied external pressure, which will be discussed in Chapter 6.





## 5. Symmetry of the charge density waves

### 5.1. Introduction

In Chapter 4 it was shown that the I-CDW is unconventional in nature. These results, and earlier work [23, 27], raise the question of orbital order in the I-CDW state and the symmetry of the I-CDW state. One way to investigate the symmetry of the I-CDW and the orbital order is to investigate the tensor atomic form factor from the I-CDW scattering signal, as discussed in detail in Section 3.2.2. This can be done using REXS, which was successfully used to investigate the symmetry of the CDW in cuprates [161, 162] and other materials [163, 164]. To obtain the different components of the tensor atomic form factor, the polarization dependence of the CDW scattering signal must be measured. This can be done by rotating the sample around the CDW wavevector, resulting in an azimuthal rotation in the Bragg condition. By comparing the signal for different incoming polarizations, such as horizontal and vertical, the tensor atomic form factor can be fitted. RIXS measurements be used to investigate if the azimuthal dependence or I-CDW signal is purely elastic.

In the case of  $\text{BaNi}_2(\text{As}_{1-x}\text{P}_x)_2$ , previous NEXAFS measurements have already shown that at the nickel  $L_{2,3}$ -edge signatures of the I-CDW can be observed [27]. Considering this along with the results in Chapter 4, it is likely that the I-CDW can be observed at the nickel resonance. The nickel edge is also more favorable than the arsenic edge as the resonance is stronger, resulting in a larger signal during the experiment.

Subsequently in this chapter, REXS and RIXS are performed at the nickel  $L_{2,3}$ -edge in order to answer the question of the potential orbital order of the two CDWs in  $\text{BaNi}_2(\text{As}_{1-x}\text{P}_x)_2$ . This also allows investigation of the local nickel symmetry of the I-CDW and C-CDW. In addition, the comparison between the I-CDW and C-CDW gives further insight into the question raised in Chapter 4 regarding the connection between the two CDWs.

Before looking at the azimuthal dependence, however, the energy dependence of the scattering signal is discussed in Section 5.3. These measurements show that the I-CDW scattering signal is maximized at the rising flank of the absorption. This energy range corresponds to the  $d_{xz,yz}$  orbitals. The energy dependence of the RIXS signal shows no inelastic contribution to the signal. All observed inelastic signals are fluorescence.

The following section discusses the azimuthal dependence and the extraction of the tensor atomic form factor. These measurements reveal that the results cannot be described using the orthorhombic structure but a monoclinic or lower symmetry is required. Furthermore, the signal likely shows, besides dipole-dipole, also dipole-quadrupole influences. In addition, the signal of the C-CDW can be described using a similar tensor to the I-CDW suggesting that, from an orbital perspective, the two CDWs are comparable.

In the last section, 5.5, the results are discussed.

First, the experimental and computational details are presented in Section 5.2. The more technical parts of this section can be skipped by readers not interested in these details. However, this chapter relies

on the scattering geometry presented in Section 5.2 and Figure 5.1. Furthermore, many results from Section 3.2.2 will be used and therefore the reader is advised to read this section first.

## 5.2. Experimental details

The REXS measurements were conducted at the XUV diffractometer at beamline UE46 PGM at Berliner Elektronenspeicherring-Gesellschaft für Synchrotronstrahlung II (BESSY II) and the RIXS end-station at beamline ID32 at the ESRF-EBS. In addition, RIXS measurements were performed at the RIXS end-station at beamline ID32 at the ESRF-EBS. More details on the beamline UE46 PGM can be found in the work of Weschke and Schierle [165]. Details of the RIXS end station at beamline ID32 are discussed by Brookes et al. [166].

The experiments were performed at the  $L_3$  edge ( $\approx 853$  eV). To reach the I-CDW and C-CDW positions in resonance, the measurements must be performed on the *ac* or *bc* side of the sample. Due to the plate-like morphology of  $\text{BaNi}_2(\text{As}_{1-x}\text{P}_x)_2$ , this corresponds to an edge of the sample. Accordingly, the samples were mounted on a copper slab, in order to tilt them by  $90^\circ$ . For the experiments examining the I-CDW the sample is directly correctly oriented for an azimuthal rotation. For the C-CDW measurements, however, the sample must be pre tilted by an additional  $\approx 19.5^\circ$  to make the C-CDW wavevector the normal vector and to be able to make an azimuthal rotation. The corresponding scattering geometries are shown in Figures 5.1a,b. The azimuthal angle  $\varphi$  is chosen in such a way that  $0^\circ$  corresponds to the *bc* plane being the horizontal/scattering plane. The samples were roughly aligned by eye. A better alignment was made using the  $\{0\ 1\ 1\}$ -Bragg peak and the CDW peaks. The samples were cleaved in air just before transferring the samples into the UHV chamber. An in-vacuum cleaving on the side of the sample was not possible but also not necessary.

In the main, results from three samples will be discussed. Samples 1 and 2 are non-substituted samples. Sample 3 is phosphorus substituted with a phosphorus content of  $x \approx 0.059 \pm 0.005$ . Sample 1 is shown in Figures 5.1c,d and was measured at beamline UE46 PGM. Samples 2 and 3 were measured at beamline ID32. An image of sample 3, along with two other mounted samples is shown in Figure 5.1. The phosphorus substitution was determined by EDX using an COXEM EM-30AXN SEM-EDX with an Oxford Instruments Aztec EDX System containing an EDX detector and AztecLiveLite Software. In Appendix B additional data from the non-substituted samples 4, 5 and 6 are presented. Samples 4 and 5 were measured at beamline UE46 PGM and were aligned with the *c*-axes being the surface normal. Sample 6 was measured at beamline ID32.

At beamline UE46 PGM, the beam was focused to a spot of  $100\ \mu\text{m} \times 50\ \mu\text{m}$ . If not stated otherwise, all measurements were performed at the resonance of the CDWs at 852.8 eV. Some alignment scans of the otherwise non-reachable Bragg peak were also performed out-of-resonance. Only linearly polarized light with different orientations was used. The signal was measured using a silicon diode. All measurements, except for the energy dependence, were performed using an entrance slit of  $200\ \mu\text{m}$ . For the energy dependence, an entrance slit of  $100\ \mu\text{m}$  was used.

At beamline ID32, the beam was focused to a spot of  $5\ \mu\text{m} \times 2\ \mu\text{m}$ . The X-ray energy was changed during the experiments, but if not stated otherwise, the incoming X-ray energy was chosen to be at the resonance of the two CDWs at 852.8 eV. Alignment scans of the Bragg peaks not reachable in resonance were also performed off-resonant. Only horizontally or vertically linear polarized light was used. For the RIXS measurements, the entrance slit was closed to  $15\ \mu\text{m}$ , resulting in an energy resolution of  $\approx 32.5$  meV. For the elastic REXS measurements, the entrance slit was opened to  $100\ \mu\text{m}$  to increase the

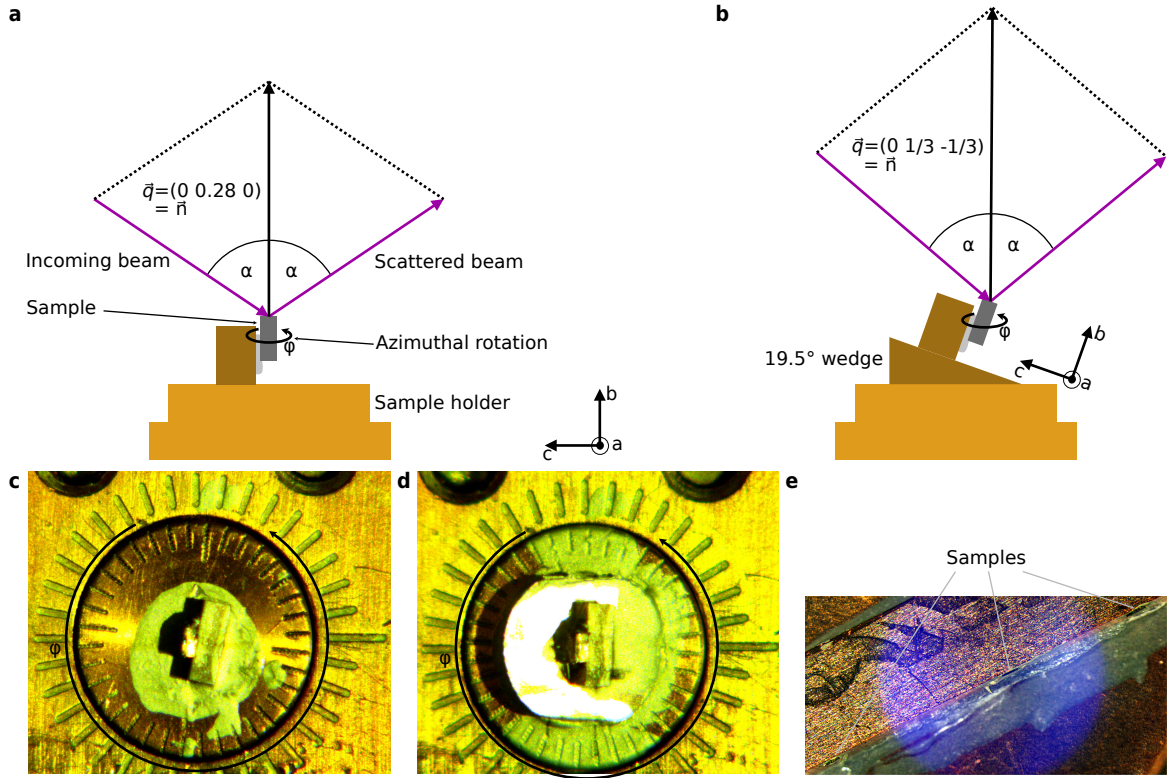


**Figure 5.1.: Sketch of the scattering geometry and images of the samples.** **a** Sketch of the scattering geometry and azimuthal rotation for the REXS measurements of the I-CDW. **b** Sketch of the scattering geometry and azimuthal rotation for the REXS measurements of the C-CDW, including the additional wedge. **c** Image of sample 1 (measured at BESSY II) mounted for the I-CDW measurements. **d** Image of sample 1 (measured at BESSY II mounted) on the additional wedge for the C-CDW measurements. **e** Image of samples 3 and two other samples measured at the ESRF-EBS.

flux. The REXS measurements were performed using the small silicon diode instead of the spectrometer arm.

The experiments at beamline UE46 PGM were performed by the author of this thesis, Dr. Igor Vinograd and Dr. Enrico Schierle. The experiments at ID32 were performed by the author of this thesis, Dr. Philippa McGuinness, Dr. Sofia-Michaela Souliou, Dr. Mehdi Frachet and Dr. Kurt Kummer.

### 5.3. Energy and temperature dependence of the charge density waves

A first insight into the nature of the I-CDW and the C-CDW is given by the energy dependence of the scattering signal, as presented in Figures 5.2a,b. Additional energy dependencies at other azimuth angles are shown in the appendix in Figure B.2. Both CDWs show a clear resonance near the nickel  $L_3$  and  $L_2$  edges. Comparing the resonance with the fluorescence signal (or total electron yield (TEY) in the appendix) depicting mainly the X-ray absorption reveals different peak energies and peak shapes. The peak resonance of the CDWs lies roughly in the middle of the rising flank of the X-ray absorption (852.8 eV) and show a shoulder at the actual maximum of the X-ray absorption. This energy was identified to be associated with the  $d_{xz,yz}$  orbitals [27], suggesting that the  $d_{xz,yz}$  orbitals are involved in the CDW formations. In general, the resonances of the I-CDW and C-CDW are very similar. The incoming photon energy dependence for both CDWs exhibits a small differences between vertical and horizontal incoming polarization, which depends on the azimuthal angle. This already indicates

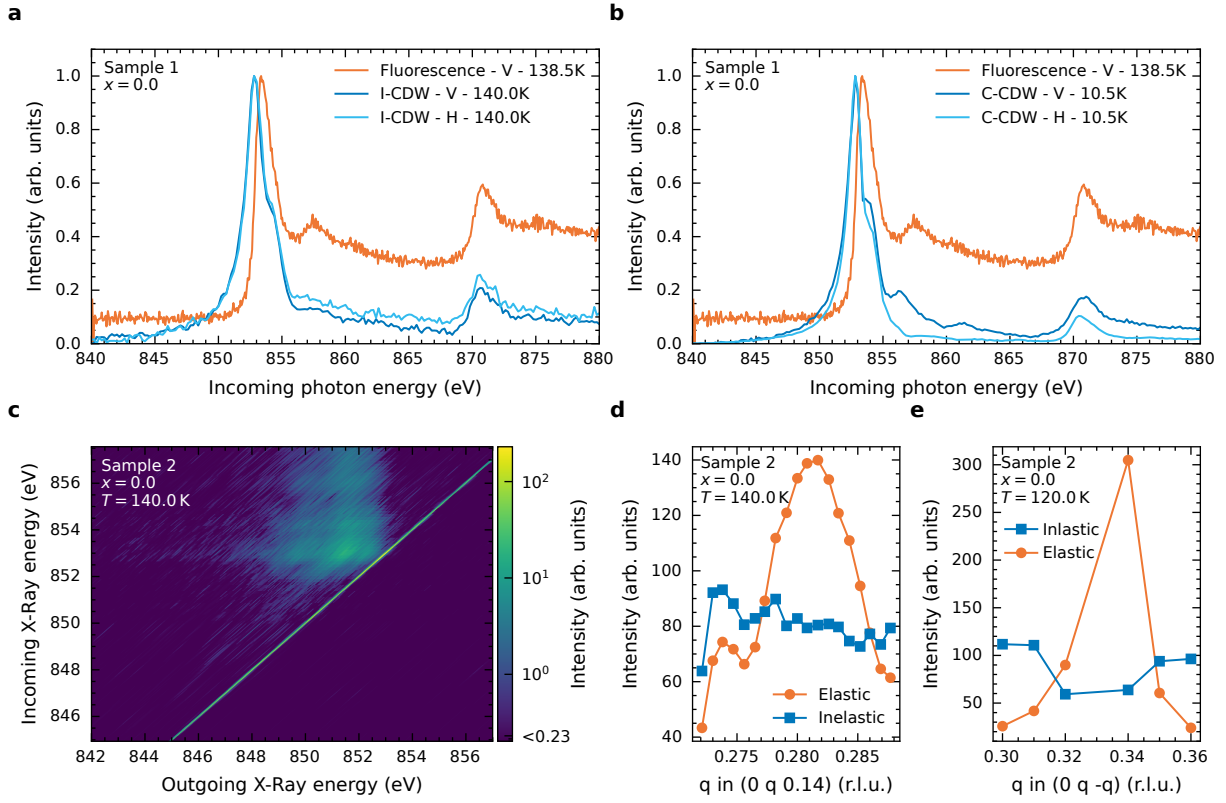


**Figure 5.2.: Energy dependence of the scattering signal of the I-CDW and C-CDW.** **a-b** Incoming energy dependence of the scattering signal of the **a** I-CDW and **b** C-CDW. The data is shown for incoming vertical and horizontal polarization at an azimuthal rotation of  $0^\circ$ . For comparison measurements of the fluorescence, which mainly show the X-ray absorption, are included. **c** Incoming and outgoing energy dependence at the I-CDW position. **d-e** Integrated intensity of the elastic and inelastic spectra for different positions around the **d** I-CDW and **e** C-CDW.

a more complicated polarization and azimuthal dependence of the scattering signal. However, to determine if the differences are significant and to enable a more detailed interpretation, additional energy dependencies at other azimuth angles would be required. All of the measurements shown here were performed at the  $(0\ 0.28\ 0)$  (I-CDW) and  $(0\ 1/3\ 1/3)$  (C-CDW) peaks. Experimentally, it would be easier to investigate peaks offset by 1 in the  $l$ -direction, as this would not require to work on the side of the plate-like sample. Similarly to the peak around  $l = 0$ , these peaks are not observed out-of-resonance in hard X-ray diffraction. Unfortunately, the peak at  $l = 1$  could not be detected even in resonance. This can be seen on the scans shown in Figure B.1 in the appendix.

The energy dependence of the scattered signal from the RIXS measurements is presented in Figure 5.2c. The most prominent signal is the elastic line, which lies on a diagonal in the plot, fulfilling the requirement that the outgoing energy is identical to the incoming energy. All of the inelastic scattering signals lay on a vertical line between 848 and 853 eV. Accordingly, the outgoing X-ray energy does not depend on the incoming X-ray energy. Together with the fact that the signal is absent below the nickel  $L_3$  edge, it is clear that all of the inelastic signals are X-ray fluorescence.

This is also confirmed by the integrated elastic and inelastic intensities of the I-CDW and C-CDW, shown in Figures 5.2d,e and in the appendix in Figure B.2. Both CDWs exhibit a clear peak in the elastic signal and an approximately constant line in the inelastic signal. Consequently, the inelastic signal is not related to the CDWs.

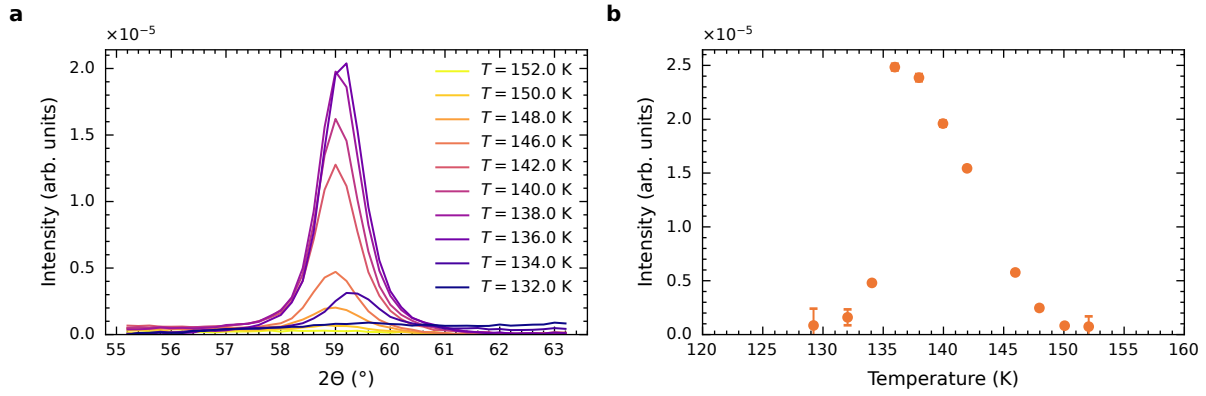


**Figure 5.3.: Temperature dependence of the scattering signal of the I-CDW.** **a**  $\theta$ - $2\theta$ -scans of the I-CDW at different temperatures. The scans were performed on sample 1. **b** Integrated intensities versus temperatures from the  $\theta$ - $2\theta$ -scans.

To determine if the resonant scattering signal of the I-CDW exhibits the same temperature dependence as the off-resonant scattering signal,  $\theta$ - $2\theta$  scans measured in resonance at different temperatures are presented in Figure 5.3a. As with all future measurements, the scans were performed at the peak of the resonance, at 852.8 eV. The scans show a clear increase in the intensity on approaching the triclinic transition. At the triclinic transition, the signal suddenly vanishes. This is confirmed by the integrated intensities in Figure 5.3b. The intensity increases below 150 K and suddenly vanishes at the triclinic transition, around 136 K. The temperature dependence can be compared with the off-resonant temperature dependencies from the TDS, as shown in Figure 4.4, or a lab-based four circle diffractometer, in the work from Yao et al. [23]. The temperature dependencies are very similar, indicating no difference between the in- and out-of-resonance measurements. A difference could suggest a different ordering temperature of the electronic system and the lattice degrees of freedom.

## 5.4. Azimuthal dependence of the charge density waves

### 5.4.1. Azimuthal dependence measurements

After determining the energy and temperature dependence, we now turn over to the azimuthal dependence. For this,  $\theta$ - $2\theta$ -scans are performed with both vertical and horizontal incoming polarization. For the next measurement point, the sample is rotated around the CDW wavevector (the azimuth) and the scans are repeated. The azimuth of  $0^\circ$  is defined as the position where the scattering plane is defined by the  $bc$ -plane. The raw scans of the I-CDW are presented in Figures 5.4a,b. These data show a clear change of the absolute intensity at different azimuthal angles. In addition, comparing the scans with incoming vertical and horizontal polarizations shows a clear difference between the two. First, the maximal possible intensity is much larger for incoming vertical polarization, and second, the maxima of intensity are at different azimuthal angles. Similar scans can also be performed for other incoming polarization angles. The integrated intensities from such a series of scans are shown in Figure 5.4c. In this plot,  $0^\circ$  incoming polarization corresponds to horizontal polarization and  $90^\circ$  to vertical polarization. In this scan series, clear differences of intensity can be observed for different polarizations. In addition, the intensity for different linear polarizations exhibits a distinct dependence on the azimuthal angle.

The dependence of the ratios of the fitted intensities for both vertical and horizontal incoming polarization are presented in Figures 5.4d,e for the I-CDW and C-CDW, respectively. Starting with the I-CDW,

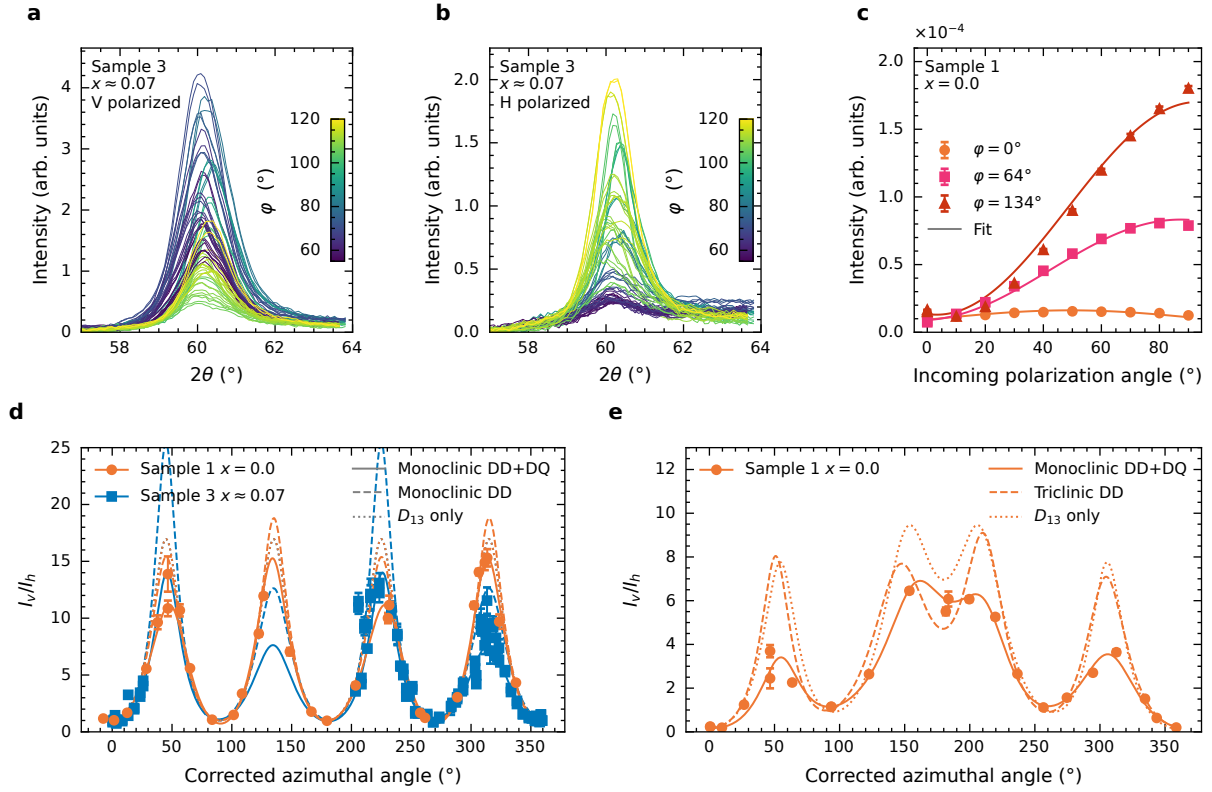


**Figure 5.4.: Azimuthal dependence of the scattering signal of the I-CDW and C-CDW.** **a-b**  $\theta$ - $2\theta$ -scans for different azimuthal rotations with incoming **a** vertically polarized X-rays and **b** horizontally polarized X-rays. **c** Intensities for different incoming linearly polarized X-rays at different azimuthal angles. The measurements were performed at 138 K. **d** Azimuthal dependence of the I-CDW scattering signal. **e** Azimuthal dependence of the I-CDW scattering signal. In addition, three different fits are shown. First, a fit with monoclinic symmetry and including dipole-dipole and dipole-quadrupole terms. Second, fits with monoclinic or triclinic symmetry including only the dipole-dipole terms and finally, a fit including only the dominant  $f_{xz}$  terms. The I-CDW measurements of sample 1 were performed at 138 K and the measurements of sample 3 were performed at 76 K. The C-CDW measurements were performed at 10.5 K.

the azimuthal dependence shows a clear fourfold structure with peaks of  $\approx 15$  at  $\varphi \approx 45^\circ + N \cdot 90^\circ$ ,  $N \in \mathbb{N}$ . At the minima of approximately 1, the intensities with incoming vertical and horizontal polarization are roughly identical. With respect to the maxima, the minima are shifted by  $45^\circ$ . There may be a difference in the height of two adjacent maxima. The non-substituted and phosphorus substituted samples show very similar behavior.

The azimuthal dependence of the C-CDW likewise exhibits four peaks, albeit with shifted positions. The positions of the two inner peaks have moved towards  $180^\circ$ . Moreover, the inner peaks are higher than the two outer and, at  $0^\circ$ , the intensity with incoming horizontal polarization is larger than with incoming vertical polarization. Some of these differences can be explained by the different scattering geometry, due to the different wavevector. This can be seen from the dotted lines in the plots, which are calculated from an identical tensor atomic form factor. The details of the fits to the experimental data and their implications will be discussed further in the following sections.

#### 5.4.2. Tensor atomic form factor of the incommensurate charge density wave

The azimuthal dependence of the scattering can be calculated using the tensor atomic form factor, as it was derived in Section 3.2.2.2. To fit the tensor atomic form factor with Equation (3.16), first the

polarization  $\vec{\epsilon}$  and wavevector  $\vec{k}$  must be expressed in a form which is dependent on the azimuthal angle. Using the definition of the azimuthal angle where  $0^\circ$  corresponds to the  $bc$ -plane being the scattering plane, the vectors can be expressed as

$$\vec{\epsilon}_{i,v} = \begin{pmatrix} \cos(\varphi) \\ 0 \\ \sin(\varphi) \end{pmatrix} \quad \vec{\epsilon}_{s,v} = \begin{pmatrix} \cos(\varphi) \\ 0 \\ \sin(\varphi) \end{pmatrix} \quad (5.1)$$

$$\vec{\epsilon}_{i,h} = \begin{pmatrix} -\sin(\varphi) \cos(\alpha) \\ \sin(\alpha) \\ \cos(\varphi) \cos(\alpha) \end{pmatrix} \quad \vec{\epsilon}_{s,h} = \begin{pmatrix} \sin(\varphi) \cos(\alpha) \\ \sin(\alpha) \\ -\cos(\varphi) \cos(\alpha) \end{pmatrix} \quad (5.2)$$

$$\vec{k} = \begin{pmatrix} -\sin(\varphi) \sin(\alpha) \\ -\cos(\alpha) \\ \cos(\varphi) \sin(\alpha) \end{pmatrix} \quad \vec{k}' = \begin{pmatrix} -\sin(\varphi) \sin(\alpha) \\ \cos(\alpha) \\ \cos(\varphi) \sin(\alpha) \end{pmatrix}. \quad (5.3)$$

In this expression, the angle  $\alpha$  that is sketched in Figure 5.1 is included. This angle can be derived from the scattering angles  $\theta$  and  $2\theta$  in the scattering condition by

$$\alpha = 90^\circ - \theta \quad (5.4)$$

$$= \frac{180^\circ - 2\theta}{2}. \quad (5.5)$$

As the same diffraction peak is probed throughout an azimuthal rotation,  $2\theta$  does not change (except due to experimental imperfections) and  $\alpha$  is therefore constant. For the fits using the tensor atomic form factor, an averaged value of  $\alpha$  is used. For the case with the wedge, the sample is additionally tilted around the  $a$  axis and hence the rotation matrix  $\mathbf{R}$  must be included. The matrix can be expressed as

$$\mathbf{R} = \begin{pmatrix} 1 & 0 & 0 \\ 0 & \cos(\beta) & \sin(\beta) \\ 0 & -\sin(\beta) & \cos(\beta) \end{pmatrix} \quad (5.6)$$

where  $\beta$  is the tilt angle of the wedge. The complete formula for the intensity ratio is then given by

$$\frac{I_v}{I_h} = \frac{|\vec{\epsilon}_{s,v}^* \mathbf{R} \mathbf{D} \mathbf{R}^T \vec{\epsilon}_{i,v} + \vec{\epsilon}_{s,h}^* \mathbf{R} \mathbf{D} \mathbf{R}^T \vec{\epsilon}_{i,v}|^2}{|\vec{\epsilon}_{s,v}^* \mathbf{R} \mathbf{D} \mathbf{R}^T \vec{\epsilon}_{i,h} + \vec{\epsilon}_{s,h}^* \mathbf{R} \mathbf{D} \mathbf{R}^T \vec{\epsilon}_{i,h}|^2}. \quad (5.7)$$

Considering the I-CDW, earlier studies suggested an orthorhombic symmetry (even though lower symmetries were not fully excluded) [27]. Moreover, no indications for magnetic order [21] were observed and therefore only charge scattering will be considered relevant to the work in this thesis. In this case, the dipole-dipole 2<sup>nd</sup> rank tensor has the form

$$\mathbf{D}_{\text{orth}} = \begin{pmatrix} D_{11} & 0 & 0 \\ 0 & D_{22} & 0 \\ 0 & 0 & D_{33} \end{pmatrix} \quad (5.8)$$

and, as the orthorhombicity is very small, a natural assumption would be  $D_{11} \approx D_{22}$ . In the experiment described in this chapter, the tensor atomic form factor can only be determined up to a (complex) number. Consequently, one of the parameters can be fixed to 1 without loss of generality. A fit only including the dipole-dipole terms does not give satisfying results. For the majority of the parameter space, only two peaks (at  $90^\circ$  and  $270^\circ$ ) exist. This is shown in Figures 5.5a,b for a series of parameter



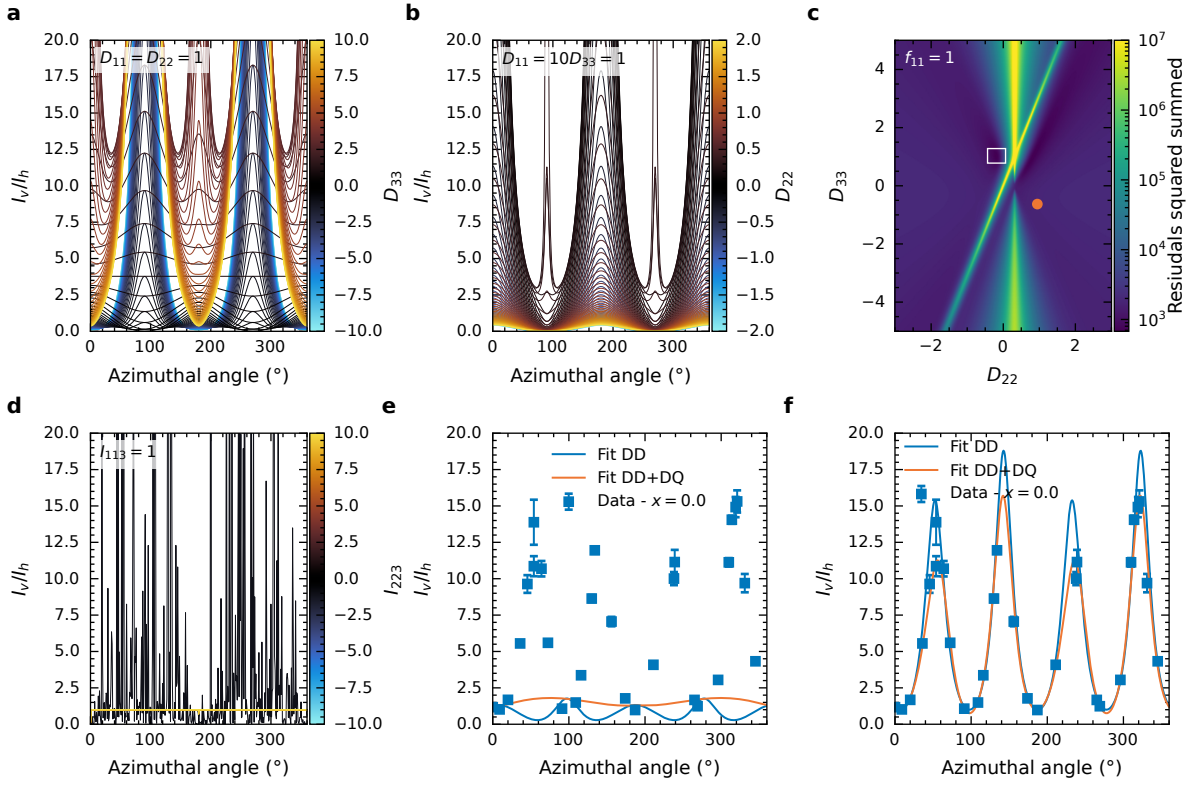


**Figure 5.5.: Azimuthal dependence of the scattering signal of the I-CDW with orthorhombic parameters.** **a-b,d** Azimuthal dependence of the I-CDW scattering signal for different **a-b** dipole-dipole and **d** dipole-quadrupole parameters in the orthorhombic symmetry. **c** residual sum of squares (RSS) for different dipole-dipole parameters in the orthorhombic symmetry. **e-f** Fits of the I-CDW scattering signal measured on sample 1 with **e** orthorhombic symmetry and **f** monoclinic symmetry. Fits including dipole-dipole and dipole-quadrupole terms are included.

combinations. Only for a small parameter set are four peaks reproduced, but they are shifted by  $45^\circ$  with respect to the experimental data. Such a large misalignment can be confidently excluded using the pictures taken at each azimuth (UE46 PGM), the high precision of the four-circle diffractometer (ID32) and the alignment of the Bragg peak. In the *Immm* structure, the nickel is at the position  $4j$  with  $mm2$  symmetry. This is a polar point group without an inversion center, which allows dipole-quadrupole interaction. According to Authier [84], for this point group the 3<sup>rd</sup> rank dipole-quadrupole tensor  $\mathbf{I}$  is given by

$$\mathbf{I}_{\text{orth}} = \begin{pmatrix} 0 & 0 & 0 & 0 & I_{131} & 0 & 0 & I_{113} & 0 \\ 0 & 0 & 0 & I_{223} & 0 & 0 & I_{232} & 0 & 0 \\ I_{311} & I_{322} & I_{333} & 0 & 0 & 0 & 0 & 0 & 0 \end{pmatrix} \quad (5.9)$$

when represented as a  $3 \times 9$  matrix. Using Equation (3.16) and including the symmetry  $I_{jkl} = I_{jlk}$  for charge scattering [84], the effective tensor atomic form factor  $\mathbf{f}$  with the dipole-dipole and dipole-quadrupole components is given by

$$\mathbf{f}_{\text{res,DD+DQ}}^{\text{eff}} = \frac{i}{2} \begin{pmatrix} D_{11} & 0 & (-I_{113} + I_{311}) \sin(\alpha) \sin(\varphi) \\ 0 & D_{22} & (-I_{223} - I_{322}) \cos(\alpha) \\ (I_{113} - I_{311}) \sin(\alpha) \sin(\varphi) & (-I_{223} - I_{322}) \cos(\alpha) & D_{33} \end{pmatrix}. \quad (5.10)$$

This can be further simplified by setting  $I_{311} = I_{322} = 0$  without changing the fit results, as only the combination of  $I_{113} - I_{311}$  and  $I_{223} + I_{322}$  are relevant. The experiment is blind to the other allowed



parameters and therefore they can also be neglected. As shown in Figure 5.5d, the dipole-quadrupole components do not generate reasonable additions to the azimuthal dependence. Accordingly, the fits in Figure 5.5e with only dipole-dipole and dipole-dipole+dipole-quadrupole components are bad. Moreover, this discrepancy is not due to missing the right parameters, as shown by the brute-force calculated RSS for a large parameter space presented in Figure 5.5c.

One possibility would be to consider quadrupole-quadrupole interactions. However, the 4<sup>th</sup>-rank quadrupole-quadrupole tensor has 21 independent components [84] for orthorhombic symmetry. The number of free components can be reduced by considering the symmetry of the tensor, but still, too many free parameters remain to get reliable results. Moreover, the quadrupole-quadrupole interaction is commonly too weak to have such a strong influence.

An inspection of the raw azimuthal dependence shows that the intensity ratio roughly follows a  $\sin^2(2\varphi)$  behavior. Inspecting the dipole-dipole tensor  $D_{jk}$  shows that, with  $D_{13} = D_{31} = 1$  and all other components 0, the intensity ratio is given by

$$\frac{I_v}{I_h} = \frac{\sin^2(2\varphi) + \cos^2(\alpha) \cos^2(2\varphi)}{\cos^2(\alpha) \cos^2(2\varphi) + \cos^4(\alpha) \sin^2(2\varphi)}. \quad (5.11)$$

Considering  $\alpha \approx 60.5^\circ$ ,  $\cos^2(\alpha) \approx 0.24$  and  $\cos^4(\alpha) \approx 0.059$ , this is a promising component of the tensor atomic form factor. In addition, the maximum of  $\approx 17$  and minimum of 1 are close to the ones observed in the experiment. The highest symmetry allowing for the  $D_{13}$  and  $D_{31}$  components is a monoclinic symmetry with the twofold axis in the  $y$ -direction. In this experiment, the  $y$  direction is parallel to the I-CDW wavevector.

In this symmetry, the dipole-dipole tensor is given by

$$\mathbf{D}_{\text{mono}} = \begin{pmatrix} D_{11} & 0 & D_{13} \\ 0 & D_{22} & 0 \\ D_{13} & 0 & D_{33} \end{pmatrix}. \quad (5.12)$$

As the  $D_{13}$  component is dominant, the component will be fixed to 1. Even with  $D_{13}$  as the only non-zero component, the data is reproduced quite well, as shown in Figure 5.4 (dotted line). Including all the allowed components slightly improves the fit. However, especially for the phosphorus substituted sample, the fits are not perfect.

Considering that, for both the currently known structure and the low temperature triclinic structure, the nickel is in a non-centrosymmetric position, it is natural to also assume this for a possible lower symmetry. This would allow in addition dipole-quadrupole terms. For a monoclinic symmetry, the two possible non-centrosymmetric point groups are  $m$  and 2. The third possible monoclinic point group,  $2/m$ , does not allow dipole-quadrupole components as there is an inversion center. For the point group 2 with the twofold axis along the  $y$ -direction, the dipole-quadrupole tensor is given by

$$\mathbf{I}_{\text{mono},2} = \left( \begin{array}{ccc|ccc|ccc} 0 & 0 & 0 & I_{123} & 0 & I_{112} & I_{132} & 0 & I_{121} \\ I_{211} & I_{222} & I_{233} & 0 & I_{231} & 0 & 0 & I_{213} & 0 \\ 0 & 0 & 0 & I_{323} & 0 & I_{312} & I_{332} & 0 & I_{321} \end{array} \right) \quad (5.13)$$

and for the point group  $m$  by

$$\mathbf{I}_{\text{mono},m} = \left( \begin{array}{ccc|ccc|ccc} I_{111} & I_{122} & I_{133} & 0 & I_{131} & 0 & 0 & I_{113} & 0 \\ 0 & 0 & 0 & I_{223} & 0 & I_{212} & I_{232} & 0 & I_{221} \\ I_{311} & I_{322} & I_{333} & 0 & I_{331} & 0 & 0 & I_{313} & 0 \end{array} \right). \quad (5.14)$$

Including again the symmetry of the tensor for charge scattering, one obtains

$$\mathbf{f}_{\text{res,DD+DQ}}^{\text{eff}} = \begin{pmatrix} f_{11} & f_{12} & f_{13} \\ -f_{12} & f_{22} & f_{23} \\ f_{13} & -f_{23} & f_{33} \end{pmatrix} \quad (5.15)$$

$$f_{11} = D_{11} - iI_{112} \cos(\alpha) \quad (5.16)$$

$$f_{12} = \frac{i}{2} \sin(\alpha)((I_{123} - I_{213}) \cos(\varphi) + (-I_{112} + I_{211}) \sin(\varphi)) \quad (5.17)$$

$$f_{13} = D_{13} - \frac{i}{2}(I_{123} + I_{312}) \cos(\alpha) \quad (5.18)$$

$$f_{22} = D_{22} - iI_{222} \cos(\alpha) \quad (5.19)$$

$$f_{23} = \frac{i}{2} \sin(\alpha)((I_{233} - I_{323}) \cos(\varphi) + (-I_{213} + I_{312}) \sin(\varphi)) \quad (5.20)$$

$$f_{33} = D_{33} - iI_{323} \cos(\alpha) . \quad (5.21)$$

for the effective tensor atomic form factor for point group 2. This can be simplified by setting  $I_{211} = I_{233} = 0$ . This is possible as only the combination  $I_{112} - I_{211}$  and  $I_{323} - I_{233}$  can be measured. The other components cannot be further simplified. By fixing  $I_{312} = -1$  in this symmetry, a total of 9 free parameters exist. To account for possible misalignment, an offset is included in the fit. In order not to include further free parameters, the offset was fixed to a value obtained with  $D_{13}$  as the only non-zero parameter. After including the dipole-quadrupole components, the fits are significantly improved, especially for the phosphorus substituted sample. Similarly to the point group 2, the tensor atomic form factor can be expressed as

$$\mathbf{f}_{\text{res,DD+DQ}}^{\text{eff}} = \begin{pmatrix} D_{11} & f_{12} & D_{13} + f_{13} \\ f_{12} & D_{22} & f_{23} \\ D_{13} - f_{13} & f_{23} & D_{33} \end{pmatrix} \quad (5.22)$$

$$f_{12} = -\frac{i}{2}(I_{122} + I_{212}) \cos(\alpha) \quad (5.23)$$

$$f_{13} = \frac{i}{2} \sin(\alpha)((I_{133} - I_{313}) \cos(\varphi) + (-I_{113} + I_{311}) \sin(\varphi)) \quad (5.24)$$

$$f_{23} = -\frac{i}{2}(I_{223} + I_{322}) \cos(\alpha) \quad (5.25)$$

considering the symmetry of point group  $m$ . Here,  $I_{212} = I_{313} = I_{113} = I_{322} = 0$  can be chosen, as these components only appear in combination with other components. By fixing  $D_{13} = 1$ , in total, seven free parameters remain. However, the fit results with the monoclinic point group 2 were better. In addition, the fits with point group  $m$  show a large correlation between the parameters and much higher fit errors. Accordingly, the fits for the point group 2 were used and are further discussed.

The general high complexity of the fit and the limited number of measurement points due to experimental time restrictions lead to extremely high fitting errors. Starting with sample 1, in a first fit  $D_{33}$  showed up to be the least significant parameter (close to 0, large error) and the  $t$ -test also suggested fixing the value to 0. This increases the RSS by only 0.34%. In a subsequent fit, the same applies for  $D_{22}$  (total increase of RSS by 1.55%). Consequently, fits where in addition  $I_{323}$  (22,65%),  $D_{11}$  (45,25%) and  $I_{222}$  (92,94 %) were fixed to 0 were attempted. However, for all of them, the increase in RSS is significant. Therefore, it seems reasonable to fix only  $D_{33}$  and  $D_{22}$  to 0. Similarly, this also applies to the substituted sample. The fits are shown in Figure 5.4 and Figure 5.5 and the fit parameters are shown in Table 5.1. In the appendix, the fit parameters are presented in Table B.1 without fixing allowed values to 0. For all fits of sample 1 an offset in the azimuth of  $-7.5^\circ$  was used. The results for sample 3 are presented in the

**Table 5.1.:** Fit parameters of the azimuthal dependence of the I-CDW for the dipole-dipole and dipole-quadrupole fits for orthorhombic and monoclinic (point group 2) symmetry. In the tensors only the allowed parameters are given. Values which are fixed are also stated but without error. The dipole-quadrupole tensor is only given with the first two  $3 \times 3$  matrices, as the third one is by symmetry identical to the second matrix. For the orthorhombic fits, the values are not rounded properly as the fit errors exceed the value and otherwise all values would be set to 0. The parameters are for the fit of sample 1.

Dipole-dipole tensor		Dipole-quadrupole tensor		RSS
Orthorhombic				
DD	$\begin{pmatrix} 00.2(280) & & \\ & 00.2(270) & \\ & & -00.2(180) \end{pmatrix}$	-		18382.76
DD+DQ	$\begin{pmatrix} -00.1(500) & & \\ & 00.06(2500) & \\ & & -00.2(8600) \end{pmatrix}$	$\left( \begin{array}{ccc ccc} & & & & & \\ & & & & & \\ 0 & 0 & 0 & 1 & 000.07(50000) & \end{array} \right)$		13278.64
Monoclinic (point group 2)				
DD	$\begin{pmatrix} 0.000(20) & & 1 \\ & 0.020(20) & \\ 1 & & 0.010(20) \end{pmatrix}$	-		578.16
DD+DQ	$\begin{pmatrix} -0.052(13) & & 0.41(8) \\ & 0 & \\ 0.41(8) & & 0 \end{pmatrix}$	$\left( \begin{array}{ccc ccc} 0 & -0.255(22) & 0 & -0.71(6) & & -0.145(26) \\ & & & & -0.624(24) & \\ & & & -0.046(19) & & -1 \end{array} \right)$		170.23

appendix in Table B.2. For the fits on sample 3, an offset of  $-111.65^\circ$  was used. The offset is larger as the sample was pre-tilted deliberately because of the limited motor range of azimuthal rotation.

Although the fit errors appear reasonable in the simplified form, the absolute values should be treated with caution. For the same reason, differences between the non-substituted sample 1 and sample 3, may not necessarily come from the substitution. Nevertheless, it can be confidently stated, for both samples, that the experimental results cannot be reproduced with dipole-dipole and dipole-quadrupole interaction and an orthorhombic symmetry.

From this, the highest possible symmetry which can reproduce the results well is the monoclinic, where the monoclinic axis is along the  $y$ -direction. Furthermore, it seems likely that there is a significant dipole-quadrupole contribution. This is also confirmed by the fact that a fit with only dipole-dipole components but where all components are allowed (triclinic symmetry) does not improve the fit significantly. This does not exclude an even lower symmetry, but such a lower symmetry would not improve the fits. It should be noted that the symmetry of the I-CDW at the nickel site is probed and not the full structure.

To confirm the obtained tensor atomic form factor, the linear polarization dependence can be calculated. The linear polarization dependence of the I-CDW for different azimuth angles is presented in Figure 5.6. Similarly to the azimuthal dependence, the raw scans show a distinct change for different incoming linear polarizations. Using the fitted tensor atomic form factor, the dependencies can be well described. Presented are fits with  $D_{13}$  only (dotted line), the dipole-dipole fit (dashed line) and the simplified dipole-dipole and dipole-quadrupole fit (solid line). The lines shown include a fitted scaling factor to reproduce the absolute intensity.

### 5.4.3. Tensor atomic form factor of the commensurate charge density wave

The considerations in the previous section also apply to the C-CDW. As the wedge must be used for the C-CDW, the rotation matrix  $\mathbf{R}$  must now be included. Similarly to the case of the I-CDW, the azimuthal dependence can already be reasonably described by only including  $D_{13}$ . However, the difference is larger than for the I-CDW case. As reported earlier, the symmetry of the averaged unit

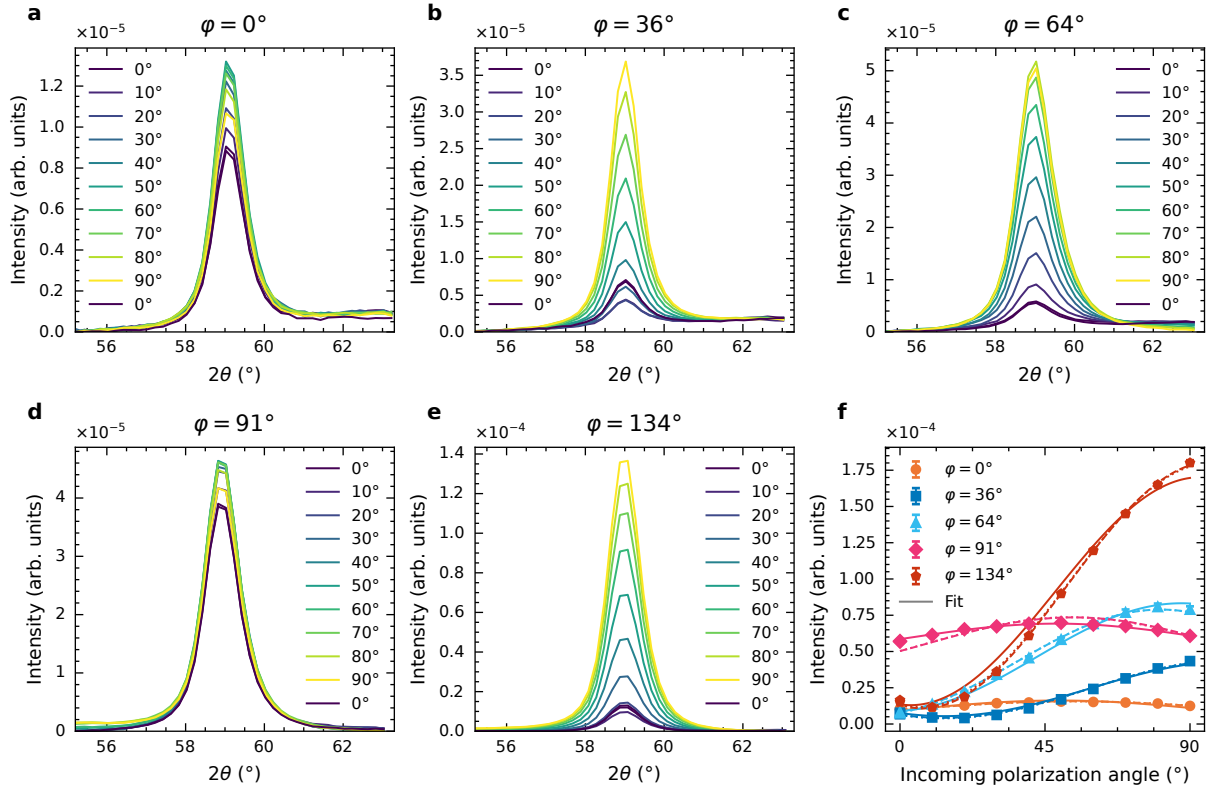


**Figure 5.6.: Linear polarization dependence of the scattering signal of the I-CDW.** a-e  $\theta$ - $2\theta$ -scans of the I-CDW for different azimuthal angles and incoming linear polarizations. f Integrated intensities from the  $\theta$ - $2\theta$ -scans. The fits corresponding to the fits shown in Figure 5.4 are indicated. All data are measured on sample 1. The solid lines correspond to fits including dipole-dipole and dipole-quadrupole components (monoclinic symmetry with reduced number of components). The fit with the dashed line only includes dipole-dipole components and the fit with the dotted lines only includes  $D_{13}$  as non-zero components. The measurements were performed at 138 K.

cell is triclinic in the C-CDW state, a symmetry which already allows the  $D_{13}$  component. As it is feasible, the dipole-dipole fit is performed considering the triclinic symmetry. However, the additional components  $D_{12}$  and  $D_{23}$  only decrease the RSS by 10%. The fit also still has a significant discrepancy at the lower peaks of the azimuthal dependence. As the nickel in the triclinic position has local symmetry 1, dipole-quadrupole terms are allowed. Note that, for proper calculations, the incoming and outgoing wavevector must be rotated with the rotation matrix  $\mathbf{R}$ . With a total of 18 free components after reducing the tensor by its symmetry, a dipole-quadrupole fit including all allowed components does not work. As the general shape of the azimuthal dependence of the C-CDW is similar to that of the I-CDW, it seems natural to use the same shape for the dipole-quadrupole fits.

By including the dipole-quadrupole terms, the quality of the fit is significantly increased, as shown in Figure 5.4. Unlike the case of the I-CDW, it is not really possible to reduce the number of components without altering the fit. The fit parameters are shown in Table 5.2. As stated previously for the I-CDW, the absolute values of the fit should be taken with caution. Nonetheless, for both the I-CDW and the C-CDW, major contributions to the azimuthal components come from terms involved in the  $f_{13}$  component of the tensor atomic form factor (e.g.  $D_{13}$ ,  $I_{123}$  and  $I_{312}$ ). Furthermore, both can only be reasonably fitted by including dipole-quadrupole terms. Even though the average structure in the C-CDW phase was found to be of triclinic symmetry, the monoclinic symmetry used for the I-CDW gives a reasonable fit for the C-CDW but with more relevant components. This, together with the

**Table 5.2.:** Fit parameters of the azimuthal dependence of the C-CDW for the dipole-dipole and dipole-quadrupole fits for triclinic and monoclinic (point group 2) symmetry, respectively. In the tensors only the allowed parameters are given. Values which are fixed are also stated but without error. The dipole-quadrupole tensor is only given with the first two  $3 \times 3$  matrices, as the third one is by symmetry identical to the second matrix.

	Dipole-dipole tensor	Dipole-quadrupole tensor	RSS
Triclinic			
DD	$\begin{pmatrix} -0.06(6) & -0.060(20) & 1 \\ -0.060(20) & -0.16(8) & -0.01(3) \\ 1 & -0.01(3) & -0.02(180) \end{pmatrix}$	-	2966.96
Monoclinic (point group 2)			
DD+DQ	$\begin{pmatrix} -0.215(24) & & 0.65(17) \\ & -0.24(4) & \\ 0.65(17) & & 0.16(5) \end{pmatrix}$	$\begin{pmatrix} 0 & -0.77(16) & 0 \\ & -0.49(5) & -0.11(8) \\ & -0.76(11) & -1 \end{pmatrix}$	324.65

nearly identical energy dependence, suggest a generally comparable orbital ordering in the two CDW states.

Similarly to the I-CDW, the linear polarization dependencies of the C-CDW show a clear change with the azimuth angle. The linear polarization dependencies for the C-CDW are presented in Figure 5.6. For all azimuths, except for the azimuth of  $\varphi = 93^\circ$ , the linear polarization dependencies are well reproduced. The fits with only  $D_{13}$  being non-zero (dotted), with only dipole-dipole components with triclinic symmetry (dashed) and the simplified dipole-dipole and dipole-quadrupole fit with monoclinic (or lower) symmetry (solid line) are shown.

## 5.5. Discussion

In summary, both CDWs exhibit a clear and unexpectedly complicated orbital dependence and symmetry. Generally, the results also indicate that the observed superstructures are, in fact, real CDWs with ordering of the electrons at the Fermi edge and not just a structural distortion. From the energy dependence, it is clear that the CDW resonance occurs at the rising flank of the X-ray absorption. At this energy NEXAFS measurements showed a temperature dependent increase in the X-ray absorption, attributed to a redistribution from  $d_{xy}$  to  $d_{xz,yz}$  orbitals. This redistribution starts around the I-CDW transition temperature and becomes more prominent in the triclinic phase. Considering the resonance of the I-CDW and C-CDW at this energy suggests that mainly  $d_{xz,yz}$  orbitals are involved in the I-CDW and C-CDW formation. This further suggests that the change in the NEXAFS signal is directly connected to the CDW formation. This supports the scenario of orbital-driven mechanisms in the formation of the I-CDW, explaining the unconventional nature revealed in Chapter 4. Together with the Raman results from Yao et al. [23] suggesting the importance of orbital fluctuations, this reemphasizes the importance of the orbitals in the formation of the different orders in  $\text{BaNi}_2(\text{As}_{1-x}\text{P}_x)_2$ . This differentiates  $\text{BaNi}_2\text{As}_2$  from the iron counterpart,  $\text{BaFe}_2\text{As}_2$  in which spin degrees of freedom are an important driving force. As no inelastic contributions could be determined in the signal from the ordered CDWs, no excitations are involved below the ordering temperature.

Furthermore, the strong azimuthal dependence clearly proves an orbital ordering of the CDWs. As these measurements probe the symmetry of the CDW locally at the nickel position, no direct statement about the average structure can be made. However, the local symmetry of the CDW is clearly not orthorhombic. Accordingly, the structure of  $\text{BaNi}_2\text{As}_2$  which includes the CDW must exhibit a lower symmetry at the nickel position. Following the principle of taking the highest possible symmetry, the

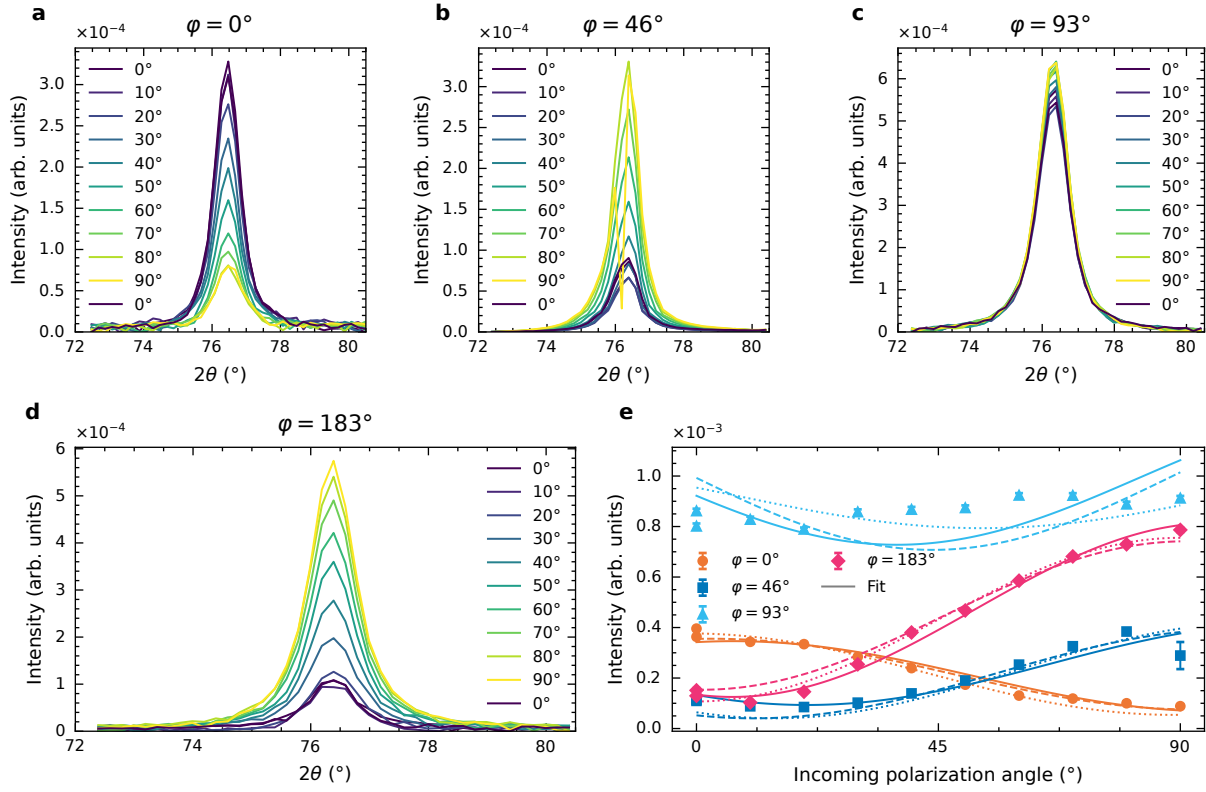


**Figure 5.7.: Linear polarization dependence of the scattering signal of the C-CDW.** a-d  $\theta$ - $2\theta$ -scans of the C-CDW for different azimuthal angles and incoming linear polarizations. e Integrated intensities from the  $\theta$ - $2\theta$ -scans. The fits corresponding to the fits shown in Figure 5.4 are included. All data are measured on sample 1. The solid lines correspond to fits including dipole-dipole and dipole-quadrupole components (monoclinic symmetry with reduced number of components). The fit with the dashed line only includes dipole-dipole components but including all components allowed by triclinic symmetry. The fits shown with dotted lines only includes  $D_{13}$  as non-zero components. The measurements were performed at 10.5 K.

nickel position must be in a monoclinic symmetry with the twofold axes along the CDW direction ( $y$ -direction in this experiment). From the fact that the fits are significantly improved by dipole-quadrupole transitions, a monoclinic point group without an inversion center is more probable. The two possible point groups are in this case  $m$  and  $2$ , while for the orthorhombic structure suggested by Merz et al. [27], the local symmetry at the nickel position is  $mm2$ . With respect to the orthorhombic structure, the mirror plane perpendicular to the  $x$  direction and the twofold rotation axes along the  $z$  directions are lost. For the point group  $2$ , the mirror plane perpendicular to the  $y$  direction is replaced with a twofold rotation axis parallel to the  $y$  axis. In the case of the point group  $m$ , the mirror plane is unchanged, making, from a symmetry consideration, this case more likely. Compared to the tetragonal symmetry ( $\bar{4}m2$ ), the fourfold rotoinversion axis along the  $z$ -direction and the twofold rotation axis along the  $[1\ 1\ 0]$ -direction are lost. For the mirror planes the discussion for the orthorhombic symmetry applies identically. The different main symmetry elements for the different structures are illustrated in Figure 5.8. Altogether, the best fit is obtained with the local symmetry  $2$ , while the symmetry  $m$  seems more likely considering the existing symmetries in the tetragonal and orthorhombic structures. Note that for the dipole-dipole interaction, there is no difference for the different monoclinic point groups [84].

When considering only dipole-dipole transitions, the dominating term of the tensor atomic form factor is  $D_{13}$ . This component is forbidden in the tetragonal and orthorhombic structures, justifying lowering

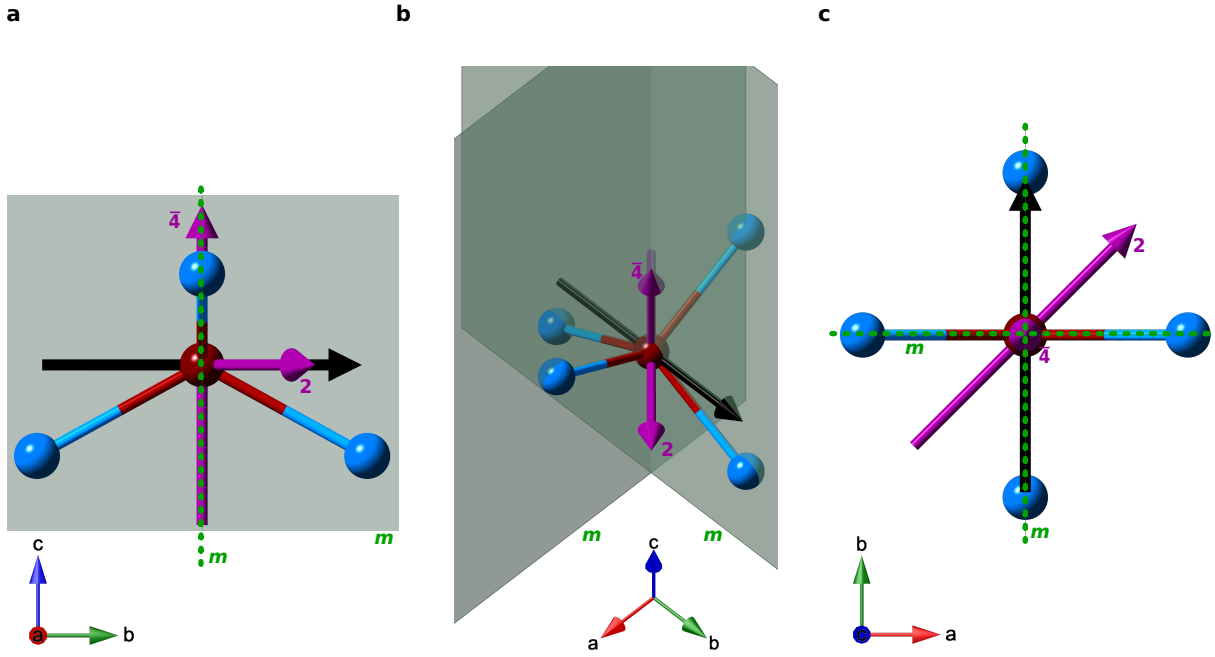


**Figure 5.8.: Sketch of the local site symmetry at the nickel position.** a-c Sketch of a nickel arsenic tetrahedron to illustrate the main symmetry elements of the local nickel symmetry. The nickel atom is shown in dark red and the arsenic atom in light blue. The fourfold rotoinversion axis in the  $z$  direction and twofold rotation axis in  $[1\ 1\ 0]$ -direction are indicated by a purple arrows. The mirror planes perpendicular to  $x$  and  $y$  are shown in dark green. The direction of the twofold axis in monoclinic symmetry is shown in black and is used for illustration only and does not directly correspond to a symmetry in the higher symmetry structures. In the tetragonal structure, all shown symmetry elements are present. In the orthorhombic structure, the purple twofold rotation is lost and the fourfold rotoinversion is replaced by a twofold rotation axis. In the monoclinic symmetry, all purple symmetry elements and at least the mirror perpendicular to  $x$  are lost.

the symmetry in the evaluation discussed above. To obtain this component of the tensor atomic form factor, terms in the Hamiltonian which mix  $J_z$  and  $J_z \pm 1$  must be found. The crystalline electric field (CEF) could lift the symmetry at the nickel position, allowing for this mixing. Two possible symmetries of the CEF, which allow the correct mixing in the Hamiltonian, are  $d_{xz}$  and  $d_{yz}$  and thus the symmetry of orbitals the CDW resonates. Therefore, arrangements must be found which would allow a CEF with the appropriate symmetries. Especially for the I-CDW, further insight could come from a high-quality XRD study which includes the superstructure peaks. A full refinement of the incommensurate structure in four-dimensional (or higher) space could reveal the symmetry of the structure with the I-CDW. Even though it is challenging, especially to include the very faint peaks found by TDS in Chapter 4, it is generally possible. For the C-CDW, an additional problem is the number of twins in the triclinic structure, which complicates the refinement.

Another route to gain further insight could be the use of  $s$ -core-level non-resonant inelastic X-ray scattering (s-NIXS) to directly image the orbitals. Even though the name is similar to IXS, technically setups for X-ray Raman scattering (XRS) are used, as in this thesis IXS is only used for inelastic X-ray scattering with meV resolution, mainly used for phonon investigations. In s-NIXS the integrated intensity or line shape of dipole forbidden transitions for example  $s \rightarrow d$  or  $s \rightarrow f$  can be investigated. As the  $s$  orbital is spherically symmetric, an angular dependence of integrated intensity of the transition directly yields the shape of the local orbital hole density of the ion in the ground state. This has been used for various insulators [167, 168] but can also be done for metals [169]. In the case of  $\text{BaNi}_2(\text{As}_{1-x}\text{P}_x)_2$ , this could be used to image the orbitals above and below the two CDW transitions

and therefore investigate the change in the orbitals. This could also give indications for orbital Peierls states responsible for the I-CDW formation discussed in Chapter 4.

As the fit results significantly improve by including dipole-quadrupole terms, it is likely that dipole-quadrupole transitions are involved in the scattering process. This further restricts the symmetry to a nickel site without inversion symmetry. In the monoclinic symmetry, a local nickel symmetry of 2 gave good results, although other, especially lower, symmetries cannot be excluded because of the variety of parameters and possibilities. Also, when the dipole-quadrupole terms are included, the tensor is dominated by components included in  $f_{13}$ .

The average structures for the I-CDW and C-CDW show clear differences. In the energy and the azimuthal dependencies, the differences are much more subtle. This suggests that the actual orbital ordering of the two CDWs is not vastly different, as best evidenced by the nearly identical energy dependence and the generally comparable fits of the azimuthal dependence. The main difference is that the C-CDW is not purely dominated by the single  $f_{13}$  component, as other components are more important compared to the I-CDW. That the orbital ordering between the two CDWs appears to be comparable is in agreement with the time resolved spectroscopy measurements, which also find a smooth transition between the modes of the two CDWs [148–150].



## 6. Pressure tuning of the charge density waves

Parts of this chapter were already published in:

- T. Lacmann, A.-A. Haghighirad, S.-M. Souliou, M. Merz, G. Garbarino, K. Glazyrin, R. Heid, and M. Le Tacon, *Physical Review B* **108**, 224115 (2023)

The raw data presented in Section 6.3 is available from the European Synchrotron Radiation Facility Data portal [171] and from the Karlsruher Institut für Technologie repository (KIT Open) [172]. The new structures found in the  $\text{BaNi}_2\text{As}_2$  high pressure phase diagram are available from the Cambridge Crystallographic Data Centre (CCDC) with deposition numbers 2289119-2289121.

The data taken on the pristine  $\text{BaNi}_2\text{As}_2$  at beamline ID15B at the ESRF-EBS were measured, but only roughly evaluated, as part of the authors' master thesis [137]. Further measurements at the Positron-Elektron-Tandem-Ring-Anlage III (PETRA III), the major part of the evaluation and understanding of the data were only performed as part of this thesis. As this cannot be strictly separated and for better understandability and completeness, the data are fully included in this thesis.

### 6.1. Introduction

After investigating and discussing the origin and symmetry of the CDWs in the Chapters 4 and 5, this chapter will focus on the external tuneability of the CDWs and the structural phases. Besides answering the question of tuneability itself, this also gives further insights into the relation of different phases, and can help to answer the question of the ordering mechanisms and origin of the different phases.

The phosphorus substitution dependence discussed in Chapter 4 and earlier works [23, 25, 27, 40, 47] already showed tuneability of both the CDW and the structural phases. Even though substitution is often simplified as chemical pressure, due to the different size of the substituent ion compared to the original ion, it can also alter the chemical properties e.g. by steric effects. Furthermore, substitution can be a source of disorder and intrinsically requires the investigation of several samples to construct the phase diagram.

Compared to chemical pressure, the use of externally applied physical pressure is a clean way to tune the system. Furthermore, with the use of hydrostatic and uniaxial pressure, the effect of both symmetry preserving and symmetry breaking perturbations can be studied. Both have been valuable in tuning the CDWs in a series of materials [93, 96, 103, 155, 173]. This is also a direct way to investigate the importance of certain symmetries for e.g. the I-CDW formation.

However, to achieve this a huge experimental price in the form of experimental limitations and effort has to be paid. Luckily, XRD and TDS, are generally compatible with hydrostatic and uniaxial pressure, proven to be suitable to investigate the CDWs in Chapter 4 and the experimental limitations still allow the experiments to be performed. Therefore, here, similar to Chapter 4, reciprocal space maps are shown in Figure 6.1. The obtained maps have an increased background, limited accessible reciprocal space and spurious diamond reflections (in the case of the use of a DAC) that make the evaluation more

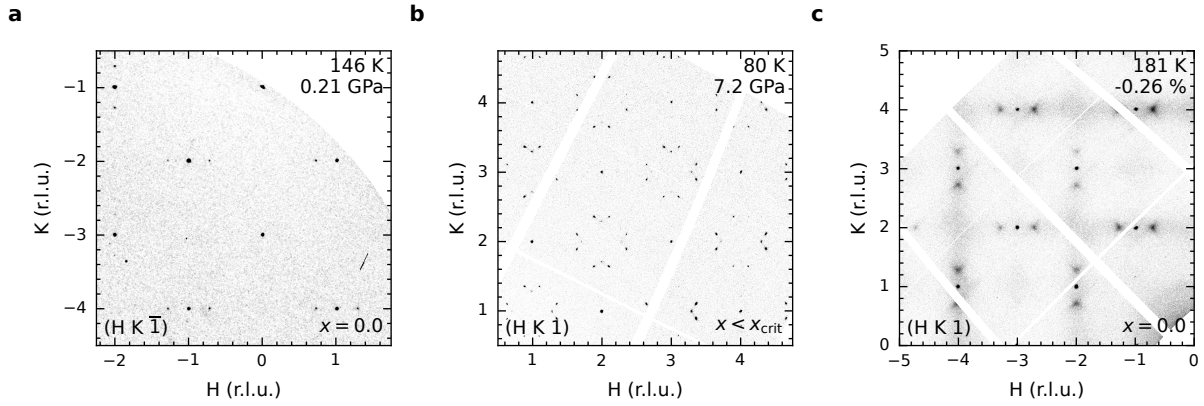


**Figure 6.1.: Reciprocal space maps as obtained under applied hydrostatic and uniaxial pressure.** **a**  $(h k \bar{l})$  reciprocal space map of a  $x = 0.0$  sample in a DAC at 146 K and 0.21 GPa with I-CDW superstructure. **b**  $(h k 1)$  reciprocal space map of a  $x < x_{\text{crit}}$  sample in a DAC at 80 K and 7.2 GPa with new I-CDW2 superstructure. **c**  $(h k 1)$  reciprocal space map of a  $x = 0$  sample in a DAC at 181 K and compression of  $-0.26\%$  with diffuse scattering of the I-CDW.

challenging. However, the data measured under applied pressure still allows the crystal structure to be solved. Finally, applying pressure on substituted samples also allows the study of the impact of both tuning parameters.

First, in Section 6.3, the high pressure XRD (HP XRD) experiments on the non-substituted  $\text{BaNi}_2\text{As}_2$  will be discussed and will reveal a high tuneability with pressure of the different phases observed. A remarkable exception to this is the unusual high resilience against the pressure of the original I-CDW, which is neither suppressed nor enhanced with pressure. A further notable observation is the discovery of two new monoclinic structures strongly tied to the appearance of new CDWs. Above  $\approx 10$  GPa all CDW-instabilities are lost and a stable monoclinic structure is observed, which can be best described as “collapsed”, showing some similarities to the cT phases in other pnictides. Interestingly, none of this is observed with substitution only.

In the following Section 6.4, high pressure (HP) is combined with phosphorus substitution showing a resemblance of the non-substituted  $p$ - $T$ -phase diagram but with all low temperature phases being suppressed similar to ambient pressure. Nonetheless, the detailed analysis reveals additional instabilities and a novel monoclinic phase, which is most likely the so far unknown structure observed at ambient pressure in  $x \approx 0.1$  substituted crystals.

After this in Section 6.5 instead of hydrostatic pressure now uniaxial symmetry breaking pressure is applied. While no new structures or CDWs were found, the experiments reveal that only the ordered I-CDW is strongly affected by uniaxial compression, especially the I-CDW cannot be ordered by the application of pressure. Moreover, the non-substituted and  $x \approx 0.1$  substituted samples show a majorly different response. Furthermore, the results do not show an easy detwinning of the I-CDW as expected from the originally suggested orthorhombic phase.

Finally, in Section 6.6, the results, including chemical pressure, are compared and discussed. This reveals the different response of different substituents and pressure to different parts of the phase diagrams. In addition, this section highlights the unusual resilience of the I-CDW1 and the importance of the Ni-As hybridization for the stabilization of the structure.

In the first Section 6.2, the exact experimental details, including all important experimental conditions, parameters and the individual samples, are introduced for all three experiments. Since this section is rather detailed and technical, and it is not necessary to understand the physics in the following sections, readers may skip it if they are not interested in those details. Note that throughout this thesis

all reciprocal vectors are given in the tetragonal notation to allow the reader to more easily compare different structures.

## 6.2. Experimental details

### 6.2.1. General

The HP XRD experiments were performed at the beamlines ID15B and P02.2 at the synchrotron sources ESRF-EBS and PETRA III at Deutsches Elektronen-Synchrotron (DESY), respectively. More details on the beamlines can be found in the papers from Merlini and Hanfland [174] and Liermann et al. [175]. All samples were mounted with the *c*-axis parallel to the beam at  $\approx 0^\circ$  rotation. The DACs or uniaxial pressure cells were mounted inside an evacuated liquid helium flow cryostat with a base temperature of  $\approx 2$  K (ID15B with DAC), 15 K (ID15B at the sample position of the uniaxial pressure cell) and 15 K (P02.2 with DAC). For all measurements, diffraction images were recorded while continuously rotating the sample. The total angular range of the rotation, the time and angular distance over which the individual images were integrated was optimized for each experiment. Images were also recorded with different incoming flux to be able to measure weak signals but also to have data in which the Bragg reflections are not saturated for structural refinements. The peak hunting, unit cell finding, integration and reciprocal space reconstructions were performed using the software CrysAlis Pro [138]. The structure solutions and refinements were performed using SHELLXS [176], SHELLXL 2014/7 [177] and Jana2006 [178]. For all hydrostatic pressure experiments, the pressure was calibrated in-situ using the fluorescence line of ruby crystals [114] which were loaded in the gasket hole together with the samples. The hydrostatic pressure was also applied in-situ by increasing the pressure in the gas membrane with a pressure controller.

### 6.2.2. Hydrostatic pressure experiments on pristine $\text{BaNi}_2\text{As}_2$

The experiments on the pure  $\text{BaNi}_2\text{As}_2$  in Section 6.3 were measured at both ID15B and P02.2. Section 6.3 encompasses measurements made on three distinct samples from the same batch which were loaded to three different DACs. In the following they are denoted as samples 1, 2 and 3. Samples 1 and 2 were loaded together with other samples into their respective DACs. The additional samples were used to crosscheck the results, but are not shown for simplicity. Between the different samples, no significant difference or discrepancy was observable. An example of  $\text{BaNi}_2\text{As}_2$  sample 1 loaded into the gasket hole and an example of the measured reciprocal space are shown in Figure 6.2. For each sample, different paths in the *p*-*T*-phase diagram were chosen. Predominantly, the samples were cooled down and then compressed to the intended pressure. In some cases, isobars were also measured in between. The exact *p*-*T*-path for each sample along with microscope images of the samples inside the DACs are shown in the appendix in Figure C.1. Sample 1 was measured at beamline ID15B while samples 2 and 3 were measured at beamline P02.2.

At beamline ID15B, a European Synchrotron Radiation Facility (ESRF)-made Le Toullec-type CuBe-alloy DAC with diamonds with culet diameters of 500  $\mu\text{m}$  were used. A Stainless-steel gasket was indented down to a thickness of 100  $\mu\text{m}$  and the gasket hole was drilled using a ESRF-made laser drilling system. The DAC was gas loaded with Helium as a pressure transmitting medium. The beam was monochromatized to an energy of 30.17 keV ( $\approx 0.411$  Å) and focused to a spot size of about 4  $\mu\text{m} \times 4$   $\mu\text{m}$ . The data were acquired using a Mar research MAR555 flat panel detector at a distance of 259.9 mm to the sample. The detector position and distance were calibrated using silicon powder and an enstatite

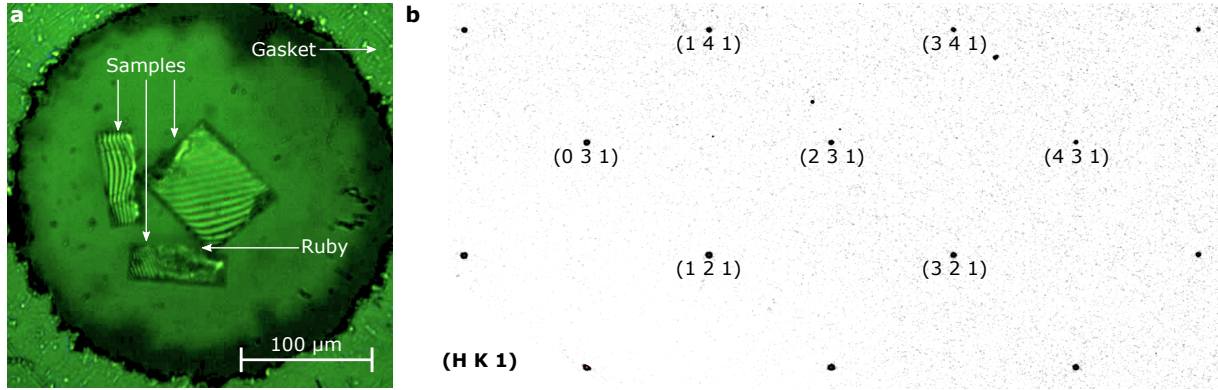


**Figure 6.2.: Microscope image of pristine  $\text{BaNi}_2\text{As}_2$  samples loaded into the DAC and reconstructed reciprocal space map.** **a** Microscope image of  $\text{BaNi}_2\text{As}_2$  single crystals and a ruby ball (as pressure indicator) inside the gasket hole loaded in the DAC. At the edges, the stainless-steel gasket is visible. The samples are loaded with the  $c$ -direction parallel diamond surface normal and to the beam at  $\approx 0^\circ$  rotation. The edges of the samples are along an  $a$ - or  $b$ -direction. **b** Reciprocal space reconstruction of the  $(h k 1)$  plane for a  $\text{BaNi}_2\text{As}_2$  single crystal at 192 K and 0.21 GPa.

single crystal using the software packages Dioptas [179] and Crysalis Pro [138]. The total rotation was set to  $\pm 32^\circ$  and the images were integrated for 0.5 s over a rotation of  $0.5^\circ$ .

At beamline P02.2 DESY-made hardened steel symmetric DACs with a diamond culet diameter of  $400\ \mu\text{m}$  were used. Rhenium gaskets were indented to a thickness of about  $80\ \mu\text{m}$  and the DACs were gas loaded with Neon as a pressure transmitting medium. The HP XRD experiments were performed using a monochromatic X-ray beam with an energy of  $42.71\ \text{keV}$  ( $\approx 0.2903\ \text{\AA}$ ) focused down to  $3\ \mu\text{m} \times 8\ \mu\text{m}$ . The diffracted beam was detected with a Perkin Elmer XRD 1621 detector at a distance to the sample of  $401.176\ \text{mm}$ . The detector position and distance was calibrated using  $\text{CeO}_2$  powder and an enstatite single crystal using the software packages Dioptas [179] and Crysalis Pro [138]. The data was acquired over a total rotation from  $-25^\circ$  to  $30^\circ$  and each image was integrated for 0.5 s over a rotation of  $0.5^\circ$ .

The DFPT calculations were performed with the experimentally determined structures with relaxed atomic positions to obtain force free conditions. The details of the calculations are similar to the calculations performed in Chapter 4, as described in Section 4.2.

The HP XRD experiments on pristine  $\text{BaNi}_2\text{As}_2$  were performed by the author of this thesis, Dr. Sofia-Michaela Souliou, Dr. Amir-Abbas Haghighirad, Dr. Gaston Garbarino and Dr. Konstantin Glazyrin. The data evaluation was done together with Dr. Amir-Abbas Haghighirad. DFPT calculations were carried out by Dr. Rolf Heid.

### 6.2.3. Hydrostatic pressure experiments on phosphorus substituted $\text{BaNi}_2\text{As}_2$

The experiments on phosphorus substituted  $\text{BaNi}_2(\text{As}_{1-x}\text{P}_x)_2$  samples were performed at beamline ID15B at the ESRF-EBS. The same beamline parameters were used as for pristine sample described in Section 6.2.2. However, instead of the Mar research MAR555 a EIGER2 X 9M CdTe flat panel detector from DECTRIS at a distance of  $178.98\ \text{mm}$  from the sample was used. The detector distance and position were calibrated using silicon powder and a vanadinite single crystal using the software packages Dioptas [179] and Crysalis Pro [138]. Three samples close to the critical substitution  $x_c \approx 0.076$  at which the triclinic phase is suppressed were loaded in a ESRF-made Le Toullec-type CuBe-alloy DAC with diamonds with culet diameters of  $500\ \mu\text{m}$ . Before the loading, the stainless steel gasket was indented to a thickness of  $70\ \mu\text{m}$  to  $90\ \mu\text{m}$  and a  $300\ \mu\text{m}$  hole was drilled with a ESRF-made laser drilling

system. The DAC was gas loaded with helium as the pressure transmitting medium. The total rotation was set to  $\pm 30^\circ$  and the images were integrated for 0.2 s over a rotation of  $0.5^\circ$ .

From the three loaded samples, the measurements were mainly performed on two. To differentiate them from the samples in Section 6.2.2 they will be denoted as samples 4 and 5. As it turned out, sample 4 had a substitution level  $x < x_c$  and therefore did show the triclinic transition. Sample 5, however, had a substitution  $x \geq x_c$  and did not show the triclinic transition to the lowest temperature measured. As the samples were loaded in the same DAC, they both followed the same  $p$ - $T$ -path. A microscope image and the exact  $p$ - $T$ -path is shown in the appendix in Figure C.2.

The HP XRD measurements on phosphorus substituted  $\text{BaNi}_2\text{As}_2$  were performed by the author of this thesis, Dr. Sofia-Michaela Souliou, Dr. Amir-Abbas Haghighirad and Dr. Gaston Garbarino.

#### 6.2.4. Uniaxial compression experiments

The uniaxial pressure experiments were carried out at beamline ID15B at the ESRF-EBS. The beamline parameters were equal to Section 6.2.2 and Section 6.2.3. The EIGER2 X 9M CdTe was mounted at a distance of 180.12 mm to the sample. The detector distance and position were calibrated using silicon powder and a vanadinite single crystal using the software packages Dioptas [179] and CrysAlis Pro [138]. To generate the uniaxial pressure, a piezoelectric pressure cell of the type CS200T from Razorbill Instruments, primarily constructed from titanium, was employed. To apply strain, a high voltage was applied with a Razorbill Instruments RP100 high voltage low current source. The capacitance from the displacement sensor of the pressure cell was measured using a Keysight E4980AL precision LCR meter or ANDEEN-HAGERLING AH 2550A capacitance bridge and used to control the strain actively with a self-written program. The capacitance reading, however, gives only the nominal strain, which is not fully transmitted to the sample. Therefore, all strain values in this thesis are calculated from the change of the refined lattice parameters and represent the actual strain of the sample. The engineering strain definition with compressive strain being negative is used in this thesis.

Samples with a substitution of  $x = 0$  and  $x \approx 0.1$  were shaped into rods using a Princeton Scientific WS-22 precision wire saw with a tungsten wire and boron carbide in glycerin as the abrasive slurry. The prepared rods have a size between  $1500 \mu\text{m} \times 200 \mu\text{m} \times 10 \mu\text{m}$  and  $3000 \mu\text{m} \times 500 \mu\text{m} \times 15 \mu\text{m}$  ( $a \times b \times c$ ). The length and width were determined by the original sample size and the performed cutting. The thickness ( $c$ -axis), however, was determined by the self-cleaving of the samples during cutting. The samples were cleaned with heated pure ethanol from the low melting point wax (PELCO Quartz Sticky Wax 70C) used to fix the samples during the cutting. Due to the tendency of  $\text{BaNi}_2(\text{As}_{1-x}\text{P}_x)_2$  to cleave during polishing, the rods were mounted as cut into home-made titanium quick exchange sample carriers, identical to the ones used by Vinograd and Souliou et al. [155]. The samples were glued with LOCTITE STYCAST 2850FT with CAT 24LV or CAT 23LV as catalyst. The sample carriers were glued with the same glue shortly before the experiment onto the pressure cell. The glue was cured at  $\approx 70^\circ\text{C}$  under vacuum. Most of the sample preparation must be carried out in air, but care was taken to minimize exposure to air and humidity, as the samples are sensitive to air/moisture. The sample temperature was measured with a silicon diode directly mounted on the pressure cell, close to the sample position. The stress was applied along the long axis/ $a$ -axis and mainly as compressive stress.

In total five different samples were investigated. However in the text mainly data from two samples with  $x = 0.0, 0.1$  will be discussed. The other samples are not discussed as they either broke early during the experiment, due to technical problems, or the results were unclear due to a partial structural transition during the compression. This will be discussed further in Section 6.5. One sample for which

this happened is discussed exemplarily in the text and more details are shown in the appendix in Appendix C.4.

An example microscope image of the cut needles before mounting are shown in Figure C.3 in the appendix.

The XRD experiments were carried out by the author of this thesis, Dr. Mehdi Frachet, Fabian Henßler, Dr. Mai Ye, Dr. Amir-Abbas Haghighirad, Dr. Philippa McGuinness and Dr. Gaston Gaberino.

### 6.3. Hydrostatic pressure tuning of pristine $\text{BaNi}_2\text{As}_2$

For simplicity, first the HP-phase diagram of the pure  $\text{BaNi}_2\text{As}_2$  is introduced. For presentation, the data can be divided into two isotherms and five isobars. Following the two isotherms at 140 K (just above the triclinic transition at ambient pressure) and 94 K (below the triclinic transition at ambient pressure) gives a good overview of the evolution of the different structures and CDWs under hydrostatic pressure and is therefore discussed first. The five isobars at  $\approx 2.2$  GPa, 4 GPa, 7.6 GPa, 10 GPa and 12 GPa give additional insight into the details and transitions observed in the HP-phase diagram.

With the diffraction images obtained via XRD, the position of the Bragg peaks can be extracted using a peak search algorithm. Those peak positions used in combination with Crysalis Pro [138] to determine the lattice parameters of the cell. Together with the integrated intensities, a complete structural solution and refinement can be performed. The obtained lattice parameters and internal structural parameters are good quantities to check for a structural phase transition. As a full structural refinement was performed for all  $p$ - $T$  points, the R values from the refinement can be used as crosscheck of the phase transitions. For the superstructures, however, it is easier to look at reciprocal space maps, linecuts in the reciprocal space and the position of additional peaks that are not indexed by the average structure. Accordingly, in the following mainly reciprocal space maps and structural parameters as e.g., lattice parameters will be shown. Note that throughout this section, as for the complete thesis, all Miller-indices are given using the tetragonal notation to allow the reader to more easily compare reciprocal space maps and wavevectors. This is done irrespective of the actual structure. For readability, the subscript “tet” is generally omitted.

#### 6.3.1. Isotherm at 140 K

Firstly, we follow the isotherm at 140 K from loading pressure to the maximum pressure used during this investigation of  $\approx 12$  GPa. At this temperature  $\text{BaNi}_2\text{As}_2$  is in the orthorhombic  $Immm$  structure at ambient pressure. Similarly, at the loading pressure of 0.3 GPa, the structural refinement gives the same orthorhombic structure. In analogy to the case at ambient pressure, the orthorhombicity is so small that the tetragonal and orthorhombic structures are nearly indistinguishable with XRD. Even though Chapter 5 provides strong evidence that the local symmetry at the nickel position in the I-CDW phase is in fact of monoclinic or lower symmetry, the phase will be denoted orthorhombic  $Immm$ . Neither in Chapter 5 nor in this section can a better structure be assigned, as the changes in the average structure remain too small to be observed. Structural refinements of other (lower) symmetry cells do not give better results. In addition, a structural refinement including the superstructure is not reliable with the experimental limitations from the DAC.

At the loading pressure a similar superstructure to the ambient pressure I-CDW with wavevector  $q_{\text{I-CDW}} \approx (0.28 \ 0 \ 0), (0 \ 0.28 \ 0)$  is observed. Hereafter, the I-CDW will be denoted as I-CDW1 to distinguish it from other superstructures. Under further compression at this temperature, the wavevector

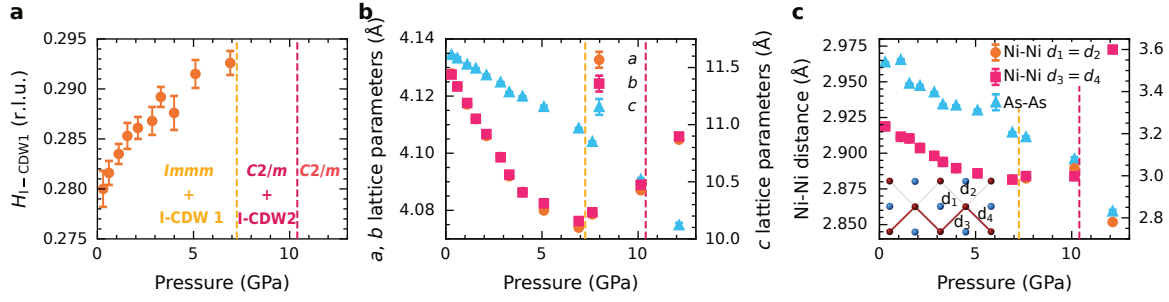


**Figure 6.3.: Pressure dependence of the I-CDW1 wavevector, lattice parameters and atomic distances at 140 K.** **a** Change of the I-CDW1 wavevector under increasing hydrostatic pressure. The different structures and superstructures are indicated. The structural phase transitions are shown by colored dashed lines. **b** Pressure dependence of the  $a$ ,  $b$  and  $c$ -lattice parameters. The lattice parameters are given for comparability in the orthorhombic setting. **c** The intralayer Ni-Ni distances and interlayer As-As distance for the different phases versus applied hydrostatic pressure. The different Ni-Ni distances are shown in the inset. All data shown are measured on sample 1 at 140 K except for the data at 12.13 GPa, which is measured on sample 3 and at 145 K.

increases from  $0.2800 \pm 0.0018$  at 0.3 GPa to  $0.2926 \pm 0.0012$  at 6.91 GPa. The increase is depicted in Figure 6.3a. This change in the wavevector also confirms that the I-CDW1 is in fact incommensurate and not commensurate with an unusual commensurability, as the wavevector would be constant for a C-CDW. At only a slightly higher pressure of 7.62 GPa, there is an abrupt change in the structure. The I-CDW1 wavevector is lost and the lattice parameters shown in Figure 6.3b also exhibit an anomaly. While the  $a$  and  $b$  lattice parameters show a continuous decrease at lower pressures, at this pressure the lattice parameters suddenly start increasing again. Also in the  $c$  lattice parameter shows a kink. This is evidence for a structural phase transition. As there is no jump and also no coexistence observable, this is likely a second-order or a rather sharp first order phase transition. The structural refinement shows that the new structure has a monoclinic symmetry in which the tetragonal  $c$ -axis slightly tilts and breaks the symmetry. In the standardized setting, the unit cell lies differently compared to the tetragonal unit cell and is of  $C2/m$  type. For differentiation, this newly observed structure will be called monoclinic IIa in the following. The unit cell and all structural parameters are given in the appendix in Table C.1.

The structural transition is also reflected in the atomic distances depicted in Figure 6.3c. Similar to the lattice parameters, first the Ni-Ni intralayer and the As-As interlayer distance shrinks under increasing pressure. At the transition to the monoclinic IIa phase, the Ni-Ni distances are extended again and become more distinct but stay close in value. Thereby, two Ni-Ni distances always stay identical, resulting in Ni-Ni zigzag chains. The As-As distance, however, does not show a significant change at the transition. At only slightly higher pressure of  $\approx 11$  GPa the As-As distance drops and the two sets of Ni-Ni distances become suddenly very distinct. Therefore, instead of the Ni-square in the tetragonal structure, now well separated Ni-Ni zigzag chains form in the Ni-plane. The sudden drop of the As-As distance and the magnitude of the As-As distance resembles the behavior at the  $cT$  transition observed in other pnictides [180, 181]. Beside these similarities, there are notable differences. First, a structural refinement reveals the same monoclinic  $C2/m$  symmetry as for the monoclinic IIa structure but with significantly altered atomic positions. Therefore, this structure is now referred as monoclinic IIb. Second, unlike for the  $cT$  structures, the Ni-As layer thickness increases as the arsenide atoms are pushed away from the nickel plane. This results in a significantly increased Ni-As layer thickness that is not observed in the  $cT$  structure. Similarly to the monoclinic IIa structure, this “collapsed” structure, or indeed any collapsed phase, was not reported so far for  $\text{BaNi}_2\text{As}_2$ .



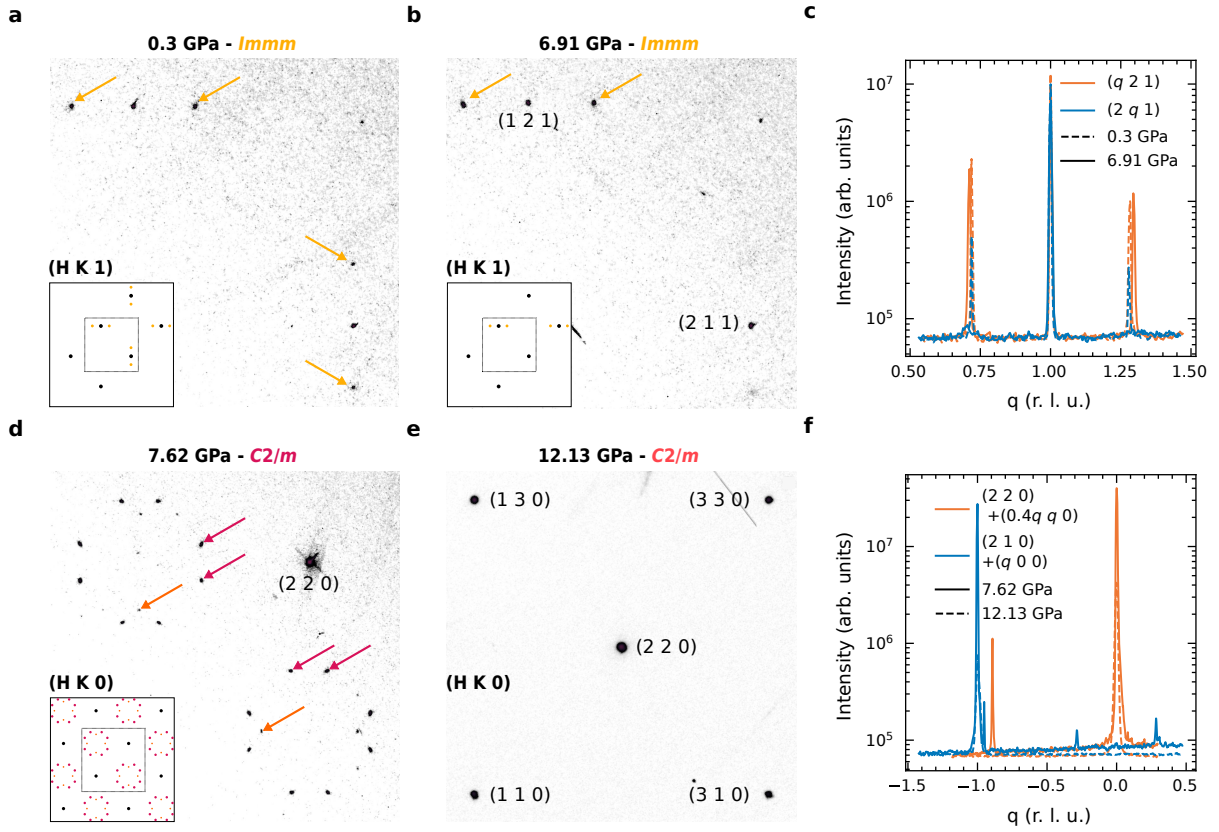


**Figure 6.4.: Reciprocal space maps and line cuts at 140 K.** **a-b** Reconstructed  $(h k 1)$  reciprocal space maps showing Bragg peaks and the I-CDW1 at **a** 0.3 GPa and **b** 6.91 GPa at 140 K. A sketch of a larger part of the reciprocal space indicates the arrangement of the superstructure peaks from I-CDW1. The inner square indicates the shown part of the reciprocal space. The superstructure peaks of I-CDW1 are highlighted by light orange arrows. **c** Linecuts along the  $h$ - and  $k$ -direction through the I-CDW position for the data shown in **a-b**. **d-e** Reconstructed  $(h k 1)$  reciprocal space maps at **d** 7.62 GPa and **e** 12.13 GPa at 140 K and 145 K, respectively. The positions of the I-CDW1' (dark orange) and I-CDW2 (magenta) superstructure peaks are indicated by arrows. **f** Linecuts through the I-CDW2 and I-CDW1' positions for the data shown in **d-e**. All data shown are measured on sample 1 at 140 K except for the data at 12.13 GPa, which is measured on sample 3 and at 145 K.

Overall, the collapse of the structure leads to a significant change in the Ni-As plane and the Ni-As bond. This is noteworthy as, at this transition, all signatures of a CDW are lost. This can be best seen in the reciprocal space maps shown in Figures 6.4a-b and d-e. In the  $(h k 1)$  reciprocal space maps at 0.3 GPa the superstructure peaks from the I-CDW1, the ambient pressure I-CDW, are strong and visible in both the  $h$  and  $k$  direction. At 6.91 GPa, besides the increased wavevector, the intensity of the peaks in the  $k$  direction drops and they are only faintly visible. The loss of the superstructure peak in one direction and the increasing wavevector are even more pronounced in the linecut through the I-CDW1 position in Figure 6.4c. As discussed in Chapters 4 and 5, the ambient pressure I-CDW is a unidirectional CDW and the peaks in both direction are most likely visible due to twinning of the structure. Accordingly, the loss of the peaks in  $k$  direction is presumably due to slight experimental imperfections leading to a tiny non-hydrostatic component which is enough to detwin the sample.

At the structural transition to the monoclinic IIa phase, the changes in the superstructures are more pronounced. The I-CDW1 is completely lost. Instead, a new I-CDW with a comparable intensity and wavevector  $q_{\text{I-CDW2}} \approx (\pm 0.358 \pm 0.10 0); (\pm 0.1 \pm 0.358 0)$  appears. This ensemble of eight superstructure peaks forms an octagonal structure centered around a forbidden Bragg peak, as depicted in Figure 6.4d. This superstructure is denoted hereafter as I-CDW2. In addition, faint peaks with a similar wavevector as I-CDW1 are also visible around forbidden Bragg reflections, denoted now as



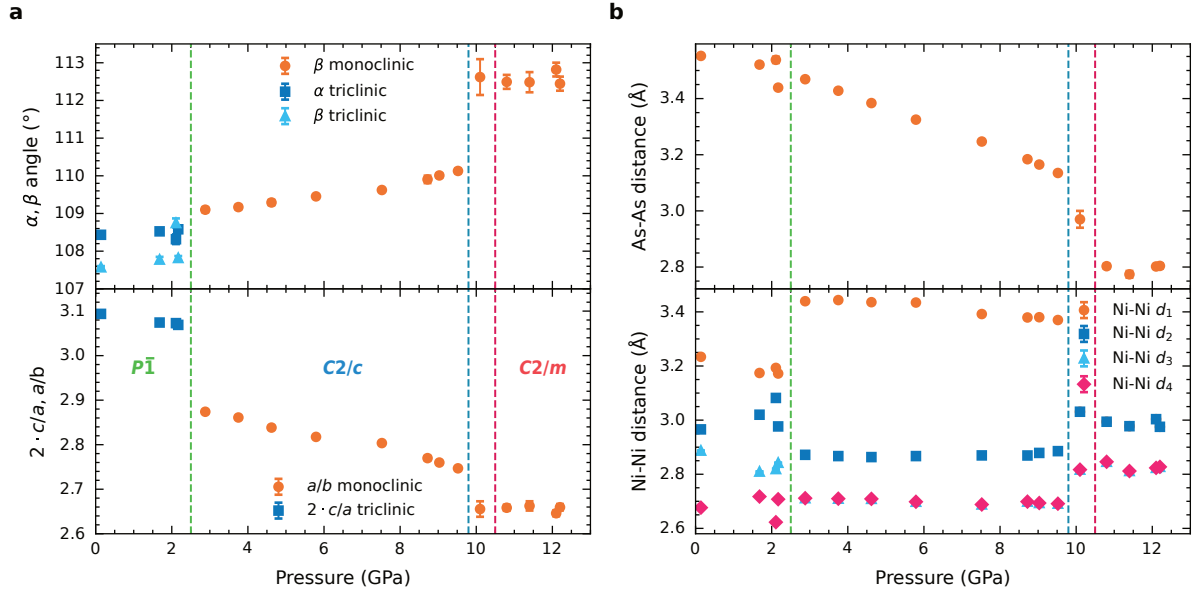


**Figure 6.5.: Pressure dependence of different structural parameters at 94 K.** **a** Change of the triclinic and monoclinic angles  $\alpha$  and  $\beta$  and the  $c/a$  or  $a/b$  ratio under hydrostatic pressure. The  $\alpha$  and  $\beta$  angle and the  $c/a$  or  $a/b$  correspond to similar quantities with different nomenclature because of the different orientation of the unit cells. The transitions from the  $P\bar{1}$  to  $C2/c$  to the  $C2/m$  with I-CDW2 to  $C2/m$  without CDW are indicated by dashed lines. **b** Pressure dependence of the interlayer As-As distance and the intralayer Ni-Ni distances. The Ni-Ni distances are named following the inset in Figure 6.3c. Most data is measured on sample 3, but also points from sample 1 and 2 are included. The points at 0.14 GPa (sample 2) and 7.52 GPa (sample 1) are measured at 104 K and 90 K, respectively.

I-CDW1'. Whilst they share the same wavevector and therefore are probably intrinsically connected to each other, the I-CDW1 and I-CDW1' are distinct in their form factors. First, the I-CDW1' is at least an order of magnitude weaker in intensity, as best seen in the linecuts. Second, the I-CDW1' is exclusively visible in parts of the reciprocal space in which the superstructure peaks of I-CDW1 are extinguished. More precisely, in contrast to the I-CDW1, the I-CDW1' is observed in the  $(h k 0)$ -plane and around forbidden Bragg reflections. The I-CDW1' is no longer detectable at a pressure of 10 GPa, but other "diagonal" peaks are visible instead. This is discussed more when the isobar at 10 GPa is considered in Section 6.3.3.

At the highest investigated pressure of 12.13 GPa, in the monoclinic  $\text{I}b$  phase, all superstructures or CDWs are lost and only the Bragg peaks remain in the reciprocal space maps. Also in the linecuts in Figure 6.4f the superstructure peaks of I-CDW1' and I-CDW2 are lost.

### 6.3.2. Isotherm at 94 K

In the isotherm at 94 K the pressure dependence of the low temperature triclinic phase can be studied. In agreement with the case at ambient pressure, at the loading pressure a triclinic  $P\bar{1}$  structure accompanied by a C-CDW with wavevector  $q_{\text{C-CDW1}} = (\pm 1/3 \ 0 \ \mp 1/3), (0 \ \pm 1/3 \ \mp 1/3)$  is observed. The C-CDW is denoted hereafter as C-CDW1. Under further compression, the  $c/a$ -ratio decreases while the  $\alpha$  and  $\beta$ -angles increase, as shown in Figure 6.5. The As-As and Ni-Ni distances show only a small variation. As expected from the structure, the Ni-Ni distances are different for all four bonds. At a pressure of  $\approx 2.5$  GPa all parameters show a jump or at least a kink. The jump is most pronounced in the  $c/a$  ratio and the Ni-Ni distances. This is an indication of a structural phase transition that is likely of first-order. At this pressure, the C-CDW1 is lost (see also Figure 6.6) and a new C-CDW

with wavevector  $q_{\text{C-CDW2}} = (\pm 1/2 \ 0 \ \mp 1/2), (0 \ \pm 1/2 \ \mp 1/2)$  appears (now called C-CDW2). The structural refinement reveals that the structure has a monoclinic symmetry. The refinement could be performed on the doubled unit cell, including the superstructure peaks, due to the higher cell symmetry and the high intensity of the commensurate superstructure peaks. This reveals a  $C2/c$  symmetry for the structure in the doubled unit cell. This new structure will now be referred to as monoclinic I. In this context the C-CDW2 is fully included in the refined structure and only denoted as such in analogy to the other structure in which due to incommensurability or lower cell symmetry the structure cannot be refined together with the superstructure.

In the monoclinic I structure, three inequivalent Ni-Ni bonds exist from which  $d_1$  is significantly larger than the other three. This results in a more complex change of the atomic positions, leading to two zigzag chains. However, dissimilar to the case at high temperature and higher pressure in the monoclinic II phase, two adjacent chains are shifted towards each other along the zigzag direction. More details about the structures are discussed in Section 6.3.4.

On further increasing pressure, the  $a/b$ -ratio (a comparable quantity to the  $c/a$  ratio in the triclinic cell) and the monoclinic  $\beta$  angle decrease and increase further, respectively. While the Ni-Ni distances show only small variations, the As-As distance shows a pronounced decrease. At just above 10 GPa, a second discontinuity is observed in all parameters. A closer look at the As-As distance and the diffraction patterns shows that there are actually two transitions, one at 10 GPa to the  $C2/m$  structure with a weak and distorted I-CDW2, and at only slightly higher pressure to the “collapsed”  $C2/m$  without any CDWs. The discontinuity indicates that the transition from the  $C2/c$  phase to the  $C2/m$  is also of first-order. At this transition, the “collapse” of the As-As distance is even more pronounced than at high temperatures.

Similarly to the case at 140 K, for the compression at 94 K there are pronounced changes in the CDWs. ( $h \ 2 \ l$ ) reciprocal space maps showing the different superstructures together with linecuts through the superstructure peaks are shown in Figure 6.6. In addition to the C-CDW1, the reciprocal space maps at 2.11 GPa show the numerous twins that are observed which are present in the triclinic phase. Contrary to the case at 140 K, no change in the wavevector is observed, proving that the CDW is commensurate. At the transition to the  $C2/c$  phase, the C-CDW1 is exchanged with C-CDW2. However, there is a coexistence between the phases (e.g. at 3.75 GPa), where a weak signal from the C-CDW1 is present. This supports the conclusion that the transition is of first-order. At a higher pressure of 5.79 GPa the C-CDW2 is still present, but with a higher intensity of the superstructure peaks along one direction. In the linecuts, the C-CDW2 peaks along the  $[1 \ 0 \ 1]$ -direction only slightly weaken, while the peaks along the  $[1 \ 0 \ \bar{1}]$ -direction are suppressed. Then, at higher pressures, with an intermediate transition to the I-CDW2, all superstructure peaks vanish and the linecuts show only a flat background (except for the measurement artifact visible in the  $[1 \ 0 \ 1]$ -cut).

### 6.3.3. Isobars and temperature dependence of the phases

After determining all the phases in the HP phase diagram of  $\text{BaNi}_2\text{As}_2$ , we now focus on the temperature dependence of these phases to finally construct the complete phase diagram in Section 6.3.6. In total five different isobars at  $\approx 2.2$  GPa, 4 GPa, 7.6 GPa, 10 GPa and 12 GPa were investigated. Similarly to the previous sections, we will first discuss the structural changes. The temperature dependence of the different isobars are shown in Figure 6.7. For comparison, the lattice parameters are given in the orthorhombic setting.

Starting with the isobar at 2.2 GPa, the lattice parameters show only a marginal change down to 115 K. At this temperature, the  $a$  and  $b$  lattice parameters first become significantly different, before

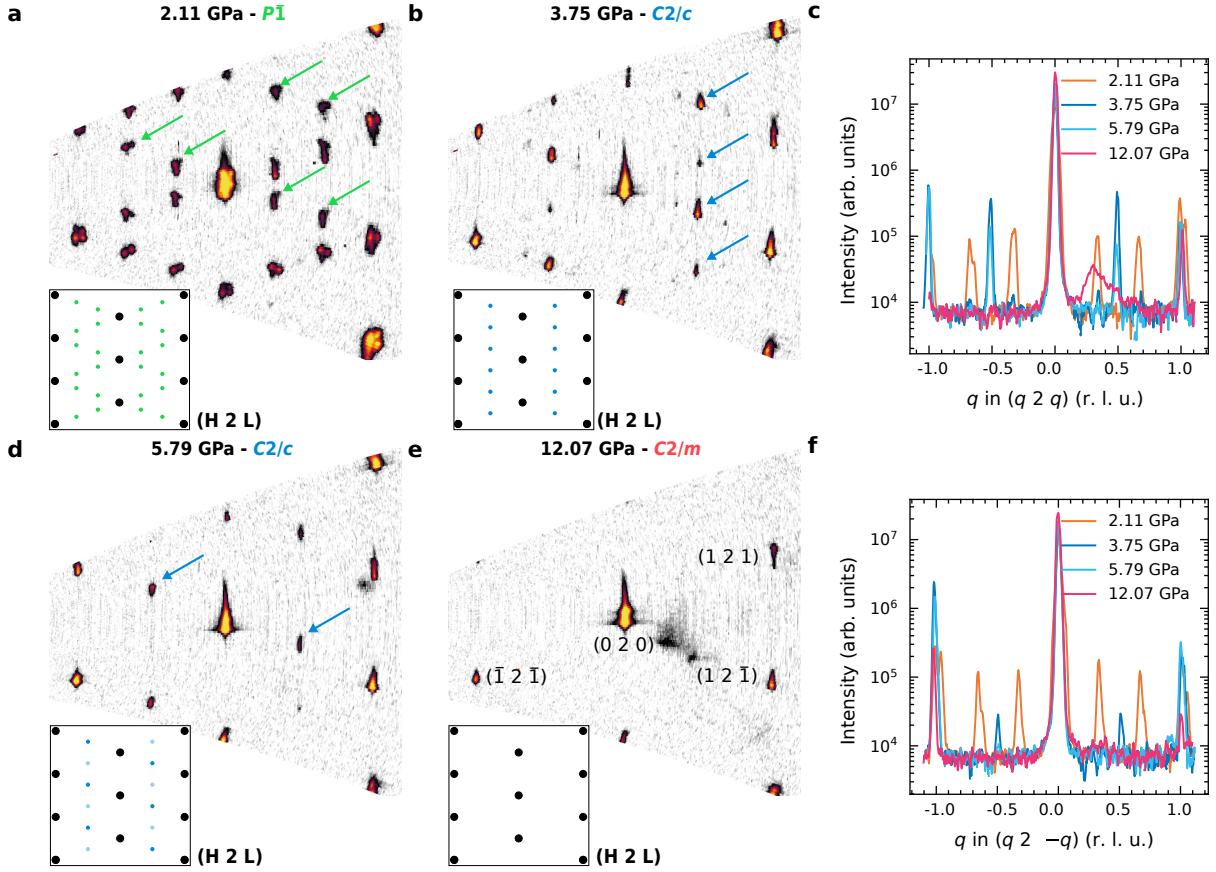


**Figure 6.6.: Reciprocal space maps and line cuts at 94 K.** **a-b, d-e** Reconstructed  $(h\ 2\ l)$  reciprocal space maps showing Bragg peaks and the superstructure peaks at **a** 2.11 GPa, **b** 3.75 GPa, **d** 5.79 GPa and **e** 12.07 GPa at 94 K. A sketch of a larger part of the reciprocal space indicates the arrangement of the superstructure peaks. The superstructure peaks are highlighted with green (C-CDW1) and blue (C-CDW2) arrows. **c, f** Linecuts along the  $[1\ 0\ 1]$  and  $[1\ 0\ \bar{1}]$ -direction through the C-CDW positions for the data shown in **a-b** and **d-e**. All data was measured on sample 3 at 94 K.

all lattice parameters show a jump. In agreement with the two isotherms, the structural refinement reveals a (first-order) structural phase transition from  $Immm$  to  $P\bar{1}$ , with coexistence at both 120 K and 115 K. Therefore, the sample is predominantly orthorhombic at 120 K and mainly triclinic at 115 K. Interestingly, this indicates that the structural phase transition is only marginally suppressed before the triclinic phase disappears.

For the isotherm at 4 GPa, data were also taken at higher temperatures and therefore in the tetragonal phase. On cooling, the  $c$  parameter slightly increases, while the  $a$  and  $b$  lattice parameters slightly shrink. Below  $\approx 140$  K the  $a$  and  $b$  lattice parameters become dissimilar and the structure changes to  $Immm$ , along with the appearance of the I-CDW1 peaks. Between 120 K and 110 K, all lattice parameters show a jump indicating a first-order phase transition to the low-temperature  $C2/c$  phase.

For the isobars at 7.6 GPa and 10.0 GPa, the structural transitions are similar, but with different temperatures. At high temperatures, the structure is still tetragonal and similar to lower pressures, the  $c$  parameter slightly increases while the  $a$  and  $b$  lattice parameters slightly shrink. For 7.6 GPa, the lattice parameters show a subtle kink just below 170 K and the structural refinement reveals the  $C2/m$  symmetry of the monoclinic  $Ila$  structure. At even lower temperatures of 120 K (7.6 GPa) and 31 K (10 GPa), the lattice parameters show a similar jump to the one observed at lower pressures and the best refinement is obtained with the monoclinic  $I$  structure. The jump and observed coexistence indicates

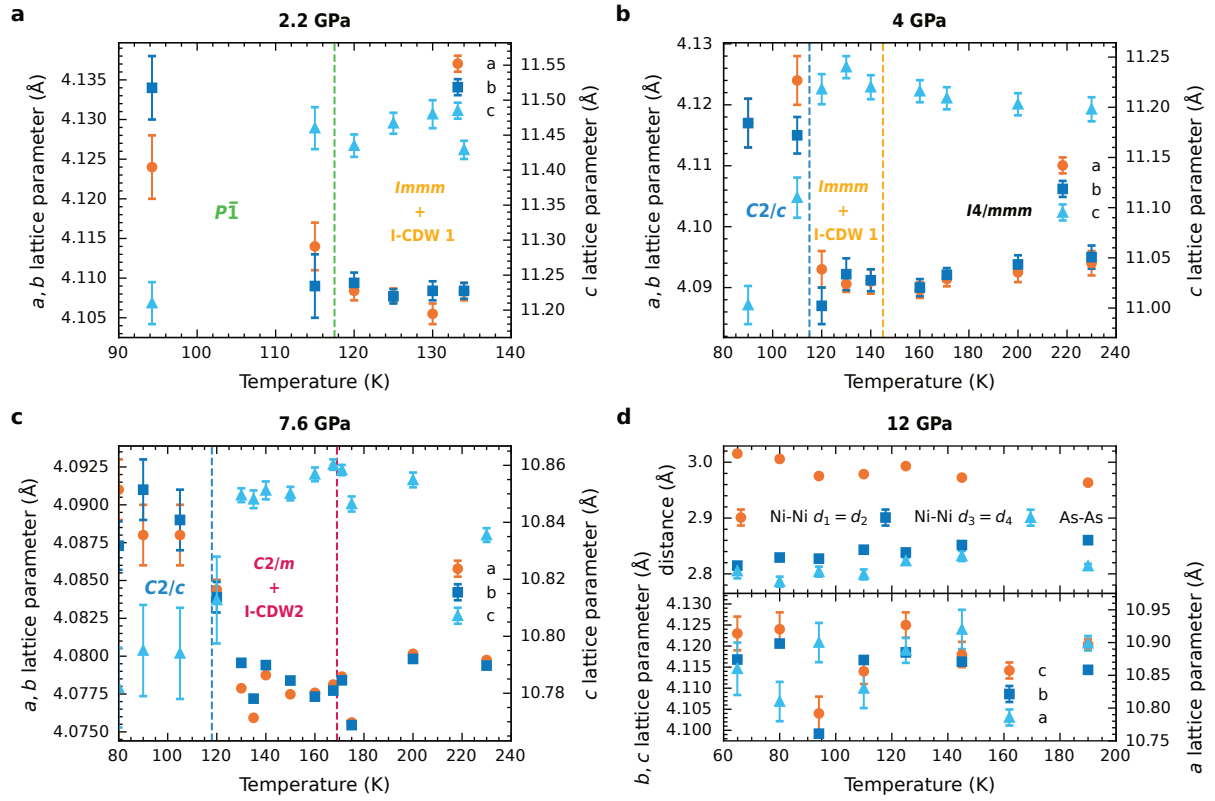


**Figure 6.7.: Lattice parameters and structural parameters for the isobars at 2.2, 4, 7.6 and 12 GPa.** a-d Temperature dependence of the  $a$ ,  $b$  and  $c$  lattice parameters a-c in the setting of the orthorhombic cell or d the monoclinic  $I4/mmm$  cell at a 2.2 GPa, b 4 GPa, c 7.6 GPa and d 12 GPa. In d in addition the interlayer As-As distance and the intralayer Ni-Ni distances are shown. The labeling of the Ni-Ni distances is according to the sketch in Figure 6.3c.

that the transition is also first-order in this case. The coexistence is particularly large for the isobar at 10 GPa, to the extent that a part of the sample is already in the monoclinic  $I$  phase at 65 K, but remnants of the monoclinic  $I4/mmm$  phase still exist at 31 K, .

The situation is different in the case of the 12 GPa isobar with the “collapsed” monoclinic  $I4/mmm$  structure. From the lowest temperature measured (65 K) to the highest temperature measured (190 K), the lattice parameters only change within the experimental uncertainty and there is no sign of a structural phase transition. Also the  $\beta$  angle, which shows a pronounced jump at the transition from  $C2/c$  to  $C2/m$ , does not change outside the bounds of the experimental uncertainty. In Figure 6.7d, the As-As interlayer and Ni-Ni intralayer distances are also shown. While the As-As distance doesn’t show a significant change, especially no sudden expansion or collapse, the two different sets of Ni-Ni distances approach each other. This means that, on heating, the zigzags become less separated and the structure approaches the case of 4 identical Ni-Ni distances, as observed in the tetragonal structure. However, the change is roughly 0.04 Å for each Ni-Ni distance and the total difference remains 0.1 Å at 190 K. So even at 190 K, the Ni-plane forms separated zigzags.

As for the isotherms, the structural changes are accompanied by changes in the CDWs or observed superstructures. Generally speaking, the changes in structure and the CDWs in the isotherms are identical to the ones observed in the isobars. More details are shown in the selected reciprocal space maps in Figure 6.8.

Starting from the 2.2 GPa isobar, the  $I$ -CDW1 is visible together with the  $Immm$  phase down to 115 K. However, as shown in the reciprocal space maps already at 120 K, indications of the triclinic phase

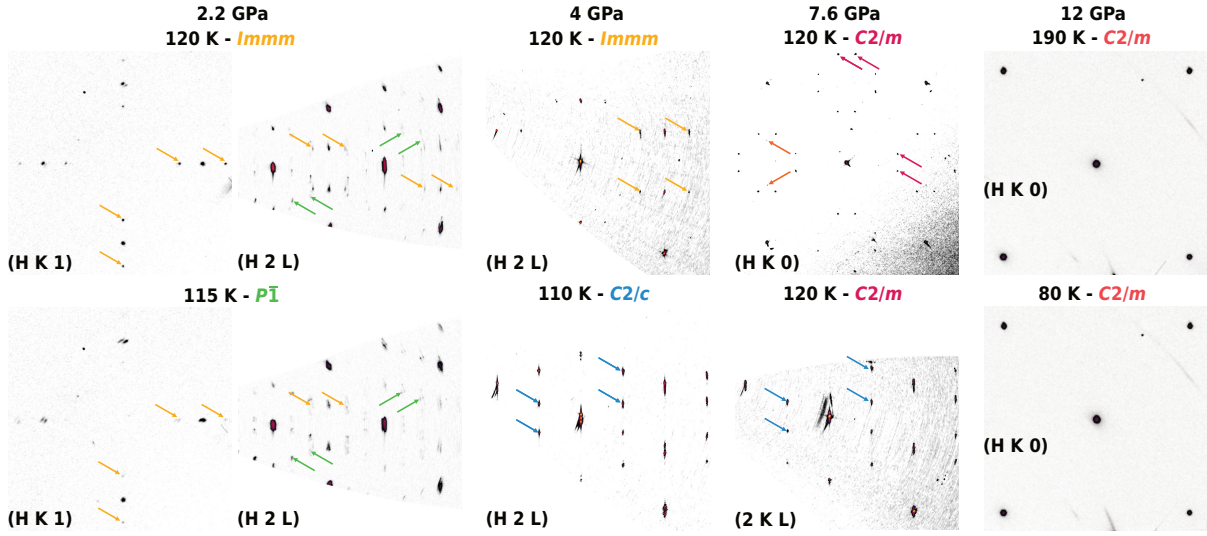


**Figure 6.8.:** Reciprocal space maps around the structural transitions for the isobars at 2.2, 4, 7.6 and 12 GPa.

Shown are reciprocal space maps close to the structural transition for the isobars at 2.2 GPa, 4 GPa and 7.6 GPa or at the low and high temperatures for the isobar at 12 GPa. The reciprocal space maps show a similar subset of reciprocal space as the maps in Figures 6.4 and 6.6. The light orange (I-CDW1), green (C-CDW1), blue (C-CDW2), dark orange (I-CDW1') and magenta (I-CDW2) arrows indicate superstructure peaks of the respective CDWs.

with the C-CDW1 are weakly visible and become dominate at 115 K. The situation is similar at 4 GPa. The I-CDW1 appears with the *Immm* phase around 140 K and is exchanged with the C-CDW2 at 110 K, when the monoclinic I phase has been entered. Unlike the transition at 2.2 GPa, no coexistence is detectable. At 7.6 GPa, the general behavior is similar but the transition temperature changes suddenly, similar to the structural transition. While the I-CDW1 was only visible below 140 K, the I-CDW2 and I-CDW1' appear around 167.5 K. The transition to the monoclinic II phase is altered as well. While at 4 GPa the sample was already completely in the monoclinic I phase, at 7.6 GPa the monoclinic IIa phase with I-CDW2 is dominant. Nonetheless, a coexistence with the monoclinic I and C-CDW2 is visible.

For the isobar at 10 GPa, the situation is more complicated. At 160 K, the highest temperature measured, the I-CDW2 is already visible with sharp and intense peaks. As mentioned in Section 6.3.1, the I-CDW1' is undetectable. Instead, weak but sharp peaks are visible on the diagonal of the octagon formed from the I-CDW2 superstructure peaks (indicated by black arrows in Figure 6.9a). In addition, half of the peaks of the octagon become more intense than the other half, showing a general distortion of the octagon. In  $(hk)$ -planes with higher  $l$ -component even more peaks are visible, but, due to the distortion and number of peaks, they are difficult to assign to a structure. On cooling, this asymmetry in peak intensity increases and the shape of the octagon is significantly distorted. At lower temperatures, the intensity of the I-CDW2 and the new peaks increases. At the lowest measured temperature, 31 K, the peaks of the I-CDW2 are still visible, but significantly weaker, strongly distorted and with a directional preference.

This increase in intensity and distortion is accompanied by a strong change in the wavevector, as shown in Figure 6.9b. The difference between the wavevector of the peaks at  $\approx (0.36 \ 0.1 \ 0)$  and  $\approx (0.36 \ -0.1 \ 0)$  or  $\approx (0.1 \ 0.36 \ 0)$  and  $\approx (-0.1 \ 0.36 \ 0)$  introduced by the “tilting”-like distortion cannot be included in the refinement of the wavevectors. Therefore, only the two wavevectors  $\approx (0.36 \ 0.1 \ 0)$  and  $\approx (0.1 \ 0.36 \ 0)$  are shown. These wavevectors change slightly with cooling from 160 K to 100 K. Below  $\approx 100$  K, the larger component of the wavevector increases strongly, while the smaller component decreases. This change especially for the larger component of the wavevector is much larger than the change is observed for the I-CDW1 by varying temperature or pressure, as shown, for example in Figure 6.3.



As discussed before for the structures, there is a large coexistence region between the I-CDW1 and C-CDW2. For example, the I-CDW2 is still visible at 31 K, but the C-CDW2 appears already in the reciprocal space maps in 65 K. Already at 80 K faint indications of C-CDW2 appear. Similar to the structure at 65 K, the  $C2/m$  with I-CDW2 is still dominant, while for 31 K the  $C2/c$  with C-CDW2 is dominant. Thus, between 7.6 and 10 GPa, the transition to the low-temperature  $C2/c$  phase with C-CDW2 broadened and the transition temperature is strongly suppressed.

It is difficult to disentangle whether these new additional peaks, the strong change of the wavevector and the asymmetry in intensity are related to the proximity to the stable monoclinic  $I1b$   $C2/m$  phase (without CDW), the large coexistence with the  $C2/c$  phase with C-CDW2 or whether it is an intrinsic behavior of the CDWs and structure at this pressure. Furthermore, the distortion leads to the disappearance and strong position change of some peaks. Along with the high number of peaks due to the overlap of at least two different superstructures, as well as experimental limitations due to the DAC, a precise evaluation of the superstructure in the low-temperature range is challenging and not reliable. While the additional peaks are already weakly visible at 160 K and therefore probably not related to the coexistence with C-CDW2, the most drastic changes in wavevector and intensity of I-CDW1 are in the coexistence region and could be related to, for example, internal strain caused by the coexistence.

#### 6.3.4. Connection of high pressure structures and atomic position changes

After determining all of the structures and their temperature dependence, a closer look at the structures gives further insight. To examine the changes in atomic positions in more detail, pictures of the tetragonal-like unit cells and Ni-As planes with all the parameters of the real structures from Table C.1 are shown in Figure 6.10. To illustrate the change to the atomic positions, arrows indicate the direction and amplitude (exaggerated by a factor of 10) of the atomic movements within the framework of the outer eight barium atoms. This also normalizes for the shrinkage of the unit cell. All changes are shown with respect to the tetragonal cell. Although the triclinic and monoclinic angles of the respective unit cells are quite different from  $90^\circ$ , the tilt of the tetragonal  $c$ -axis is less than  $1^\circ$  for all structures shown and does not affect this evaluation significantly.

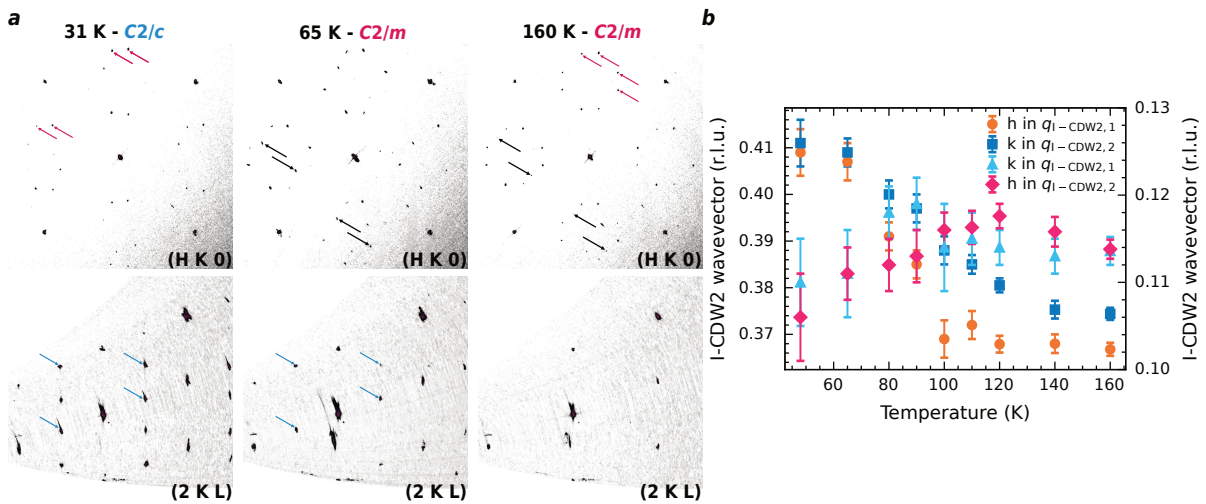


**Figure 6.9.: Reciprocal space maps and I-CDW2 wavevector at 10.14 GPa.** a  $(h k 0)$  and  $(2 k l)$  reciprocal space maps at 160 K, 65 K and 31 K. b Temperature dependence of the two I-CDW2 wavevectors. The superstructure peaks are indicated by magenta (I-CDW2), black (new I-CDW) and blue (C-CDW2) arrows.

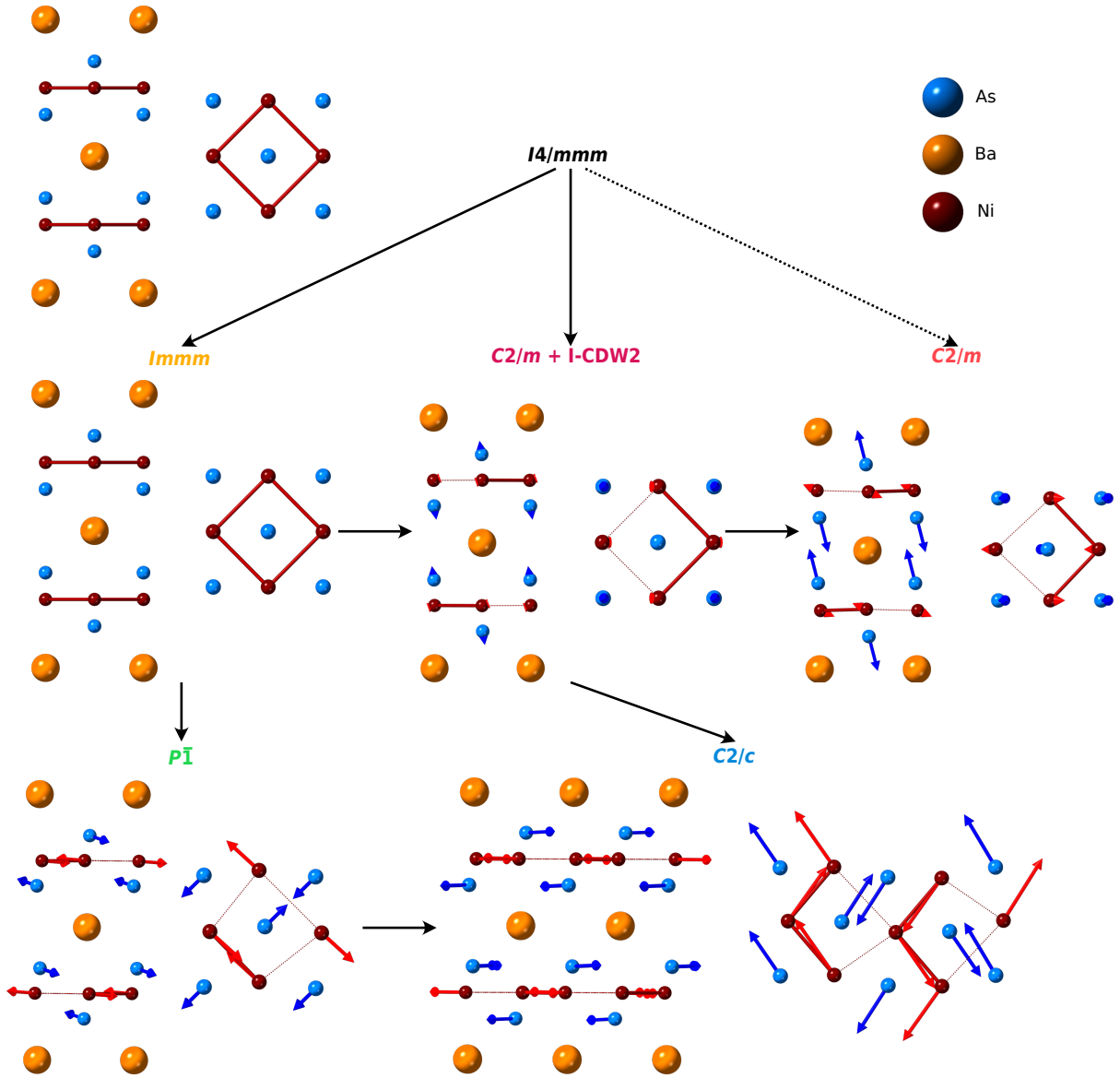


**Figure 6.10.: Change of the atomic positions for the different structures.** Sketch of the different experimentally observed structures in the HP phase diagram of pristine  $\text{BaNi}_2\text{As}_2$ . The shown structures and atomic positions based on the structural refinements with the parameters shown in Table C.1 in the appendix. The structures and Ni-As planes are shown to resemble the tetragonal unit cell. The real unit cells belonging to the structure are shown in Table C.1. The Ni-Ni bonds are shown with red lines. Full lines indicate shorter bonds and dotted lines longer bonds. Black arrows show the relationship between the structures. The direction and magnitude of position changes of the atoms with respect to the tetragonal structure are indicated by red (Ni) and blue (As) arrows. All changes are shown in the coordinate system created by the outer barium atoms to normalize for changes in the unit cell. Red arrows correspond to the Ni-atoms and blue arrows correspond to the As atoms. For visualization, the magnitude of the movement is exaggerated by a factor of 10. The changes in the orthorhombic  $Imm$  cell are too small to be seen and are therefore omitted.

Starting again to follow the isotherm at 140 K, we track the changes from  $Imm$  to  $C2/m$  with I-CDW2 and then to the stable  $C2/m$  structure. While additional freedom in atomic positions is introduced into the orthorhombic structure, all changes remain small as also the orthorhombicity is small. This makes the changes, for example of the Ni square and an introduced Ni buckling, too small to be visualized and no arrows are drawn. At higher pressures, in the monoclinic  $Ila$  phase ( $C2/m$  with I-CDW2), only small changes are visible. First, the As atoms separate from the Ni layer with larger out-of-plane and

smaller in-plane components. The As above the Ni plane moves in the opposite direction to the four lower As atoms. This also leads to an increased width of the Ni-As plane and makes the movement of the As atoms appear shear-like. Furthermore, the Ni-Ni bonds become unequal, forming zigzag chains by moving two Ni atoms in a positive direction (e.g. along the tetragonal  $b$ -axis) and the other two in the opposite direction. All motions in the lower Ni-As plane are opposite to those in the upper one due to symmetry, as is true for all the other structures observed. In general, the absolute changes to this structure remain small. At higher pressures, in the stable monoclinic IIb phase, the motions of the Ni and As atoms are similar but much larger. This leads to a very short As-As interlayer distance, which is reminiscent of the previously discussed cT phase. However, the width of the Ni-As plane is also greatly increased by this motion. In addition, the Ni-Ni zigzags become more separated from each other as the amplitude of the Ni motion increases.

At lower temperatures, along the 94 K isobar, we start in the triclinic  $P\bar{1}$  phase. In this phase, the top (above the Ni plane) As and bottom As atoms move closer to each other, decreasing the Ni-As plane width. Since the larger in-plane movement of the top and bottom As is in opposite directions, the As-As intraplane distances become unequal. The Ni movement stays mainly in-plane. Thereby, two Ni atoms move closer to each other, forming the Ni dimer, while the other two separate in the opposite direction. This leads to unequal Ni-Ni bonds and a strongly distorted Ni-As plane.

At higher pressures, in the monoclinic I phase ( $C2/c$ ), the Ni-As plane again becomes more ordered. Now all the motions of the atoms, with respect to the tetragonal cell, remain mainly within the Ni-As plane. Since the unit cell is doubled compared to the tetragonal unit cell (due to the C-CDW2), we have to consider two tetragonal cells. The Ni atoms move mainly in zigzags along the Ni-Ni bonds, resulting in the formation of separated zigzag chains. However, two adjacent chains are not aligned due to the opposing motion. This is different than the monoclinic II phase and results in three different Ni-Ni bond lengths. The component along the tetragonal  $b$  axis (to the right in Figure 6.10) points in the same direction for all As atoms above the Ni plane, while the As atoms below the Ni point in the opposite direction. This is not true for the component along the tetragonal  $a$  axis. Two adjacent chains of As atoms in the same plane (i.e. either above or below the Ni plane) have opposite components along the tetragonal  $a$  axis. The motion along the tetragonal  $a$  axis is greater than the motion along the tetragonal  $b$  axis. There is only a tiny out-of-plane component, so the As-As interlayer distance is not changed significantly. This results in a complex rearrangement of the Ni and As atoms as shown in Figure 6.10. At higher pressures, the structure undergoes a transition to the stable monoclinic IIb ( $C2/m$ ) with atomic positions as described above.

### 6.3.5. First principles calculations

As discussed in Chapter 4, particularly in Section 4.3.5, DFPT calculations reveal that the ambient pressure I-CDW is unconventional in nature, as it does not show nesting features in the JDOS or a broadened phonon linewidth  $\gamma_{\text{EPC}}$  which could show locally enhanced EPC. To investigate whether the CDWs under pressure, especially the newly observed CDWs, are also unconventional in nature, we next discuss DFPT calculations performed with the experimentally determined crystal structures. The calculations were performed with the lattice parameters and atomic positions determined from a structural refinement. To maintain force-free conditions, the atomic positions were relaxed. The results of the calculations for the structures for the structures observed along the 140 K isotherm are shown in Figure 6.11.

Starting from the orthorhombic phase at 1.56 GPa, the situation is mostly comparable to the behavior at ambient pressure. The phonon dispersion shows an instability close to the experimental I-CDW1



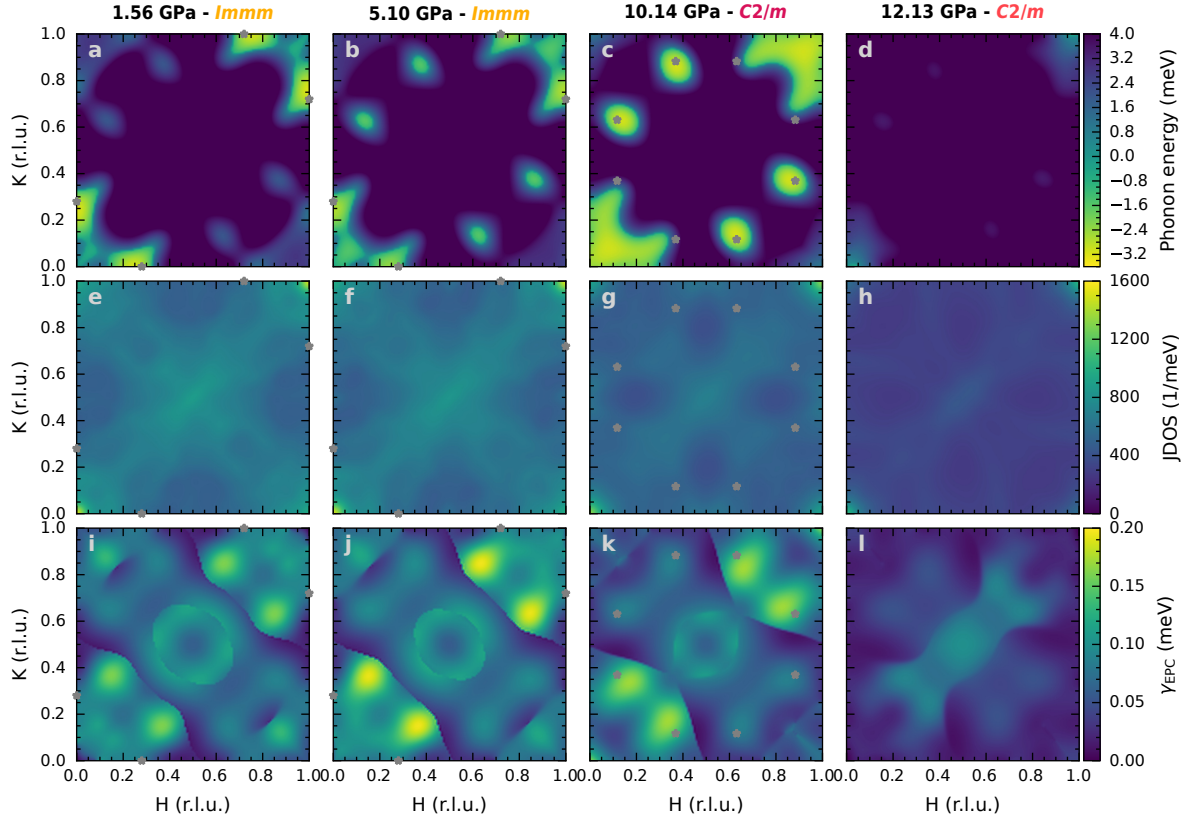


**Figure 6.11.:** Calculated lowest phonon mode energy, joint density of states and phonon linewidth for the experimental structures at 140 K. **a-d** ( $h k$ )-map of the DFPT calculated phonon energy of the lowest phonon branch for the 140 K experimentally observed crystal structures at **a** 1.56 GPa, **b** 5.10 GPa, **c** 10.14 GPa and **d** 12.13 GPa. Grey stars indicate the experimentally observed I-CDW positions. **e-h** ( $h k$ )-map of the calculated JDOS from the same DFPT calculations as in **a-d**. **i-l** ( $h k$ )-map of the calculated phonon linewidth  $\gamma_{\text{EPC}}$  due to EPC of the lowest phonon branch from the same DFPT calculations as in **a-d**.

wavevector, as can be seen by the negative energy due to imaginary eigenvalues in the DFPT calculations (see Figure 6.11a). It is noteworthy that the calculations already at this pressure show also a softened, but not unstable, mode close to the wavevector of the I-CDW2. However, IXS measurements at ambient pressure, where the softening in the calculations is also already visible, do not show a clear signature of an instability for a  $x = 0.1$  substituted sample. In diffuse scattering, however, signs are already visible, though less pronounced than in the calculations. For more details, see Appendix D.

There are no prominent features in the map of the JDOS, especially no peak close to the I-CDW1 wavevector, which would indicate a potential Peierls-like nesting in the Fermi surface. Furthermore, the phonon linewidth  $\gamma_{\text{EPC}}$  of the lowest lying phonon branch shows only weak and broad maxima coinciding with the I-CDW2 rather than the I-CDW1 wavevector. Accordingly, an ordering due to locally enhanced EPC is also unlikely. Recall that a peak in the linewidth can indicate such a locally enhanced EPC, in particular if the linewidth divided by the JDOS also shows this peak, as this indicates that the peak in the linewidth comes from the matrix element  $g_{kn, \vec{k}+\vec{q}m}^{\vec{q}\lambda}$ .

At slightly higher pressure of 5.10 GPa, the maps are, in the main, similar. The main difference is that, at this pressure, the calculations show an instability at the I-CDW2 position, even though it is not yet observed, and the instability at the I-CDW1 is now less pronounced. Nonetheless, the I-CDW1 is the most pronounced instability in the calculations. Similarly to the experiment, the wavevector of I-CDW1 slightly increases. In addition, the EPC at the I-CDW2 position is enhanced. At 10.14 GPa an

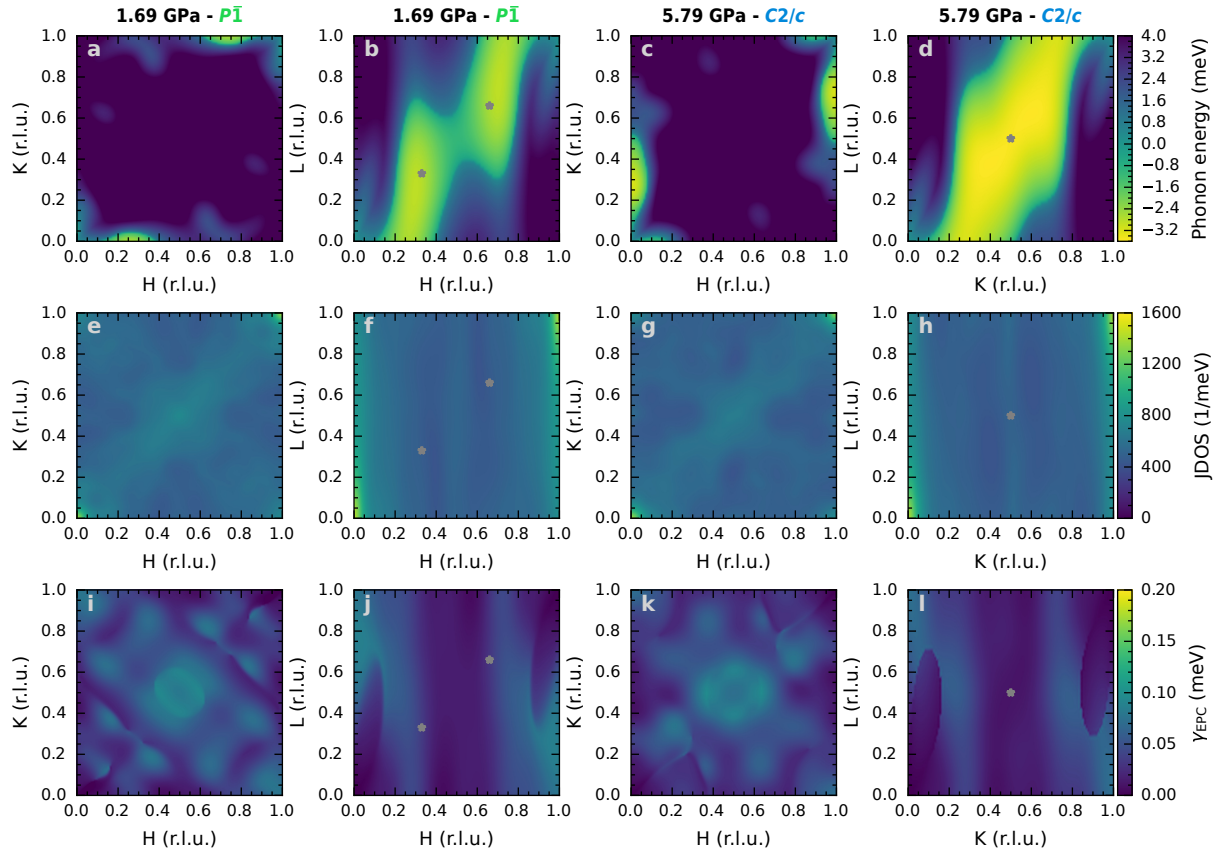


**Figure 6.12.:** Calculated lowest phonon mode energy, joint density of states and phonon linewidth for the experimental structures at 94 K. **a** ( $h k$ )-, **b** ( $h l$ )-, **c** ( $h k$ )- and **d** ( $k l$ )-maps of the DFPT calculated phonon energy of the lowest phonon branch for the at 94 K experimentally observed crystal structures at **a-b** 1.69 GPa and **c-d** 5.79 GPa. Grey stars indicate the experimentally observed C-CDW positions. **e-h** ( $h k$ )-map of the calculated JDOS from the same DFPT calculations as in **a-d**. **i-l** ( $h k$ )-map of the calculated phonon linewidth  $\gamma_{\text{EPC}}$  due to EPC of the lowest phonon branch from the same DFPT calculations as in **a-d**.

using the monoclinic  $I/a$   $C2/m$  structure, the instability at the I-CDW1 position disappears. Instead, the calculations show a strong instability close to the experimental I-CDW2 wavevectors. The map of the JDOS does not show any pronounced features, excluding a nesting origin of the I-CDW2. This is not the case for the linewidth, where there are maxima close to the I-CDW2 wavevector. However, in the positions where the instability in the phonon energy is more pronounced, the EPC is significantly weaker. Also overall the EPC stays below 0.18 meV, well below the value observed for e.g. the dichalcogenides [126, 129, 182] and is actually smaller than the value obtained for 5.1 GPa. In total, an ordering of I-CDW2 due to locally enhanced EPC cannot be excluded, but it is unlikely that the EPC alone leads to the I-CDW2 formation.

In the monoclinic  $I/b$  phase without I-CDW2 at 12.13 GPa, all soft modes or instabilities disappear. This confirms the experimental finding of the disappearance of all CDWs and that the monoclinic  $I/b$  phase is a stable structure. Furthermore, the broad peaks in the map of the phonon linewidth disappear and a basically featureless map remains. Similarly, the map showing the JDOS is reduced in magnitude and shows even fewer features.

The phonon energy and phonon linewidth of the lowest phonon branch and JDOS for the triclinic structure with C-CDW1 and for the monoclinic  $I$  structure with C-CDW2 are shown in Figure 6.12. The calculations for the monoclinic  $I$  structure at 5.79 GPa were performed using only the single and

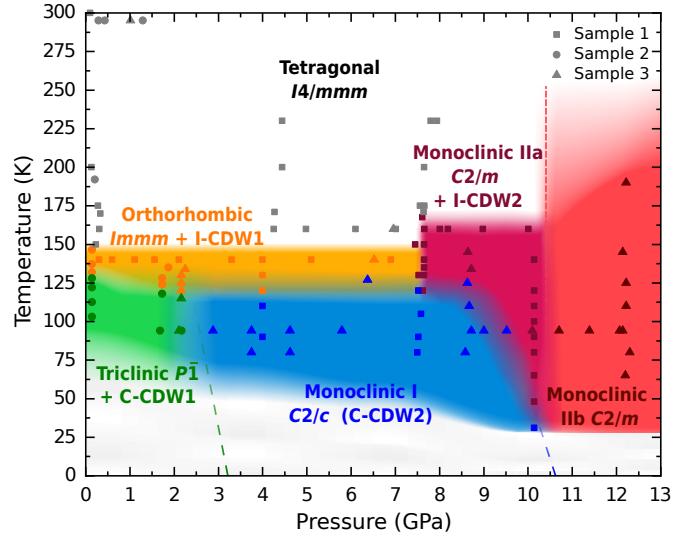


**Figure 6.13.: Pressure-temperature phase diagram of  $\text{BaNi}_2\text{As}_2$ .** The phase space of each structure and CDW is indicated by the background color. The markers indicate all measured points at which structural refinements were performed. The colors indicate the refined structure and the shape reflects on which sample the point was measured. With the exception of the monoclinic I structure the superstructures were not included in the refinement.

not the doubled unit cell (in this setting  $C2/m$  symmetry). For both cases the  $(h\ k)$ -maps do not show an instability, nesting feature in the JDOS or pronounced peaks in the linewidth. Note that the instabilities visible in the phonon energy are the instabilities emerging from the C-CDW1 and the C-CDW2 extending into the  $(h\ k)$  plane. In particular, they are not the I-CDW1 instability. For both structures, broad instabilities exist in the  $(h\ l)$ - and  $(k\ l)$ -maps, respectively. The instabilities are centered around the C-CDW1 and C-CDW2 wavevectors, in agreement with the experiment. However, in the JDOS and linewidth maps no features are visible. Accordingly, both the C-CDW1 and C-CDW2 seem also unconventional in nature. Note that the ellipses visible in the linewidth maps are artifacts from the calculations.

### 6.3.6. Phase diagram and summary

The findings in the Sections 6.3.1 to 6.3.3 can be summarized in the pressure-temperature phase diagram in Figure 6.13. For each of the more than 100 points in the phase diagram, HP XRD was performed and the structure was refined. The structural parameters of all observed structures are summarized in Table C.1 in the appendix. In summary, the phase diagram shows a strong dependence of both the structure and the CDWs on hydrostatic pressure, but with a distinct pressure dependence of the high and low-temperature structures. In the phase diagram two new major CDWs appear. The I-CDW2, and all instabilities in the same phase space as the I-CDW1', were not previously reported. For the second C-CDW, the C-CDW2, a C-CDW with same wavevector was only observed in the strontium substituted system and attributed to a triclinic phase [26]. Both C-CDW transitions coincide with a structural phase transition but to two different newly observed monoclinic phases. Only above  $\approx 10$  GPa are no CDWs observed. At this pressure, the structure is best described as a "collapsed" monoclinic phase. All monoclinic structures were not previously reported for this system.

## 6.4. Substitution effect on the high-pressure phases diagram

In this section, the HP results of sample 4, which is below the critical substitution level  $x_{\text{crit}} \approx 0.076$  at which the triclinic transition is completely suppressed, and sample 5, with  $x > x_{\text{crit}}$ , are discussed. In general, the samples exhibit the same phases and a largely comparable phase diagram to the non-substituted samples in Section 6.3. Therefore, in the subsequent sections, the discussion will follow the isotherms at 80 K (above the triclinic transition of sample 4) and 25 K (below the triclinic transition of sample 4). As for the other sections, all Miller indices are given in the tetragonal notation.

### 6.4.1. Isotherm at 80 K

Starting with the isotherm at 80 K the two samples show a difference in the structural refinement already at the loading pressure. Sample 4 is best described with the orthorhombic  $Immm$  structure. Despite the evidence for a local monoclinic or lower symmetry in the I-CDW state at the nickel position from Chapter 5, the changes in the average structure cannot be resolved in this experiment, as described in Section 6.3. Sample 5, however, is best described by a monoclinic  $C2/m$  structure, which is however significantly different from the monoclinic II  $C2/m$  structure discussed previously. This structure is hereafter called monoclinic III. The unit cell is  $45^\circ$  rotated, similar to the  $Fmmm$  cell in  $\text{BaFe}_2\text{As}_2$ , with an additional monoclinic tilt. As this structure is also found in the  $x \approx 0.1$  uniaxial pressure sample at nominal zero pressure (see Section 6.5) it is likely that this is also the ambient pressure structure of the so far unknown structural phase transition for  $x > x_{\text{crit}}$ , as evidenced by Meingast et al. [25]. More details about the structure and all the structural details are shown in Appendix C.2 in the appendix. At higher pressures, a reliable refinement is challenging and the assignment in the phase diagram is primarily done via the observed superstructure. Therefore, at higher pressure the actual structure could be different and more detailed analysis is needed.

The further changes for pressures above the loading pressure are shown for both samples in Figure 6.14. As for the pristine sample under application of pressure, all lattice parameters shrink for both samples. Around 7 GPa, there is a sudden change of the  $a$  and  $b$  lattice parameters. This indicates the transition to the monoclinic IIa phase, in line with the change of the structure and the I-CDW1 to I-CDW2 transition. However, other than the pristine case, the change of the  $a$  and  $b$  lattice parameters only flattens out and does not increase directly. An increase is only visible above 10 GPa (sample 4) and 12 GPa (sample 5).

In the details, though, there are differences. One difference is that the  $a$  and  $b$  lattice parameters (in the orthorhombic setting) significantly differ for sample 5 in the monoclinic IIa and b phases. Looking at the absolute values of the  $c$  lattice parameter shows a further difference. The pristine samples and sample 4 both reduce the lattice parameter from approximately 11.5 Å to 10 Å. For sample 5, however, the reduction of the  $c$  lattice parameter is smaller and only from 11.5 Å to 10.5 Å. Probably related to this, the loss of the I-CDW2, which is associated with the transition to the monoclinic IIb phase in the pristine sample, is shifted by at least 2 GPa to around 13 GPa for sample 5. The absolute value of  $c$  and the fact that there might be faint remnants of the I-CDW2 visible in the reciprocal space maps shown later in this section, may suggest that the monoclinic IIb phase is not (yet) reached at the highest pressure measured. For sample 4, the loss of the I-CDW2/monoclinic IIb phase is increased much less compared to the non-substituted case (to around 11.5 GPa). Nevertheless, a  $c$  lattice parameter of 10 Å is only reached at 13 GPa. Note that for both samples the I-CDW2 is lost with a  $c$  lattice parameter of  $\leq 10.5$  Å, such that the real of value  $c$  below which on the pristine  $\text{BaNi}_2\text{As}_2$  is in the monoclinic IIb phase probably lies between 10 Å to 10.5 Å. Due to the limited possibility of dense pressure sampling in HP XRD experiments, the point cannot be better defined. Interestingly, the shift of the transition from orthorhombic/monoclinic III to monoclinic IIa is small for both samples.

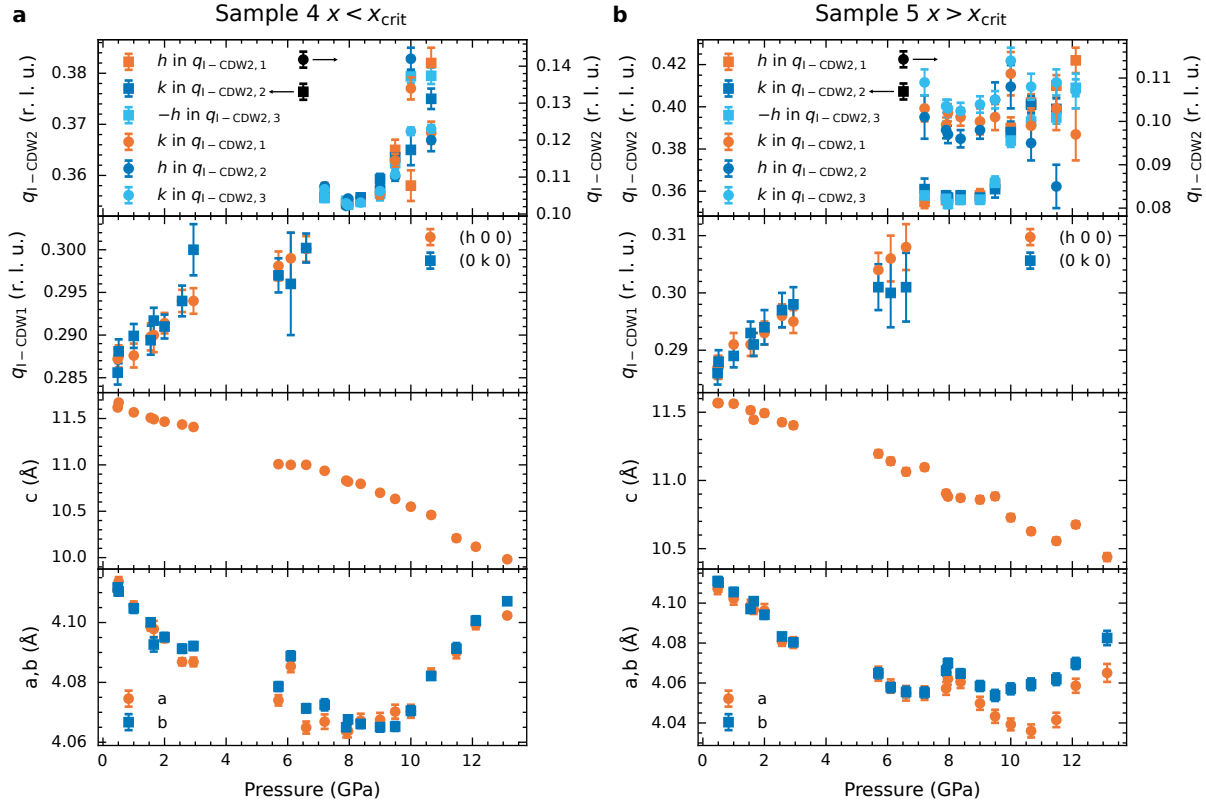


**Figure 6.14.: Lattice parameters and wavevectors at 80 K.** Lattice parameters, I-CDW1 and I-CDW2 wavevectors for **a** sample 4 and **b** sample 5 at 80 K. All lattice parameters and wavevectors are shown in the orthorhombic setting.

For the I-CDW1 wavevector, however, the situation is very similar for both samples and the pristine case. For increasing pressure, the wavevector increases with a slight flattening out just before the transition to I-CDW2 around 7 GPa. Only the absolute value increases for higher phosphorus content, as expected from the substitution dependence in Chapter 4. The absolute change of  $\approx 0.015$  r.l.u. from 0 GPa to 7 GPa is also similar for all three cases.

The changes with temperature for the I-CDW2 wavevector are much stronger. While the difference in wavevector between the two samples due to the substitution remains small, both samples show an enormous increase in the wavevector. Up to 10 GPa the change is similar for both samples, but sample 5 shows even greater changes, as the I-CDW2 is visible to higher pressures. These values must be taken with some caution, however, as the I-CDW2 is significantly distorted at higher pressures.

To investigate the CDWs in more detail, reciprocal space maps are shown in Figure 6.15. At this temperature, the measurements on the two samples exhibit very similar reciprocal space maps. At low pressure, the I-CDW1 is visible in both directions. The I-CDW1 remains visible up to around 7 GPa, after which the I-CDW2 appears. For sample 5, however, slightly higher pressures are needed. At 7.2 GPa, sample 4 already shows strong I-CDW2 peaks while sample 5 seems to be at the edge of the transition and mainly shows I-CDW1 peaks. Nonetheless, sample 5 also exhibits peaks from I-CDW2. Despite this, sample 4 also shows weak signatures of the I-CDW1. Note that such a coexistence of I-CDW1 and I-CDW2 was not observed for pristine samples, but it is difficult to say if this is intrinsic or only due to the limited pressure sampling. Similar to the non-substituted samples, I-CDW1' appears.

At the next highest pressure of 10.66 GPa, both samples show a strong but already distorted I-CDW2. Similarly to the unsubstituted case, sample 5 also shows additional peaks lying on the diagonal. As

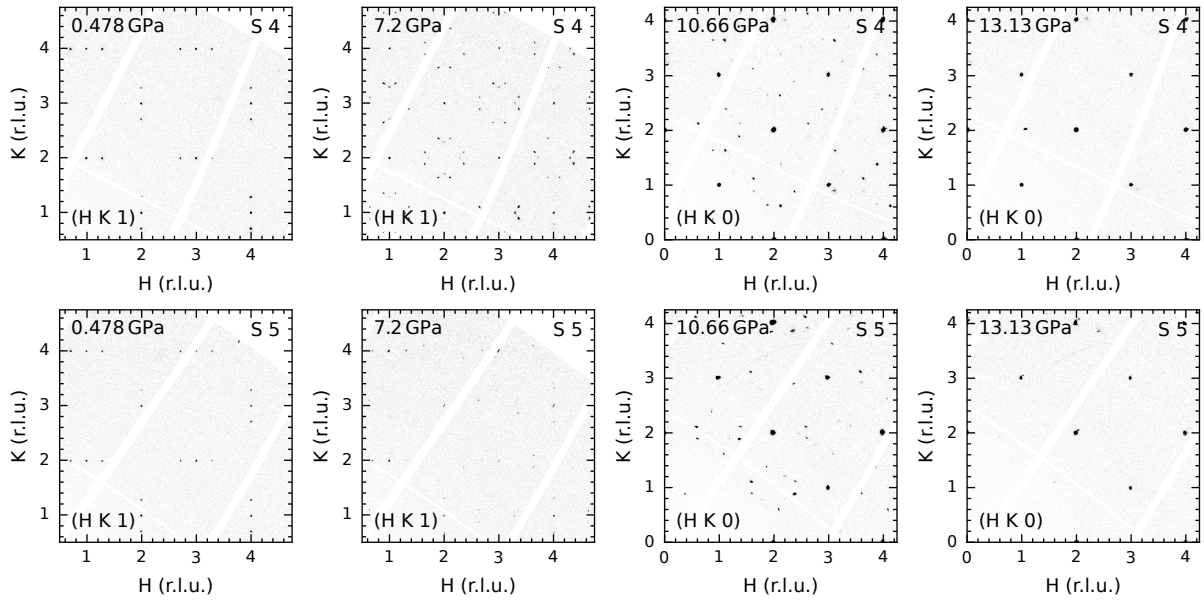


**Figure 6.15.: Reciprocal space maps for different pressures at 80 K.** ( $h k l$ ) reciprocal space maps at 0.478 GPa, 7.2 GPa, 10.66 GPa and 13.13 GPa for sample 4 and sample 5 showing the I-CDW1, I-CDW2 and absence of any CDW.

this sample doesn't exhibit the low temperature phases, as discussed in the next section, one can rule out that their appearance is related to the low temperature  $C2/c$  phase. In addition, this pressure is at least 2 GPa smaller than that required to lose the I-CDW2, therefore it is also unlikely that it is purely related to the proximity to the stable monoclinic  $Ib$  phase. This then suggests that also these peaks are an intrinsic instability of the system.

Finally, at the highest pressure measured, 13.13 GPa, the I-CDW2 has disappeared. Only for sample 5, there may be faint single peaks remaining, suggesting that a slightly higher pressure would be needed to fully suppress the I-CDW2 and reach the fully stable phase. This is in line with the results above, that the transition for sample 5 is shifted to higher pressures.

The CDWs, especially I-CDW1, can be evaluated further by performing linecuts and looking at the intensities of the peaks. The results show a general decrease in intensity on approaching the transition to the I-CDW2. However, the peaks along the  $h$  and  $k$  direction not necessarily follow the same trend. More details are discussed, along with the linecuts, in Appendix C.3 in the appendix.

#### 6.4.2. Isotherm at 25 K

After discussing the high temperature phases, we now switch to the isotherm at 25 K for which sample 4 exhibits the low temperature triclinic structure at the loading pressure. In contrast, sample 5 doesn't display any sign of the triclinic phase. This makes the isotherm different from the one at 80 K, where both samples mostly showed the same phases.

Therefore, the lattice parameters in Figure 6.16 also show differences. While for sample 5,  $a$  and  $b$  are rather similar, sample 4 shows a large variation and generally more scatter of the lattice parameters. However, both follow the same trend, with a decrease of all lattice parameters up to 12 GPa followed by a drop of the  $c$  lattice parameter to around 10 Å and an increase in the  $a$  and  $b$  lattice parameters.



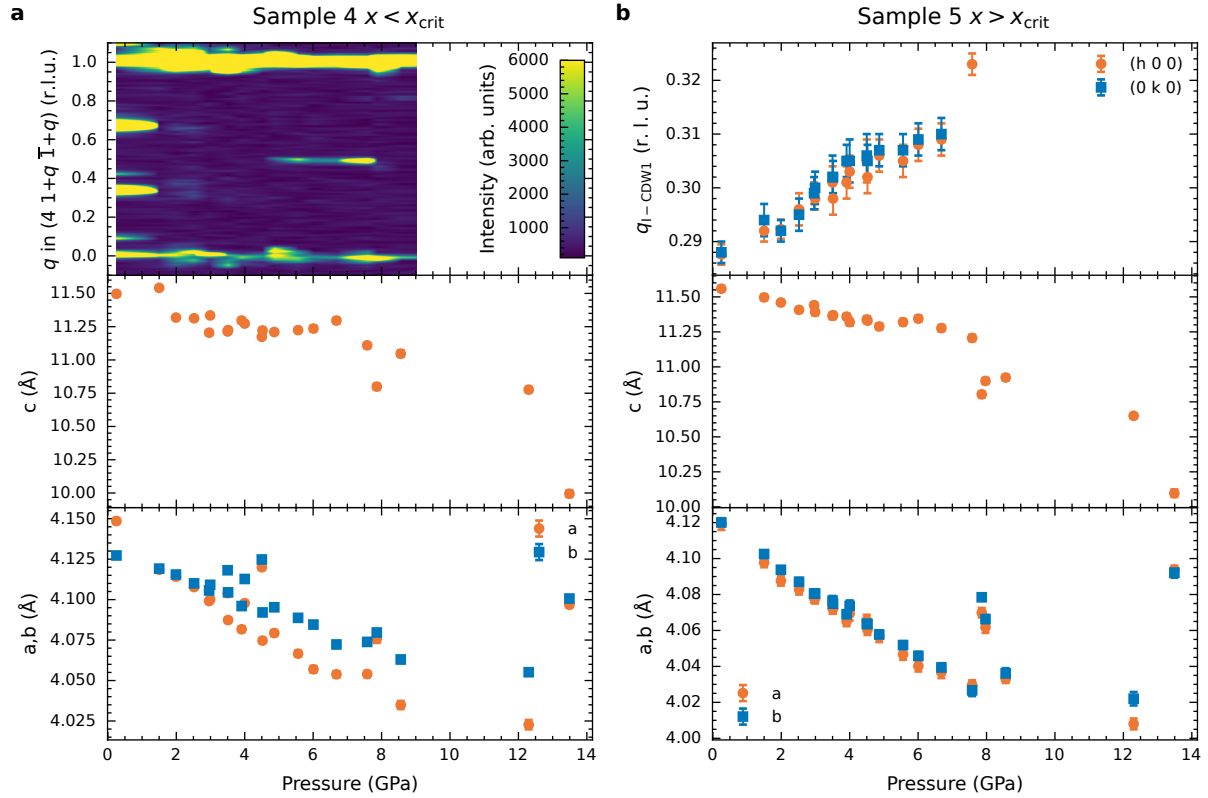


**Figure 6.16.: Lattice parameters, CDW intensity map wavevectors at 25 K. a** Lattice parameters and intensity map showing the C-CDW intensities for different pressures for sample 4 at 25 K. **b** Lattice parameters, I-CDW1 wavevectors of sample 5 at 80 K. All lattice parameters and wavevectors are shown in the orthorhombic setting.

When considering the full details, however, there are differences between the samples. Sample 4 shows a massive coexistence of the triclinic and orthorhombic phases, except for the first point. At around 4 GPa, the first anomaly in the lattice parameters is visible. From this pressure upwards, the monoclinic phase I is also visible, resulting in a coexistence of three different phases. This may explain the large variance in the lattice parameters. In addition, the phases show an enormous hysteresis which is best visible at a point measured on heating at 100 K and around 5 GPa, which still exhibits a coexistence of the orthorhombic, triclinic and monoclinic I phase. Therefore, it is important to keep in mind that the data was not measured on one single compression.

Only above 6 GPa, are the signs of the triclinic phase lost. Around 7.5 GPa a coexistence together with the I-CDW2 is visible before the C-CDW is lost around 8 GPa. This can also be seen in the intensity map in Figure 6.16. Here, first a strong C-CDW1 is visible, before it is significantly weakened because of the coexistence with the I-CDW1 and then, around 4 GPa, the C-CDW2 sets in before being lost again around 8 GPa. Finally, above 12 GPa to 13.5 GPa all CDWs are lost.

For sample 5, the situation is much easier. The sample shows only one anomaly, at around 8 GPa, at which the transition to the monoclinic IIa phase appears, and a drop at the last measured pressure, which indicates the transition to the monoclinic IIb phase. Also the I-CDW1 wavevector change is nearly identical to the one measured at 80 K. The only difference from the case at higher temperature or to the pristine samples occurs in the measurements around 8 GPa where  $a$  and  $b$  and the I-CDW1 wavevector are very dissimilar from the other pressures. This is probably related to an even greater number of appearing, which will be discussed now using the reciprocal space maps.

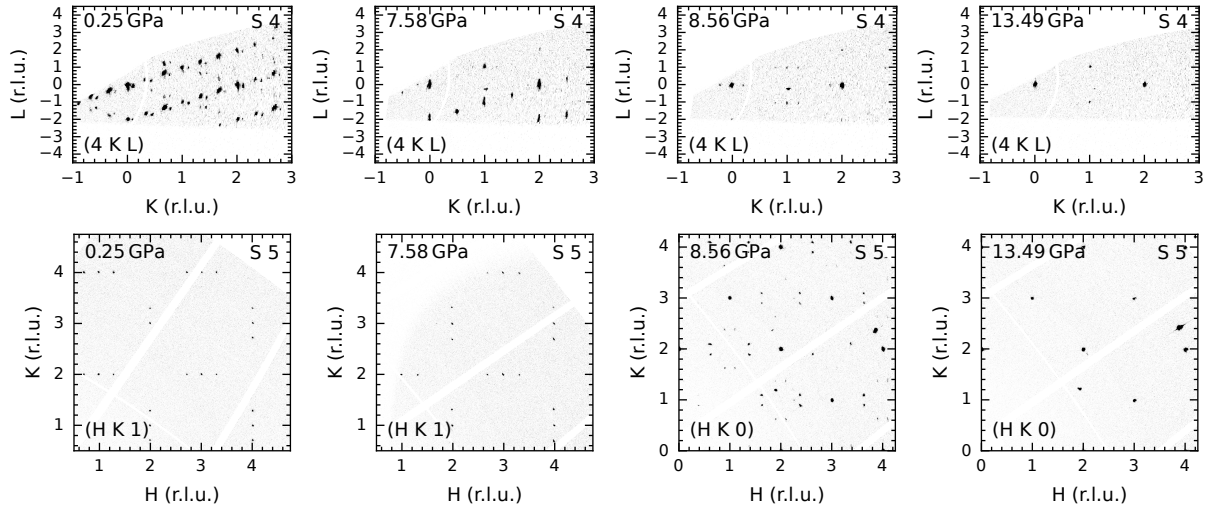


**Figure 6.17.: Reciprocal space maps for different pressures at 25 K.**  $(4\ k\ l)$  and  $(h\ k\ l)$  reciprocal space maps at 0.25 GPa, 7.58 GPa, 8.56 GPa and 13.49 GPa for sample 4 and sample 5, respectively.

In Figure 6.17, reciprocal space maps from measurements of samples 4 and 5 are shown. Starting with the  $(4\ k\ l)$  maps measured on sample 4 at the loading pressure, the triclinic structure with all the different twins and the peaks of C-CDW1 are clearly visible. At higher pressures of 7.58 GPa, strong peaks of C-CDW2 with faint peaks of I-CDW1 are visible, indicating the large coexistence discussed before. At a slightly higher pressure of 8.56 GPa in the  $(4\ k\ l)$  plane only I-CDW1 peaks are visible. Nevertheless, in other planes, strong peaks of I-CDW2 dominate, similar to the reciprocal space map of sample 5. Finally, at the highest pressure, no additional peaks are observed and the stable monoclinic IIb phase is formed.

For sample 5, the situation is very similar to that at higher temperature, even though the transitions are at slightly higher pressures. First only the I-CDW1 is detectable before, at 8.56 GPa, the I-CDW2 appears and at the highest pressure no additional peaks are visible.

The dataset measured at 7.58 GPa contrasts with the others, as even more peaks were measured. The corresponding reciprocal space maps are shown in Figure 6.18. Beside peaks resembling the I-CDW1, but with a suddenly increased wavevector, also peaks in the  $l = N + 1/2; N \in \mathbb{N}$  planes

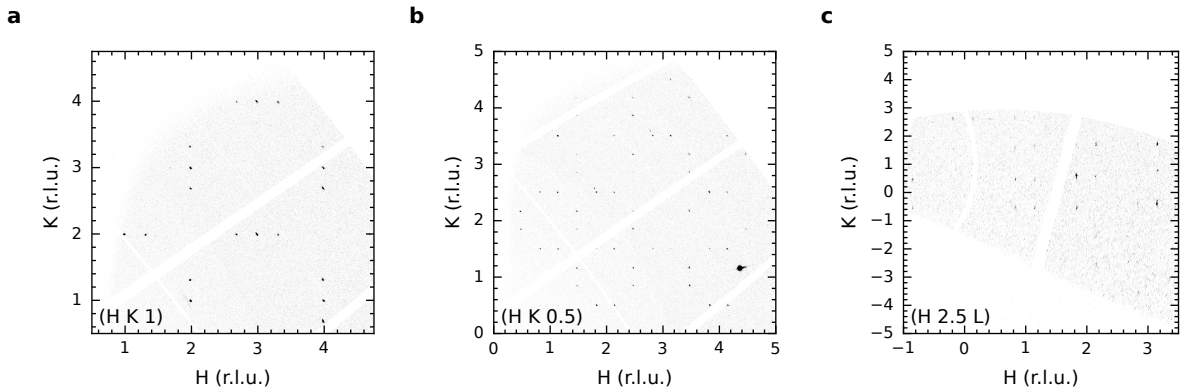


**Figure 6.18.: Reciprocal space maps with C-CDW3 at 25 K and 7.58 GPa.** **a**  $(h\ k\ 1)$ , **b**  $(h\ k\ 0.5)$  and **c**  $(h\ 2.5\ l)$  reciprocal space maps showing I-CDW1 and C-CDW3 at 25 K and 7.58 GPa. The measurements were performed on sample 5.



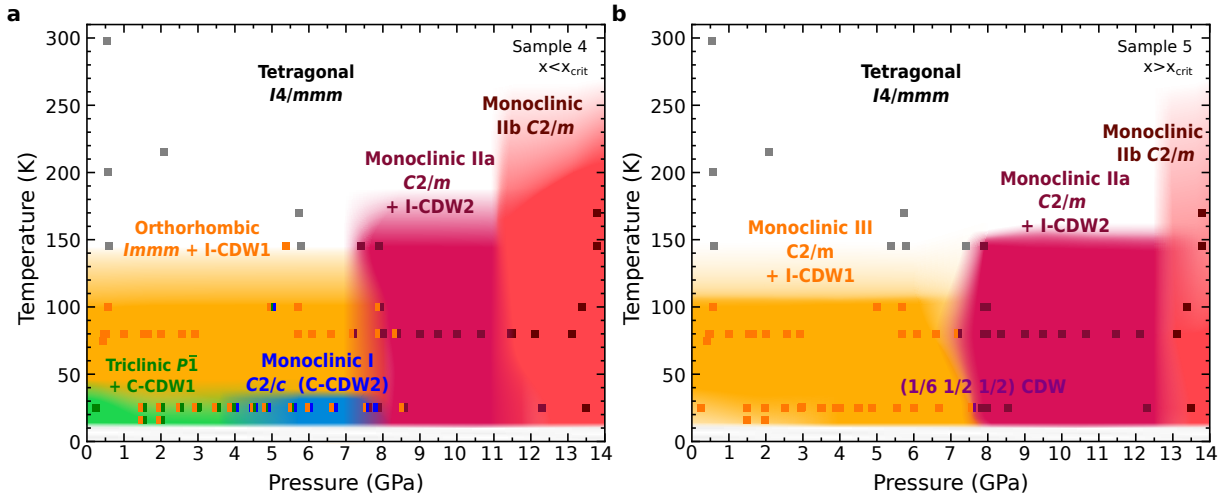


**Figure 6.19:** Pressure-temperature phase diagram of  $\text{BaNi}_2(\text{As}_{1-x}\text{P}_x)_2$  with  $x < x_{\text{crit}}$  and  $x > x_{\text{crit}}$ . Pressure-temperature phase diagram for **a** sample 4 with  $x < x_{\text{crit}}$  and **b** sample 5 with  $x > x_{\text{crit}}$ . The phase space of each structure and CDW is indicated by the background color. The markers indicate all measured  $p - T$  points. The color indicate the assigned structures. To indicate coexistence of several structures several colors are used for the point.

appear with a wavevector of  $q_{\text{C-CDW3}} = (\pm 1/6 \pm 1/2 \ 1/2); (\pm 1/2 \pm 1/6 \ 1/2)$  within experimental resolution. Accordingly, this instability appears to be commensurate and is now denoted as C-CDW3. The appearance of C-CDW3 might explain the anomaly in the lattice parameters. However, a structural assignment is not possible. Probably the monoclinic IIa and monoclinic III phase coexist, which makes a structural refinement impossible and could partly explain the anomaly in the lattice parameters. The new C-CDW3 is basically only visible at this  $p - T$  point. There are only extremely weak peaks at slightly higher pressures.

### 6.4.3. Phase diagrams and summary

The results from the HP XRD investigations on the phosphorus substituted samples 4 and 5 are summarized in the phase diagrams in Figure 6.19. These phase diagrams show clear similarities compared to the diagram of non-substituted  $\text{BaNi}_2\text{As}_2$  in Figure 6.13 in Section 6.3.6. In particular, the same phases are observed as for the pristine case, and, with some simplification, the phase diagrams could be described as a convolution of the phosphorus substitution phase diagram and the pressure-temperature phase diagram. Hence, the low temperature triclinic phase is suppressed with increased phosphorus content. It is noteworthy that the monoclinic I phase is suppressed in a similar fashion as the triclinic phase, indicating that they are closely tied and accordingly identically influenced by substitution.

Nonetheless, the monoclinic IIa and IIb structures are only marginally influenced by the phosphorus substitution, more similar to the orthorhombic/monoclinic III phase. But while the transition to the monoclinic IIa phase is only marginally shifted, the change of the transition pressure to the monoclinic IIb phase is more significant. The transition pressure from triclinic to monoclinic I seems to increase, even though it is difficult to pinpoint the transition exactly due to the huge coexistence range and hysteresis. At the same time, the transition pressure from the monoclinic I to monoclinic IIa is again only marginally changed.

Focusing on the CDWs, they are, similarly to the non-substituted case, tightly bound to the structural transitions. Interestingly, also with phosphorus substitution, the changes to the I-CDW1 under applied pressure are marginal.

To summarize, it appears that the majority of the effects of phosphorus substitution, chemical pressure, and external physical hydrostatic pressure are largely independent of each other in  $\text{BaNi}_2(\text{As}_{1-x}\text{P}_x)_2$ . This probably also explains the strong difference between the substitution and pressure phase diagrams.

### 6.5. Uniaxial pressure tuning on pure and phosphorus substituted $\text{BaNi}_2\text{As}_2$

After discussing the results from symmetry preserving hydrostatic pressure in the previous chapters, now we will break the original tetragonal symmetry by the application of uniaxial pressure in the  $a$  direction. This automatically breaks the fourfold rotational symmetry if it is not already broken by the structural phase transition to the I-CDW1 phase. Other than in the case of spontaneous symmetry breaking, the application of compressive pressure leads to a much higher orthorhombicity, as the orthorhombicity in  $\text{BaNi}_2(\text{As}_{1-x}\text{P}_x)_2$  always stays in the order of  $10^{-4}$ . As the orthorhombicity is so small in the orthorhombic phase, small strain values would already be enough to detwin the sample. In the case of a presumably monoclinic structure, as suggested from Chapter 5 and for  $x > x_{\text{crit}}$  as suggested from Section 6.4, detwinning is not so simple.

In this section, one non-substituted sample and one  $x = 0.1 > x_{\text{crit}}$  sample will be discussed. Additional data from a second non-substituted sample at lower temperatures is shown in the appendix in Appendix C.4. In this thesis, the engineering definition of strain will be used, in which compressive strain is negative.

Starting at (nominal) zero pressure measurements at low temperatures, the  $x = 0.1$  sample exhibits the same monoclinic III phase observed in the HP XRD experiments. Nonetheless, for better comparison with the tetragonal and orthorhombic structures, the wavevectors and lattice parameters are given in the orthorhombic setting.

Under application of uniaxial pressure, the lattice parameters change. While typically the evaluation of the strain relies on the nominal strain measured with the capacitance sensor of the uniaxial pressure cell, the XRD measurement allows in-situ measurement of the actual strain. Therefore, all strain values are the real strain values as calculated from

$$\epsilon_{xx} = \frac{a_x(\epsilon_{xx}) - a_x(0)}{a_x(0)} \quad (6.1)$$

with the strained  $a_x(\epsilon_{xx})$  and unstrained  $a_x(0)$   $a$ -lattice parameter.

From the response of the other lattice parameters, the Poisson's ratio can be calculated using

$$\nu_{ij} = -\frac{\epsilon_{jj}}{\epsilon_{ii}} = -\frac{\frac{\Delta a_i}{a_i}}{\frac{\Delta a_j}{a_j}} \quad (6.2)$$

with  $a_{i,j}$  being the corresponding lattice parameter. As the pressure is applied in the  $a$  or  $x$  direction, the Poisson's ratios  $\nu_{xy}$  and  $\nu_{xz}$  can be determined. As long as the Poisson's ratio does not change under applied pressure, the best method to determine the Poisson's ratio is a linear fit of the corresponding lattice parameter versus  $\epsilon_{xx}$ . Then the Poisson's ratio  $\nu_{ij}$  is given by

$$\nu_{xj} = -\frac{m_j}{c_j} \quad (6.3)$$

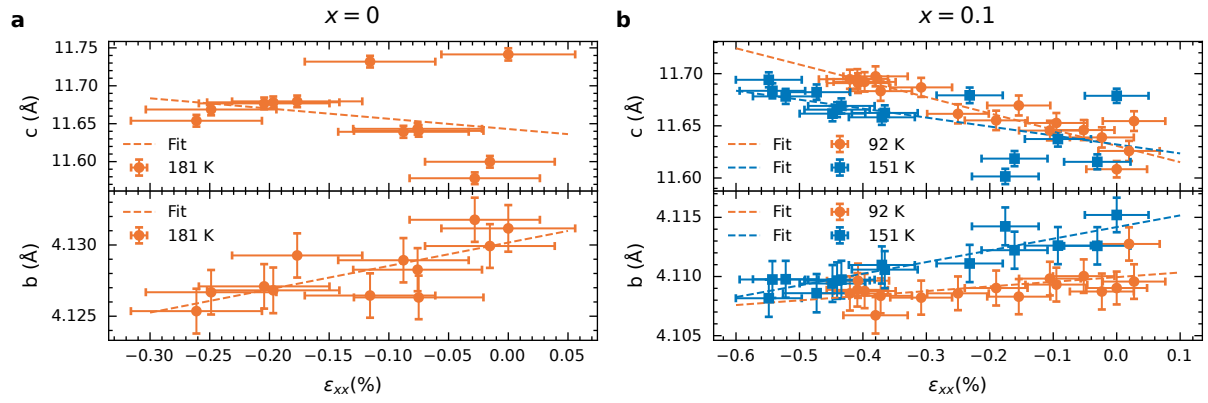


**Figure 6.20.:** Lattice parameters versus strain  $\epsilon_{xx}$ . **a**  $b$  and  $c$  lattice parameters versus strain  $\epsilon_{xx}$  for the pristine sample at 181 K and **b** for the  $x \approx 0.1$  sample at 151 K and 92 K.

with the slope of the linear  $m_j$  and the constant value of the linear  $c_j$ .

In Figure 6.20, the lattice parameters are shown. Already from the raw lattice parameters, a significantly different response of the  $b$  and  $c$  lattice parameters is visible. For all three cases, the  $b$  lattice parameter decreases, meaning that  $b$  gets smaller if one compresses  $a$ . This is already surprising, as this leads to a negative Poisson's ratio and typically the opposite would be expected.

For the  $c$  lattice parameter, as expected, an increase is observed. However, this parameter is larger and generally more noisy. The noise probably comes from the fact that the cutting during preparation of the samples leads to several spots along the  $c$  direction, probably due to the sliding of some planes, which make  $c$  less defined. This can be best seen in the reciprocal space maps in Figure C.7. The plane itself is not distorted and is well-defined.

All of the Poisson's ratios obtained from the uniaxial compression XRD experiments are summarized in Table 6.1. Besides this scattering experiment, the Poisson's ratios can also be calculated from the elastic constants. The determination of which elastic constants must be combined to obtain the right Poisson's ratio is not particularly difficult, but rather lengthy and tedious to do. Following the work from Ballato [183], the Poisson's ratio for a tetragonal symmetry are given by

$$\nu_{xy} = -\frac{s_{12}}{s_{11}} = -\frac{\frac{c_{33}}{c_{33}(c_{11}+c_{12})-2c_{13}^2} - \frac{c_{66}}{c_{66}(c_{11}+c_{12})-2c_{16}^2}}{\frac{c_{33}}{c_{33}(c_{11}+c_{12})-2c_{13}^2} + \frac{c_{66}}{c_{66}(c_{11}+c_{12})-2c_{16}^2}} \quad (6.4)$$

$$\nu_{xz} = -\frac{s_{13}}{s_{11}} = 2 \frac{\frac{c_{13}}{c_{33}(c_{11}+c_{12})-2c_{13}^2}}{\frac{c_{33}}{c_{33}(c_{11}+c_{12})-2c_{13}^2} + \frac{c_{66}}{c_{66}(c_{11}+c_{12})-2c_{16}^2}} \quad (6.5)$$

with  $s_{ij}$  being the individual components of the compliance tensor and  $c_{ij}$  the corresponding entries in the elasticity tensor. With the elastic constants, calculated as part of the DFPT calculations used in Chapter 4, the value of Poisson's ratios are  $\nu_{xy} = -0.2999$  and  $\nu_{xz} = 1.006$ .

**Table 6.1.:** Poisson's ratio extracted from the lattice parameter response under uniaxial compression and DFPT calculations.

	Experiment			DFT
$x$	0.0	0.1	0.1	0.0
$T$ in K	181	151	92	-
$\nu_{xy}$	-0.40(12)	-0.240(29)	-0.10(12)	-0.299
$\nu_{xz}$	1.2(13)	0.74(27)	1.34(15)	1.006

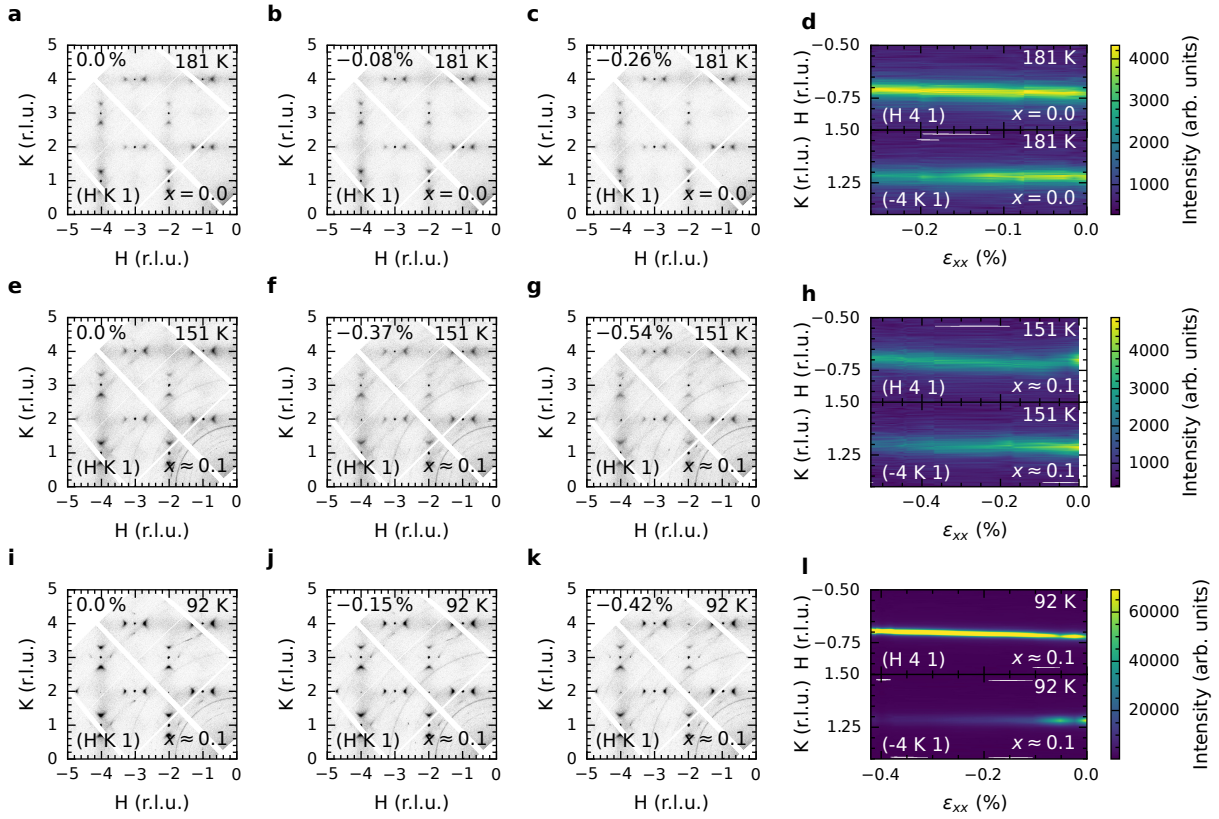


**Figure 6.21.: Reciprocal space maps and linecut for different compression values.**  $(h\ k\ 1)$  reciprocal space maps showing the I-CDW1 and the diffuse scattering surrounding it for **a-c**  $x = 0$  181 K, **e-g**  $x \approx 0.1$  151 K and  $x \approx 0.1$  92 K and different strain values. **d, h** and **l** Intensity maps of the intensities from linecuts through I-CDW1 in  $h$  and  $k$  direction versus  $\epsilon_{xx}$ .

The extracted Poisson's ratios from both experiment and the first-principles calculations show rather unusual absolute numbers. For a metal, a Poisson's ratio of about  $1/3$  is expected [183]. In this study, however, a value of around  $-0.25$  for  $\nu_{xy}$  and  $1$  for  $\nu_{xz}$  is observed, differing quite significantly from an "easy" metal. Especially, the  $\nu_{xz}$  is huge and at the same time  $\nu_{xy}$  is negative. Despite this, the experiment and theory show a good agreement.

There is also quite some change from these values for the different substitution levels and temperatures. While, due to the less well-defined  $c$  parameter, a discussion of the changes  $\nu_{xz}$  would probably be an over-interpretation of the data, the  $\nu_{xy}$  value should be more robust. The most prominent change is between the 151 K and 92 K data for the  $x \approx 0.1$  sample, where  $\nu_{xy}$  more than halves. Therefore, the change between  $x = 0$  and  $x \approx 0.1$  is still sizeable and greater than the error, but smaller than the temperature effect. At the same time, the difference itself could be only due to temperature, such that a more detailed study is needed.

Similar to the HP XRD measurements, the CDWs can also be investigated. Due to the lower background, as there is no diamond in the beam, even the diffuse scattering in the crystal is visible.  $(h\ k\ 1)$  maps showing the I-CDW1 at different strain values are presented in Figure 6.21. The diffuse scattering exhibits, similar to Chapter 4, a triangular shape and is not significantly altered by compression. The situation is different for the sharp and intense ordered peaks in the center of the diffuse cloud and in the orthogonal direction. The peaks in the  $k$ -direction (perpendicular to the applied pressure) lose intensity. On the other hand, the peaks along the  $h$  direction increase in intensity.

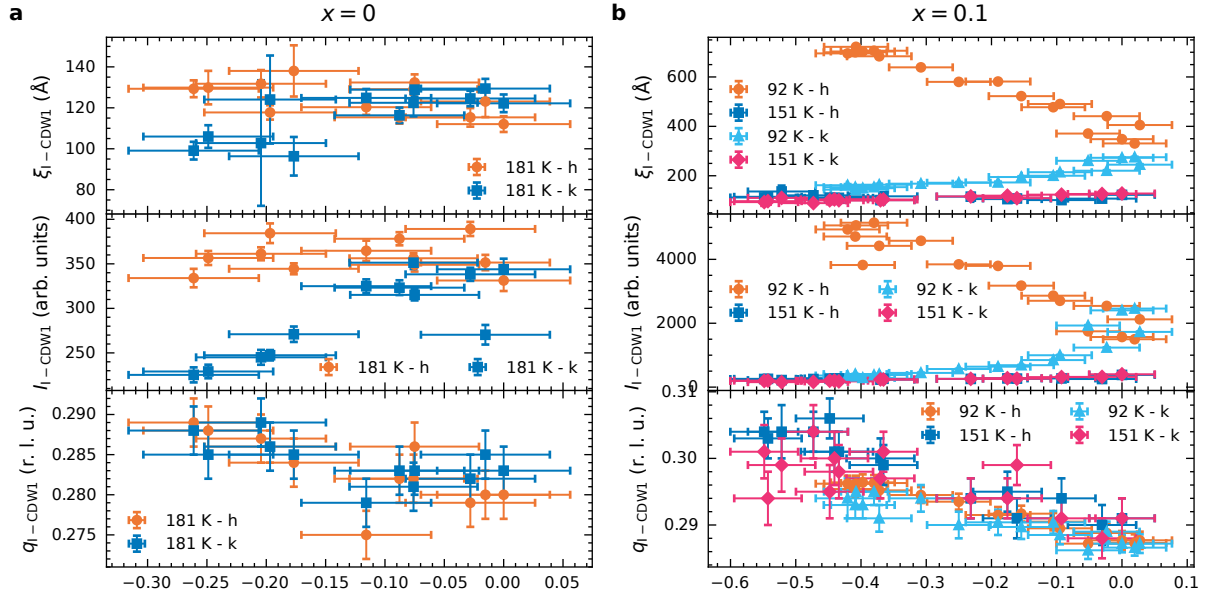


**Figure 6.22.:** I-CDW wavevector, intensity and correlation length in the  $a$  and  $b$  direction versus strain  $\epsilon_{xx}$ . I-CDW1 wavevector, correlation length and intensity versus strain  $\epsilon_{xx}$  **a** for the pristine sample at 181 K and **b** for the  $x \approx 0.1$  sample at 151 K and 92 K.

This can be seen better by performing linecuts through the I-CDW1 peaks in the  $h$  and  $k$  directions. From the intensity maps created from the linecuts and shown in Figure 6.21 for all three cases, a shift in the wavevector is visible. While there is a slight decrease in intensity for the  $x = 0$  and  $x \approx 0.1$  at 181 K and 151 K (above the ordering temperature) in the  $k$  direction, this is much more prominent for the case of an ordered CDW ( $x \approx 0.1$  92 K).

For the case of the ordered CDW for the  $x = 0.0$  samples, the situation is more complicated. For all samples that were measured in the ordered phase, under increasing strain a coexistence of the triclinic and orthorhombic phase was observed. It was not possible, however, at the achievable compression, to reach a fully triclinic sample. Due to the coexistence and the jump of the lattice parameters at the triclinic transition, the data and also a definition of a strain are not reliable. Exemplarily, one sample is shown and discussed in the appendix in Appendix C.4.

From fits to the peaks, the intensity can be quantified and also the correlation length in the  $a$  and  $b$  direction can be extracted. Together with the wavevector, the parameters are shown in Figure 6.22. All three cases have in common that the wavevector increases. Interestingly, the wavevectors in the  $h$  and  $k$  directions increase in a comparable manner. There is only a very slight tendency to increase less in the  $k$  direction, but as the error in the  $k$  direction increases due to the lower intensity, it stays basically within the experimental errors.

For the correlation length and intensity the situation is different. In the fluctuating I-CDW1 regime ( $x = 0$  181 K and  $x \approx 0.1$  151 K), the correlation length is around 100 Å and the changes are small. There is a trend of decorrelating/loss in intensity along  $k$ , but there is no significant increase in ordering in the  $h$  direction. Especially, it is not possible, within the achievable strain, to force the I-CDW1 from an unordered to an ordered state with a correlation length above 250 Å (see Chapter 4).

For the  $x \approx 0.1$  sample in the ordered CDW state, the changes are much more severe. For these measurements, the intensity, and correlation length more than doubles in the  $h$  direction, while along the  $k$  direction the intensity decreases and correlation length approaches the uncorrelated value

( $\leq 250$  Å) at higher temperatures. These changes are incompatible with a pure detwinning of an orthorhombic structure. First, the estimated orthorhombicity is in the order of  $10^4$  and accordingly a small strain would already be enough to detwin the sample. Second, in such a case, one would expect a transfer from the intensity from one twin to the other. But in this case, the increase in intensity is larger, and we also find a significant increase in the correlation length. As also the structural refinement suggests a monoclinic structure and a (full) detwinning by applied pressure in the  $a$  is not possible.

Considering the  $x = 0$  and  $x \approx 0.1$  samples, there is no significant difference in the fluctuating regime. In the ordered regime on the other hand, there is no comparable increase in order detected for the  $x = 0$  sample, but influences from the triclinic phase (see Appendix C.4).

## 6.6. Comparison of chemical, hydrostatic and uniaxial pressure and discussion

The results from the HP XRD experiments are best summed up by the obtained pressure-temperature phase diagrams shown in Section 6.3 and Section 6.4. Those diagrams highlight a qualitatively different pressure dependence between the low and high temperature phases. First, the triclinic phase is already suppressed after  $\approx 2.5$  GPa or  $\approx 4$  GPa, much earlier than the orthorhombic/monoclinic III phase, which survives up to  $\approx 7$  GPa. Both phases have in common that the transition temperature is not ( $Immm$ ) or only slightly ( $P\bar{1}$ ) altered.

This is similarly true for the monoclinic IIa and monoclinic I phase, which seem to be the descendants of the orthorhombic and triclinic phase, respectively. For example, they are comparably influenced by the phosphorus substitution and are also closer in the internal structure.

The complete pressure phase diagram itself is in strong contrast with the phase diagrams achieved with chemical substitution or “chemical pressure”. For all reported substituents – phosphorus [23, 25, 40], strontium [26, 41], cobalt [22, 42] and copper [43] – both the orthorhombic/I-CDW and triclinic/C-CDW phase are suppressed. A major difference between chemical substitution and hydrostatic pressure which could lead to this is the change of the lattice parameters.

Hydrostatic pressure, for most parts of the phase diagram, reduces all lattice parameters, whereas chemical substitution tends to have the opposite effect both in- and out-of-plane. Phosphorus and cobalt both compress the plane and increase the  $c$ -direction and efficiently suppress the triclinic phase [25, 42]. However, copper, which expands the plane and compresses the  $c$ -direction, also efficiently suppresses the triclinic phase [43]. Nevertheless, the changes to the  $c$  lattice parameter remain small. How the I-CDW behaves, or whether it actually exists with copper substitution, is not reported. Strontium substitution, however, is the least efficient in suppressing the triclinic phase. Strontium substitution mainly compresses the  $c$ -axis and only marginally compresses  $a$  up to the disappearance of the triclinic phase. Further, a C-CDW with the same wavevector as the C-CDW2 or doubling of the unit cell has been reported. However, the transition to this C-CDW was not associated with a structural phase transition to  $C2/c$  [26, 41]. The fact that a C-CDW with unit cell doubling and no or only relatively modest suppression of the triclinic phase is only observed for strontium substitution and hydrostatic pressure, the two external parameters which efficiently compress the  $c$ -axis, emphasizes the importance of the out-of-plane structural details in controlling the different phases in  $\text{BaNi}_2\text{As}_2$ . This is similar to the iron-based pnictides [184, 185].

This conclusion is in line with another recent work on  $\text{Ba}_{1-x}\text{Sr}_x\text{Ni}_2\text{As}_2$  and hydrostatic pressure that was conducted at a similar time as this thesis. The work from Collini et al. [186] on the pristine  $\text{BaNi}_2\text{As}_2$

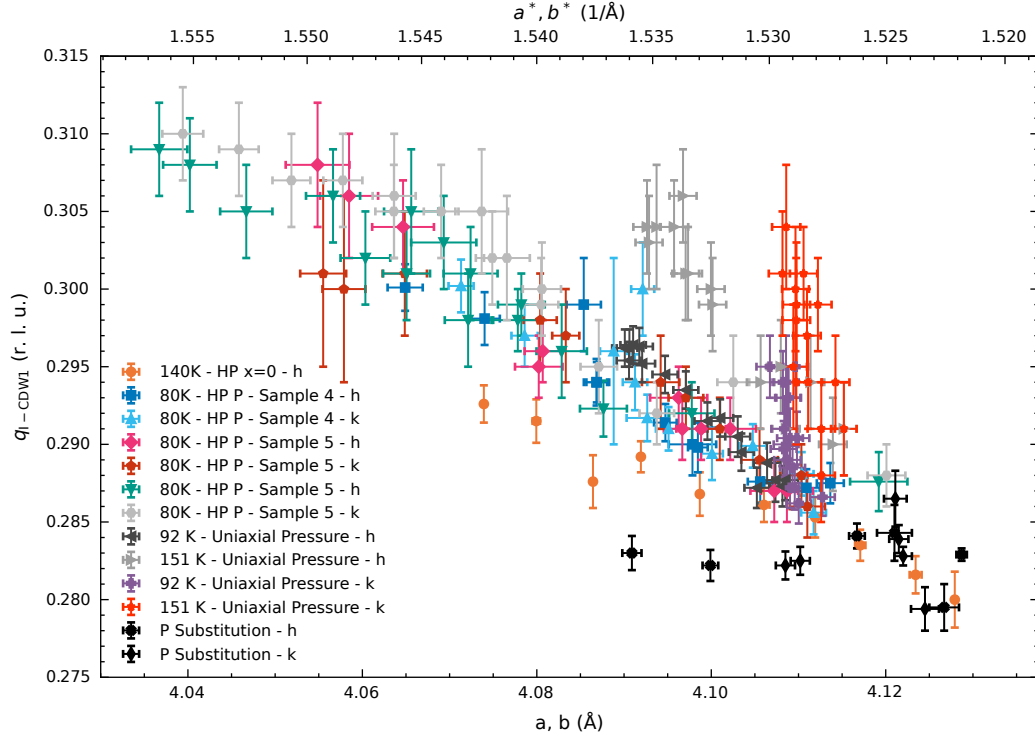


**Figure 6.23.: I-CDW wavevector versus  $a$  and  $b$  lattice parameter.** Shown is the I-CDW1 wavevector versus  $a$  and  $b$  lattice parameter for measurements under hydrostatic, uniaxial and chemical pressure.

leads to similar results, showing the appearance of the C-CDW2 and a collapse of the cell at high pressures, even though the monoclinic structures, exact structural details and the I-CDW2 were not reported. From transport measurements on 60% strontium substituted samples, the low temperature phase can be suppressed and the superconducting  $T_c$  increased with pressures smaller than 0.5 GPa. This suggests that, in fact, strontium substitution and hydrostatic pressure are more comparable tuning parameters. This is not true for phosphorus substitution, as shown from the mostly decoupled effect of phosphorus substitution and pressure in Section 6.4.

On the other hand, the influence on the I-CDW1 seems to be different. As shown in Figure 6.23, the change of the I-CDW1 wave vector is dependent on the  $a$  or  $b$  lattice parameter. Overall, across all the measurements, despite their differences in the tuning parameter and the behavior of the  $c$  lattice parameter or  $c/a$  ratio, there is a common line on which most data points seem to lie. The most prominent exceptions from this are the uniaxial strain measurements in the unordered state and a temperature dependence (not shown in Figure 6.23, included in Chapter 4). From this one can conclude that the I-CDW1 wavevector, at least as long as the I-CDW1 is ordered, is strongly influenced by the change to the  $a$ -lattice parameter. As the  $c$  lattice parameter changes differently within the various investigations, the change to the I-CDW1 is presumably not connected to this value. In this sense, it would be interesting whether this holds for an increasing  $a$  lattice parameter.

In general, the I-CDW1 and orthorhombic/monoclinic III phase are unusually robust against pressure and do not show a significant change to the transition temperature. The I-CDW1 is also robust under phosphorus substitution. This makes the I-CDW1 distinct. For most CDW systems, such as the  $R\text{Te}_3$  [187, 188],  $\alpha$ -U [189], the kagome metals [103, 158] and some dichalcogenides [173, 190], the CDW



transition temperature is rapidly suppressed after only a few GPa. Only for a few CDW systems, such as some dichalcogenides, does the CDW survive to higher pressures [101]. For rare and notable exceptions, such as  $\text{VSe}_2$  [191] or the  $\text{RNiC}_2$  [192], the transition temperature even increases. To the best of my knowledge, no other CDW system is so weakly influenced by hydrostatic pressure as the I-CDW1. This resilience makes the I-CDW1 unique. There may also be connections with the unconventional character of the I-CDW1, as discussed in Chapter 4, and the resilience of the I-CDW1 against optical excitation [149].

Furthermore, the resilience could be related to the nematic liquid observed in  $\text{BaNi}_2(\text{As}_{1-x}\text{P}_x)_2$  at ambient pressure, which sets in well above the I-CDW transition. In this nematic liquid, strong nematic fluctuations couple to the  $E_g$  phonons. These are the same phonons from which the unstable phonon branch of the I-CDW emerges. As these degenerate fluctuations are expected to be only weakly influenced by strain, this could explain the resilience of the I-CDW1.

This could also explain that, in the fluctuating regime, the scattering around the I-CDW1 position is not significantly affected by uniaxial compression. The difference between the pristine and substituted sample might be directly related to the existence of the triclinic phase. Similarly to the measurements under compression, the sample seems to undergo a (partial) transition to the triclinic phase, preventing the I-CDW1 to enhance. Also on cooling, the I-CDW1 intensity grows until it is abruptly stopped at the triclinic transition. Accordingly, also in the case of the uniaxial compression, the triclinic phase could prevent the I-CDW1 to grow further in intensity. Nonetheless, it is still difficult to pinpoint what exactly leads to the stabilization of the triclinic phase. Throughout all the tuning mechanisms – chemical substitution, hydrostatic pressure and uniaxial pressure – used in this thesis, there is not a clear quantity which seems to favor or disfavor the triclinic phase. As there are so many close-lying structures, it more seems that small differences can favor different structures.

The Poisson's ratio also shows that the structure wants to stay close to the original in-plane square lattice and compensates by a huge change in the out-of plane direction. Comparing the absolute value with the ones for different iron-pnictides [193–195], YBCO [155] and other superconductors [196–198] the values are rather unusual. The values of the Poisson's ratio are more extreme (smaller or larger) or at least close to the extreme values observed in other materials. Even though, in principle, negative Poisson's ratios exist, e.g., in  $\text{Ba}_{0.5}\text{K}_{0.5}\text{Fe}_2\text{As}_2$  for [110] compression, this is rather unusual for metals. Furthermore, the huge difference between the in-plane and out-of-plane Poisson's ratios is different from most other materials. Taken together with the pronounced softening of the Young's modulus, as shown by Meingast et al. [25] and the large temperature effect of the Poisson's ratio in a similar temperature range, this observation makes the elastic moduli special. The temperature itself roughly corresponds to the transition to the monoclinic III phase and the I-CDW1 formation. This suggests a detailed, temperature dependent measurement of the elastic constants in  $\text{BaNi}_2(\text{As}_{1-x}\text{P}_x)_2$ .

Following up on the multiple structures observed in these measurements, a further conclusion from the phase diagrams is, that all changes in the CDWs are associated with a structural phase transition. As shown in Section 6.3.4, these structural changes lead to Ni-dimers (C-CDW1), shifted (C-CDW2) or aligned Ni-zigzags (I-CDW2), indicating the importance of the Ni orbitals in the formation of the instabilities. This is in good agreement with earlier NEXAFS measurements, which show the importance of Ni-zigzags at ambient pressure and the related spectral weight transfer in the  $t_{2g}$  orbitals that occurs with Ni-zigzag formation. The Ni states are also the primary states crossing the Fermi-level and determining the Fermi surface [39, 52]. However, only with the formation of well separated (aligned) zigzags and the strong change of the As positions does the structure become stable and all CDWs disappear. Accordingly, the hybridization of the Ni and As atoms is important in the stabilization of the structure. This is also in line with the results from Chapter 5 showing a clear orbital ordering for both CDW.



This is also confirmed by the DFPT calculations, which show a strong impact of the As 4p and Ni 3d orbitals, and accordingly the Ni-As and As-As distance, on the electron-phonon interaction. This is also the case despite the fact that the As states only have a small spectral weight at the Fermi level. Even though the observed crystal structures were not predicted by earlier a priori calculations [39, 52] as they are generally challenging, the DFPT calculations with the experimental crystal structures show the unconventional nature of all CDWs. For all CDWs, no nesting feature exists in the JDOS and no, or only very little, locally enhanced EPC is observed. However, the calculations have a small caveat, as the precursors of the I-CDW2 instability are overestimated by the calculations. This is shown by the IXS measurements at ambient pressure in a phosphorus substituted sample and the diffuse scattering (see Appendix D). Nonetheless, the calculations show generally a good agreement with the data. The calculations themselves give further insight into the instabilities. The I-CDW1 and I-CDW2 show some differences. First, the calculations show that, while for the I-CDW1 instability only the Ni and As atoms are involved, for the I-CDW2 instability the Ba atoms also move. Second, at the I-CDW2 position, there is a small, but existing peak in the EPC. This indicates a difference between the two CDWs and calls for a more detailed investigation of the phonon instability around the I-CDW2 position.

Generally,  $\text{BaNi}_2\text{As}_2$  is prone to a complete series of instabilities. There are four superstructures (I-CDW1, I-CDW2, C-CDW1 and C-CDW2) which exist in larger phase space and at least three further instabilities (I-CDW1', C-CDW3, diagonal peaks in the I-CDW2 phase) which are only observed in a narrow phase space. The DFPT calculations shown in this chapter and in Chapter 4 are very sensitive to the exact parameters and relaxation of the atomic position. A theoretical study from Lei et al. [39] also finds two possible structures that are close in energy. Taken together, this suggests that all the instabilities are energetically very close and the exact arrangement of the atoms decides which instabilities, or the stable structure, are favored. At the same time, the close relationship between the lattice structure and the CDWs also shows a strong coupling of the lattice and electronic degrees of freedom.



## 7. Conclusion and outlook

In summary, in this thesis the origin, symmetry and tuneability of the I-CDW and C-CDW in non-substituted and phosphorous substituted  $\text{BaNi}_2\text{As}_2$  were investigated experimentally. For these purposes, TDS, IXS, REXS, RIXS and XRD measurements were employed. The measurements were combined with chemical substitution, hydrostatic pressure and uniaxial pressure in order to tune the system. In addition, the experimental data were compared to DFPT and TDS intensity calculations, which are in good agreement with the experimental findings.

The measurements revealed that the I-CDW is soft phonon driven, but no conventional ordering mechanism — Fermi surface nesting or locally enhanced EPC— could be identified. This could indicate a significant influence of the orbital order on the I-CDW formation. This is supported by both the REXS measurements and the hydrostatic pressure results. The former clearly shows an orbital order. From the resonance energy in the energy dependence, the orbital order is probably related to the  $d_{xz,yz}$  orbitals. The latter highlights the importance of the hybridization of the nickel and arsenic orbitals, since all of the CDW instabilities are suppressed in a “collapsed” monoclinic phase within which the nickel-arsenic bonds are significantly altered.

The TDS and IXS study further showed that the I-CDW formation is very similar throughout the phosphorus substitution series. The only change is that the transition as indicated by the correlation length is broadened and lowered in temperature with increasing phosphorus content. In the TDS measurements, the formation of Bragg-like peaks at the I-CDW position, which unambiguously indicate the transition to the static I-CDW phase, remains elusive for the highest substitution contents. For the C-CDW, a soft phonon driving the transition could not be found experimentally. In the phonon spectra, the transition is abrupt and no precursor could be observed. This suggests, from the phonon point of view, that there is no close connection between the two CDWs or that the transition to the C-CDW is a lock-in of the I-CDW. This is different than the indications from the REXS experiments, which suggest a very similar orbital order. The azimuthal dependence of the I-CDW can be well described by a tensor atomic form factor with a monoclinic local nickel symmetry when both dipole-dipole and dipole-quadrupole transitions are included. The azimuthal and energy dependence of the C-CDW is very similar to that of the I-CDW. The pressure dependence, on the other hand, is rather different for the two CDWs. The C-CDW1 is replaced by the C-CDW2 at a rather low pressure of  $\approx 2$  GPa but the I-CDW1 is unusually resilient against pressure and is only suppressed above 7 GPa, indicating that the two CDW orders are not directly linked.

In general, the  $p$ - $T$  phase diagram is rich and includes two new monoclinic phases and new CDWs. All changes in the CDWs are accompanied by structural changes, especially to the nickel and arsenic arrangement. The DFPT calculations show unstable phonons very close to the experimental superstructure wavevector, hinting towards the existence of a soft phonon which drives the new CDW transitions. The combination of hydrostatic pressure with phosphorus substitution suppresses partially or fully the low temperature structures and the associated CDW instabilities. The suppression is, in general, comparable to the suppression of the triclinic phase at ambient pressure with increasing phosphorus content. The effect of uniaxial pressure along the  $a$  direction is different. Under applied uniaxial pressure, no new structure was found. In the ordered state of the I-CDW, an enhancement

of the I-CDW along the pressure direction and suppression in the orthogonal direction was observed. However, this change is incompatible with an orthorhombic detwinning. In the fluctuating regime, the effects of uniaxial pressure are rather small. Aside from the behavior of the I-CDW, the measurements revealed an unusual Poisson's ratio, probably related to other anomalies in the elastic constants which were previously observed [25].

Altogether, this thesis highlights the importance of the exact orbital arrangement for the CDW formation and a coupling of each CDW to a related average crystal structure. This strongly suggests orbital dominated CDW ordering mechanisms. Some possibilities would be orbital dependent EPC or orbitally driven Peierls states. The CDW order is likely also related to the nematic fluctuations seen in the nematic liquid phase present at higher temperatures, which are proposed to stem from charge/orbital fluctuations [23]. The suggested weak pressure dependence of this phase also fits with the results gained from applying hydrostatic and uniaxial pressure.

One path for possible future studies is to investigate the differences between the various CDW instabilities. In this direction, the most promising route would be an investigation of the I-CDW2 by IXS under applied hydrostatic pressure. This is, from the DFPT calculations, the only CDW which showed signatures of (weak) EPC at the CDW wavevector. As the unusually high resilience of the I-CDW may be related to the nematic liquid behavior at elevated temperatures, Raman investigations of the  $E_g$  phonon modes and electronic Raman scattering under applied hydrostatic or uniaxial pressure would also be insightful. Regarding the hydrostatic pressure study, an obvious future investigation would be the measurement of the superconducting transition temperature as the CDWs and crystal structures change. Focusing more on the I-CDW, a future detailed XRD study which includes the I-CDW superstructure peaks could help to determine the exact symmetry of the I-CDW. This detailed XRD study would enable a full structural refinement of the structure including the I-CDW. This would help to narrow down the possible local nickel symmetries described in Chapter 5. Ultimately, the aforementioned investigations, together with the discovery of the importance of the orbital degrees of freedom to the CDW formation in  $\text{BaNi}_2\text{As}_2$  in this thesis, could reveal the exact orbital arrangements, subtleties which favor one phase over another and the connection to the other phases observed in  $\text{BaNi}_2\text{As}_2$ , thus significantly expanding the understanding of the physics of  $\text{BaNi}_2\text{As}_2$  and potentially other pnictides.

# Acknowledgements

Like all Ph.D. theses, this one would not have been possible without the help of many people in preparing and conducting the experiments, and in evaluating and ultimately understanding the results. Especially since this thesis is very beamtime heavy, I am deeply grateful for the help of everyone involved in these stressful weeks at any time of day or night and weekend, as every beamtime is its own final enemy. I want to specially highlight the help of the following people:

First, I would like to thank my supervisor Matthieu Le Tacon for enabling the possibility to conduct my Ph.D. at the Institute for Quantum Materials and Technologies and having a great time at the institute. The discussion and continuous support, even in busy weeks, were always fruitful and a crucial part for success of this thesis.

Furthermore, I am thankful to Jörg Schmalian for reading and supervising this thesis.

A significant contribution to the success of the thesis is also the day to day help and introduction to different topics. Accordingly, I am obliged to Michaela Souliou for the introduction to the high pressure and IXS experiments, the continuous guidance, help and reviewing this thesis. Moreover, I thank Amir-Abbas Haghighirad for the help in growing and preparing the crystals, analyzing the HP data and the help during various beamtimes. The great theoretical support and help for all problems regarding phonons from Rolf Heid was also an essential part for the successful experiments and understanding of the data, for which I am deeply grateful. In a thesis like this, it is essential to know the exact structure and quality of the crystal before each experiment, and one finds oneself struggling with crystallographic problems and questions. For these, Michael Merz was always willing to help, for which I would like to thank him.

In addition, a good atmosphere in the office and at beamtimes also contributes significantly to the success of such a thesis. Therefore, I want to thank Fabian Henßler for being a great office mate, always willing to discuss over colors, helping to keep a cool head in summer and the help and precise planning during beamtimes. I also thank Mehdi Frachet, Philippa McGuinness, Mai Ye and Igor Vinograd for being great colleagues and the magnificent help during beamtimes, whether we were hunting for real and imaginary animals from our stronghold, needed a cook, guide or translator or had to build up stress. In particular, I would like to express my gratitude to Philippa McGuinness and Fabian Henßler for their help with correcting this thesis.

The probably most important people during a beamtime are the local contacts. Accordingly, I thank Gaston Gaberino, Daniel Chaney, Konstantin Glazyrin, Kurt Kummer and Enrico Schierle for their great support before, during and after the beamtimes, always being willing to help and cheering up at late hours. Furthermore, I thank Alexei Bossak, Artem Korshunov, Davide Comboni, Tomasz Poreba, Luigi Paolasini, Björn Wehinger and Nicholas Brookes and all beamline staff for their help during and after the beamtimes.

Having a good and fun working environment helps a lot in motivating going through all the work and pain of a Ph.D. My colleagues are an integral part to fulfill this. Therefore, I want to thank the current and former members of the Inelastic Photon Scattering group — Paolo Battistioni, Arthur von Ungern-Sternberg Schwark, Mark Graf von Westarp, Antoine Baron, Huanhuan Shi, Esther Geiger and

Yi Yao — and all members of the Institute for Quantum Materials and Technologies for making the work fun and for the help with countless smaller issues.

A PhD thesis in experimental physics also requires good support from the workshop to build and adapt several experimental setups. I would like to thank all members of the electronics and mechanics workshop, especially the heads of the mechanics workshop Michael Hesselschwerdt and Michael Schlenker, for always being helpful and meeting even much too short deadlines for the production of parts needed for beamtimes. I would also like to thank Otto Walz for his help with all computer problems and for his help with orders and shipping. I am also deeply grateful for the great help of the secretaries Carmen Dörflinger and Dorothea Trautmann with countless administrative issues and open questions for my travels.

I acknowledge the support of the Deutsche Forschungsgemeinschaft (DFG; German Research Foundation) through the collaborative research center “ELASTO-Q-MAT” (Project ID 422213477- TRR 288) in project B03 and support from the state of Baden-Württemberg through bwHPC.

This work would not have been possible without the provision of beamtime from large-scale synchrotron radiation facilities. Accordingly, I acknowledge DESY (Hamburg, Germany), a member of the Helmholtz Association HGF, for the provision of experimental facilities. Parts of this research were carried out at PETRA III using beamline P02.2. Beamtime was allocated for Proposal No. I-20200263. In addition, I thank the Helmholtz-Zentrum Berlin für Materialien und Energie for the allocation of synchrotron radiation beamtime at BESSY II under the proposal 221-10813-ST. Finally, I acknowledge the European Synchrotron Radiation Facility (ESRF) for provision of synchrotron radiation facilities under proposal numbers HC-4234, HC-4328, HC-4442, HC-4946, HC-5080, HC-5156, HC-5233 and HC-5340 at beamlines ID15B, ID28 and ID32.

Last but not least, I am deeply grateful to my family — my brother Pascal and my parents Anita and Stephan. Even if they did not always understand what I was doing in this thesis, they were always supportive and helped me during my undergraduate and Ph.D. studies, whether it was easy or difficult times. The help and inspiration of my family is the most important driving force for me.

## Bibliography

- [1] H. Kamerlingh Onnes, Koninklijke Nederlandse Akademie van Wetenschappen, Proceedings **13** **II**, 1274 (1911).
- [2] H. Fröhlich, Proceedings of the Royal Society of London. Series A. Mathematical and Physical Sciences **223**, 296 (1954).
- [3] R. E. Peierls, *Quantum theory of solids* (Oxford University Press, Oxford, 1955).
- [4] A. W. Overhauser, Physical Review **128**, 1437 (1962).
- [5] L. Šmejkal, J. Sinova, and T. Jungwirth, Physical Review X **12**, 040501 (2022).
- [6] B. Keimer, S. A. Kivelson, M. R. Norman, S. Uchida, and J. Zaanen, Nature **518**, 179 (2015).
- [7] R. M. Fernandes, A. V. Chubukov, and J. Schmalian, Nature physics **10**, 97 (2014).
- [8] G. Venditti and S. Caprara, Condensed Matter **8**, 54 (2023).
- [9] S. Lederer, Y. Schattner, E. Berg, and S. A. Kivelson, Physical Review Letters **114**, 097001 (2015).
- [10] E. Gati, L. Xiang, S. L. Bud'ko, and P. C. Canfield, Annalen der Physik **532**, 2000248 (2020).
- [11] Y.-S. Li, M. Garst, J. Schmalian, S. Ghosh, N. Kikugawa, D. A. Sokolov, C. W. Hicks, F. Jerzembeck, M. S. Ikeda, Z. Hu, B. J. Ramshaw, A. W. Rost, M. Nicklas, and A. P. Mackenzie, Nature **607**, 276 (2022).
- [12] S. M. Souliou, A. Bosak, G. Garbarino, and M. Le Tacon, Superconductor Science and Technology **33**, 124004 (2020).
- [13] E. DiMasi, M. C. Aronson, J. F. Mansfield, B. Foran, and S. Lee, Physical Review B **52**, 14516 (1995).
- [14] A. Thompson, D. Attwood, E. Gullikson, M. Howells, K.-J. Kim, J. Kirz, J. Kortright, I. Lindau, Y. Liu, P. Pianetta, A. Robinson, J. Scofield, J. Underwood, G. Williams, and H. Winick, *X-ray data booklet*, edited by A. C. Thompson, 3, LBNL/PUB-490 Rev. 3 (Lawrence Berkley National Laboratory, Oct. 2009), 176 pp.
- [15] A. Q. Baron, “High-resolution inelastic x-ray scattering i: context, spectrometers, samples, and superconductors”, in *Synchrotron light sources and free-electron lasers* (Springer International Publishing, 2016), pp. 1643–1719.
- [16] J. Fink, E. Schierle, E. Weschke, and J. Geck, Reports on Progress in Physics **76**, 056502 (2013).
- [17] S. Pascarelli, M. McMahon, C. Pépin, O. Mathon, R. F. Smith, W. L. Mao, H.-P. Liermann, and P. Loubeyre, Nature Reviews Methods Primers **3**, 82 (2023).
- [18] A. E. Böhrer, J.-H. Chu, S. Lederer, and M. Yi, Nature Physics **18**, 1412 (2022).
- [19] J. Paglione and R. L. Greene, Nature Physics **6**, 645 (2010).
- [20] A. S. Sefat, M. A. McGuire, R. Jin, B. C. Sales, D. Mandrus, F. Ronning, E. D. Bauer, and Y. Mozharivskyj, Physical Review B **79**, 094508 (2009).
- [21] K. Kothapalli, F. Ronning, E. D. Bauer, A. J. Schultz, and H. Nakotte, Journal of Physics: Conference Series **251**, 012010 (2010).

- [22] S. Lee, G. d. La Peña, S. X.-L. Sun, M. Mitrano, Y. Fang, H. Jang, J.-S. Lee, C. Eckberg, D. Campbell, J. Collini, J. Paglione, F. M. F. d. Groot, and P. Abbamonte, *Physical review letters* **122**, 147601 (2019).
- [23] Y. Yao, R. Willa, T. Lacmann, S.-M. Souliou, M. Frachet, K. Willa, M. Merz, F. Weber, C. Meingast, R. Heid, A.-A. Haghighirad, J. Schmalian, and M. Le Tacon, *Nature Communications* **13**, 4535 (2022).
- [24] F. Ronning, N. Kurita, E. D. Bauer, B. L. Scott, T. Park, T. Klimczuk, R. Movshovich, and J. D. Thompson, *Journal of Physics: Condensed Matter* **20**, 342203 (2008).
- [25] C. Meingast, A. Shukla, L. Wang, R. Heid, F. Hardy, M. Frachet, K. Willa, T. Lacmann, M. Le Tacon, M. Merz, A.-A. Haghighirad, and T. Wolf, *Physical Review B* **106**, 144507 (2022).
- [26] S. Lee, J. Collini, S. X.-L. Sun, M. Mitrano, X. Guo, C. Eckberg, J. Paglione, E. Fradkin, and P. Abbamonte, *Physical review letters* **127**, 027602 (2021).
- [27] M. Merz, L. Wang, T. Wolf, P. Nagel, C. Meingast, and S. Schuppler, *Physical Review B* **104**, 184509 (2021).
- [28] M. Pfisterer and G. Nagorsen, *Zeitschrift für Naturforschung B* **35**, 703 (1980).
- [29] A. Mewis, *Zeitschrift für Naturforschung B* **39**, 713 (1984).
- [30] M. Pfisterer and G. Nagorsen, *Zeitschrift für Naturforschung B* **38**, 811 (1983).
- [31] Z. G. Chen, G. Xu, W. Z. Hu, X. D. Zhang, P. Zheng, G. F. Chen, J. L. Luo, Z. Fang, and N. L. Wang, *Physical Review B* **80**, 094506 (2009).
- [32] I. R. Shein and A. L. Ivanovskii, *Physical Review B* **79**, 054510 (2009).
- [33] B. Zhou, M. Xu, Y. Zhang, G. Xu, C. He, L. X. Yang, F. Chen, B. P. Xie, X.-Y. Cui, M. Arita, K. Shimada, H. Namatame, M. Taniguchi, X. Dai, and D. L. Feng, *Physical Review B* **83**, 035110 (2011).
- [34] N. S. Pavlov, T. K. Kim, A. Yaresko, K.-Y. Choi, I. A. Nekrasov, and D. V. Evtushinsky, *The Journal of Physical Chemistry C* **125**, 28075 (2021).
- [35] T. Noda, K. Kudo, M. Takasuga, M. Nohara, T. Sugimoto, D. Ootsuki, M. Kobayashi, K. Horiba, K. Ono, H. Kumigashira, A. Fujimori, N. L. Saini, and T. Mizokawa, *Journal of the Physical Society of Japan* **86**, 064708 (2017).
- [36] Y. Guo, M. Klemm, J. S. Oh, Y. Xie, B.-H. Lei, L. Moreschini, C. Chen, Z. Yue, S. Gorovikov, T. Pedersen, M. Michiardi, S. Zhdanovich, A. Damascelli, J. Denlinger, M. Hashimoto, D. Lu, C. Jozwiak, A. Bostwick, E. Rotenberg, S.-K. Mo, R. G. Moore, J. Kono, R. J. Birgeneau, D. J. Singh, P. Dai, and M. Yi, *Physical Review B* **108**, l081104 (2023).
- [37] D. M. Narayan, P. Hao, R. Kurlito, B. S. Berggren, A. G. Linn, C. Eckberg, P. Saraf, J. Collini, P. Zavalij, M. Hashimoto, D. Lu, R. M. Fernandes, J. Paglione, and D. S. Dessau, *Science Advances* **9**, eadi4966 (2023).
- [38] T. Qin, R. Zhong, W. Cao, S. Shen, C. Wen, Y. Qi, and S. Yan, *Nano Letters* **23**, 2958 (2023).
- [39] B.-H. Lei, Y. Guo, Y. Xie, P. Dai, M. Yi, and D. J. Singh, *Physical Review B* **105**, 144505 (2022).
- [40] K. Kudo, M. Takasuga, Y. Okamoto, Z. Hiroi, and M. Nohara, *Physical Review Letters* **109**, 097002 (2012).
- [41] C. Eckberg, D. J. Campbell, T. Metz, J. Collini, H. Hodovanets, T. Drye, P. Zavalij, M. H. Christensen, R. M. Fernandes, S. Lee, P. Abbamonte, J. W. Lynn, and J. Paglione, *Nature Physics* **16**, 346 (2019).



- 
- [42] C. Eckberg, L. Wang, H. Hodovanets, H. Kim, D. J. Campbell, P. Zavalij, P. Piccoli, and J. Paglione, *Physical Review B* **97**, 224505 (2018).
  - [43] K. Kudo, M. Takasuga, and M. Nohara, *Copper doping of  $\text{BaNi}_2\text{As}_2$ : giant phonon softening and superconductivity enhancement*, Apr. 17, 2017, arXiv:1704.04854 [cond-mat.supr-con].
  - [44] Y. Chen, N. Giles-Donovan, J. Guo, R. Chen, H. Fukui, T. Manjo, D. Ishikawa, A. Q. R. Baron, Y. Song, and R. J. Birgeneau, *Charge density fluctuations with enhanced superconductivity at the proposed nematic quantum critical point*, Oct. 4, 2024, arXiv:2410.03956 [cond-mat.supr-con].
  - [45] T. Park, H. Lee, E. D. Bauer, J. D. Thompson, and F. Ronning, *Journal of Physics: Conference Series* **200**, 012155 (2010).
  - [46] W. J. Duncan, O. P. Welzel, C. Harrison, X. F. Wang, X. H. Chen, F. M. Grosche, and P. G. Niklowitz, *Journal of Physics: Condensed Matter* **22**, 052201 (2010).
  - [47] M. Frachet, P. Wiecki, T. Lacmann, S. M. Souliou, K. Willa, C. Meingast, M. Merz, A.-A. Haghighirad, M. Le Tacon, and A. E. Böhrer, *npj Quantum Materials* **7**, 1 (2022).
  - [48] K. Chen, Z. Zhu, Y. Xie, A. D. Hillier, J. S. Lord, P. Dai, and L. Shu, *Multi-condensate lengths with degenerate excitation gaps in  $\text{BaNi}_2\text{As}_2$  revealed by muon spin relaxation study*, Jan. 9, 2024, arXiv:2401.04546 [cond-mat.supr-con].
  - [49] C. Yu, Z. Zhang, L. Song, Y. Wu, X. Yuan, J. Hou, Y. Tu, X. Hou, S. Li, and L. Shan, *Chinese Physics B* **33**, 066802 (2024).
  - [50] N. Kurita, F. Ronning, Y. Tokiwa, E. D. Bauer, A. Subedi, D. J. Singh, J. D. Thompson, and R. Movshovich, *Physical Review Letters* **102**, 147004 (2009).
  - [51] N. Kurita, F. Ronning, C. F. Miclea, Y. Tokiwa, E. D. Bauer, A. Subedi, D. J. Singh, H. Sakai, J. D. Thompson, and R. Movshovich, *Journal of Physics: Conference Series* **273**, 012097 (2011).
  - [52] A. Subedi and D. J. Singh, *Physical Review B* **78**, 132511 (2008).
  - [53] S. Lederer, E. Berg, and E.-A. Kim, *Physical Review Research* **2**, 023122 (2020).
  - [54] L. Song, J. Si, T. Fennell, U. Stuhr, G. Deng, J. Wang, J. Liu, L. Hao, H. Luo, M. Liu, S. Meng, and S. Li, *Physical Review B* **109**, 104518 (2024).
  - [55] K. Chen, Z. Zhu, Y. Xie, A. D. Hillier, J. S. Lord, P. Dai, and L. Shu, *Physical Review B* **109**, 024513 (2024).
  - [56] G. Grüner, *Density waves in solids* (CRC Press, Mar. 2018).
  - [57] G. Grüner, *Reviews of Modern Physics* **60**, 1129 (1988).
  - [58] S. van Smaalen, *Acta Crystallographica Section A Foundations of Crystallography* **61**, 51 (2004).
  - [59] W. Kohn, *Physical Review Letters* **2**, 393 (1959).
  - [60] X. Zhu, Y. Cao, J. Zhang, E. W. Plummer, and J. Guo, *Proceedings of the National Academy of Sciences* **112**, 2367 (2015).
  - [61] J. Pouget, S. Kagoshima, C. Schlenker, and J. Marcus, *Journal de Physique Lettres* **44**, 113 (1983).
  - [62] F. Denoyer, F. Comès, A. F. Garito, and A. J. Heeger, *Physical Review Letters* **35**, 445 (1975).
  - [63] J.-P. Pouget, M. D. Mays, and D. O. Cowan, *J. Mater. Chem.* **5**, 1629 (1995).
  - [64] L. Su, C.-H. Hsu, H. Lin, and V. M. Pereira, *Physical Review Letters* **118**, 257601 (2017).
  - [65] C.-W. Chen, J. Choe, and E. Morosan, *Reports on Progress in Physics* **79**, 084505 (2016).
  - [66] D. I. Khomskii and S. V. Streltsov, *Chemical Reviews* **121**, 2992 (2020).

- [67] D. I. Khomskii and T. Mizokawa, *Physical Review Letters* **94**, 156402 (2005).
- [68] J. Als-Nielsen, *Elements of modern x-ray physics*, edited by D. McMorrow, Second edition (Wiley, Chichester, West Sussex, 2017), 419 pp.
- [69] L. J. P. Ament, M. van Veenendaal, T. P. Devereaux, J. P. Hill, and J. van den Brink, *Reviews of Modern Physics* **83**, 705 (2011).
- [70] H. Reichert and V. Honkimäki, “High-energy x-ray scattering and imaging”, in *Synchrotron light sources and free-electron lasers* (Springer International Publishing, 2016), pp. 1557–1577.
- [71] N. Carmignani, J. Jacob, B. Nash, and S. White, en, *Proceedings of the 8th Int. Particle Accelerator Conf. IPAC2017*, Denmark (2017).
- [72] D. T. Attwood, *Soft x-rays and extreme ultraviolet radiation, Principles and applications* (Cambridge Univ. Press, Cambridge [u.a.], 2007), 470 pp.
- [73] T. Schmidt and M. Calvi, *Synchrotron Radiation News* **31**, 35 (2018).
- [74] J.-C. Huang, H. Kitamura, C.-K. Yang, C.-H. Chang, C.-H. Chang, and C.-S. Hwang, *Physical Review Accelerators and Beams* **20**, 064801 (2017).
- [75] M.-E. Couprie, F. Briquez, G. Sharma, C. Benabderrahmane, F. Marteau, O. Marcouillé, P. Berteaud, T. El Ajjouri, J. Vétéran, L. Chapuis, and M. Valléau, in *Spie proceedings*, edited by S. G. Biedron (May 2015).
- [76] K. Zhang and M. Calvi, *Superconductor Science and Technology* **35**, 093001 (2022).
- [77] G. Keresztury, *Raman spectroscopy: theory*, edited by J. M. Chalmers, Dec. 2001.
- [78] V. E. Dmitrienko, A. Kirfel, and E. N. Ovchinnikova, “Tensorial properties of local crystal susceptibilities”, in *International tables for crystallography: physical properties of crystals*, Vol. D, edited by A. Authier, 2nd ed. (International Union of Crystallography, 2013).
- [79] M. Blume, in *Proceedings of the new rings workshop (ssrl 83/02)*, edited by Cantwell (1983).
- [80] M. Blume, *Journal of Applied Physics* **57**, 3615 (1985).
- [81] M. Blume, “Magnetic effects in anomalous dispersion, Theory and applications”, in *Resonant anomalous x-ray scattering*, edited by G. Materlik, C. J. Sparks, and K. Fischer (North-Holland, Amsterdam [u.a.], 1994).
- [82] W. Schülke, *Electron dynamics by inelastic x-ray scattering*. Oxford Series on Synchrotron Radiation (Oxford University Press, Oxford, 2007), p. 464, 1606 pp.
- [83] Y. Joly, S. D. Matteo, and O. Bunău, *The European Physical Journal Special Topics* **208**, 21 (2012).
- [84] A. Authier, ed., *International tables for crystallography: physical properties of crystals*, 2. ed., Vol. D, *International Tables for Crystallography Physical properties of crystals* (International Union of Crystallography, Chichester, Dec. 2013), 564 pp.
- [85] R. D. Johnson, S. R. Bland, C. Mazzoli, T. A. W. Beale, C.-H. Du, C. Detlefs, S. B. Wilkins, and P. D. Hatton, *Physical Review B* **78**, 104407 (2008).
- [86] T. A. W. Beale, T. P. A. Hase, T. Iida, K. Endo, P. Steadman, A. R. Marshall, S. S. Dhesi, G. van der Laan, and P. D. Hatton, *Review of Scientific Instruments* **81**, 073904 (2010).
- [87] U. Staub, V. Scagnoli, Y. Bodenthin, M. García-Fernández, R. Wetter, A. M. Mulders, H. Grimmer, and M. Horisberger, *Journal of Synchrotron Radiation* **15**, 469 (2008).
- [88] S. Huotari, T. Pylkkänen, R. Verbeni, G. Monaco, and K. Hämäläinen, *Nature Materials* **10**, 489 (2011).

- 
- [89] E. Burkel, *Inelastic scattering of x-rays with very high energy resolution*, Springer Tracts in Modern Physics Ser. v.125 (Springer Berlin / Heidelberg, Berlin, Heidelberg, 1991), 1120 pp.
  - [90] A. Q. R. Baron, “High-resolution inelastic x-ray scattering ii: scattering theory, harmonic phonons, and calculations”, in *Synchrotron light sources and free-electron lasers* (Springer International Publishing, 2016), pp. 1721–1757.
  - [91] B. Fåk and B. Dorner, *Physica B: Condensed Matter* **234–236**, 1107 (1997).
  - [92] J. van den Brink, “Resonant inelastic x-ray scattering onelementary excitations, Lecture notes of the autumn school on correlated electrons 2016 : at forschungszentrum jülich, 12-16 september 2016”, in *Quantum materials: experiments and theory*, edited by E. Pavarini, E. Koch, J. Brink, and G. Sawatzky, Schriften des Forschungszentrums Jülich. Reihe Modeling and Simulation Band 6 (Forschungszentrum, Zentralbibliothek, Jülich, 2016).
  - [93] H.-H. Kim, S. M. Souliou, M. E. Barber, E. Lefrançois, M. Minola, M. Tortora, R. Heid, N. Nandi, R. A. Borzi, G. Garbarino, A. Bosak, J. Porras, T. Loew, M. König, P. J. W. Moll, A. P. Mackenzie, B. Keimer, C. W. Hicks, and M. Le Tacon, *Science (New York, N.Y.)* **362**, 1040 (2018).
  - [94] M. E. Barber, H.-h. Kim, T. Loew, M. Le Tacon, M. Minola, M. Konczykowski, B. Keimer, A. P. Mackenzie, and C. W. Hicks, *Physical Review B* **106**, 184516 (2022).
  - [95] Z. Guguchia, D. Das, C. N. Wang, T. Adachi, N. Kitajima, M. Elender, F. Brückner, S. Ghosh, V. Grinenko, T. Shiroka, M. Müller, C. Mudry, C. Baines, M. Bartkowiak, Y. Koike, A. Amato, J. M. Tranquada, H.-H. Klauss, C. W. Hicks, and H. Luetkens, *Physical Review Letters* **125**, 097005 (2020).
  - [96] S. M. Souliou, H. Gretarsson, G. Garbarino, A. Bosak, J. Porras, T. Loew, B. Keimer, and M. Le Tacon, *Physical Review B* **97**, 020503 (2018).
  - [97] T. Kissikov, R. Sarkar, M. Lawson, B. T. Bush, E. I. Timmons, M. A. Tanatar, R. Prozorov, S. L. Bud’ko, P. C. Canfield, R. M. Fernandes, and N. J. Curro, *Nature Communications* **9**, 1058 (2018).
  - [98] Y. Mizuguchi, F. Tomioka, S. Tsuda, T. Yamaguchi, and Y. Takano, *Applied Physics Letters* **93**, 152505 (2008).
  - [99] A. E. Böhrer, A. Sapkota, A. Kreyssig, S. L. Bud’ko, G. Drachuck, S. M. Saunders, A. I. Goldman, and P. C. Canfield, *Physical Review Letters* **118**, 107002 (2017).
  - [100] R. Schmidt, I. Niehues, R. Schneider, M. Drüppel, T. Deilmann, M. Rohlfig, S. M. de Vasconcellos, A. Castellanos-Gomez, and R. Bratschitsch, *2D Materials* **3**, 021011 (2016).
  - [101] D. C. Freitas, P. Rodière, M. R. Osorio, E. Navarro-Moratalla, N. M. Nemes, V. G. Tissen, L. Cario, E. Coronado, M. García-Hernández, S. Vieira, M. Núñez-Regueiro, and H. Suderow, *Physical Review B* **93**, 184512 (2016).
  - [102] C. Guo, C. Putzke, S. Konyzheva, X. Huang, M. Gutierrez-Amigo, I. Errea, D. Chen, M. G. Vergniory, C. Felser, M. H. Fischer, T. Neupert, and P. J. W. Moll, *Nature* **611**, 461 (2022).
  - [103] F. Stier, A.-A. Haghighirad, G. Garbarino, S. Mishra, N. Stölkerich, D. Chen, C. Shekhar, T. Lacmann, C. Felser, T. Ritschel, J. Geck, and M. Le Tacon, *Physical Review Letters* **133**, 236503 (2024).
  - [104] A. Dewaele and P. Loubeyre, *High Pressure Research* **27**, 419 (2007).
  - [105] S. Klotz, J.-C. Chervin, P. Munsch, and G. Le Marchand, *Journal of Physics D: Applied Physics* **42**, 075413 (2009).
  - [106] A. Celeste, F. Borondics, and F. Capitani, *High Pressure Research* **39**, 608 (2019).

- [107] R. S. Manna, B. Wolf, M. de Souza, and M. Lang, *Review of Scientific Instruments* **83**, 085111 (2012).
- [108] N. Fujiwara, Y. Uwatoko, and T. Matsumoto, *Journal of Physics: Conference Series* **500**, 032008 (2014).
- [109] D. Yamazaki, E. Ito, T. Yoshino, N. Tsujino, A. Yoneda, X. Guo, F. Xu, Y. Higo, and K. Funakoshi, *Physics of the Earth and Planetary Interiors* **228**, 262 (2014).
- [110] Y. Akahama and H. Kawamura, *High Pressure Research* **27**, 473 (2007).
- [111] L. Smeller, H. Roemich, and R. Lange, *Biochimica et Biophysica Acta (BBA) - Proteins and Proteomics* **1764**, 329 (2006).
- [112] A. Eiling and J. S. Schilling, *Journal of Physics F: Metal Physics* **11**, 623 (1981).
- [113] H. K. Mao, P. M. Bell, J. W. Shaner, and D. J. Steinberg, *Journal of Applied Physics* **49**, 3276 (1978).
- [114] K. Syassen, *High Pressure Research* **28**, 75 (2008).
- [115] Y. Akahama and H. Kawamura, *Journal of Applied Physics* **100**, 043516 (2006).
- [116] C. W. Hicks, M. E. Barber, S. D. Eddins, D. O. Brodsky, and A. P. Mackenzie, *Review of Scientific Instruments* **85**, 065003 (2014).
- [117] J. Cao, E. Ertekin, V. Srinivasan, W. Fan, S. Huang, H. Zheng, J. W. L. Yim, D. R. Khanal, D. F. Ogletree, J. C. Grossman, and J. Wu, *Nature Nanotechnology* **4**, 732 (2009).
- [118] J. H. Park, J. M. Coy, T. S. Kasirga, C. Huang, Z. Fei, S. Hunter, and D. H. Cobden, *Nature* **500**, 431 (2013).
- [119] J. Diaz, C. Putzke, X. Huang, A. Estrý, J. G. Analytis, D. Sabsovich, A. G. Grushin, R. Ilan, and P. J. W. Moll, *Journal of Physics D: Applied Physics* **55**, 084001 (2021).
- [120] M. He, L. Wang, F. Ahn, F. Hardy, T. Wolf, P. Adelmann, J. Schmalian, I. Eremin, and C. Meingast, *Nature Communications* **8**, 504 (2017).
- [121] M. Shayegan, K. Karrai, Y. P. Shkolnikov, K. Vakili, E. P. De Poortere, and S. Manus, *Applied Physics Letters* **83**, 5235 (2003).
- [122] S. M. Souliou, T. Lacmann, R. Heid, C. Meingast, M. Frachet, L. Paolasini, A.-A. Haghighirad, M. Merz, A. Bosak, and M. Le Tacon, *Physical Review Letters* **129**, 247602 (2022).
- [123] M. Hoesch, A. Bosak, D. Chernyshov, H. Berger, and M. Krisch, *Physical Review Letters* **102**, 086402 (2009).
- [124] E. Comes, B. Renker, L. Pintschovius, R. Currat, W. Gläser, and G. Scheiber, *physica status solidi (b)* **71**, 171 (1975).
- [125] J. P. Pouget, B. Hennion, C. Escribe-Filippini, and M. Sato, *Physical Review B* **43**, 8421 (1991).
- [126] X. Shen, R. Heid, R. Hott, A.-A. Haghighirad, B. Salzmänn, M. dos Reis Cantarino, C. Monney, A. H. Said, M. Frachet, B. Murphy, K. Rossnagel, S. Rosenkranz, and F. Weber, *Nature Communications* **14**, 7282 (2023).
- [127] J. Diego, A. H. Said, S. K. Mahatha, R. Bianco, L. Monacelli, M. Calandra, F. Mauri, K. Rossnagel, I. Errea, and S. Blanco-Canosa, *Nature Communications* **12**, 598 (2021).
- [128] P. Monceau, *Advances in Physics* **61**, 325 (2012).
- [129] F. Weber, S. Rosenkranz, J.-P. Castellan, R. Osborn, R. Hott, R. Heid, K.-P. Bohnen, T. Egami, A. H. Said, and D. Reznik, *Physical Review Letters* **107**, 107403 (2011).

- [130] M. Le Tacon, A. Bosak, S. M. Souliou, G. Dellea, T. Loew, R. Heid, K.-P. Bohnen, G. Ghiringhelli, M. Krisch, and B. Keimer, *Nature Physics* **10**, 52 (2013).
- [131] H. Li, T. T. Zhang, T. Yilmaz, Y. Y. Pai, C. E. Marvinney, A. Said, Q. W. Yin, C. S. Gong, Z. J. Tu, E. Vescovo, C. S. Nelson, R. G. Moore, S. Murakami, H. C. Lei, H. N. Lee, B. J. Lawrie, and H. Miao, *Physical Review X* **11**, 031050 (2021).
- [132] D. Subires, A. Korshunov, A. H. Said, L. Sánchez, B. R. Ortiz, S. D. Wilson, A. Bosak, and S. Blanco-Canosa, *Nature Communications* **14**, 1015 (2023).
- [133] M. D. Johannes and I. I. Mazin, *Physical Review B* **77**, 165135 (2008).
- [134] M. Krisch and F. Sette, “Inelastic x-ray scattering from phonons”, in *Light scattering in solid ix*, edited by M. Cardona and R. Merlin (Springer Berlin Heidelberg, Berlin, Heidelberg, 2007), pp. 317–370.
- [135] A. Girard, T. Nguyen-Thanh, S. M. Souliou, M. Stekiel, W. Morgenroth, L. Paolasini, A. Minelli, D. Gambetti, B. Winkler, and A. Bosak, *Journal of Synchrotron Radiation* **26**, 272 (2019).
- [136] Y. Yao, *Study of lattice, spin and charge dynamics in cr- and ni-based pnictide superconductors*, PhD thesis (2021).
- [137] T. Lacmann, *Single crystal growth, chemical and hydrostatic pressure tuning of BaNi<sub>2</sub>As<sub>2</sub>*, Master Thesis (Karlsruhe Institute of Technology, Nov. 30, 2020).
- [138] Rigaku Oxford Diffraction, *CrysAlisPro Software system, version 1.171.42.57a*, Rigaku Corporation, Wroclaw, Poland, 2022.
- [139] S. G. Louie, K.-M. Ho, and M. L. Cohen, *Physical Review B* **19**, 1774 (1979).
- [140] B. Meyer, C. Elsässer, and M. Fähnle, *Fortran90 program for mixed-basis pseudopotential calculations for crystals*, Max-Planck-Institut für Metallforschung, Stuttgart (unpublished), 1997.
- [141] D. R. Hamann, M. Schlüter, and C. Chiang, *Physical Review Letters* **43**, 1494 (1979).
- [142] G. B. Bachelet, D. R. Hamann, and M. Schlüter, *Physical Review B* **26**, 4199 (1982).
- [143] D. Vanderbilt, *Physical Review B* **32**, 8412 (1985).
- [144] J. P. Perdew, K. Burke, and M. Ernzerhof, *Physical Review Letters* **77**, 3865 (1996).
- [145] R. Heid and K.-P. Bohnen, *Physical Review B* **60**, R3709 (1999).
- [146] A. Mirone and B. Wehinger, *ab2tds, version 1.1*, *European Synchrotron Radiation Facility*, version 1.1, Grenoble, France: European Synchrotron Radiation Facility.
- [147] Y. Song, S. Wu, X. Chen, Y. He, H. Uchiyama, B. Li, S. Cao, J. Guo, G. Cao, and R. Birgeneau, *Physical Review B* **107**, l041113 (2023).
- [148] A. Mejaš, *Collective mode in BaNi<sub>2</sub>As<sub>2</sub>*, Diploma Thesis (2021).
- [149] A. R. Pokharel, V. Grigorev, A. Mejas, T. Dong, A. A. Haghighirad, R. Heid, Y. Yao, M. Merz, M. Le Tacon, and J. Demsar, *Communications Physics* **5**, 141 (2022).
- [150] A. R. Pokharel, *Time resolved spectroscopy of strongly correlated materials*, PhD thesis (2023).
- [151] F. Flicker and J. van Wezel, *Nature Communications* **6**, 7034 (2015).
- [152] S. V. Streltsov and D. I. Khomskii, *Physical Review B* **89**, 161112 (2014).
- [153] J. Chang, E. Blackburn, A. T. Holmes, N. B. Christensen, J. Larsen, J. Mesot, R. Liang, D. A. Bonn, W. N. Hardy, A. Watenphul, M. v. Zimmermann, E. M. Forgan, and S. M. Hayden, *Nature Physics* **8**, 871 (2012).
- [154] M. Fujita, H. Goka, K. Yamada, and M. Matsuda, *Physical Review Letters* **88**, 167008 (2002).

- [155] I. Vinograd, S. M. Souliou, A.-A. Haghighirad, T. Lacmann, Y. Caplan, M. Frachet, M. Merz, G. Garbarino, Y. Liu, S. Nakata, K. Ishida, H. M. L. Noad, M. Minola, B. Keimer, D. Orgad, C. W. Hicks, and M. Le Tacon, *Nature Communications* **15**, 3277 (2024).
- [156] C.-S. Lian, C. Si, and W. Duan, *Nano Letters* **18**, 2924 (2018).
- [157] L. Fang, P. Zou, Y. Wang, L. Tang, Z. Xu, H. Chen, C. Dong, L. Shan, and H. Wen, *Science and Technology of Advanced Materials* **6**, 736 (2005).
- [158] F. H. Yu, D. H. Ma, W. Z. Zhuo, S. Q. Liu, X. K. Wen, B. Lei, J. J. Ying, and X. H. Chen, *Nature Communications* **12**, 3645 (2021).
- [159] N. N. Wang, K. Y. Chen, Q. W. Yin, Y. N. N. Ma, B. Y. Pan, X. Yang, X. Y. Ji, S. L. Wu, P. F. Shan, S. X. Xu, Z. J. Tu, C. S. Gong, G. T. Liu, G. Li, Y. Uwatoko, X. L. Dong, H. C. Lei, J. P. Sun, and J.-G. Cheng, *Physical Review Research* **3**, 043018 (2021).
- [160] M. Leroux, V. Mishra, C. Opagiste, P. Rodière, A. Kayani, W.-K. Kwok, and U. Welp, *Physical Review B* **102**, 094519 (2020).
- [161] R. Comin, R. Sutarto, F. He, E. H. Da Silva Neto, L. Chauviere, A. Fraño, R. Liang, W. N. Hardy, D. A. Bonn, Y. Yoshida, H. Eisaki, A. J. Achkar, D. G. Hawthorn, B. Keimer, G. A. Sawatzky, and A. Damascelli, *Nature materials* **14**, 796 (2015).
- [162] C. McMahon, A. J. Achkar, E. H. Da Silva Neto, I. Djianto, J. Menard, F. He, R. Sutarto, R. Comin, R. Liang, D. A. Bonn, W. N. Hardy, A. Damascelli, and D. G. Hawthorn, *Science advances* **6**, eaay0345 (2020).
- [163] P. Leininger, M. Rahlenbeck, M. Raichle, B. Bohnenbuck, A. Maljuk, C. T. Lin, B. Keimer, E. Weschke, E. Schierle, S. Seki, Y. Tokura, and J. W. Freeland, *Physical Review B* **81**, 085111 (2010).
- [164] A. J. Princep, A. M. Mulders, E. Schierle, E. Weschke, J. Hester, W. D. Hutchison, Y. Tanaka, N. Terada, Y. Narumi, and T. Nakamura, *Journal of Physics: Condensed Matter* **24**, 075602 (2012).
- [165] E. Weschke and E. Schierle, *Journal of large-scale research facilities JLSRF* **4**, A127 (2018).
- [166] N. Brookes, F. Yakhov-Harris, K. Kummer, A. Fondacaro, J. Cezar, D. Betto, E. Velez-Fort, A. Amorese, G. Ghiringhelli, L. Braicovich, R. Barrett, G. Berruyer, F. Cianciosi, L. Eybert, P. Marion, P. van der Linden, and L. Zhang, *Nuclear Instruments and Methods in Physics Research Section A: Accelerators, Spectrometers, Detectors and Associated Equipment* **903**, 175 (2018).
- [167] H. Yavaş, M. Sundermann, K. Chen, A. Amorese, A. Severing, H. Gretarsson, M. W. Haverkort, and L. H. Tjeng, *Nature Physics* **15**, 559 (2019).
- [168] A. Amorese, B. Leedahl, M. Sundermann, H. Gretarsson, Z. Hu, H.-J. Lin, C. T. Chen, M. Schmidt, H. Borrmann, Y. Grin, A. Severing, M. W. Haverkort, and L. H. Tjeng, *Physical Review X* **11**, 011002 (2021).
- [169] L. H. Tjeng, “Imaging orbitals with x-rays, Autumn school on correlated electrons”, in *Orbital physics in correlated matter*, Vol. correl23, edited by E. Pavarini and E. Koch, Schriften des Forschungszentrums Jülich (Forschungszentrum Jülich, Jülich, 2023).
- [170] T. Lacmann, A.-A. Haghighirad, S.-M. Souliou, M. Merz, G. Garbarino, K. Glazyrin, R. Heid, and M. Le Tacon, *Physical Review B* **108**, 224115 (2023).
- [171] T. Lacmann, S. M. Souliou, G. Gabarino, and M. Le Tacon, *High pressure study of charge density wave ordering in BaNi<sub>2</sub>As<sub>2</sub>* [Dataset] (European Synchrotron Radiation Facility, 2023).
- [172] T. Lacmann, S. M. Souliou, A.-A. Haghighirad, K. Glazyrin, and M. Le Tacon, *High pressure study of charge density wave ordering in BaNi<sub>2</sub>As<sub>2</sub>* [Dataset] (Karlsruhe Institute of Technology, 2023).

- 
- [173] S. Lee, T. B. Park, J. Kim, S.-G. Jung, W. K. Seong, N. Hur, Y. Luo, D. Y. Kim, and T. Park, *Physical Review Research* **3**, 033097 (2021).
- [174] M. Merlini and M. Hanfland, *High Pressure Research* **33**, 511 (2013).
- [175] H.-P. Liermann, Z. Konôpková, W. Morgenroth, K. Glazyrin, J. Bednarčík, E. E. McBride, S. Petitgirard, J. T. Delitz, M. Wendt, Y. Bican, A. Ehnes, I. Schwark, A. Rothkirch, M. Tischer, J. Heuer, H. Schulte-Schrepping, T. Kracht, and H. Franz, *Journal of Synchrotron Radiation* **22**, 908 (2015).
- [176] G. M. Sheldrick, *Acta Crystallographica Section A Foundations of Crystallography* **64**, 112 (2007).
- [177] G. M. Sheldrick, *Acta Crystallographica Section C Structural Chemistry* **71**, 3 (2015).
- [178] V. Petříček, M. Dušek, and L. Palatinus, *Zeitschrift für Kristallographie - Crystalline Materials* **229**, 345 (2014).
- [179] C. Prescher and V. B. Prakapenka, *High Pressure Research* **35**, 223 (2015).
- [180] M. Tomić, R. Valentí, and H. O. Jeschke, *Physical Review B* **85**, 094105 (2012).
- [181] P. G. Naumov, K. Filsinger, O. I. Barkalov, G. H. Fecher, S. A. Medvedev, and C. Felser, *Physical Review B* **95**, 144106 (2017).
- [182] F. Weber, S. Rosenkranz, J.-P. Castellan, R. Osborn, G. Karapetrov, R. Hott, R. Heid, K.-P. Bohnen, and A. Alatas, *Physical Review Letters* **107**, 266401 (2011).
- [183] A. Ballato, *IEEE Transactions on Ultrasonics, Ferroelectrics and Frequency Control* **43**, 56 (1996).
- [184] Z. P. Yin, S. Lebègue, M. J. Han, B. P. Neal, S. Y. Savrasov, and W. E. Pickett, *Physical Review Letters* **101**, 047001 (2008).
- [185] T. Yildirim, *Physical Review Letters* **102**, 037003 (2009).
- [186] J. Collini, D. J. Campbell, D. Sneed, P. Saraf, C. Eckberg, J. Jeffries, N. Butch, and J. Paglione, *Physical Review B* **108**, 205103 (2023).
- [187] A. Sacchetti, C. L. Condon, S. N. Gvasaliya, F. Pfünz, M. Lavagnini, M. Baldini, M. F. Toney, M. Merlini, M. Hanfland, J. Mesot, J.-H. Chu, I. R. Fisher, P. Postorino, and L. Degiorgi, *Physical Review B* **79**, 201101 (2009).
- [188] D. A. Zocco, J. J. Hamlin, K. Grube, J.-H. Chu, H.-H. Kuo, I. R. Fisher, and M. B. Maple, *Physical Review B* **91**, 205114 (2015).
- [189] S. Raymond, J. Bouchet, G. H. Lander, M. Le Tacon, G. Garbarino, M. Hoesch, J.-P. Rueff, M. Krisch, J. C. Lashley, R. K. Schulze, and R. C. Albers, *Physical Review Letters* **107**, 136401 (2011).
- [190] M. Leroux, I. Errea, M. Le Tacon, S.-M. Souliou, G. Garbarino, L. Cario, A. Bosak, F. Mauri, M. Calandra, and P. Rodière, *Physical Review B* **92**, 140303 (2015).
- [191] D. Song, Y. Zhou, M. Zhang, X. He, and X. Li, *Frontiers in Materials* **8**, 710849 (2021).
- [192] B. Woo, S. Seo, E. Park, J. H. Kim, D. Jang, T. Park, H. Lee, F. Ronning, J. D. Thompson, V. A. Sidorov, and Y. S. Kwon, *Physical Review B* **87**, 125121 (2013).
- [193] P. Wiecki, M. Frachet, A.-A. Haghighirad, T. Wolf, C. Meingast, R. Heid, and A. E. Böhmer, *Nature Communications* **12**, 4824 (2021).
- [194] N. K. Omboga, C. O. Otieno, and P. W. O. Nyawere, *The Scientific World Journal* **2020**, 1 (2020).
- [195] Y. Wen, D. Wu, R. Cao, L. Liu, and L. Song, *Journal of Superconductivity and Novel Magnetism* **30**, 1749 (2017).

- [196] M. Kholil and M. Bhuiyan, Solid State Communications **322**, 114053 (2020).
- [197] M. H. Rahman, M. Z. Rahaman, M. Motalab, and A. A. Hossain, Materials Today Communications **31**, 103785 (2022).
- [198] A. Benamara, N. Moulay, Y. Azzaz, M. Ameri, M. Rabah, Y. Al-Douri, A. Bouhemadou, and C. Moumen, Materials Today Communications **35**, 105545 (2023).
- [199] “Sur la révision du système international d’unités (si)”, in *Comptes rendus de la 26e réunion de la conférence générale des poids et mesures (novembre 2018)*, *Conférence générale des poids et mesures* (Bureau International des Poids et Mesures, Sèvres, 2018).



## List of figures

2.1.	Sketch of the different crystal structures of $\text{BaNi}_2\text{As}_2$ .	5
2.2.	Phosphorus, strontium and cobalt substitution phase diagrams of $\text{BaNi}_2\text{As}_2$ .	6
2.3.	Hydrostatic pressure phase diagram of $\text{BaNi}_2\text{As}_2$ up to 2.74 GPa.	7
2.4.	Elastoresistance and $E_g$ phonon mode splitting in $\text{BaNi}_2\text{As}_2$ .	8
2.5.	Superconducting gap, muon spin relaxation rate and superfluid density in strontium and non-substituted $\text{BaNi}_2\text{As}_2$ .	9
3.1.	Sketch of the atom arrangement and band structure of a one-dimensional metallic chain in the normal and charge density wave state.	11
3.2.	Sketch of the Fermi surface nesting in the one- and nearly one-dimensional system.	12
3.3.	Sketch of the Kohn anomaly at different temperatures.	13
3.4.	Sketch of a synchrotron radiation facility and a undulator insertion device.	16
3.5.	Sketch of a subset of the possible interactions of X-rays with a crystal.	18
3.6.	Sketch of the scattering geometry.	19
3.7.	Sketch of the possible excitations measured with inelastic X-ray scattering.	24
3.8.	Sketch of the possible excitations measured with resonant inelastic X-ray scattering.	26
3.9.	Sketch of a membrane type diamond anvil cell.	27
3.10.	Sketch of a piezoelectric uniaxial pressure cell and rendering of the setup used.	28
4.1.	Two- and three-dimensional reciprocal space reconstructions for different temperatures.	35
4.2.	Reciprocal space maps and linecuts of the I-CDW at different temperatures and substitution levels.	36
4.3.	Linecuts through the different peaks observed in the reciprocal space maps.	38
4.4.	Fit parameters of the I-CDW peaks and intensity of the longitudinal and diagonal peaks.	39
4.5.	Temperature and substitution dependence of the I-CDW wavevector.	40
4.6.	Integrated intensity of the longitudinal and diagonal peaks in TDS.	41
4.7.	Thermal diffuse scattering calculations and comparison to experiment.	42
4.8.	Measured and calculated phonon dispersion along the transverse direction.	44
4.9.	Temperature dependence of the phonon spectra at the I-CDW position.	45
4.10.	Phonon dispersion at 3.75 K and 2.2 K.	46
4.11.	Measured and calculated phonon dispersion along the longitudinal direction.	47
4.12.	Measured and calculated phonon dispersion along the diagonal direction.	47
4.13.	Calculated phonon linewidth, joint-density of states and phonon dispersion.	48
4.14.	Reciprocal space maps around the triclinic transition temperature.	49
4.15.	Phonon dispersion in the direction of the C-CDW.	50
4.16.	Temperature dependence of the phonon spectra at the C-CDW position and l-dependence.	51
4.17.	Measured and calculated phonon dispersion in the C-CDW-direction around the triclinic transition.	51
4.18.	Phase diagram of $\text{BaNi}_2(\text{As}_{1-x}\text{P}_x)_2$ .	53
5.1.	Sketch of the scattering geometry and images of the samples.	59
5.2.	Energy dependence of the scattering signal of the I-CDW and C-CDW.	60

5.3.	Temperature dependence of the scattering signal of the I-CDW. . . . .	61
5.4.	Azimuthal dependence of the scattering signal of the I-CDW and C-CDW. . . . .	62
5.5.	Azimuthal dependence of the scattering signal of the I-CDW with orthorhombic parameters. . . . .	64
5.6.	Linear polarization dependence of the scattering signal of the I-CDW. . . . .	68
5.7.	Linear polarization dependence of the scattering signal of the C-CDW. . . . .	70
5.8.	Sketch of the local site symmetry at the nickel position. . . . .	71
6.1.	Reciprocal space maps as obtained under applied hydrostatic and uniaxial pressure. . . . .	74
6.2.	Microscope image of pristine $\text{BaNi}_2\text{As}_2$ samples loaded into the DAC and reconstructed reciprocal space map. . . . .	76
6.3.	Pressure dependence of the I-CDW1 wavevector, lattice parameters and atomic distances at 140 K. . . . .	79
6.4.	Reciprocal space maps and line cuts at 140 K. . . . .	80
6.5.	Pressure dependence of different structural parameters at 94 K. . . . .	81
6.6.	Reciprocal space maps and line cuts at 94 K. . . . .	83
6.7.	Lattice parameters and structural parameters for the isobars at 2.2, 4, 7.6 and 12 GPa. . . . .	84
6.8.	Reciprocal space maps around the structural transitions for the isobars at at 2.2, 4, 7.6 and 12 GPa. . . . .	85
6.9.	Reciprocal space maps and I-CDW2 wavevector at 10.14 GPa. . . . .	86
6.10.	Change of the atomic positions for the different structures. . . . .	87
6.11.	Calculated lowest phonon mode energy, joint density of states and phonon linewidth for the experimental structures at 140 K. . . . .	89
6.12.	Calculated lowest phonon mode energy, joint density of states and phonon linewidth for the experimental structures at 94 K. . . . .	90
6.13.	Pressure-temperature phase diagram of $\text{BaNi}_2\text{As}_2$ . . . . .	91
6.14.	Lattice parameters and wavevectors at 80 K. . . . .	93
6.15.	Reciprocal space maps for different pressures at 80 K. . . . .	94
6.16.	Lattice parameters, CDW intensity map wavevectors at 25 K. . . . .	95
6.17.	Reciprocal space maps for different pressures at 25 K. . . . .	96
6.18.	Reciprocal space maps with C-CDW3 at 25 K and 7.58 GPa. . . . .	96
6.19.	Pressure-temperature phase diagram of $\text{BaNi}_2(\text{As}_{1-x}\text{P}_x)_2$ with $x < x_{\text{crit}}$ and $x > x_{\text{crit}}$ . . . . .	97
6.20.	Lattice parameters versus strain $\epsilon_{xx}$ . . . . .	99
6.21.	Reciprocal space maps and linecut for different compression values. . . . .	100
6.22.	I-CDW wavevector, intensity and correlation length in the $a$ and $b$ direction versus strain $\epsilon_{xx}$ . . . . .	101
6.23.	I-CDW wavevector versus $a$ and $b$ lattice parameter. . . . .	103
A.1.	( $h$ $k$ 1) reciprocal space maps for different temperatures and substitution levels. . . . .	133
A.2.	( $h$ 4 $l$ ) reciprocal space maps for different temperatures and substitution levels. . . . .	134
A.3.	Atom dependent thermal diffuse scattering intensity calculations. . . . .	135
A.4.	Comparison of the IXS spectra between the pristine and substituted samples. . . . .	135
B.1.	Scans around the (0 0.28 1) position. . . . .	137
B.2.	Energy dependence of the I-CDW and C-CDW scattering signal. . . . .	138
B.3.	RIXS scans and integrated intensities through the C-CDW. . . . .	139
C.1.	Chosen $p$ - $T$ -paths and microscope images of the pristine $\text{BaNi}_2\text{As}_2$ sample for HP XRD. . . . .	141
C.2.	Chosen $p$ - $T$ -paths and microscope images of the phosphorus substituted $\text{BaNi}_2\text{As}_2$ sample for HP XRD. . . . .	142
C.3.	Microscope images of the cut needles before mounting on the uniaxial pressure cell. . . . .	142
C.4.	Crystal structure of the monoclinic III phase. . . . .	143

C.5. Linecuts through the different CDWs for different pressures. . . . .	146
C.6. Intensity of the I-CDW1 versus hydrostatic pressure. . . . .	147
C.7. Reciprocal space maps, lattice parameters and I-CDW1 parameters for a $x=0$ sample at 140 K. . . . .	148
D.1. Inelastic X-ray scattering spectra and fitted dispersion around the I-CDW2 position. . . . .	149



## List of tables

3.1.	List of different X-ray techniques and their common type of interaction with a crystal.. . .	17
5.1.	Fit parameters of the azimuthal dependence of the I-CDW. . . . .	67
5.2.	Fit parameters of the azimuthal dependence of the C-CDW. . . . .	69
6.1.	Poisson's ratio extracted from the uniaxial compression experiments and DFPT calculations.	99
B.1.	Extended fit parameters of the azimuthal dependence of the I-CDW. . . . .	138
B.2.	Extended fit parameters of the azimuthal dependence of the I-CDW for sample 3. . . . .	140
C.1.	Structure parameters of the observed structures in the $\text{BaNi}_2\text{As}_2$ HP-phase diagram. . . .	144
C.2.	Structure parameters of the monoclinic III structure. . . . .	145



# Symbols

Symbol	Description
$J_z$	Angular momentum in z-direction
$\varphi$	Azimuthal angle. Chosen in such a way that it corresponds in the experiment to the angle $\varphi$ of the Euler angles used in a four circle diffractometer.
$k_B$	Boltzmann constant — $k_B = 1.380\,649 \times 10^{-23}$ J/K [199]
$\psi$	Phase of the charge density wave
$\rho(\vec{r})$	Position dependent charge density
$\rho_0$	Unperturbed charge density
$s_{ij}$	Element $ij$ of the compliance tensor. The full tensor is the inverse of the elasticity tensor.
$W_d$	Debye-Waller factor
$\Delta\Omega$	Solid angle covered by for example the X-ray detector
$g_{kn,\vec{k}+\vec{q}m}^{\vec{q}\lambda}$	Electron-phonon coupling matrix element — The matrix element describes the probability of the scattering of an electron with an phonon of branch $\lambda$ with momentum $\vec{q}$ .
$\left(\frac{d\sigma}{d\Omega}\right)$	Differential cross-section
$d$	Dimension
$D_i^n$	Dipole component for the incoming beam $i$ or scattered beam $s$ corresponding to state $ n\rangle$ .
$D_{jk}$	Component of the rank-2 tensor describing the dipole-dipole interaction.
$I_{jkl}$	Component of the rank-3 tensor describing the dipole-quadrupole interaction.
$u$	Magnitude of the lattice distortion
$D(E)$	Density of states at energy $E$ .
$\left(\frac{d^2\sigma}{d\Omega dE}\right)$	Double differential cross-section
$S(\vec{q}, \tilde{\omega})$	Dynamical structure factor, e.g. from a phonon, used to describe inelastic scattering process.
$S_i(\vec{q}, \tilde{\omega})$	Dynamical structure factor from $i$ phonons.
$e$	Elementary charge — $e = 1.602\,176\,634 \times 10^{-19}$ C [199]
$c_{ij}$	Element $ij$ of the elasticity tensor. Often also just refered as elastic constants. The full tensor is the inverse of the compliance tensor.
$E_i$	Energy of the state $ i\rangle$
$\tilde{\omega}$	Difference between the incoming and the scattered photon energy. In the simplest case it is also the energy of an excitation as a phonon. In an inelastic scattering process, the energy is given by the difference of the incident and scattered photon energies $\hbar\tilde{\omega} = \hbar\omega - \hbar\omega'$ . In literature also $\Omega$ or $\omega$ are used for the excitation energy.
$E_F$	Fermi energy
$f(\vec{k})$	Fermi function
$k_F$	Fermi wavevector
$\gamma_{\text{EPC}}$	Phonon HWHM due to EPC.
$\mathcal{H}$	Hamiltonian
$\gamma_{\vec{q}j}$	HWHM of a phonon at $\vec{q}$ and index $j$

Symbol	Description
$\rho^{\text{ind}}(\vec{q})$	Induced charge density
$\Phi_0$	Incoming flux — photons passing through a unit area per second
$\omega$	Incoming photon energy
$\vec{\tau}$	Vector to a Bragg reflection in reciprocal space.
$\chi(\vec{q})$	Lindhard response function
$\Gamma$	Linewidth
$A_{jkl}$	Polarization factor associated with the orbital magnetic moment for non-resonant magnetic scattering.
$B_{jkl}$	Polarization factor associated with the spin magnetic moment for non-resonant magnetic scattering.
$m$	Mass — in this thesis mainly the (effective) electron mass.
$\mathbf{D}$	Rank-2 tensor describing the dipole-dipole interaction. The individual components are $D_{jk}$ .
$\mathbf{I}$	Rank-3 tensor describing the dipole-quadrupole interaction. The individual components are $I_{jkl}$ .
$\mathbf{f}$	Effective tensor atomic form factor — $3 \times 3$ matrix.
$\vec{p}$	Momentum operator in the Hamiltonian.
$P_g$	Occupation probability of the state $ g\rangle$
$f_{1p}(\vec{\tau}, \vec{Q}, j)$	One-phonon structure factor
$\vec{O}(\vec{k})$	Operator used for simplification of calculations in subsection 3.2.2. The operator is defined in Equation 3.10.
$\omega'$	Scattered photon energy
$\vec{\sigma}_i$	Pauli matrix $i$ with $i$ being one of the cartesian coordinates.
$\omega_{\vec{q}j}$	Energy of the phonon at $\vec{q}$ and index $j$ .
$L_{\vec{q}j}(\vec{\omega}, T)$	Phonon line shape and phonon occupation factor
$\Delta_{\vec{q}j}$	Shift of the phonon mode in the nonharmonic correction.
$\tilde{\omega}_{\text{ren}}$	From the Kohn anomaly renormalized phonon energy
$\vec{Q}$	Phonon wavevector in the first Brillouine zone.
$\nu_{ij}$	The Poisson's ratio describing a relative lattice change in the $j$ direction reacting to a relative lattice change in the $i$ direction. The definition is given in Equation 6.2.
$\vec{\epsilon}$	Incoming polarization
$\vec{\epsilon}'$	Scattered polarization
$\vec{r}$	Position vector
$\Phi(\vec{q})$	Potential
$Q_i^n$	Quadrupole component for the incoming beam $i$ or scattered beam $s$ corresponding to state $ n\rangle$ .
$Q_{jklm}$	Component of the rank-4 tensor describing the quadrupole-quadrupole interaction.
$\hbar$	Reduced Planck constant — $\hbar = \frac{6.626\,070\,15 \times 10^{-34} \text{ J s}}{2\pi}$ [199]
$\Omega_{\vec{q}j}(\vec{\omega})$	Renormalized energy of the phonon at $\vec{q}$ and index $j$ .
$\mathbf{R}$	Rotation matrix used in the REXS experiments accounting for the rotation from the wedge.
$f(\vec{k}, \vec{k}', \vec{\epsilon}, \vec{\epsilon}')$	Scattering amplitude
$\vec{q}$	Scattering vector defined by the difference of the incoming and outgoing wavevectors $\vec{q} = \vec{k} - \vec{k}'$ . In a different context, $\vec{q}$ is also used for the wavevector of excitations (which in this case is the scattering vector minus a lattice vector if necessary).



Symbol	Description
$I_{sc}$	Scattered intensity
$c$	Speed of light — $c = 299\,792\,458\text{ m/s}$ [199]
$\vec{s}_i$	Spin angular momentum given by $s_i^j = \frac{\hbar\sigma_j}{2}$ using the Pauli matrices $\vec{\sigma}_i$ .
$\epsilon_{xx}$	Element of the strain tensor describing the relative change of the lattice along the $x$ or $a$ direction. The definition is given in Equation 6.1.
$x$	Substitution level — In this thesis mainly the phosphorus substitution level in $\text{BaNi}_2(\text{As}_{1-x}\text{P}_x)_2$ . In the context of Cartesian coordinates, $x$ can also be one of the Cartesian coordinates.
$\alpha$	Angle between the the scattering vector and the incoming wavevector.
$\beta$	Angle of tilt around the $a$ axis from the wedge in the REXS experiments.
$\chi$	One of three Euler angles using the common four circle diffractometer nomenclature. At $\theta = 0$ the roation axis is parallel to the X-ray beam.
$\theta$	One of three Euler angles using the common four circle diffractometer nomenclature. $\theta$ rotates the $\chi$ circle and the attached $\varphi$ circle around an axis perpendicular to the beam. This also rotates the sample attached to the $\varphi$ circle. In the typically definition is $\theta$ -rotation axis parallel to $z$ and the $2\theta$ -rotation axis. Sometimes $\theta$ is also referred as $\omega$ .
$2\theta$	One of the four angles of a four circle diffractometer in the Euler geometry. $2\theta$ rotates the detector around an axis parallel to the $\theta$ -axis. $2\theta$ defines the absolute value of the probed reciprocal lattice vector. While experimentally often used in a mode where $2 \cdot \theta = 2\theta$ are $\theta$ and $2\theta$ are generally independent.
$T_{CDW}$	Charge density wave transition temperature
$T$	Temperature
$f'_{jk}(\vec{k}', \vec{k}, \omega)$	Element $i, j$ of the real part of the resonant part of the tensorial atomic form factor.
$f''_{jk}(\vec{k}', \vec{k}, \omega)$	Element $i, j$ of the imaginary part of the resonant part of the tensorial atomic form factor.
$f_{jk}(\vec{k}', \vec{k})$	Element $i, j$ of the tensorial atomic form factor.
$f_0(\vec{q})$	Thompson scattering atomic form factor.
$W_{ i\rangle \rightarrow  f\rangle}$	Transition rate from state $ i\rangle$ to state $ f\rangle$ .
$\vec{A}(\vec{r}_i)$	The vector potential of the electromagnetic field at position $\vec{r}_i$ from which the electrical field and the magnetic flux density can be calculated.
$V$	Volume.
$\vec{k}$	Incoming wavevector
$\vec{k}'$	Scattered wavevector



## Acronyms

Acronyms	Full Name
ARPES	angle-resolved photoemission spectroscopy
BCS	Bardeen-Cooper-Schrieffer
BESSY II	Berliner Elektronenspeicherring-Gesellschaft für Synchrotronstrahlung II
C-CDW	commensurate charge density wave
CCDC	Cambridge Crystallographic Data Centre
CDW	charge density wave
CEF	crystalline electric field
cT	collapsed tetragonal
DAC	diamond anvil cell
DESY	Deutsches Elektronen-Synchrotron
DFPT	density functional perturbation theory
DHO	damped harmonic oscillator
EDX	energy dispersive X-ray spectroscopy
EPC	electron-phonon coupling
ESRF	European Synchrotron Radiation Facility
ESRF-EBS	European Synchrotron Radiation Facility-Extremely Brilliant Source
FEL	free electron laser
FIB	focused ion beam
FWHM	full width at half maximum
HP	high pressure – used in the context of high hydrostatic pressure
HP XRD	high pressure X-ray diffraction
HWHM	half width at half maximum
I-CDW	incommensurate charge density wave
INS	inelastic neutron scattering
IXS	(non-resonant) inelastic X-ray scattering
JDOS	joint density of states
KIT	Karlsruher Institut für Technologie
NEXAFS	near edge X-ray absorption fine structure
PETRA III	Positron-Elektron-Tandem-Ring-Anlage III
PLD	periodic lattice distortion
REXS	resonant elastic X-ray scattering
RIXS	resonant inelastic X-ray scattering
RSS	residual sum of squares
s-NIXS	s-core-level non-resonant inelastic X-ray scattering
SDW	spin density wave
STM	scanning tunneling microscope
TDS	thermal diffuse scattering
TEY	total electron yield

Acronyms	Full Name
UHV	ultra-high vacuum
XAS	X-ray absorption spectroscopy
XRD	X-ray diffraction
XRF	X-ray fluorescence
XRS	X-ray Raman scattering

## A. Appendix to Chapter 4

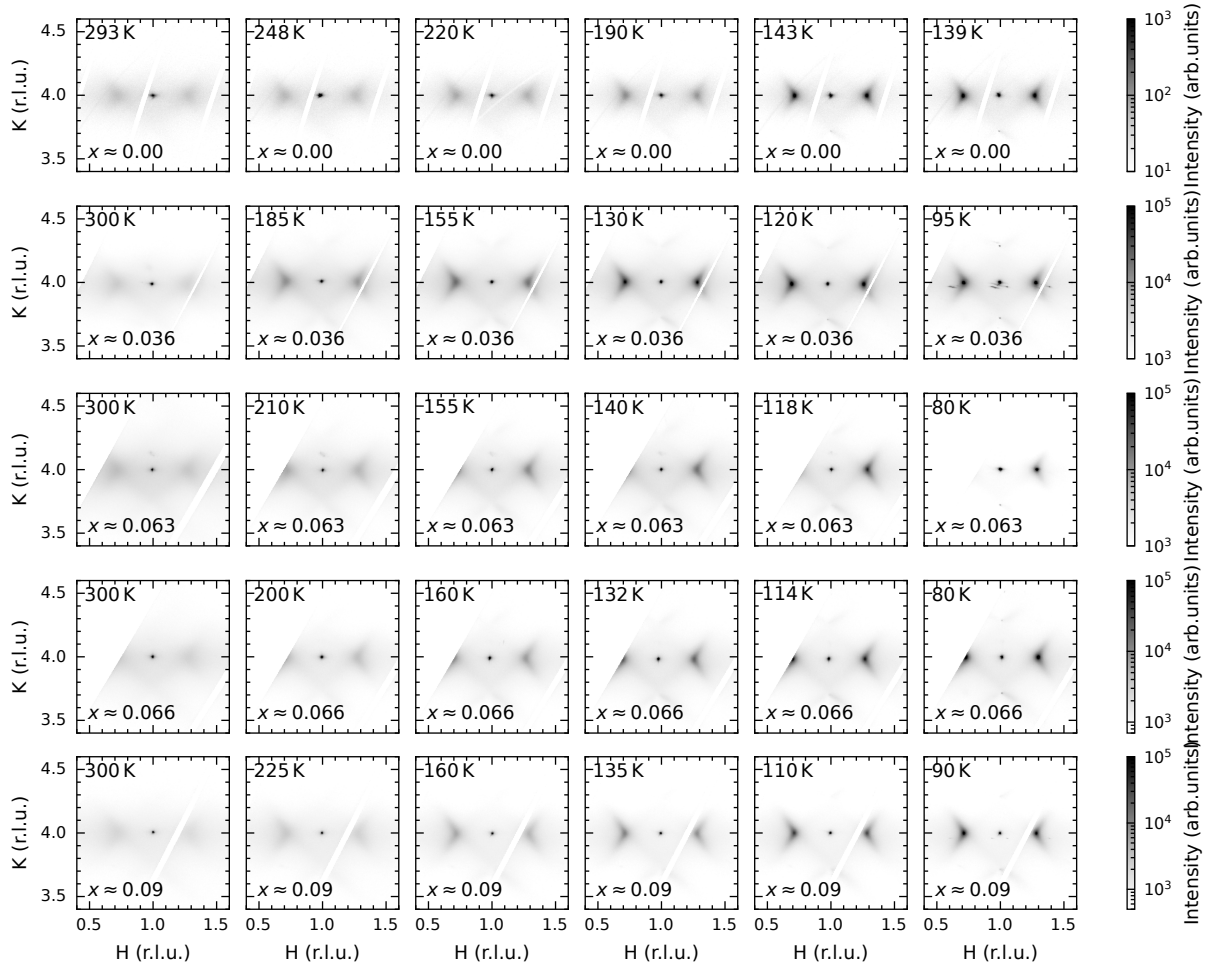


**Figure A.1.:  $(h k 1)$  reciprocal space maps for different temperatures and substitution levels.**  $(h k 1)$  reciprocal space maps of the TDS intensity for different temperatures and substitution levels. The area around the  $(1\ 4\ 1)$ -Bragg peak is shown with the diffuse and ordered I-CDW.

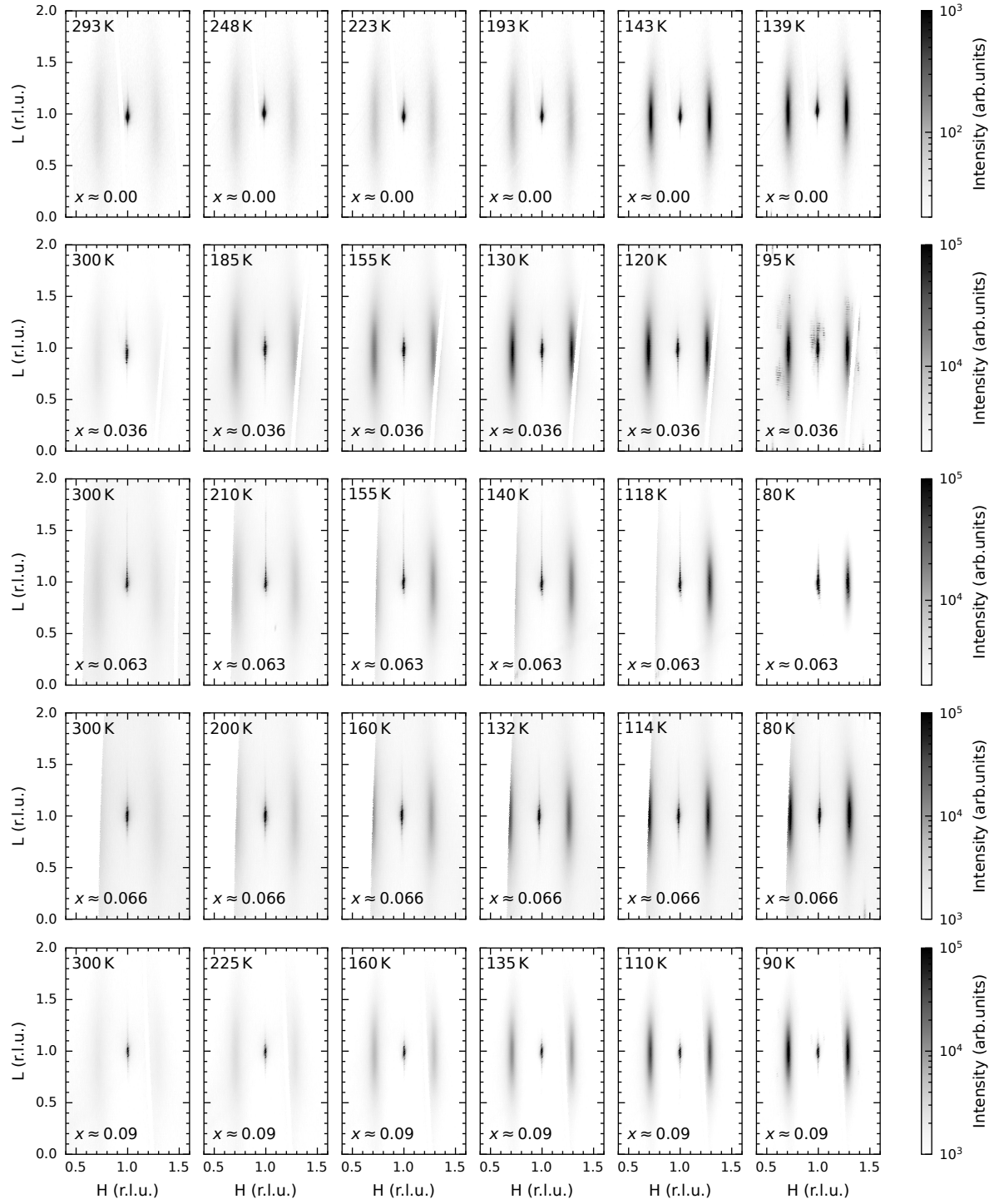


**Figure A.2.:  $(h\ 4\ l)$  reciprocal space maps for different temperatures and substitution levels.**  $(h\ 4\ l)$  reciprocal space maps from TDS measurements for different temperatures and substitution levels. The area around the  $(1\ 4\ 1)$ -Bragg peak is shown with the diffuse and ordered I-CDW.

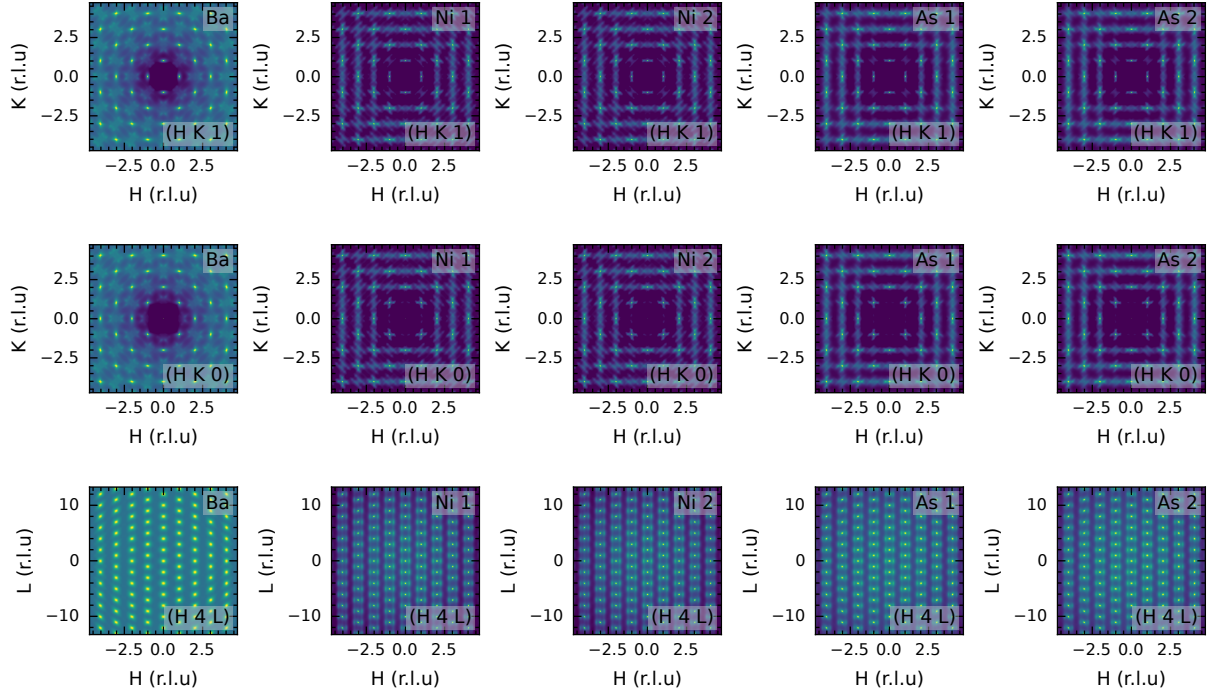


**Figure A.3.: Atom dependent thermal diffuse scattering intensity calculations.** Calculated  $(h k 1)$ ,  $(h k 0)$  and  $(h 4 l)$  reciprocal space maps for the TDS intensity from the different atoms in the primitive unit cell of  $\text{BaNi}_2\text{As}_2$ .

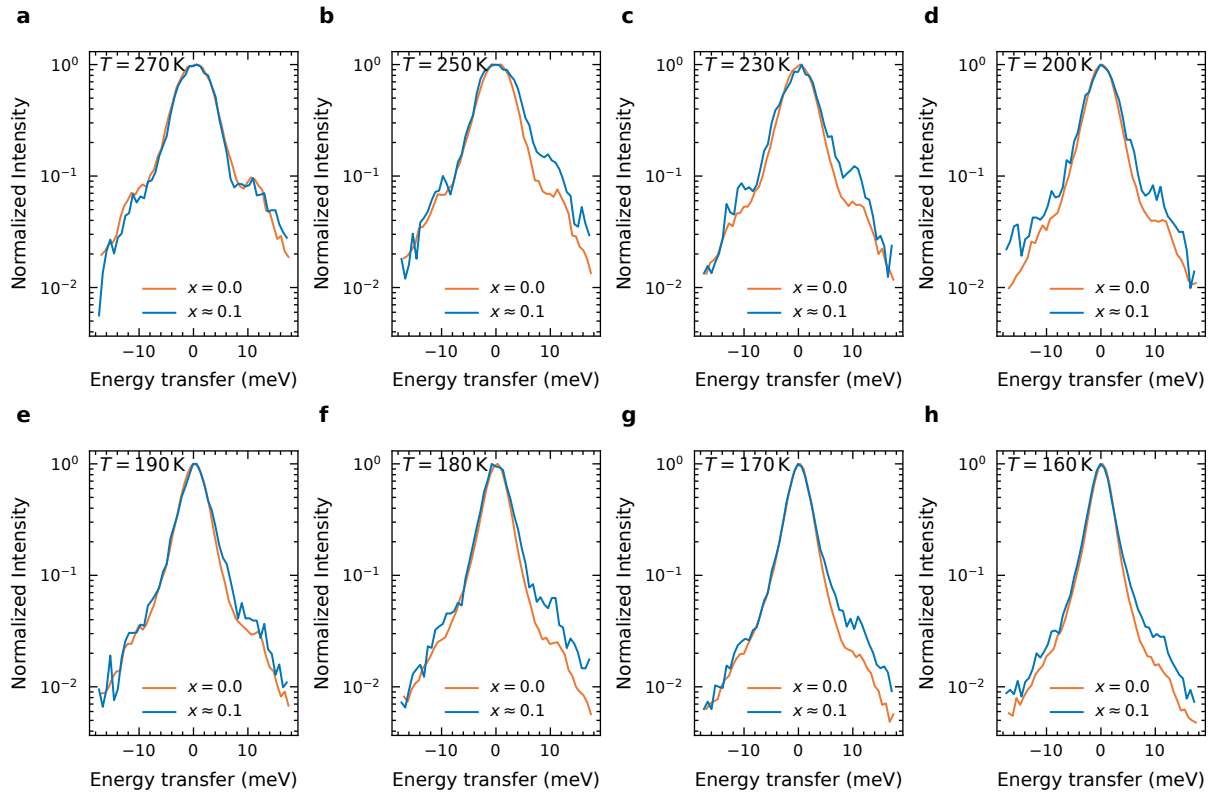


**Figure A.4.: Comparison of the IXS spectra between the pristine and substituted samples.** Direct comparison of the IXS spectra at the I-CDW position for non-substituted and phosphorus substituted  $\text{BaNi}_2\text{As}_2$  for different temperatures.





## B. Appendix to Chapter 5

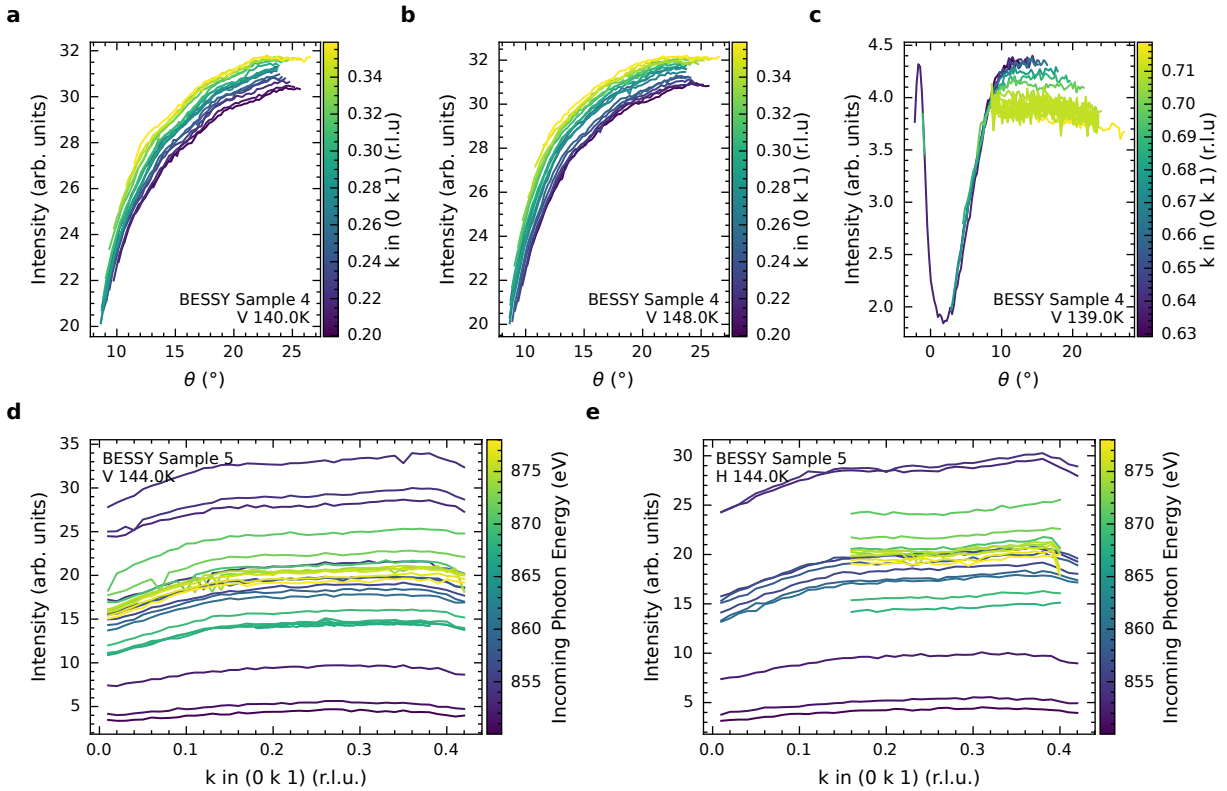


**Figure B.1.: Scans around the  $(0\ 0.28\ 1)$  position.** a-c  $\theta$ - $2\theta$  scans around the  $(0\ k\ 1)$  position for different values of  $k$  at **a** 140 K, **b** 148 K and **c** 139 K. Measurements were performed on sample 4 at BESSY II. **d,e** Scans along the  $k$ -directions around the  $(0\ k\ 1)$  position for different incoming photon energies at 144 K with **d** incoming vertical polarization and **e** incoming horizontal polarization. Measurements were performed on sample 5 at BESSY II.

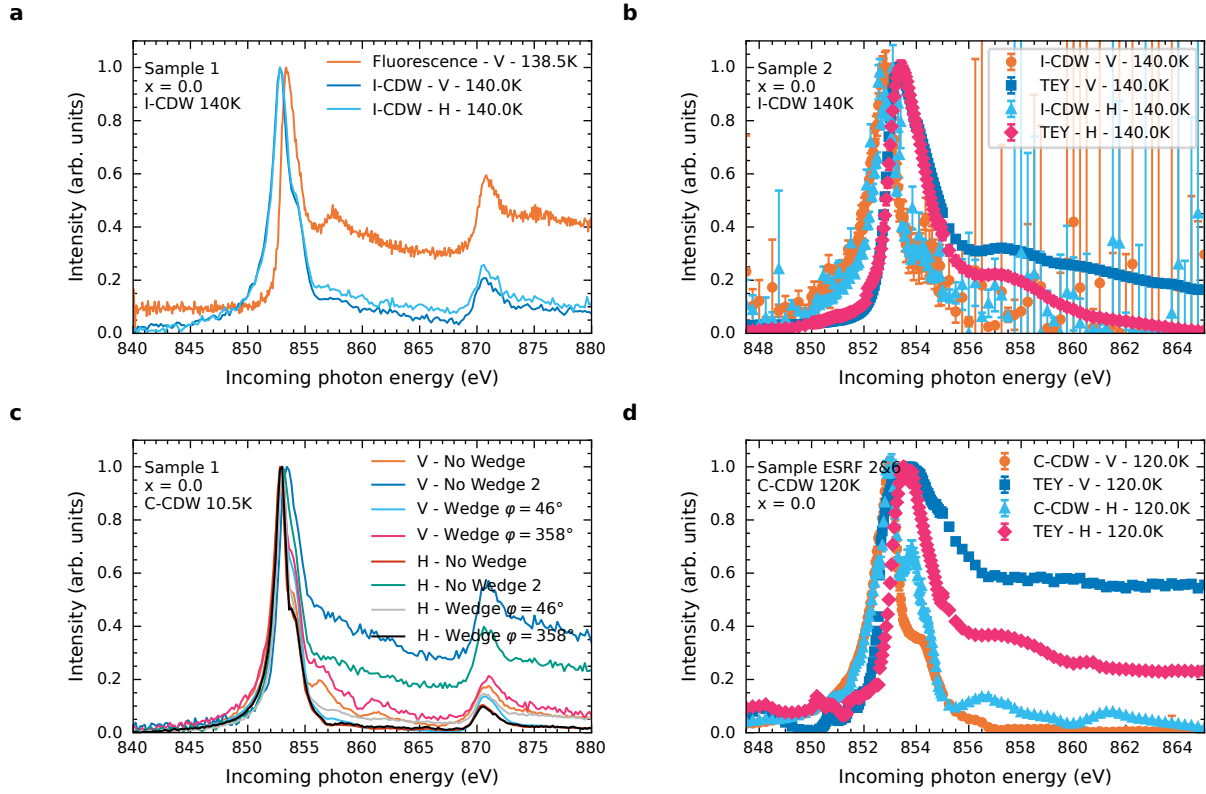


**Figure B.2.:** Energy dependence of the I-CDW and C-CDW scattering signal. **a-b** Energy dependence of the scattering signal at the I-CDW position, TEY or fluorescence at 140 K measured on **a** sample 1 (BESSY II) and **b** sample 2 (ESRF-EBS). **c-d** Energy dependence of the scattering signal at the C-CDW position or TEY at **c** 10.5 K measured on sample 1 (BESSY II) and **d** 120 K measured on sample 2 and 6 (ESRF-EBS). For the C-CDW measurements different orientations of the sample are shown.

**Table B.1.:** Fit parameters of the azimuthal dependence of the I-CDW for the dipole-dipole and dipole-quadrupole fits for orthorhombic and monoclinic (point group 2) symmetry. In the tensors only the allowed parameters are given. Values which are fixed are also stated but without error. The dipole-quadrupole tensor is only given with the first two  $3 \times 3$  matrices, as the third one is by symmetry identical to the second matrix. For some fits the values are not rounded properly as the fit errors exceed the value and otherwise all values would be set to 0. The fit parameters are for sample 1.

Dipole-dipole tensor		Dipole-quadrupole tensor		RSS
Orthorhombic				
DD	$\begin{pmatrix} 00.2(280) & & \\ & 00.2(270) & \\ & & -00.2(180) \end{pmatrix}$	-		18382.76
DD+DQ	$\begin{pmatrix} -00.1(500) & & \\ & 00.06(2500) & \\ & & -00.2(8600) \end{pmatrix}$	$\begin{pmatrix} & & & 000.07(50000) \\ 0 & 0 & 0 & 1 \end{pmatrix}$		13278.64
Monoclinic (point group 2)				
DD	$\begin{pmatrix} 0.1(50) & & 1 \\ & 0.020(20) & \\ 1 & & -0.09(500) \end{pmatrix}$	-		578.16
DD+DQ	$\begin{pmatrix} -0.052(13) & & 0.41(8) \\ & 0 & \\ 0.41(8) & & 0 \end{pmatrix}$	$\begin{pmatrix} & & & -0.71(6) & & -0.145(26) \\ 0 & -0.255(22) & 0 & -0.624(24) & & -1 \\ & & & -0.046(19) & & \end{pmatrix}$		170.23
Monoclinic all parameters				
DD+DQ	$\begin{pmatrix} -0.1(17) & & 00.2(130) \\ & -0.1(50) & \\ 00.2(130) & & -0.02(260) \end{pmatrix}$	$\begin{pmatrix} & & & -0.9(60) & & -0.1(50) \\ 0 & -0.2(70) & 0 & -0.8(60) & & -1 \\ & & & -0.05(400) & & \end{pmatrix}$		165.80

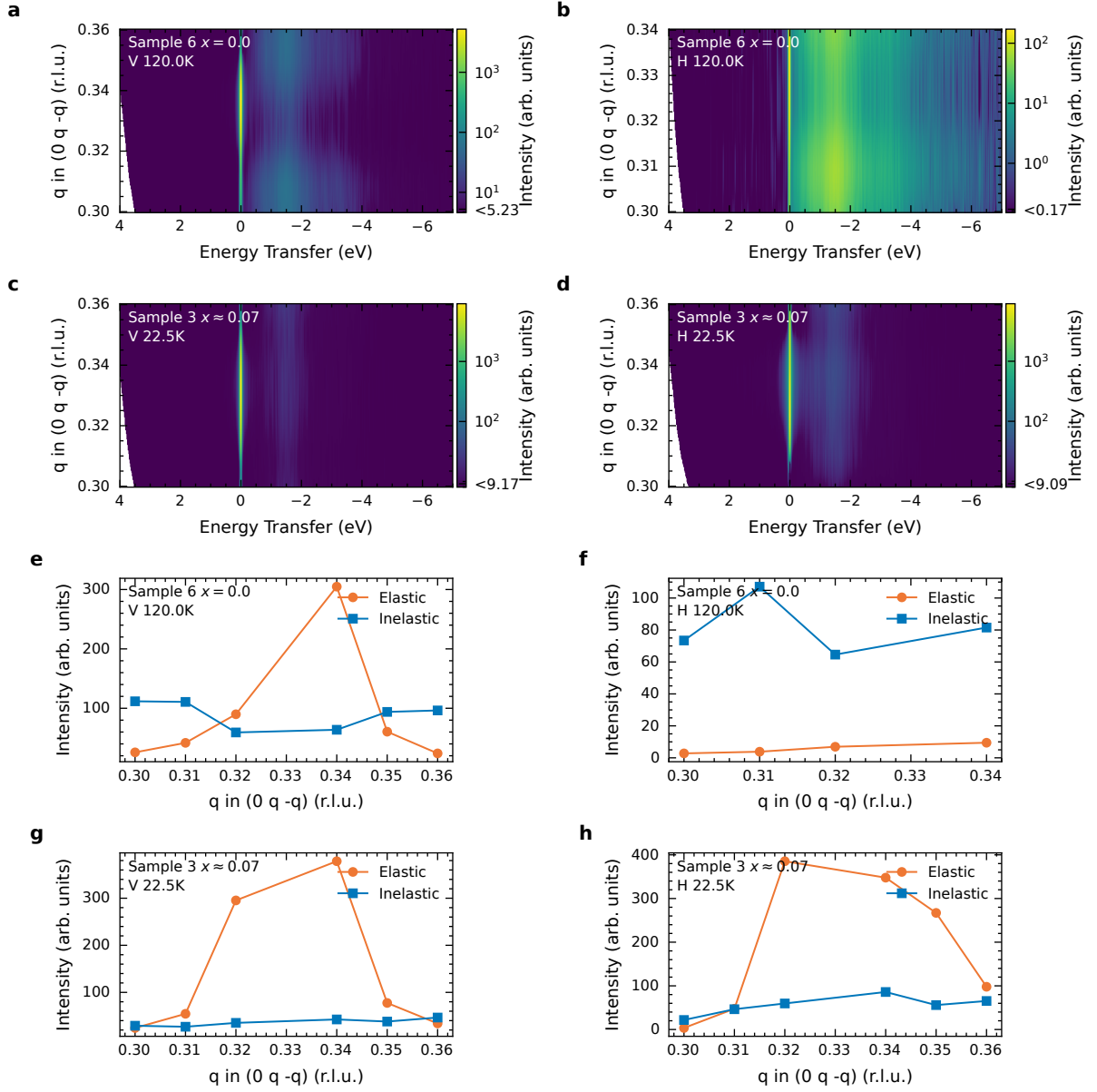


**Figure B.3.: RIXS scans and integrated intensities through the C-CDW.** **a-d** Intensity maps of the RIXS signal for different positions around the C-CDW measured at **a,b** 120 K on sample 6 with incoming vertical and horizontal polarization and **c,d** 22.5 K on sample 3 with incoming vertical and horizontal polarization, respectively. **e-h** Integrated intensity of the elastic and inelastic signal of the colormaps in **a-d**.

**Table B.2.:** Fit parameters of the azimuthal dependence of the I-CDW for the dipole-dipole and dipole-quadrupole fits for orthorhombic and monoclinic (point group 2) symmetry. In the tensors only the allowed parameters are given. Values which are fixed are also stated but without error. The dipole-quadrupole tensor is only given with the first two  $3 \times 3$  matrices, as the third one is by symmetry identical to the second matrix. For some fits the values are not rounded properly as the fit errors exceed the value and otherwise all values would be set to 0. The fit parameters correspond to sample 3.

	Dipole-dipole tensor	Dipole-quadrupole tensor	RSS
Orthorhombic			
DD	$\begin{pmatrix} 000.2(1400) & & \\ & 000.4(2300) & \\ & & 00.3(1900) \end{pmatrix}$	-	11674.26
Monoclinic (point group 2)			
DD	$\begin{pmatrix} -0.070(20) & & 1 \\ & -0.100(20) & \\ 1 & & -0.07(3) \end{pmatrix}$	-	5159.72
DD+DQ	$\begin{pmatrix} -0.07(17) & & 1 \\ & 0 & \\ 1 & & 0 \end{pmatrix}$	$\left( \begin{array}{ccc ccc} 0 & -0.2(5) & 0 & 0.6(4) & & 0.05(120) \\ & & & & 0.9(6) & \\ -0.38(19) & & & & & 0.6(7) \end{array} \right)$	1645.05
Monoclinic all parameters			
DD+DQ	$\begin{pmatrix} -00.05(2200) & & 1 \\ & 00.02(1000) & \\ 1 & & -0.008(9000) \end{pmatrix}$	$\left( \begin{array}{ccc ccc} 0 & -00.3(600) & 0 & 000.4(1100) & & 000.03(18000) \\ & & & & 000.8(1000) & \\ -00.3(400) & & & & & 000.4(1600) \end{array} \right)$	1636.05

## C. Appendix to Chapter 6

### C.1. Samples and pressure paths

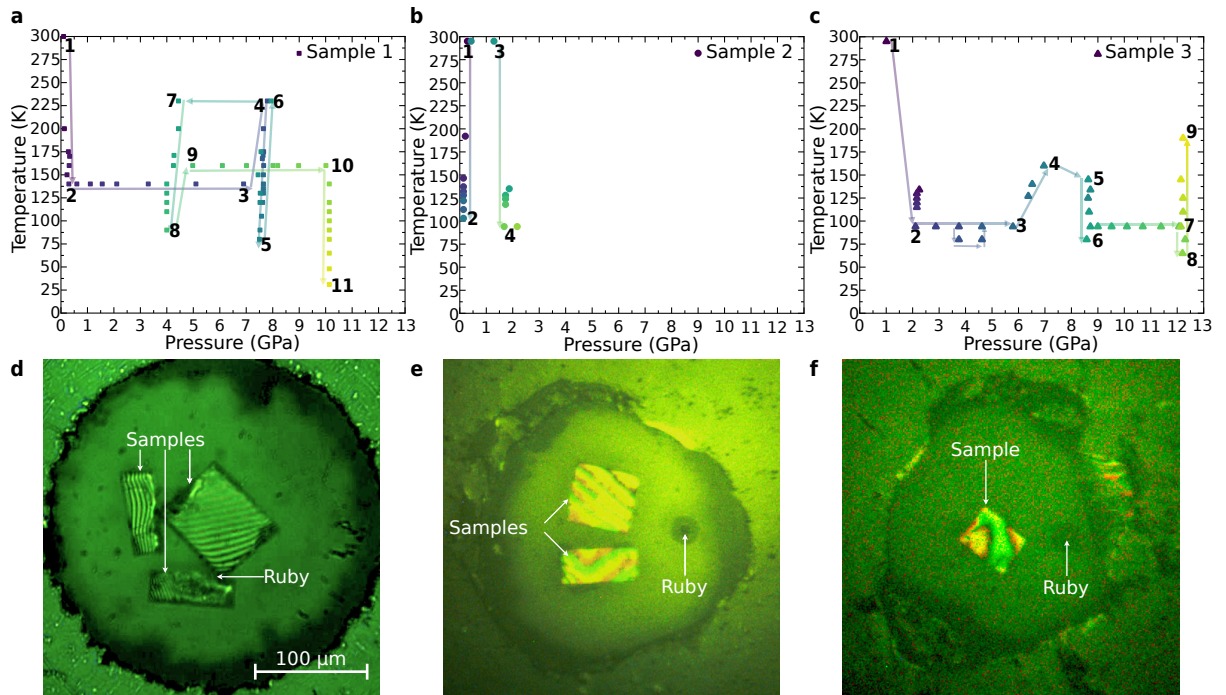


**Figure C.1.:** Chosen  $p$ - $T$ -paths and microscope images of the pristine  $\text{BaNi}_2\text{As}_2$  sample for HP XRD. **a-c** Measurement points in the  $p$ - $T$  phase diagrams for the samples **a** 1, **b** 2 and **c** 3. The chronological order of the measurements points is given by the numbers, arrows, and color of the measurement points (dark blue — first point to light yellow — last point). **d-f** Microscope image of the different samples loaded into the gasket hole into the DACs. The sample and ruby positions are indicated by arrows. **d** Sample 1 (and two other samples that are not shown in the thesis) loaded in the DAC at 0.1 GPa and 298 K. **e** Loading of sample 2 (and an additional sample not discussed in the thesis) at 1.3 GPa and 298 K. **f** Sample 3 at 12.22 GPa and 190 K.

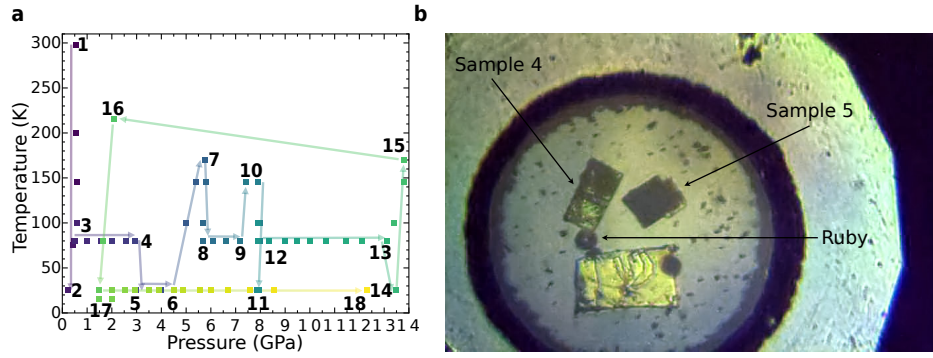


**Figure C.2.:** Chosen  $p$ - $T$ -paths and microscope images of the phosphorus substituted  $\text{BaNi}_2\text{As}_2$  sample for HP XRD. **a** Measurement points in the  $p$ - $T$  phase diagrams for the samples 4 and 5. The chronological order of the measurements points is given by the numbers, arrows, and color of the measurement points (dark blue — first point to light yellow — last point). **b** Microscope image of the samples 4 and 5 into the gasket hole into the DAC. The sample and ruby positions are indicated by arrows. The image was taken at 300 K at the loading pressure of 0.5 GPa.

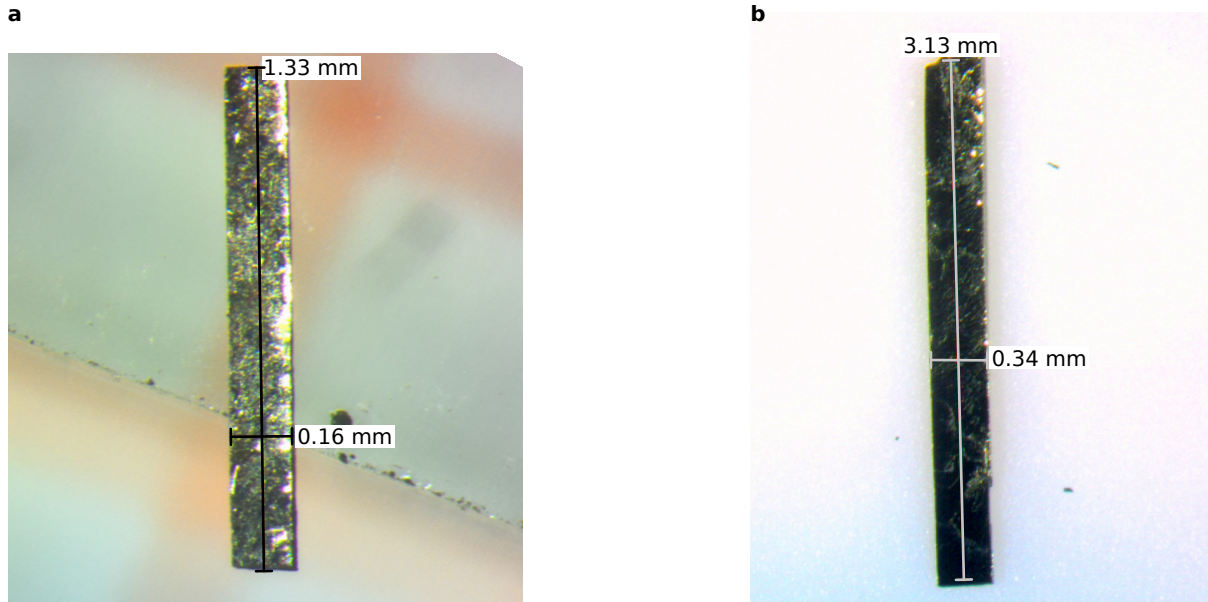
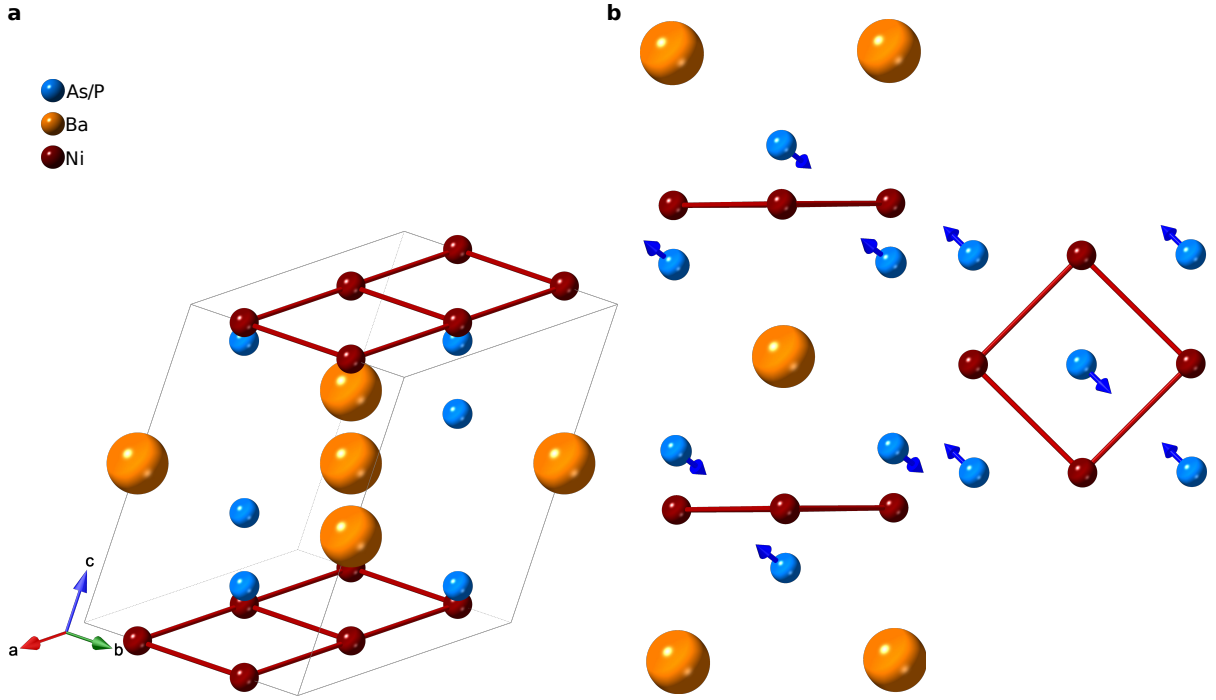


**Figure C.3.:** Microscope images of the cut needles before mounting on the uniaxial pressure cell. **a** The  $x = 0.0$  sample shown in Section 6.5 before mounting to the sample holder and the uniaxial pressure cell. **b** The  $x = 0.1$  sample shown in Section 6.5 before mounting to the sample holder and the uniaxial pressure cell.

## C.2. Structural details

The details of all structures observed in the non-substituted  $p$ - $T$  phase diagram discussed in Section 6.3 are given in Table C.1. The changes with respect to the original tetragonal unit cell are already discussed in Section 6.3.4 and will not be discussed further here.

The additional observed monoclinic III structure in the phosphorus substituted HP XRD measurements in Section 6.4 is shown in Figure C.4a. The changes regarding the tetragonal unit cell remain minimal. The only visible change is a distortion of the arsenic position. The change in the arsenic atomic positions with respect to the original tetragonal unit cell are shown by blue arrows in Figure C.4b. At a first glance, the change seems similar to what is observed in the monoclinic II structure, however the change in the tetragonal  $c$ -direction are smaller and the in plane changes are along the tetragonal  $a$  and  $b$

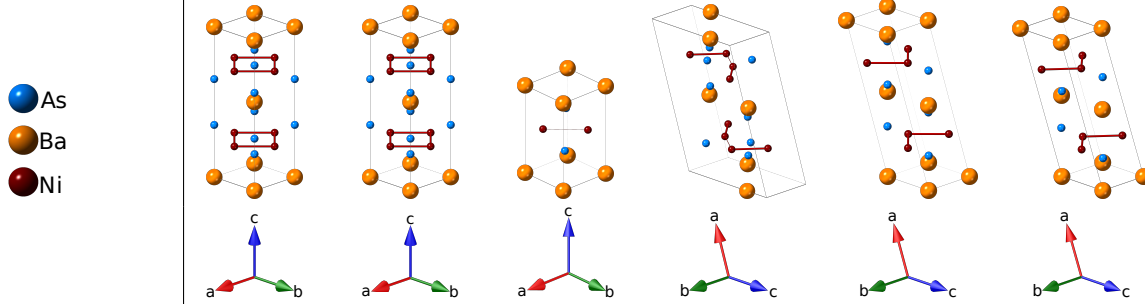


**Figure C.4.: Crystal structure of the monoclinic III phase.** **a** Crystal structure of the monoclinic III phase at 25 K and 0.25 GPa. **b** Structural changes with respect to the original tetragonal unit cell. The Ni-Ni bonds are shown with red lines. The direction and magnitude of the position changes of the arsenic atoms with respect to the tetragonal structure are indicated by blue arrows. All changes are shown in the coordinate system created by the outer barium atoms to normalize for changes in the unit cell. For visualization, the magnitude of the movement is exceeded by a factor of 200. The changes in the nickel are too small and are therefore omitted.

direction (meaning in the direction of the new  $a$  direction as the unit cell is rotated by  $45^\circ$ ) and not along the tetragonal  $a$  direction. In addition, the total changes are at least an order of magnitude smaller than what is observed in the monoclinic I and monoclinic II structure.



**Table C.1.:** Overview of the unit cell, space group, lattice parameters  $a, b, c$ , angles  $\alpha, \beta, \gamma$ , R-factors, the positions and atomic displacement parameters of barium, nickel and arsenic a for all six observed phases. For each data set the corresponding pressure and temperature is stated.

	Tetragonal	Orthorhombic	Triclinic	Monoclinic I	Monoclinic IIa	Monoclinic IIb
Pressure (GPa)	0.21	0.29	0.14	4.6	8.64	11.39
Temperature (K)	192	146	128	94	145	94
						
Space Group	$I4/mmm$	$Immm$	$P\bar{1}$	$C2/c$	$C2/m$	$C2/m$
$a$ (Å)	4.1275(1)	4.1227(14)	4.1380(8)	11.697(13)	11.434(19)	10.882(4)
$b$ (Å)	4.1275(1)	4.1230(12)	4.1625(8)	4.1210(15)	4.0901(3)	4.0874(1)
$c$ (Å)	11.606(6)	11.614(7)	6.385(4)	8.235(2)	4.093(23)	4.0961(45)
$V$ (Å <sup>3</sup> )	197.74(1)	197.43(1)	98.64(7)	374.6(3)	178.52(3)	168.3(1)
$\alpha$ (°)	90	90	108.47(3)	90	90	90
$\beta$ (°)	90	90	107.695(3)	109.29(7)	111.17(12)	112.48(26)
$\gamma$ (°)	90	90	90.78(16)	90	90	90
$x$ (Ba)	0	0	0	0	0	0
$y$ (Ba)	0	0	0	0.0017(7)	0	0
$z$ (Ba)	0	0	0	1/4	0	0
$x$ (As)	0	0	0.3650(6)	0.3478(15)	0.3529(4)	0.362(1)
$y$ (As)	0	0	0.3652(4)	0.0452(14)	0	0
$z$ (As)	0.3474(5)	0.3475(5)	0.6897(3)	0.4385(9)	0.3506(6)	0.353(1)
$x$ (Ni)	0	1/2	0.2225(9)	0.2498(2)	0.7503(8)	0.747(12)
$y$ (Ni)	1/2	0	0.7788(2)	0.0530(18)	0	0
$z$ (Ni)	1/4	0.25002(69)	0.4984(9)	0.1431(1)	0.253(1)	0.261(14)
ADPs						
Ba						
$U_{11}$ (Å <sup>2</sup> )	0.0144(5)	0.01277(47)	0.01044(18)	0.02472(25)	0.01532(52)	0.0263(9)
$U_{22}$ (Å <sup>2</sup> )	0.0144(5)	0.01351(46)	0.01332(4)	0.00325(17)	0.00825(48)	0.00274(77)
$U_{33}$ (Å <sup>2</sup> )	0.0421(57)	0.01014(76)	0.00601(11)	0.00496(3)	0.0142(1)	0.00602(13)
As						
$U_{11}$ (Å <sup>2</sup> )	0.01869(58)	0.02319(71)	0.00588(18)	0.02780(31)	0.01016(74)	0.0416(1)
$U_{22}$ (Å <sup>2</sup> )	0.01869(58)	0.02318(73)	0.05065(38)	0.00434(19)	0.01065(6)	0.00455(9)
$U_{33}$ (Å <sup>2</sup> )	0.02562(78)	0.02233(13)	0.01222(14)	0.00575(33)	0.01320(15)	0.0095(1)
Ni						
$U_{11}$ (Å <sup>2</sup> )	0.02562(78)	0.01685(58)	0.00619(26)	0.02221(38)	0.0341(1)	0.0148(1)
$U_{22}$ (Å <sup>2</sup> )	0.02562(78)	0.01752(56)	0.00170(22)	0.00515(24)	0.01535(9)	0.0079(1)
$U_{33}$ (Å <sup>2</sup> )	0.0274(1)	0.00044(14)	0.04125(26)	0.00589(4)	0.02005(16)	0.00873(2)
$R_{\text{int}}$	0.0281	0.0180	0.0204	0.0210	0.0104	0.0254
$R_1$	0.0170	0.0243	0.0279	0.0299	0.0258	0.0302
$wR_2$	0.0460	0.0632	0.0578	0.0745	0.0540	0.0561



**Table C.2.:** Overview of the unit cell, space group, lattice parameters  $a, b, c$ , angles  $\alpha, \beta, \gamma$ , R-factors, the positions and atomic displacement parameters of barium, nickel and arsenic for the monoclinic III structure.

	Monoclinic III
Pressure (GPa)	0.25
Temperature (K)	25
Space Group	$C2/m$
$a$ (Å)	5.8206(19)
$b$ (Å)	5.8197(9)
$c$ (Å)	6.471(7)
$V$ (Å <sup>3</sup> )	195.8
$\alpha$ (°)	90
$\beta$ (°)	116.71(8)
$\gamma$ (°)	90
$x$ (Ba)	0
$y$ (Ba)	0
$z$ (Ba)	1/2
$x$ (As/P)	0.346546
$y$ (As/P)	0
$z$ (As/P)	0.194401
$x$ (Ni)	0
$y$ (Ni)	0.24990(18)
$z$ (Ni)	0
Substitution level	0.075
ADPs	
Ba	
$U_{11}$ (Å <sup>2</sup> )	0.0082(5)
$U_{22}$ (Å <sup>2</sup> )	0.0098(5)
$U_{33}$ (Å <sup>2</sup> )	0.0132(26)
As	
$U_{11}$ (Å <sup>2</sup> )	0.0119(6)
$U_{22}$ (Å <sup>2</sup> )	0.0147(8)
$U_{33}$ (Å <sup>2</sup> )	0.020(5)
Ni	
$U_{11}$ (Å <sup>2</sup> )	0.0164(7)
$U_{22}$ (Å <sup>2</sup> )	0.0213(11)
$U_{33}$ (Å <sup>2</sup> )	0.009(5)
$R_{\text{int}}$	0.0129
$R_1$	0.0143
$wR_2$	0.0180

### C.3. I-CDW1 intensity and linecuts

In Figure C.5 the linecuts through the CDW positions for the phosphorus substituted samples 4 and 5 are shown. Starting with the linecuts in the  $[1\ 0\ 0]$ - and  $[0\ 1\ 0]$ -directions through the I-CDW position, both samples show the superstructure reflections of the I-CDW1 at 80 K. Sample 5 exhibits the peaks also at 25 K. For both samples a loss of the two additional I-CDW1 peaks around the Bragg peaks can be observed around 7 GPa. This is due to the transition to the I-CDW2 phase and the I-CDW2 superstructure peaks do not lie on the linecut.

The linecuts in the  $[0\ 1\ 1]$ -direction from sample 4 at 25 K are different. At the lowest pressure, clear C-CDW1 peaks and shoulder peaks from the twins are visible. They are rapidly suppressed, before at moderately higher pressures the peak of C-CDW2 can be observed.

The change of intensity is more difficult and noisy. Part of this is due to the increased background from the diamond scattering. Nonetheless, the peaks can be fitted and the resulting intensities are shown in Figure C.6. All cases have in common that the intensity decreases to zero around the transition to the I-CDW2. Though, at lower pressures in sample 4 at 80 K and sample 5 at 25 K (second compression) an increase in the intensity in one direction ( $h$  or  $k$ ) is observed, while for the other direction the intensity decreases. For sample 5 at 80 K and 25 K (first compression) the intensity in both direction is suppressed comparably. This might be related to small non-hydrostaticity, as in the ordered phase uniaxial components can influence the I-CDW1 intensity as shown in Section 6.5.

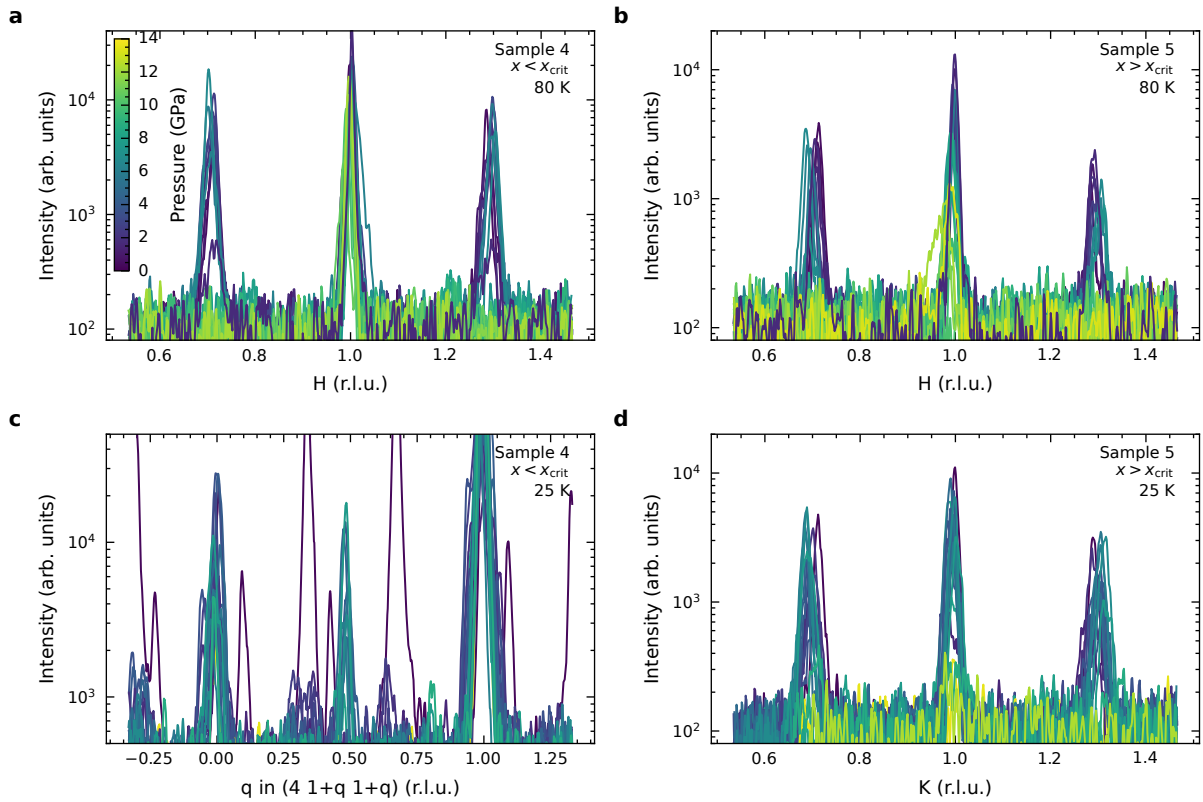


**Figure C.5.: Linecuts through the different CDWs for different pressures.** Linecuts through the different CDWs for a sample 4 at 80 K, b sample 5 at 80 K, c sample 4 at 25 K and d sample 5 at 25 K for two different compressions.

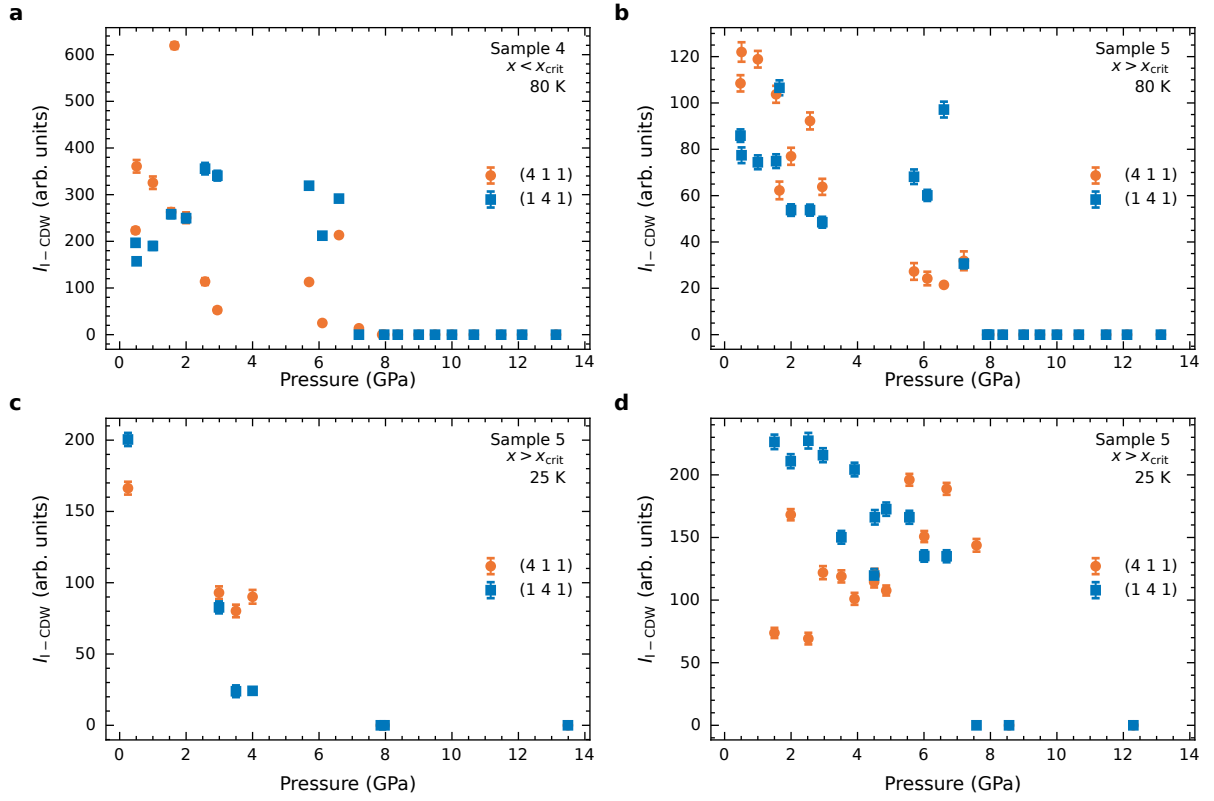


**Figure C.6.: Intensity of the I-CDW1 versus hydrostatic pressure.** Intensity versus hydrostatic pressure for **a** sample 4 at 80 K, **b** sample 5 at 80 K and **c-d** sample 5 at 25 K for two different compressions.

#### C.4. Uniaxial compression of a $x=0$ sample at 140 K

In Figure C.7 the reciprocal space maps and extracted parameters from a second  $x = 0$  sample at 140 K are shown. The reciprocal space maps show comparable diffuse and ordered I-CDW1 peaks at nominal zero compression. In the  $(h \bar{4} l)$ -maps the different peaks in the  $l$ -direction, probably introduced from slipping of planes during the cutting process, are shown.

With a first compression to -0.19% strain, no significant changes can be observed. However, with further increasing nominal strain, the last reciprocal space maps can be obtained. In those clearly different twins, similar to what is observed in the triclinic phase can be observed. Further, also C-CDW1 reflections appear, but the I-CDW1 peaks remain. This suggests a coexistence of the orthorhombic and triclinic phase. This could also explain that the extracted strain values are smaller.

Similar, the extracted  $b$  and  $c$  lattice parameters do not show a clear trend. Furthermore, the wave vector, intensity, and correlation length of the I-CDW1 do not show reliable results, most likely due to the coexistence of the two phases. Therefore, the data was not included in the main text.

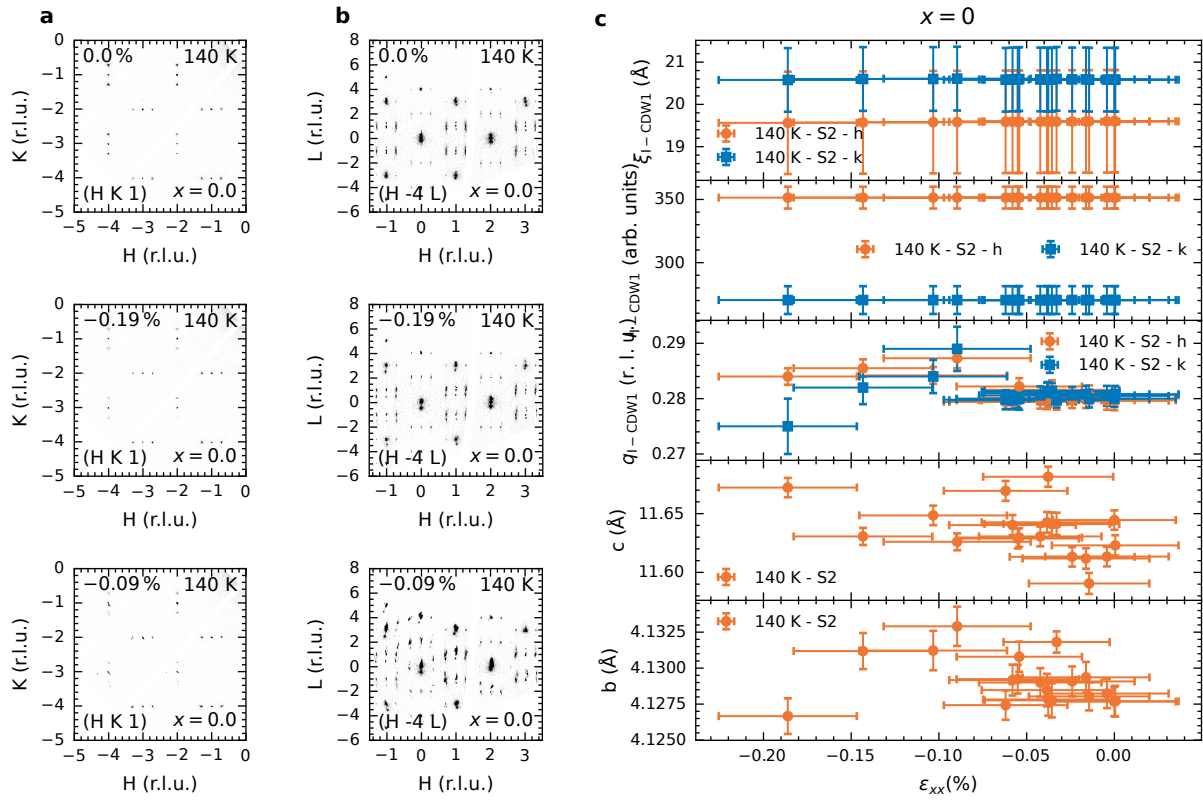


**Figure C.7:** Reciprocal space maps, lattice parameters and I-CDW1 parameters for a  $x=0$  sample at 140 K. **a**  $(h k l)$  and **b**  $(h -4 l)$  reciprocal space map for a  $x = 0.0$  sample at 140 K for different strain values. **c**  $b$ ,  $c$  lattice parameters, I-CDW1 wave vector, intensity, and correlation length for a  $x = 0.0$  sample at 140 K.

## D. Inelastic X-ray scattering at the I-CDW2 position in an P-substituted $x=0.1$ sample at ambient pressure

As shown in Section 6.3.5, first-principles calculations show a phonon anomaly close to the I-CDW2 already at low pressures. In fact, it turns out that calculations on the ambient pressure structure also show this anomaly (see Section 4.3.2). As the IXS measurements on the  $x = 0.1$   $\text{BaNi}_2(\text{As}_{1-x}\text{P}_x)_2$  sample were performed chronologically after the HP XRD measurements and the DFPT calculations on the pristine sample, this allowed to check for the anomaly at ambient pressure. Calculations using the experimentally determined tetragonal crystal structure at a substitution of  $x = 0.1$  also exhibits the anomaly. Together with the observation of the I-CDW2 in Section 6.4 in both samples above and below the critical substitution level suggests that the substitutes sample should behave similar to a pristine sample. Note, however, that the DFPT calculations were not performed considering the actual

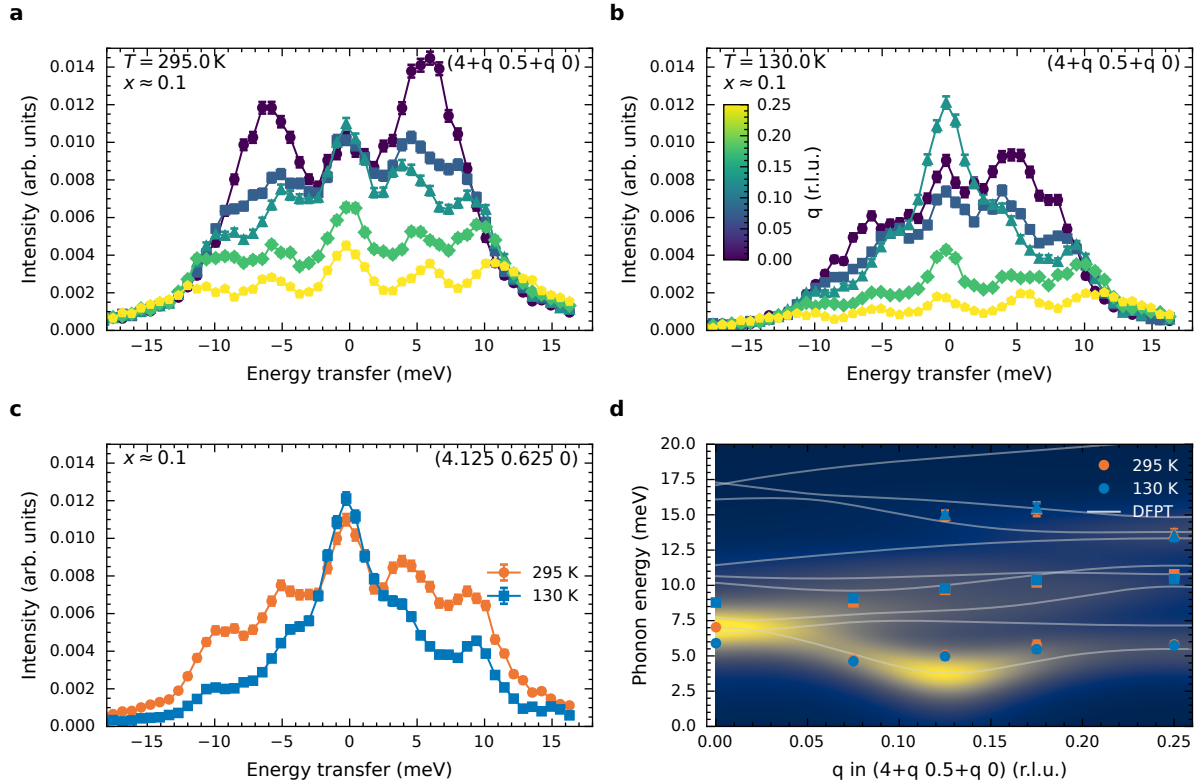


**Figure D.1.: Inelastic X-ray scattering spectra and fitted dispersion around the I-CDW2 position.** **a-b** IXS spectra along  $(4 + q \frac{1}{2} + q \ 0)$  crossing close to an I-CDW2 position at **a** 295 K and **b** 130 K measured on the  $x = 0.1$  sample investigated in Section 4.3.3. **c** Comparison of the IXS spectra closest to the I-CDW2 position at 295 K and 130 K. **d** Fitted phonon dispersion extracted from the IXS spectra in **a-b**. In the background, the calculated phonon dispersion and IXS intensities are shown. The IXS intensity is broadened with the experimental resolution function.

exchange of phosphorus atoms for arsenic atoms, as this is generally difficult to do with DFPT. The IXS measurements were performed on the same  $x = 0.1$  sample (sample 2) during the same beamtime as the measurements in Section 4.3.3.

The measured IXS spectra and the fitted dispersion are shown in Figure D.1. The spectra along the  $(4+q\ 1/2+q\ 0)$ -line do not show an anomaly neither at 295 K nor at 130 K – below the I-CDW2 ordering temperature also in the substituted compound. The spectra do not change significantly between 295 K and 130 K. This is also true for the point closest to the I-CDW2 position in Figure D.1c, that mainly show the difference because of the different phonon occupation because of the Bose-Einstein distribution. It must be noted that the position is only an approximation of the I-CDW2 position as also the position shows a strong change and the calculations show a slightly different wavevector. Especially, if the anomaly is sharp in reciprocal space it is possible that the anomaly was just missed. However, in the complete dispersion in Figure D.1d there is no clear anomaly and only little change between the two temperatures. This suggests that the DFPT calculations overestimate the I-CDW2 instability, similar to what was observed in the TDS measurements in Section 4.3.2. Nevertheless, the measured dispersion shows overall a good agreement with the DFPT calculations. The smaller difference could come from close by phonon branches and the limited energy resolution.

The calculations also show a major difference of between the I-CDW1 and I-CDW2. As shown in the maps in Figure A.3 for the diffuse scattering at the I-CDW2 position, all types of atoms are involved. This is different to the I-CDW1, for which only the Ni and As atoms are involved. Further, not a single type atom shows the complete structure observed in TDS. So only the combination of all atoms give the right pattern. As the patterns from single atoms show some kind of asymmetry, this might also explain the distortion of the I-CDW2 observed at high pressures, as the different kinds of atoms may react different to the applied pressure.